Cranfield University

Silvana Corkovic

Piezoelectric Thick Films for Microelectromechanical Systems Application

School of Applied Sciences

PhD Thesis

Cranfield University

School of Applied Sciences

Department of Materials

Nanotechnology Group

PhD Thesis

2007

Silvana Corkovic

Piezoelectric Thick Films for Microelectromechanical Systems Application

Dr. Q. Zhang

19 March 2007

© Cranfield University, 2007. All rights reserved. No part of this publication may be reproduced without the written permission of the copyright holder.

This thesis is submitted in partial fulfilment of the requirements for the degree of PhD.

Abstract

This thesis concerns the processing and characterization of thick PZT sol-gel films for potential applications in MEMS devices. The deposition method was spin-coating. The aim was to reduce the number of coatings in the film processing by increasing the thickness of a single coating, with the restriction that the processed films must be crack-free and dense. Only by retaining the thick film dense, pore-free and crack-free one can obtain the piezoelectric properties in thick films that make the PZT thin sol-gel films attractive for the MEMS applications.

Three PZT compositions, PZT 40/60, PZT 60/40 and PZT 52/48 were investigated. Each one of these PZT compositions has different crystallographic structure and thus differences in the piezoelectric properties were expected.

The processing of thickness-increased sol-gel films was investigated. A combination of analysis techniques was employed. The stress development was monitored via ex-situ wafer deflection measurement after various fabrication steps. The ongoing processes in the sol-gel film were identified and correlated to certain temperature ranges and to the stress that is induced with each process in the film. It was found that crack-free films could be fabricated if a stress-controlled heating profile was applied. The PZT films were deposited on platinised silicon substrate and it was found that stress-related recrystallization was taking place in the platinum electrode which affected the total stress. After the platinum recrystallization the stress state in the bottom electrode and in the substrate was stable.

Films up to 5 μm thick were obtained by repeated deposition of 200 nm thick single layers. The maximum thickness of a single coating was increased to 500 nm and a 2.5 μm film was fabricated by only 5 repeated coatings.

The crystallographic orientation of all three employed PZT compositions was studied systematically on Pt/Si substrate at different thicknesses. Also, individual PZT films were deposited onto platinised sapphire substrates, or on LNO/Si substrate. It was found that the orientation of the films changes gradually with each coating.

The residual stresses in all three PZT compositions were studied. A stress model for composite structures was applied for the first time in PZT films stress analysis. The results have shown that the residual stress at the room temperature is due to thermal

expansion mismatch between the individual layers. Furthermore, a large orientation dependent stress variation was found in PZT 52/48 films that could be only explained if anisotropic thermal expansion in PZT were considered. The lattice parameters of all PZT compositions were determined and were in good agreement with the residual stress results. Thus, using the stress model it was possible to understand the origin of stress in PZT films.

Finally, the electrical properties of the PZT films were determined. It was found that the piezoelectric, dielectric and ferroelectric properties of PZT films vary with PZT composition, film thickness and depend on the substrate type. Based on the finding it was proposed that there must be an interfacial layer that is responsible for domain wall pinning and thus reduced PZT properties in films below 5 μm thickness. In thick PZT 40/60 films enhanced piezoelectric properties were found making these PZT compositions very promising candidates for MEMS application.

Acknowledgements

First of all I would like to thank my supervisor, Dr. Q. Zhang, for his competent guidance and tremendous help and support. I would like to express my gratitude towards Prof. R. Whatmore for supervisory guidance throughout this project while he was at regular basis at Cranfield University.

I wish to thank all from the Nanotechnology Group for the inspiring discussions and helping hand, especially to Mr. R. Wright and Mr. G. Leighton, Dr. S. Marson, Dr. C. Bertoni, Dr. C. Shaw and Mr. A. Stallard. I also want to thank all from the Nanotechnology group for the welcomed breaks from the work; to all who are still there and those who left long time ago.

Last but not least, my warmest thanks go to Max Mergen, to all my friends and family for bringing joy into my scientific and everyday life.

TABLE OF CONTENTS

ABSTRACT
ACKNOWLEDGEMENTS
TABLE OF CONTENTS i
LIST OF FIGURES vii
LIST OF TABLES xv
LIST OF SYMBOLS xvii
LIST OF EQUATIONS xix

INTRODUCTION TO THE THESIS 1

CHAPTER 1: INTRODUCTION: BACKGROUND AND LITERATURE SURVEY...3

1 Introduction to the Chapter.. 3
1.1 Brief historical background...3
1.2 Background.. 4
1.2.1 Polarity of crystal classes... 4
1.2.2 Formation of ferroelectric domains..5
1.2.3 Ferroelectricity and hysteresis loop..6
1.3 The system lead titanate - lead zirconate (PT-PZ).......................................8
1.3.1 Domain formation in PZT films...9
1.3.2 The piezoelectricity of PZT..11
1.4 Applications of piezoelectric materials...15
1.4.1 Summary..19
1.5 Chemical solution deposition of PZT (CSD)..20
1.5.1 Sol-gel processing of thin films.. 22
1.5.1.1 Spin coating... 24
1.6 Thick sol-gel films.. 26
1.7 Residual stress in PZT films... 30
1.8 Summary... 32

1.9 Aim and the objectives of the study....33

CHAPTER 2: EXPERIMENTAL PROCEDURES: PROCESSING AND CHARACTERISATION OF PZT FILMS.... 37

2.1 Introduction to the Chapter....37
2.2 Deposition techniques....37
2.2.1 Physical vapour deposition techniques (PVD)....37
2.2.1.1 PVD sputtering....37
2.2.1.2 PVD thermal evaporation....39
2.2.2 Preparation of sol precursor....39
2.2.2.1 Synthesis of PZT sol precursors....40
2.2.2.2 Synthesis of $LaNiO_3$ and PbO sols 41
2.2.3 Thermal oxidation....41
2.3 Thick film processing....41
2.4 Sample preparation for electrical characterization....42
2.4.1 Poling 43
2.4.1.1 Contact poling....43
2.4.1.2 Corona poling....43
2.5 Analytical techniques and methods....44
2.5.1 Analytical techniques for microstructure characterization....44
2.5.1.1 Optical microscopy....45
2.5.1.2 Scanning electron microscopy (SEM)....45
2.5.1.2.1 Chemical composition analysis with EDX....46
2.5.1.3 Atomic force microscopy (AFM)....46
2.5.1.4 X-Ray diffraction (XRD)....47
2.5.1.4.1 Qualitative phase analysis....48
2.5.1.4.2 Crystallinity and preferred orientation....49
2.5.1.4.3 Calculation of lattice parameters 50
2.5.1.4.4 Crystallite size and microstrain....51
2.5.2 Characterization of physical properties....52
2.5.2.1 Dielectric properties and capacitance measurement....52

2.5.2.2 Ferroelectric polarization measurement.............................. 53
2.5.2.3 Determination of piezoelectric constants............................ 54
2.5.2.4 Sheet resistivity measurements.. 54
2.5.3 Stress analysis 55
2.5.3.1 Townsend-model for stress calculation...............................55
2.5.3.2 Determination of wafer curvature by surface profilometry 58

CHAPTER 3: RESULTS AND DISCUSSION..61

3.1 Introduction to the Chapter... 61
3.2 PZT thick film processing...62
3.2.1 Increase of single layer thickness..62
3.2.2 Investigation of key processing parameters.................................... 63
3.2.3 Stress related deflection development in multilayer film deposition... 70
3.2.4 The effect of the platinised silicon substrate on the total wafer bending.. 72
3.2.5 Stress related wafer deflection and processing of sol-gel PZT films on different substrates.. 82
3.2.6 Deflection in single layer of three PZT compositions on platinum during sol-gel film processing... 85
3.2.7 Summary of the section and future work... 88
3. 3 Crystallographic orientation of PZT thick films...91
3.3.1 Introduction to the section..91
3.3.2 Film morphology..91
3.3.3 Crystallographic orientation of PZT films on Pt(111).................... 92
3.3.3.1 Tetragonal PZT 40/60.. 93
3.3.3.2 Rhombohedral PZT 60/40...99
3.3.3.3 Phase characterization and orientation of PZT 52/48.......... 102
3.3.4 The effect of post-annealing on the orientation of the PZT films... 104

3.3.5 The effect of PbO buffer layer 105
3.3.6 The effect of single layer thickness on orientation 106
3.3.7 Crystallographic orientation in 5 µm thick films 107
3.3.8 Effect of the bottom electrode on the orientation of thick PZT films 107
3.3.8.1 PZT 52/48 on $LaNiO_3$/Si substrate 108
3.3.8.2 PZT on Pt(200)/Si(100) substrate 110
3.3.8.3 Effect of the sapphire substrate (Al_2O_3) on the PZT film orientation 111
3.3.9 Chemical analysis of PZT films 113
3.4 Residual stress analysis 114
3.4.1 Introduction to the section 114
3.4.2 Preliminary characterizations 114
3.4.2.1 Initial consideration 114
3.4.2.2 Stress in as-sputtered platinum 116
3.4.2.3 Curvature simulation 117
3.4.2.4 The parameter variation 119
3.4.3 Residual stress in PZT films with different composition 125
3.4.4 Residual stress and film orientation 129
3.4.5 Stress on compressive substrate 134
3.4.6 Wafer size influence 138
3.4.7 Stress controlled phase formation 140
3.5 Microstructural characterization 143
3.5.1 Lattice parameter of PZT films with different compositions 143
3.5.2 Crystallite size of PZT films with different compositions 151
3.5.3 Morphology of PZT films 155
3.6 Electric properties of PZT films 163
3.6.1 Introduction to the section 163
3.6.2 Dielectric properties 163
3.6.2.1 Dielectric properties on different substrates 167
3.6.2.2 Measurement of the dielectric constant in a

temperature range....169
3.6.3 Ferroelectric hysteresis of PZT films in the temperature range between 20°C and 170°C....171
3.6.4 Contact poling of PZT films....184
3.6.5 Piezoelectric properties....189
3.6.6 Observation of ferroelectric domains....193

CHAPTER 4: GENERAL DISCUSSION....198

4.1 Introduction to the Chapter....198
4.2 PZT nucleation....198
4.2.1 Nucleation of PZT 40/60....201
4.2.1.2 The role of the intermetallic phase Pt_3Pb formation....204
4.2.1.3 The role of stress on the orientation....204
4.2.2 Nucleation in PZT 52/48....206
4.3 On the residual stress....207
4.3.1 Calculation assumption....207
4.3.2 Sources of error in stress calculation....209
4.3.3 Stress results correlation to the results determined using the Stoney equation....211
4.3.4 Residual stress in PZT films....212
4.3.5 Residual stress and fracture....214
4.4. Piezoelectric response of PZT films....215

CHAPTER 5: CONCLUSIONS AND FURTHER WORK 219

5.1 Conclusions....219
5.1.1 Thick film processing....219
5.1.2 Control of crystallographic orientation....220
5.1.3 Residual stress....220
5.1.4 Piezoelectric properties....222
5.2 Further work....222

5.2.1 Further film thickness increase....... 222
5.2.2 Measurement of the piezoelectric coefficient $d_{31,f}$ coefficient and the coupling coefficient $k_{31,f}$....... 223
5.2.3 Improvement of piezoelectric properties....... 224
5.2.4 Stress modelling....... 224
5.2.5 Lattice parameters....... 225
5.2.6 Domain switching in films during poling....... 225

REFERENCES....... 226

APPENDIX.......243

Fig. 1.1: Classification of the related phenomena. The ferroelectrics are usually both pyroelectrics and piezoelectric, whereas the pure piezoelectrics do not necessarily exhibit pyroelectric or ferroelectrics effect.

Fig. 1.2: The direct (left) and converse (right) piezoelectric effect. If field is applied, the polarization will align along the field direction and cause a change in dimension of the piezoelectric. This effect can be reversed by application of mechanical force. The change of dimensions induces strain upon which an electric charge is generated.

Fig. 1.3: Domain formation upon cooling, arrows show the polarization direction of the individual domains.

Fig. 1.4: Hysteresis loop. The polarization D is a function of applied electric field E.

Fig. 1.5: Bulk PZT phase diagram after [4].

Fig. 1.6: The perovskite PZT unit cell.

Fig. 1.7: Domain configuration in tetragonal PZT at the transition temperature after [8].

Fig. 1.8: Unit cell deformation upon the paraelectric (cubic) to ferroelectric transition (rhombohedral) for PZT with $x>52$.

Fig. 1.9: Intrinsic response due to crystal lattice and the extrinsic contribution of 180° and non-180° domain walls motion to the piezoelectric and dielectric properties, after [17].

Fig. 1.10: Structural elements used in piezoelectric MEMS, after [23].

Fig. 1.11: Schematic of sol-gel processing. The coating and heating steps can be repeated to produce thick film.

Fig. 1.12: Pyrochlore structure, taken from [70].

Fig. 1.13: Stages of spin coating technique: a) Spin up step, b) fluid spin-off stage, c) solvent evaporation stage after [86].

Fig. 2.1: The sputtering process shown schematically after [136].

Fig. 2.2: Structural model of PVD condensates after Thornton et al [138].

Fig. 2.3: Flow chart of the sol precursor production after [141].

Fig. 2.4: Principle of corona poling.

Fig. 2.5: Generation of radiation due to interaction of incident beam electrons with specimen atoms, in cross section.

Fig. 2.6: Schematic diagram of sample examination directions.

Fig. 2.7: Positions of (200)/(002) peaks in all three PZT compositions.

Fig. 2.8: Positions of (111) peak of all three PZT compositions.

Fig. 2.9: Dielectric constant vs. frequency. In different frequency ranges a different polarization mechanism is active.

Fig. 2.10: Schematic of Four-Point-Probe after [153].

Fig. 2.11: Bending of the substrate due to film stress. Left: concave bending is due to tensile stresses in the film while convex bending (right) is due to compressive stresses in the film.

Fig. 2.12: A composite with n-layers. All layers are stretched due to force f to have same thickness.

Fig. 2.13: After the force f is released, the compounds will bend due to the bending moment. This state would correspond to the film cooled down to room temperature if the film and substrate had the same length at processing temperature.

Fig. 2.14: Wafer with the primary flat and the scan direction for wafer deflection measurement.

Fig. 2.15: Maximum deflection at the centre of the wafer.

Fig. 3.1: Relationship between spin speed and layer thickness of 0.6 M concentrated sol.

Fig. 3.3: Wafer deflection in the temperature interval of 200 nm thick PZT40/60 sol-gel film deposited onto a 2” platinised silicon substrate.

Fig. 3.4: Thickness reduction during film processing for 4 different spin speeds of 1 M concentrated sol.

Fig. 3.5: XRD pattern of the PZT 40/60sol-gel film treated at 450°C and 475°C.

Fig. 3.6: XRD pattern of the PZT 40/60sol-gel film treated at 500°C and 550°C.

Fig. 3.7: Development of deflection in multilayer PZT films. The deflection was determined after each heating step, after the film was cooled down to room temperature.

Fig. 3.8: Rocking curve of as-sputtered and 10 minutes annealed platinum.

Fig. 3.9: XRD patterns of as-sputtered and annealed platinum. Note the logarithmic scale.

Fig. 3.10. a) to g): AFM images of platinum surface after various annealing time.

Fig. 3.11: Grain size calculated from the XRD results from Fig. 3.9.

Fig. 3.12: Deflection in platinised silicon layer with different titanium thickness.

Fig. 3.13: Sheet resistance in platinum layer with different titanium thickness.

Fig. 3.14: A comparison of wafer deflection with PZT film on three different substrates.

Fig. 3.15: Single layer deflection in three different PZT compositions with the same sol concentration.

Fig. 3.16: Planar view of the damaged film through delamination (left) and a delaminated patch (right).

Fig. 3.17: Polished cross section of a 3 µm thick PZT 52/48 film.

Fig. 3.18: Typical surface morphology of PZT films.

Fig. 3.19: Fracture section of PZT 52/48 films.

Fig. 3.20: Diffractograms of one PZT 40/60 film at three different thicknesses.

Fig. 3.21: Comparison of diffractograms for a PZT powder and for the PZT film.

Fig. 3.22: Typical decrease of (111) orientation, here in (111) oriented film.

Fig. 3.23: A schematic cross section of a PZT film with thickness dependent change of orientation.

Fig. 3.24: Fracture through columnar grains, possibly due to change of orientation with thickness.

Fig. 3.25: Diffractograms of one PZT 60/40 film at three different thicknesses.

Fig. 3.26: Thickness dependent change of orientation.

Fig. 3.27: Diffractorgrams of a PZT 52/48 films at three different thicknesses.

Fig. 3.28: A diffractogram of a 3µm thick film before and after final annealing step.

Fig. 3.29: A comparison of two PZT 52/48 3 µm thick films, with and without PbO buffer layer.

Fig. 3.30: A diffractogram of crystalline LNO bottom electrode.

Fig. 3.31: Diffractograms of PZT 52/48 deposited on LNO/Si substrate.

Fig. 3.32: Diffractograms of PZT 52/48, PZT 40/60 and PZT 60/40 on Pt(200)/Si.

Fig. 3.33: Two 1µm thick PZT 52/48 and PZT 40/60 film on sapphire substrates.

Fig. 3.34: Two PZT 40/60 films deposited on sapphire substrate with and without Pt(111) electrode.

Fig. 3.35: Measured deflection in the substrate and the PZT film together with the calculated deflection for PZT film.

Fig. 3.36: Influence of the Thermal Expansion Coefficients (TEC) variation of PZT on the total deflection of the 4-layers structure.

Fig. 3.37: Influence of the Thermal Expansion Coefficients (TEC) variation of SiO_2 on the total deflection of the 4-layers structure.

Fig. 3.38: Influence of the Thermal Expansion Coefficients (TEC) variation of Si on the total deflection of the 4-layers structure.

Fig. 3.39: Influence of the Thermal Expansion Coefficients (TEC) variation of Pt on the total deflection of the 4-layers structure.

Fig. 3.40: Influence of the Young's Modulus variation of SiO_2 on the total deflection of the 4-layers structure.

Fig. 3.41: Influence of the Young's Modulus variation of Pt on the total deflection of the 4-layers structure.

Fig. 3.42: Influence of the Young's Modulus variation of Si on the total deflection of the 4-layers structure.

Fig. 3.43: Influence of the Young's Modulus variation of PZT on the total deflection of the 4-layers structure.

Fig. 3.44: Thermal strain of PZT 60/40 vs. temperature, reproduced from the dilatometry results from [193].

Fig. 3.45: Residual stress in a PZT 60/40 film with increasing film thickness. 25 layers with 200 nm single layer thickness were deposited and the wafer curvature was measured (at room temperature) after crystallization of each layer. Sample: PZT 60/40-Pt(111)/Si/2" - 5 µm - film 6.

Fig. 3.46: Residual stress in PZT 40/60 film with increasing thickness. 10 layers were deposited onto 2“ platinised silicon substrate, each layer was 200 nm thick. Sample: PZT 40/60- Pt(111)/Si/2” - 2 µm film 11.

Fig. 3.47: Residual stress in PZT 52/48 film with increasing thickness. 20 layers were deposited onto platinised silicon substrate; each layer was 200 nm thick. PZT 52/48- Pt(111)/Si/2”- 2 µm - film 21.

Fig. 3.48: a) Thermal deformation of the unit cell in tetragonal PZT. The same contraction as in (100) direction is found also in (010), not shown in the figure. b) Thermal deformation of a PZT film with *a* and *c* domains during cooling.

Fig. 3.49: The phase transition from cubic to tetragonal (above). The elongation of the unit cell in c-direction and the contraction in a-directions are depicted. The lattice plane (111) is highlighted with blue colour. Below: the influence of the tetragonal distortion on the lattice planes (111) whereby only the lattice planes (111) are extracted from the upper picture. The dimensions of the cubic and tetragonal (111) lattice planes are depicted in-plane of the film and their dimensions are projected into the plane of the film with the orthogonal coordinates x,y,z.

Fig. 3.50: Measured deflection in the PZT 40/60 film with platinum layer on the back.

Fig. 3.51: Residual stress in PZT 40/60 film deposited on platinised sapphire substrate.

Fig. 3.52: Diffractograms of PZT 40/60 films deposited onto platinised silicon wafers of different size.

Fig. 3.53: Diffractograms of the films with change in phase content due to stress. The diffractograms of PZT 40/60 and PZT 60/40 films are included.

Fig. 3.54: *c/a*-ratio in PZT 40/60 films with increasing (100) relative intensity.

Fig. 3.55: c/a-ratio in PZT 40/60 films with the relative fraction of (001) to (100) domains.

Fig. 3.56: Thermal expansion or contraction in PZT films due to thermal expansion mismatch between PZT film and substrate and the effect of in-plane strain on the lattice spacing.

Fig. 3.57: Relationship between the tetragonal c/a-ratio and rhombohedral phase content in (100) orientation.

Fig. 3.58: Relationship between the rhombohedral lattice parameter *a* and rhombohedral phase content in (100) orientation.

Fig. 3.59: Williamson-Hall Plot for a PZT 52/48 film.

Fig. 3.60: Peak broadening found in PZT 40/60 films on (002)/(200) peak doublet indicating very small crystallite size.

Fig. 3.61: Surface of a PZT 40/60 film The brighter areas within individual crystallites were related to domain in the topographic mode and will be discussed at later point.

Fig. 3.62: Typical fracture section of PZT 40/60 films.

Fig. 3.63: Typical surface morphology of PZT 60/40 films.

Fig. 3.64: Surface images of recrystallized platinum (left) and PZT 60/40 film (right).

Fig. 3.65: Residual not crystallized phase of PZT 60/40 films on platinum surface after etching away the PZT film.

Fig. 3.66: Fracture section of PZT 60/40 film, etched with HF before examination.
Fig. 3.67: Fracture section of a PZT 60/40 film viewed with BSE contrast.

Fig. 3.68: Same sample area as Fig. 3.67 viewed with SE contrast.

Fig. 3.69: Surface morphology of PZT 52/48 grown under tensile stress.

Fig. 3.71: Fracture section of PZT 52/48 film grown under tensile stress.

Fig. 3.72: Fracture section of PZT 52/48 film grown under compressive stress.

Fig. 3.73: Dielectric constant and loss of PZT 40/60 film with different orientation before and after poling.

Fig. 3.74: Dielectric constant of PZT 52/48 film with different orientation and rhombohedral phase content.

Fig. 3.75: Dielectric constant of 2µm thick PZT 52/48 and PZT 40/60 during heating and cooling. Samples: PZT 52/48-Pt(200)/Si/3"- 2 µm-film 19, PZT 40/60-Pt(111)/Si/2" - 2 µm film 11.

Fig. 3.75: Dielectric constant of 2µm thick PZT 52/48 and PZT 40/60 during heating and cooling.

Fig. 3.76: Dielectric loss of 2µm thick PZT 52/48 and PZT 40/60 during heating and cooling.

Fig. 3.77: Hysteresis loop of (100) and (111) oriented PZT 40/60 films. Driving field was 160 kV/cm for both films.

Fig. 3.78: Temperature dependent polarization in PZT 40/60 films. Driving field was 160 kV/cm for all films.

Fig. 3.79: Temperature dependent coercive field in PZT 40/60 films at driving field 160 kV/cm.
Fig. 3.80: Temperature dependent polarization in PZT 60/40 films at driving field 200 kV/cm. The P_s was equal to -(-P_s).

Fig. 3.81: Temperature dependent coercive field in PZT 60/40 films. Driving field was 200 kV/cm for all films.

Fig. 3.82: Temperature dependent polarization in PZT 52/48 films. The P_s was equal to -(-P_s).

Fig. 3.83: Temperature dependent coercive field in PZT 52/48 films at driving field 200 kV/cm.

Fig. 3.84: Comparison of hysteretic loops at room temperature and at 170°C of PZT 40/60 a) with (100) and b) (111) orientation, c) PZT 60/40 and d) PZT 52/48. All loops compared at the same driving field.

Fig. 3.85: Hysteresis loops of 5 µm PZT films compared to 3 µm films, at room temperature. a) PZT 40/60, b) PZT 52/48, c) PZT 60/40. The driving field for all compared films was equal.

Fig. 3.86: Temperature dependent polarization of PZT 40/60 films with compressive residual stress (film 15, film 17) compared with a 3µm thick and (111) oriented PZT 40/60 film under tensile stress at RT (film 2).

Fig. 3.87: Temperature dependent coercive field of PZT 40/60 films with compressive residual stress.

Fig. 3.88: Thermal strain of PZT 70/30. Diagram reproduced from Fig. 3.44.

Fig. 3.89: Poling conditions and measured $d_{33,f}$ for a 2 µm PZT 40/60 film.

Fig. 3.90: Poling conditions and measured $d_{33,f}$ for 5 µm PZT 60/40 films.

Fig. 3.91: Comparison of the effect of poling conditions on the $d_{33,f}$ of 5 µm PZT 40/60 and 4 µm PZT 52/48 film and measured $d_{33,f}$.

Fig. 3.92: Poling conditions and $d_{33,f}$ of a compressive 2 µm PZT 40/60.

Fig. 3.93: Surface image of PZT 52/48 grown under tensile stress. Some of the different kind of domain patterns were highlighted with black lines.

Fig. 3.94: Surface image of a PZT 52/48 film deposited onto compressed substrate. Some grain boundaries are highlighted with black lines.

Fig. 3.95: Domains imaging in a poled PZT 40/60 films.

Fig. 3.96: Enlargement of the same film as in Fig. 3.95. Some of the observed domain patterns are highlighted with black lines.

Fig. 4.1: Stress measurement and orientation reproducibility.

Fig. 5.1: Design of piezoelectric unimorph microactuator.

Tab. 1.1: Summary of PZT thick films employed into MEMS design and fabrication.

Tab. 1.2: Summary of the achieved film thicknesses using sol-gel and related methods. The properties of the films are as reported. Not all data was available for all films.

Tab. 2.1: PVD sputtering conditions for bottom electrode deposition.

Tab. 3.1: Spin-coating parameters of used sol concentrations with the maximum obtainable crack-free layer thickness.

Tab. 3.2: Relative peak intensity for all appearing peaks in PZT 40/60 films, in percent. The processing parameters for each film are attached ahead the orientation results.

Tab. 3.3: Relative integral intensities for all detected peaks in PZT 60/40.

Tab. 3.4: Orientation and phase content at different thicknesses in three PZT 52/48 films.

Tab. 3.5: Phase content and orientation of PZT 52/48 films.

Tab. 3.6: Intensities of all peak groups before and after annealing step in percent of the total intensity.

Tab. 3.7: Influence of the single layer thickness on the orientation.

Tab. 3.8: Integral intensities of PZT on LNO/Si, in percent.

Tab. 3.9: Integral intensities (in percent) of PZT films on sapphire substrates.

Tab. 3.10: Results of the chemical analysis in PZT films with different composition.

Tab. 3.11: Parameters used in the stress calculation.

Tab. 3.12: Orientation of the PZT 40/60 film deposited onto compressive and tensile substrates under the same processing conditions, 2µm thick.

Tab. 3.13: Orientation of PZT 40/60 films.

Tab. 3.14: Orientation (in percentage) of PZT 40/60 films processed under the same conditions but deposited onto different wafer size. All films were 2 µm thick.

Tab. 3.15: Lattice parameter for PZT 52/48 films on Side A and Side B.

Tab. 3.16: Lattice parameter of PZT films deposited in Pt(111)/Si substrates.

Tab. 3.17: Lattice parameters of PZT films deposited on various substrates.

Tab. 3.18: Lattice parameters determined for PZT 52/48 films deposited on different substrates.

Tab. 3.19: Crystallite size in all PZT compositions on Pt(111)/Si and Pt(200)/Si.

Tab. 3.20: Crystallize size of PZT films deposited on various substrate.

Tab. 3.21: Dielectric constant of PZT films deposited on Pt(111)/Si and Pt(200)/Si.

Tab. 3.22: Dielectric properties of PZT films on Pt(100)/Si substrates. The results from Tab. 3.21 are included for comparison.

Tab. 3.23: Dielectric constant and loss of films deposited on different substrates than Pt/Si.

Tab. 3.24: Dielectric of PZT 52/48 films at different thicknesses.

Tab. 3.25: Dielectric constant of 5µm and 4µm thick films.

Tab. 3.26: Piezoelectric coefficients in PZT films.

Tab. 3.27: Piezoelectric coefficients of PZT films deposited on Pt(200)/Si substrate.

Tab. 3.28: $d_{33,f}$ in films with increased single layer thickness but similar total thickness.

Tab. 3.29: Piezoelectric coefficients $d_{33,f}$ and $e3_{1,f}$ of 5 µm thick PZT films.

Tab. 4.1: Percentages of (111) orientation in 1µm PZT 40/60 and PZT 60/40 films and 2 µm PZT 52/48. Each value represents one sample, the films with grey shading were processed under the same conditions.

Tab. 4.2: Strain in PZT films of different composition, based on the stress results, section 3.

Tab. 4.3: Summary of sol-gel related residual stress reported in literature.

a - domain with the in-plane orientation such as (100)
a, b, c - the unit cell parameters
B - peak broadening as full width at half maximum (FWHM)
c - domain with out-of-plane orientation such as (001)
D - dielectric displacement
d - deflection
d - distance
$d_{(hkl)}$ - lattice spacing
d_{ij} - piezoelectric coefficients
E - electric field strength
e_{ij} - piezoelectric coefficients
F - force
$I_{rel,(hkl)}$ - Relative integral intensity of lattice plane (hkl) to the summ of integral intensities of all detected lattice planes (hkl)
$I_{(hkl)}$ - Integrated intensity of single (hkl)
I - current
K - curvature
k - coefficient
l - length
k_{ij} - coupling coefficients
M - mass
n - order parameter
p - exponent
R - radius of curvature
r - radius
s^{E}_{ij} - compliance tensor
T - temperature
t - layer thickness
tan δ - dielectric loss
V - voltage
Y - Young's Modulus
x, y, z - coordinates in orthogonal system

α	-	thermal expansion coefficients, also abreviated as TEC
α, β, γ	-	the angle between the unit cell axis
β	-	inverse crystallite size
ε^{σ}	-	permittivity
ε_{ij}	-	strain tensor
γ	-	acceleration
λ	-	wavelength
ν	-	Poissons ratio
π	-	zero strain plane
ρ	-	sheet resistivity
σ	-	mechanical stress
θ	-	diffraction angle
ω	-	rotational speed

(1.1) $(r_A + r_O)t = \sqrt{2}(r_B + r_O)$

(1.2) $D = d\sigma + \varepsilon^{\sigma} E$

(1.3) $\varepsilon = s^E \sigma + dD$

(1.4) $e_{31,f} = \dfrac{d_{31,f}}{s_{11}^E + s_{12}^E}$

(1.5) $F = M\gamma$

(2.1) $n\lambda = 2d\sin\theta$

(2.2) $I_{rel,(hkl)} = \dfrac{I_{(hkl)}}{I_{(100)} + I_{(110)} + I_{(111)}}$

(2.3) $\tau = \dfrac{\lambda k}{B_c \cos\theta}$

(2.4) $B_\varepsilon = 4\varepsilon \tan\theta$

(2.5) $B_t = B_{instrument} + B_{sample}$

(2.6) $\rho = \dfrac{V}{I} 2\pi s$

(2.7) $\varepsilon_{i,0} = \ln(\dfrac{l_0}{l_i})$

(2.8) $\varepsilon_i = \varepsilon_{i,0} + \varepsilon_{i,f}$

(2.9) $\varepsilon_i = \varepsilon_{i,0} + \varepsilon_{i,f} + \varepsilon_{i,M}$

(2.10) $\varepsilon_{i,M} = (\pi - z)K$

(2.11) $\sigma_i = Y_i \left[-\ln(l_i) + \dfrac{\sum_j Y_j t_j \ln(l_j)}{\sum_j Y_j t_j} + (\pi - z)K \right]$

(2.12) $\ln(l_i) = \alpha_i \Delta T + \ln(l_{i,0})$

(2.13) $$\sigma_i = Y_i\left[-(\ln(l_{i,0}) + \alpha_i \Delta T) + \frac{\sum_j Y_j t_j (\ln(l_{i,0}) + \alpha_i \Delta T)}{\sum_j Y_j t_j} + (\pi - z)K\right]$$

(2.14) $$K = \frac{\Delta T \sum_i Y_i \gamma_i \frac{t_i}{2}\left[-\alpha_i + \frac{\sum_j Y_j t_j \alpha_j}{\sum_j Y_j t_j}\right]}{\sum_i Y_i t_i \left[\left(\frac{\pi t}{2} - \frac{t^2}{3}\right) + (t - \pi)\frac{\gamma_i}{2} - \frac{1}{12}\left(3\gamma_i^2 + t_i^2 - t^2\right)\right]}$$

(2.15) $$\pi = \frac{t}{2} - \left(\frac{\sum_i Y_i \gamma_i \frac{t_i}{2}}{\sum_i Y_i t_i}\right)$$

(2.16) $$R(x) = \frac{(1 + y'^2)^{\frac{3}{2}}}{y''}$$

(2.17) $$d = \frac{r^2}{2 \cdot R}$$

(3.1) $$t = k\omega^{-p}$$

(3.2) $$\alpha_{PZT} = \alpha_{para} \cdot \frac{(T_a - T_c)}{\Delta T} + \alpha_{ferro} \frac{T_c}{\Delta T}$$

(3.3) $$\alpha = \frac{2\alpha_a + \alpha_c}{3}$$

(3.4) $$I_{rel,(100)} = \frac{I_{(100)}}{I_{(100)} + I_{(110)} + I_{(111)} + I_{(001)}}$$

(3.5) $$I_{rel,(100)R} = \frac{I_{(100)R}}{I_{(100)T} + I_{(110)} + I_{(111)T} + I_{(111)R} + I_{(001)T} + I_{(100)R}}$$

(4.1) $$\sigma = \frac{1}{6}\left(\frac{1}{R_{post}} - \frac{1}{R_{pre}}\right)\frac{Y}{(1-\upsilon)}\frac{t_s^2}{t_f}$$

Introduction to the thesis

Among the available ferroelectric materials, lead zirconate titanate, $Pb(Zr_xTi_{1-x})O_3$ (PZT), is the most popular due to its superior dielectric constant, piezoelectric constants, and thermal stability. The ability to pole ferroelectric ceramics in any desired direction offers a great advantage in design flexibility [1]. PZT finds broad application as capacitors, transducers, sensors and actuators. The growing need of miniaturization of such devices and their implementation onto a silicon chip in CMOS technology lead to the development of microelectromechanical systems (MEMS).

To exploit the good PZT properties in a wide range of piezoelectric actuator applications in MEMS devices thick films are needed, from several microns to several 10's micron [2]. Chemical solution deposition (CSD) is preferred for many applications because it offers both compositional control and reduced-temperature processing of highly uniform, dense, crack-free films. However, the limited crack-free coating thickness of CSD films below 0.1 μm requires successive coating [3] which is time consuming and impractical in the industries. Moreover, there is a maximum total thickness above which films crack.

Many attempts were undertaken to increase the single layer thickness and so to reduce the quantity of the processing steps. When the thickness of a single layer increases, it simultaneously increases the internal stress in the film which easily leads to the cracks. The main aim of this project was to study the factors that influence the stress in the film and find the key processing parameters to control the stress which in turn enables the fabrication of thickness increased single coating. Using the results obtained from the study of PZT sol-gel processing, thick films need to be deposited and their microstructure and properties need to be investigated.

To use attractive piezoelectric properties of PZT films in MEMS devices, the characterization of piezoelectric coefficients such as $d_{33,f}$ and $e_{31,f}$ is required [1]. Also of great importance is the characterization of the dielectric constant and loss, piezoelectric coefficient $d_{31,f}$ and coupling coefficient $k_{31,f}$. With the available equipment the coefficients $k_{31,f}$ and $d_{31,f}$ can only be characterized in the cantilever or membrane design and thus require surface and bulk machining processing. Thus, the

characterization of $d_{31,f}$ and $k_{31,f}$ coefficients is beyond the scope of this project and a subject of future work.

This thesis is divided into 5 chapters. This is the first chapter and this chapter focuses on the literature survey. The literature survey addresses the background of the ferroelectrics and piezoelectrics, the processing of sol-gel PZT films, state-of-the art processing of thickness increase PZT films, and their potential applications in MEMS devices. Chapter 1 concludes with the aims and objectives of this project. Chapter 2 summarizes all the experimental procedures that were used within this project.

The results and discussion are presented in Chapter 3 which is subdivided into 5 main sections. Each of these sections focuses on different aspects of film fabrication and characterization. In the first section, the processing of thick films and the issues related to sol-gel films processing are summarized. The preferred crystallographic orientation of PZT films is introduced in the second section. Section 3 focuses on the residual stress analysis and modeling. Section 4 goes deeper into the microstructural characterization of the films and links the results from section two and section three. This fourth section deals with the morphology and lattice parameters of PZT films. In Section 5 the electric properties are introduced and discussed.

In Chapter 4 outlines the general discussion and links the results from the different sections from Chapter 3. Finally, summary, concluding remarks and directions for further work are presented in Chapter 5.

Chapter 1: Introduction: Background And Literature Survey

1 Introduction to the Chapter

A brief introduction to piezoelectrics and ferroelectrics, and in particular lead zirconate titanate (PZT) will be presented in this chapter since their detailed descriptions can be found in Ref. [4]. This is followed by a review of piezoelectric thin and thick film applications in microelectromechanical systems (MEMS). The sol-gel thin film processing will be presented and the fabrication of sol-gel thick films will be reviewed. Residual stress in sol-gel PZT films and its effects on the film performance will be discussed. Finally the motivation for the project and the objectives will be given.

1.1 Brief historical background

The discovery of piezoelectricity by J. Curie and P. Curie in 1880 [5] followed the experiments on the pyroelectricity. The pyroelectricity is the ability of some materials to exhibit a spontaneous electric dipole moment when their temperature changes. These studies led to piezoelectricity, or the generation of charge by application of mechanical stress. The ferroelectricity, the ability of polarization reversal at reversed electric field, was discovered much later because the resulting net polarization of such crystals is very small and it was difficult to detect it. The formation of domains in ferroelectrics, or the formation of differently oriented polarization within virgin single crystals leads to a lack of any net polarization and to very small pyroelectric and piezoelectric response. The classification of these phenomena is depicted in Fig. 1.1. Only in 1920 Valasek discovered that the polarization of Rochelle salt ($NaKC_4H_4O_6$ x $4H_2O$) could be reversed by application of an external electric field. Around and after 1938 ferroelectricity was discovered in other materials than Rochelle salt, and resulted in discovery of complete series of ferroelectric materials, like KH_2PO_4 and in 1945 the $BaTiO_3$. Shortly after the investigation of lead zirconate titanate $PbZr_xTi_{1-x}O_3$ ceramics was started, Jaffe found the highest permittivity in the composition $PbZr_{0.53}Ti_{0.47}O_3$ and subsequently patented it and named it shortly PZT.

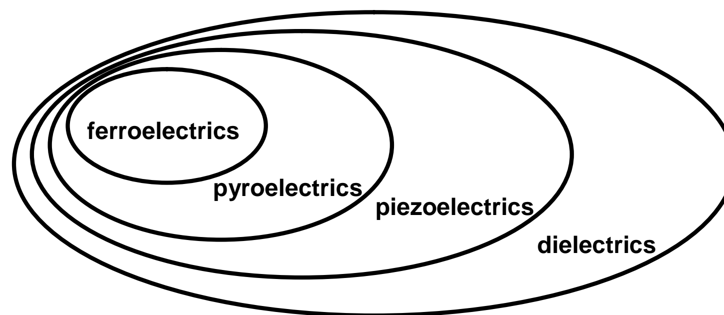

Fig. 1.1: Classification of the related phenomena. The ferroelectrics are usually both pyroelectrics and piezoelectric, whereas the pure piezoelectrics do not necessarily exhibit pyroelectric or ferroelectrics effect.

1.2 Background

1.2.1 Polarity of crystal classes

Depending on the crystal geometry there are 7 major crystal systems like cubic, hexagonal, orthorhombic, monoclinic, tetragonal, triclinic and trigonal. These crystal groups can be subdivided into point groups (crystal classes) according to their symmetry with respect to a point. In total, there are 32 such classes and 11 of them posses a centre of symmetry. If e.g. a uniform stress is applied to such a centrosymmetrical crystal the resulting small movement of charge is symmetrically distributed about the centre of symmetry. The relative displacement is fully compensated. The remaining 21 non-centrosymmetric classes, all except one, exhibit polarity when subject to stress. The polarity is linear with stress and the reversal of the stimulus results in a reversal of the response. This effect is termed piezoeffect. In Fig. 1.2 a direct and converse piezoelectric effect are depicted.

Of the 20 piezoelectric crystal classes only 10 have a unique polar axis. Crystals belonging to these classes are called polar because they posses a spontaneous polarization or electric moment per unit volume. The spontaneous polarization in such crystals is temperature dependent and its existence can be detected by observing the

flow of charge to and from the surface on change of temperature. This is the pyroelectric effect and the 10 polar classes are often referred to as the pyroelectric classes.

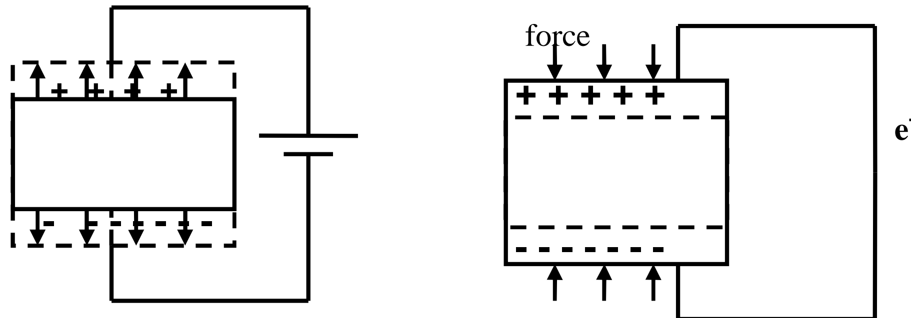

Fig. 1.2: The direct (left) and converse (right) piezoelectric effect. If field is applied, the polarization will align along the field direction and cause a change in dimension of the piezoelectric. This effect can be reversed by application of mechanical force. The change of dimensions induces strain upon which an electric charge is generated.

1.2.2 Formation of ferroelectric domains

Upon transition below the Curie point the piezoelectric crystals undergo a transformation from the paraelectric to ferroelectric phase. In absence of electric field there are at least two directions along which the spontaneous polarization P_s may occur.

In non-ideal crystals that contain surfaces and defects some depolarization along with the polarization can occur. The depolarization energy arises due to the accumulation of charges on impurities or close to the surface (deviation from the ideal crystal) where P_s decreases to zero. A decreasing polarization P_s close to a surface can act as a source of the depolarization field.

In order to minimize the depolarization energy the different regions of the crystals polarize in different direction, Fig. 1.3. Each volume part of uniform polarization is referred to as a domain, separated by the boundaries which are referred to as domain walls. A certain amount of energy is associated with the domain walls.

The depolarization fields which appear on cooling are usually sufficient to prevent any net polarization. The final domain configuration is determined by

minimizing an appropriate free energy including the term of depolarization energy and domain wall energy. In equilibrium, when all depolarizing fields are compensated, the minimum energy in the absence of defects would correspond to a single domain configuration. However, such an equilibrium state is rarely achieved in a virgin crystal in absence of electric fields and thus, multidomains form. The domain pattern depends on many factors including the crystal symmetry, the electrical conductivity, the defect structure, the magnitude of spontaneous polarization and elastic and dielectric compliances, as well as the crystal preparation and sample geometry.

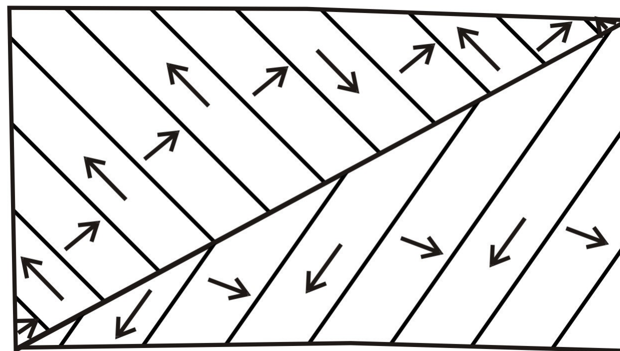

Fig. 1.3: Domain formation upon cooling, arrows show the polarization direction of the individual domains.

1.2.3 Ferroelectricity and hysteresis loop

A primary feature distinguishing ferroelectrics from other pyroelectrics is that the spontaneous polarization can be reversed with an applied electric field. A typical hysteresis loop is shown in Fig. 1.4. At low fields well below the coercive field E_c and at high fields above the coercive field E_c a ferroelectric behaves like an ordinary dielectric but at the coercive field E_c polarization reversal occurs giving a large dielectric non-linearity. The area within a loop is a measure of the energy required to twice reverse the polarization. At zero electric field the electric displacement within a single domain can have two values corresponding to the opposite orientations of the spontaneous polarization. In a multi-domain crystal the average electric displacement at zero field can have any value between these two extremes. In principle the spontaneous polarization is equal to the saturation value of the electric displacement extrapolated to

zero field, as shown in Fig. 1.4. The remanant polarization P_r (the displacement at zero field) may be different from spontaneous polarization P_s if reverse nucleation occurs before the applied field reverses. This can happen in the presence of internal (or external) stress or if the free charges below the surfaces cannot reach their equilibrium distribution during each half-cycle of the loop. Additionally, if the material is constraint the saturated polarization may not be achieved.

The defects such as impurities affect the dielectric properties and the switching behavior. The defects in any crystalline lattice generally cause deformation of the surrounding volume and modification of the local fields. The defects induce an additional term of polarization. When the polarization of a crystal is reversed by an applied field, the difference in polarization between the perfect crystal and real crystals, latter one including the defects, does not necessarily need to reverse. If it does reverse then the coercive field will depend on both the field required to switch the defects and the sign and magnitude of the polarization difference. In general the presence of defects tends to increase the coercive field. If the polarization does not reverse in an external field the defects can have a marked effect on the switching properties depending on the distribution of the polarization difference throughout the crystal volume. If all the defect dipoles have same direction the hysteresis loop will appear biased, e.g. shifted along the axis of electric field [6].

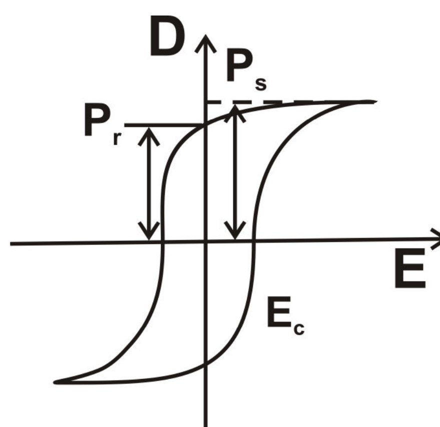

Fig. 1.4: Hysteresis loop. The polarization D is a function of applied electric field E.

1.3 The system lead titanate - lead zirconate (PT-PZ)

The PZT bulk phase diagram is depicted in Fig. 1.5. Upon cooling from the cubic paraelectric phase (above the Curie temperature) the PZT undergoes phase transformation to ferroelectric state (below the Curie temperature) except for compositions above x=94% $PbZrO_3$ which are antiferroelectric.

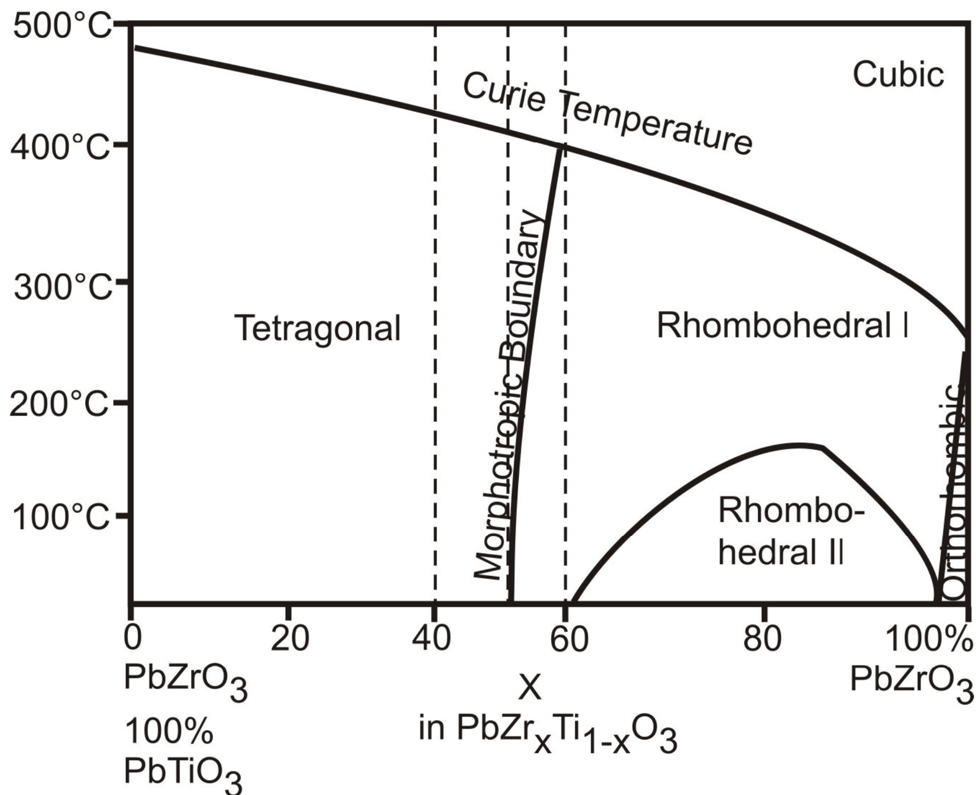

Fig. 1.5: Bulk PZT phase diagram after [4].

The compositions that were used in this work are marked with the dotted lines. They are ferroelectric compositions: $PbZr_{0.40}Ti_{0.60}O_3$ (PZT 40/60), $PbZr_{0.60}Ti_{0.40}O_3$ (PZT 60/40) and $PbZr_{0.52}Ti_{0.48}O_3$ (PZT 52/48). Their crystallographic structure at room temperature according to the bulk phase diagram Fig. 1.5 is tetragonal (space group P4mm), rhombohedral (space group R3m) and a coexistence of tetragonal and rhombohedral phase, respectively. The ferroelectricity occurs at the Curie point as a result of crystallographic symmetry reduction, e.g. cubic to tetragonal or cubic to rhombohedral

[4]. The cubic structure of PZT is a perovskite structure ABO_3 where the required unit cell dimensions obey the following law

$$(r_A + r_O)t = \sqrt{2}(r_B + r_O) \tag{1.1}$$

with r as the ion radii of the atoms at the positions of the unit cell, Fig. 1.6, and t as a tolerance factor or Goldschmidt factor that takes values between 0.8 and 1.1 [7]. The ideal cubic perovskite structure in PZT, with the space group Pm3m, can be found only above the Curie temperature.

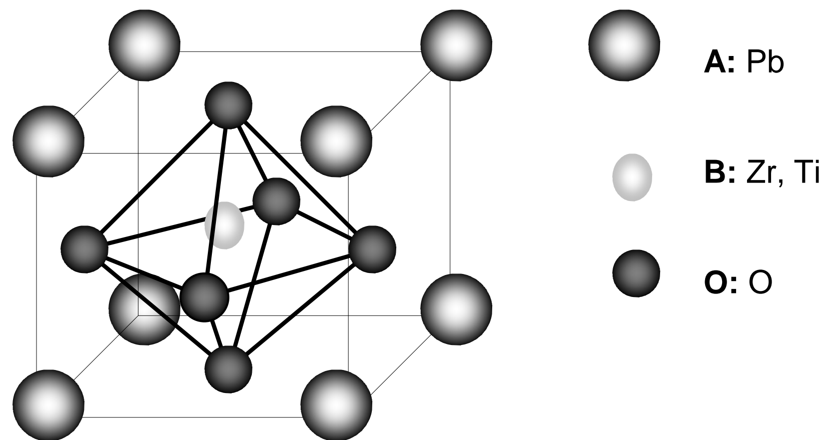

Fig. 1.6: The perovskite PZT unit cell.

The polarization in PZT is caused by the shift of the cations at site B along a particular direction. The polarization directions in tetragonal PZT lie along the [001] directions with total of 2 equivalent directions and in the rhombohedral structure along the [111] with the total of 4 equivalent directions.

1.3.1 Domain formation in PZT films

According to the phase diagram [4] for bulk PZT ceramic, all the PZT compositions undergo structural transformations at the Curie temperature. The tetragonal PZT experiences the cell elongation in [001] and contraction in [100] and [010] direction,

Fig. 1.7, which leads to three different configurations, a_1, a_2 and c domains. A considerable strain can build up, around 2.8% [8] but in films, more likely, the accumulated strain at the Curie temperature is relaxed through the formation of the in-plane and out-of-plane domains [9] and to release the mechanical strain an equilibrium domain pattern is formed [10]. The role of stress on the domain orientation at the Curie temperature was first reported by Tuttle et al [11] who found that a particular domain orientation was a function of stress at the Curie temperature.

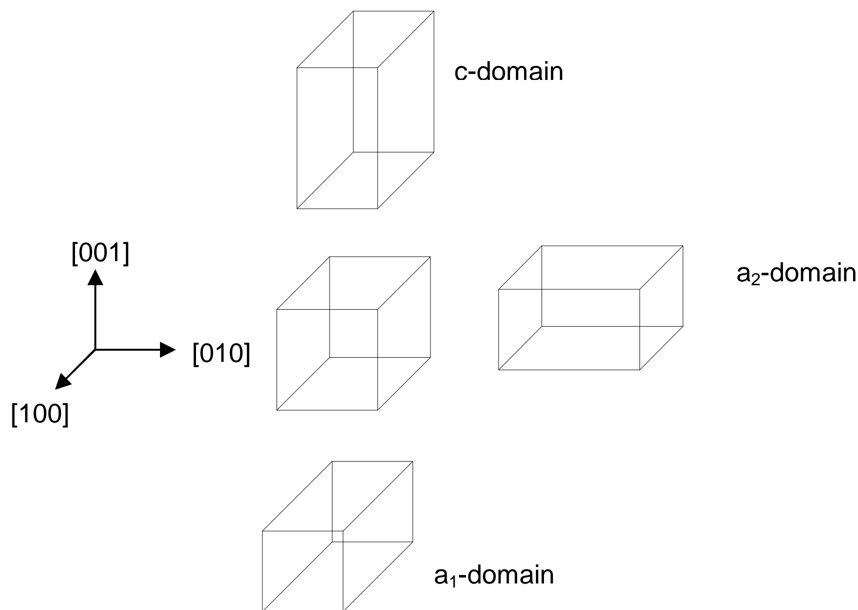

Fig. 1.7: Domain configuration in tetragonal PZT at the transition temperature after [8].

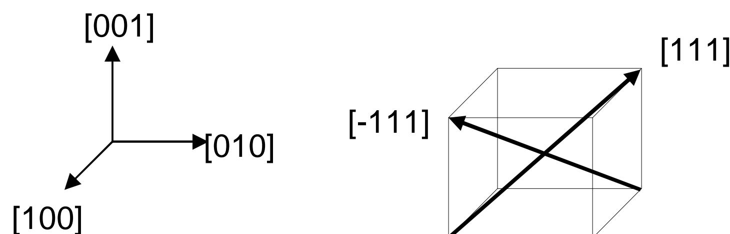

Fig. 1.8: Unit cell deformation upon the paraelectric (cubic) to ferroelectric transition (rhombohedral) for PZT with x>52.

The unit cell of rhombohedral PZT experiences stretching along one of [111] directions upon phase transition from cubic to rhombohedral structure [12], Fig. 1.8. The formation of 90° (or 71° in rhombohedral phase) and 180° oriented domains can be created. The 90° or 180° domains refer to the angle between the polarization vectors of two neighboring domains.

The PZT 52/48 can transform to either the rhombohedral structure or the tetragonal structure or both. In PZT films at the morphotropic phase boundary, the phase formation is also dictated by the stain between the substrate and the film. There are two different approaches to the phase stability. The first approach is based on the thermomechanical model where a single state domain is stable and only one phase, e.g. orthorhombic is stable for a wide strain range at room temperature, regardless if strain is tensile or compressive. This approach, based on the thermodynamical calculations, needs a priori assumption of the domain pattern including domain wall orientation to calculate the volume fraction of domains that minimize the total free energy and the substrate constraint. The second approach, first reported for PZT films by Li et al 2003 is regarded as phase-field approach where the spontaneous polarization is chosen as an order parameter [13]. The phase-field approach needs no assumptions regarding the domain state but enables predictions of the phase transition temperature, the volume fraction of oriented domains, the detailed domain structure and their temporal evolution during ferroelectric transition as a function of strain. The difference between the results of these two approaches can be made clear on the following example. According to the thermodynamical calculations the only stable phase under tensile strain of $\varepsilon=0.005$ at room temperature is the rhombohedral phase in PZT 52/48. The phase field simulation showed a mixture of distorted rhombohedral phase, tetragonal and orthorhombic phase at the same strain and temperature.

1.3.2 The piezoelectricity of PZT

The piezoelectric effect is described through constitutive equations which relate the dielectric displacement D to the mechanical stress σ and the electric field E:

$$D = d\sigma + \varepsilon^{\sigma} E \quad (1.2)$$

$$\varepsilon = s^{E}\sigma + dD \quad (1.3)$$

where d is the piezoelectric constant, ε^{σ} the permittivity, s^{E} the compliance tensor, and ε denotes the strain tensor. The first equation (1.2) is the direct and the Eq. (1.3) represents the converse effect. Both equations are linear at small fields and deformations. All parameters in Eqs. (1.2) and (1.3) are tensors. The piezoelectric tensor is of significant importance for piezoelectric materials. It is a third rank tensor with 27 coefficients, which reduce to three non-zero independent constant for tetragonal PZT, due to crystal symmetry [14]:

$$d_{ij} = \begin{pmatrix} 0 & 0 & 0 & 0 & d_{15} & 0 \\ 0 & 0 & 0 & d_{15} & 0 & 0 \\ d_{31} & d_{31} & d_{33} & 0 & 0 & 0 \end{pmatrix}$$

The indices tensor notations 1,2,3 refer to x,y and z axis in the orthographic coordinate system, and 4, 5 and 6 refer to rotations around these axis, respectively. In films on a thick substrate the x and y-axis are also considered as in-plane directions, and z-axis as out-of-plane-direction. Thus the d_{33} coefficient refers to the motion utilized parallel to the electric field. For a film this means that the application of stress is in the same direction as the collection of the generated charge, namely out-of-plane or perpendicular to the film surface. The d_{33} mode is also called the longitudinal mode. The d_{31} uses the motion in the direction perpendicular to the electric field, and in d_{15} mode, or the shear mode, the electric field is perpendicular to the polarization. For PZT 52/48 ceramics at compositions near the morphotropic boundary, d_{33} = 223 pC/N, d_{31} = - 94 pC/N, and d_{15} = 494 pC/N were reported by Jaffe [4].

The tensor e_{ij} related to the direct, transverse piezoelectric effect has also 3 non-zero, independent constants of the following form:

$$e_{ij} = \begin{pmatrix} 0 & 0 & e_{13} \\ 0 & 0 & e_{13} \\ 0 & 0 & e_{33} \\ 0 & e_{13} & 0 \\ e_{13} & 0 & 0 \\ 0 & 0 & 0 \end{pmatrix}$$

The relationship between the direct piezoelectric coefficient e_{31}, the converse piezoelectric coefficient $d_{31,f}$ and the compliance is given as follows:

$$e_{31,f} = \frac{d_{31,f}}{s_{11}^{E} + s_{12}^{E}} \quad (1.4)$$

The dielectric permittivity is also a tensor with 2 independent constants ε_{11} and ε_{33}. All the mentioned tensors are valid only for tetragonal structure.

The piezoelectric properties of thin films are different from those of bulk materials. The main reason lies in the fact that a film is clamped to a substrate. Therefore, stresses and strains generated by the piezoelectric film are influenced by the substrate constraint, resulting in usually lower effective piezoelectric coefficients than those for the unclamped material. Torah et al [15] investigated the behavior of PZT ceramics before and after clamping to a substrate. A significant reduction of the $d_{33,f}$ coefficient was found after the ceramic was bonded to the substrate.

Piezoelectric responses in PZT commonly are explained as being due to a combination of intrinsic and extrinsic contributions, Fig. 1.9 [16]. The intrinsic effect results from the homogeneous unit cell deformation by the electric field and the extrinsic effect are the elastic deformations generated by the motion of non-180° domain walls and phase boundaries. The oscillation of 180° domain walls is also an extrinsic effect but involves no strain.

Xu et al. [17] intensively studied the dielectric and piezoelectric response from PZT films with different thicknesses, grain sizes, and preferred orientations [17]. They found that the extrinsic contribution to the dielectric constant of PZT films was mainly attributed to 180° domain wall motion. However, ferroelastic non-180° domain wall

motion in thin films was limited, especially, in fine grain PZT films less than 1.5 μm in thickness. To observe substantial nonlinear behavior in the piezoelectric response, the films need to be thicker (> 5 μm).

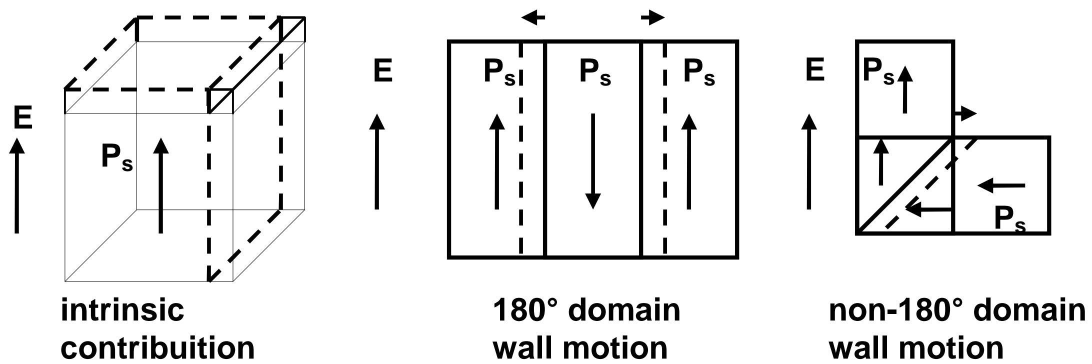

Fig. 1.9: Intrinsic response due to crystal lattice and the extrinsic contribution of 180° and non-180° domain walls motion to the piezoelectric and dielectric properties, after [18].

The piezoelectric and dielectric properties are dependent on the direction of polarization and thus on the crystallographic orientation of the crystal. The relation of these properties with the crystallographic orientation in films was studied by Du et al [19]. The calculations performed by Du et al have shown that for tetragonal PZT film the maximum dielectric permittivity ε_{33}=499 can be expected for in-plane polarization and thus for (100) oriented domains.

The highest piezoelectric coefficient $d_{33,f}$= 162 pN/C was obtained for (001) and out-of-plane polarization. In rhombohedral films the highest dielectric constant is ε_{33}=530. Du et al predicted that the values for the highest $d_{33,f}$ =189 pC/N in rhombohedral films would be found 56.7° away from the polarization direction which would correspond to the quasi-cubic (100) orientation. Soon after Taylor and Damjanovic [20] measured high $d_{33,f}$ in rhombohedral films 54° away from the polarization direction and thus the values were in good agreement to the values predicted by Du et al [19].

1.4 Applications of piezoelectric materials

The piezoelectric ceramics have found a wide range of applications in last the 60 years since their discovery. The four main fields where piezoelectric ceramics were implemented are:

- the generation of charge at high voltages
- the detection of mechanical vibration and for actuators
- the detection of sepcific frequency or transducers
- the generation of acoustic and ultrasonic vibrations [21].

The growing need of miniaturization of such devices and their implementation onto a silicon chip in CMOS technology lead to the development of microelectromechanical systems (MEMS).

MEMS have been developed since the 1970s for sensors, actuators, accelerometers, and other sensor devices. MEMS devices vary in their design and processing; offer high energy densities, efficiently transmit high forces and torques with high sensitivity and low noise; and can be directly integrated with signal amplification and conditioning circuitry using the microelectronics technology [22]. The energy conversion through the piezoelectric effect bears many application possibilities in MEMS devices. The main elements that the MEMS devices are constructed of are cantilevers, bridges, diaphragms or arrays of such elements, Fig. 1.10. The cantilever design is described through large length to width ratio of the active unit, fixed at one end. The bridge is similar to the cantilever design with the difference that it is fixed at two ends. The membrane is also fixed at two ends whereby the width of the active part can be equal or larger that its length resulting in a plate-like geometry. In this section only a brief review will be given of some of the realized applications using the piezoelectric effect and PZT films.

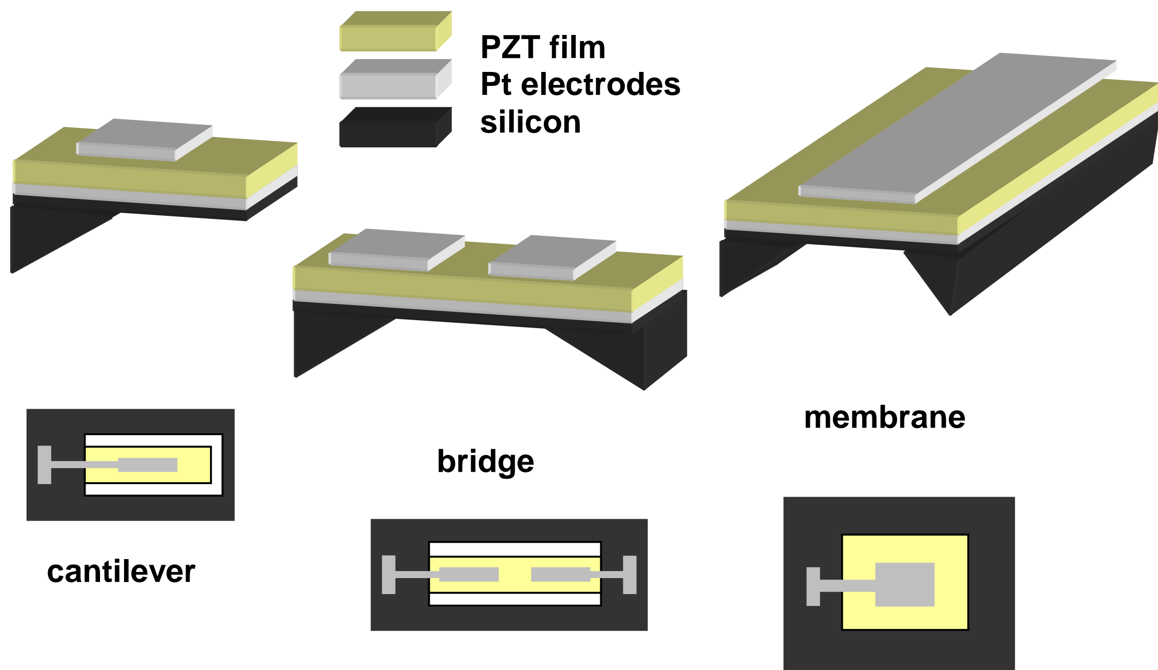

Fig. 1.10: Structural elements used in piezoelectric MEMS, after [23].

The signal transduction in microsensors and accelerators is a conversion of e.g. mechanical excitation into an electrical signal. In the microactuators the electrical signal is being converted into a motion. There are several options for signal transduction using different modes like piezoresistor and capacitance but in this work only the piezoelectric and resonant vibration modes are relevant and only devices using the latter two modes will be introduced. The resonant mode is excited through an ac electric field. If the excitation frequency of the electric signal matches the fundamental resonant frequency of the piezoelectrics the vibration is amplified and has highest deflection. The resonant frequency of the piezoelectric is defined through its dimensions. The choice of resonant mode - lateral or transversal depends on the polarization direction and the direction of the field. The high electromechanical coupling of PZT is attractive for such application.
The main fields where piezoelectric films were implemented or are being currently developed are:

- Ultrasonic transducers; the conventional transducers and piezoelectric micromachined ultrasonic transducers (pMUTs)

- Accelerometers
- Pressure sensors and microphones
- actuators in general, e.g. micromirrors
- Acoustic motors
- Power generators.

The principle of **ultrasonic transducers** is the emission of a short acoustic pulse and the detection of its echo by an object located in the far field region. The common ultrasonic transducer is a sonar which uses the bulk piezoelectrics but has certain limitations regarding the frequency due to the size. These limitations can be overcome by the advances of MEMS technology which is emerging for high frequency, 3D real time imaging, and low cost applications. Current ultrasonic transducers, also referred to as conventional ultrasonic transducers, consist of electroded and poled PZT stripes (dimensions on the order of millimeters) in the thickness direction. They operate as thickness extensional mode resonators. In this mode of operation, the fundamental frequency of the transducer is governed by its thickness. The half wavelength of speed of sound in PZT equals to the thickness of the stripe. The main potential of such transducers is in the medical application where a certain frequency range between 30 to 60 MHz is needed. If higher frequencies were used, increased tissue attenuation can occur [24]. Several transducer devices using PZT as the active layer were designed with application for microfluidic driver in medical application [25], for intercardiac ultrasound scanner [26- 27], the eye ultrasound scanner [28] or ultrasonic transducers in general [24, 29-30].

Piezoelectric micromachined ultrasonic transducers (pMUTs) represent a new approach to ultrasound generation and detection. In pMUTs, the sound-radiating element is a micromachined multi-layered membrane actuated by a piezoactive layer, typically a thin PZT film. Typical membrane dimensions are of the order of micrometers in thickness and 10’s of micrometers in the lateral direction [31]. The device uses the k_{31} bending mode, with PZT poling direction perpendicular to film surface. By applying an out-of-plane electric field, the lateral strain induces membrane bending, causing a pressure sound wave to propagate in the medium in contact. The sound wave detection is based

on the converse effect. In this scheme, the frequency is governed by the dimensions and the layering materials of the membrane and can thus be controlled independent of the PZT layer thickness, offering more design flexibility and control over the frequency.

The major work on pMUT transducers development is performed by Muralt and Baborowski [32-35]. Some different designs and fabrications were reported by [31, 36-37].

A micro-diaphragm transducer based on PZT for gas sensor application was designed by Shin et al [38] and a pMUT for handwriting recognition was developed by Yang et al [39].

The principle of the **accelerometer** is to sense the force F created by a seismic mass M under an acceleration γ :

$$F = M\gamma \tag{1.5}$$

This force is transformed into a bending moment applied on a piezoelectric bimorph. An annular diaphragm accelerometer was reported by [40-41] and [27].

The **pressure sensors** are based on the principle of vibration in resonance. A mass can be detected by loading a piezoelectric device with pressure which changes or shifts the resonant frequency. At the oscillator fundamental frequency, the strain distribution along the active element gives rise to a shape vibrational mode corresponding to a quarter of wavelength ($\lambda/4$). In these conditions and surrounded by a medium, e.g. air, the disk moves perpendicularly to its surface giving rise to plane pressure waves.

Using the resonant mode various pressure sensors were developed for application such as atomic force microscopy (AFM) and micropumps [42-44], scanning force microscopy [45-46], for high-precision coordinate measuring machines [47] or as mass sensors for application in chromatography [48].
Based on the same principles a gravimetric sensor [49] and a microphone device were fabricated [50].

Traveling waves **ultrasonic motors,** as an alternative to magnetic motors, find increasing application possibilities in zoom and autofocus for cameras and automobile components, where a transient actuation with a high blocking torque and fast response time is required [51]. The first MEMS piezo-motor was made at MIT robotic laboratory on a bulk micromachined silicon membrane and sol-gel PZT [52]. The rotor was a small glass lens excited in an asynchronous manner by a standing wave. A synchronous motor was made in Switzerland in relation with the watch industry [53- 54] and in Japan by [55].

More recently a potential application of piezoelectrics as a **power generator** for powering wireless sensor nodes has been discussed [56-58]. This device would exploit the ambient vibrational energy and convert it by using the piezoelectric energy harvesting. It would provide power for wireless MEMS sensors without batteries. A thin film piezoelectric power generator was developed by Jeon et al [57] using a d_{33} mode of piezoelectric transducer as cantilever. A 0.48 µm thick PZT film was employed.

Other device design propositions would employ a 100 µm PZT [58] and a power generator for application in total knee replacement implant [59] is under conception.

The **actuators** in general consist of a combination of elements depicted in Fig. 10 with the actuated PZT layer and have potential for various applications. PZT actuated cantilevers were fabricated by various researchers [60-64]. Some of the applications are 1D and 2D scanner [65], a micro-mirror [66] or 2D ultrasonic transducers [67-68]

1.4.1 Summary

A brief review of MEMS devices where the application of PZT film was realized was given. The magnitude of the PZT element output depends upon the piezoelectric properties of the deposited layer, its thickness and the stress or voltage applied. In some applications e.g. in conventional transducers, there is a relationship between the thickness and the frequency and thus the frequency range has very specific requirements on PZT thickness. The thickness of the majority of PZT films discussed in the previous

section are summarized in Tab. 1.1, and the application method was given if other method than sol-gel was used.

Tab. 1.1: Summary of PZT thick films employed into MEMS design and fabrication.

	PZT film thickness					
conventional Transducers	192µm[0] [25]	100µm[0] [26],[27]	80µm[1] [30]	9 µm[3] [29]	12 to 25 µm [24]	
pMUT	2µm [32-34]	0.5 µm [38]	2µm [36]	1µm [31]	0.4 µm [37]	
actuators	0.5µm [60]	1µm [66]	0.8µm[5] [62-63]	3.5 µm [68]	50 µm[1] [61]	1.5µm [65]
accelero-meters	5.6 - 7µm [41]			**motors**	0.6µm [53]	
sensors	1.45 µm [45]	22 µm[4] [48]	140 µm[4], [49]	10 µm[3] [46]	1µm [50]	
power generator	0.48 [57]	100µm[4] [58]				

[0]made from bulk ceramic, [1]screen printing, [2]composite technology, [3]hydorthermal method [4]paste, [5] sputter deposition

Except for conventional transducer applications and some sensor applications, most of the films were prepared using the sol-gel method for thin films. In the majority of the works reported the films with 9 to 15 layers were coated to achieve a thickness around 1 µm.

1.5 Chemical solution deposition of PZT (CSD)

The use of CSD for the fabrication of perovskite thin films was well reviewed in 1997 by Schwartz [69] and recently by Bhuiyan et al [70]. The development of CSD processes for perovskite thin films dates to Mid-1980s. Fukushima et al [71] in 1984 published their work on metallo-organic deposition (MOD) processing of thin films of PZT, a wide used ferroelectric material, and right after that, Budd et al [72-73] published their work on the sol-gel processing of thin films of PZT. These pioneers' works demonstrated that it is possible to obtain the desirable properties of bulk perovskite materials in thin-film form. The early work by these investigators and others led to a rapid expansion of research in this area [73-75].

CSD processes, mainly including metallo-organic deposition (MOD) and sol-gel process, have been the subjects of considerable research interest relative to the deposition of thin film electric ceramics. MOD and sol-gel process differ in the chemistry in the solution. They afford the potential to control both chemical composition and microstructure to the levels required in electronic materials processing applications. In addition, experimental evidence indicates that temperature-time requirements for the subsequent crystallization/densification processing can often be minimized due to the high degree of chemical homogeneity in the polymeric ceramic precursor systems.

The general principle of CSD involved in the solution deposition of ceramic films is to prepare a "homogeneous" solution of the necessary cation species that may later be applied to a substrate. The homogeneity of solution is the most important in assuring a high quality thin film, which is often neglected or less considered by the CSD users. Other important parameters that will define the solution precursor properties are the precursor size, structure and shape [76-77]. The starting reagents are dissolved in a common solvent. The selection of the starting reagents, depending on the solution routes, is dictated by solubility, accessibility and reactivity considerations of solution precursor species desired.

The advantages of the CSD process over other techniques are the high purity of the oxide products, easy control of composition, low processing temperature and low cost and implementation [2, 78-79]. Other benefits are the ability to coat large areas uniformly and the possibility of using lower temperature compared to other methods [22].

The approach used to synthesise PZT sols in this work is called the "hybrid" or "chelate" route, which also utilises alkoxide compounds as starting reagents for the B-site species. In this process, A-site short–chain carboxylate precursors are dissolved in an excess of carboxylic acid (e.g., acetic acid) and B-site alkoxide compounds. These processes are referred to as "hybrid" because they utilize both carboxylate and alkoxide precursors, and the alkoxides react with the carboxylic acid to form oligomers and small polymers. They are also called "chelate" processes because these routes rely heavily on the molecular modifications with chelating ligands, such as, acetic acid, acetylacetone, or amine compounds. Carboxylic acid also serves as a solvent to

dissolve the carboxylate, which is only slightly soluble in alcohols such as methonal, ethanol, or propanol. Typically, the carboxylic acid groups coordinate the metal species in a bidentate fashion, and frequently act as bridging ligands, linking metals together to form oligomers. Chelation of the alkoxides by these carboxylate groups results in the formation of precursors that possess reduced sensitivity toward hydrolysis.

While chelate processes are simple and rapid, the chemistry involved in solution preparation is quite complex due to the number of reactions that occur. These reactions have been studied in detail using nuclear magnetic resonance (NMR) and Fourier transform infrared (FTIR) spectroscopy [80]. Key reactions were found to be chelation, esterification, and hydrolysis and condensation. The complexity of the reactions results in a diminished ability to control the precursor structure compared to true sol-gel approaches, and thus the gain in process simplicity thus comes at a cost. Another drawback of chelate processes is that continued reactivity in the precursor solution following synthesis can result in a change in precursor characteristic over time (weeks to months) [77] and thereby a degradation in film properties [81]. This occurs because constituent groups such as acetate, while less susceptible to hydrolysis than alkoxy groups, may still be attacked by water, resulting in a change in the molecular structure, and other reactions result in continued oligomerization and re-alkoxylation of the species, eventually causing precipitation.

Despite these disadvantages, thin films with excellent electrical and microstructural properties have been prepared by this approach, and a number of research groups routinely use it as their primary method of film fabrication.

1.5.1 Sol-gel processing of thin films

The CSD can be deposited using spin-coating or dip-coating technology, or can be sprayed onto a surface [70]. The process of sol deposition and spin-coating, which was implemented in this work, followed by heating is schematically depicted in Fig. 1.11.

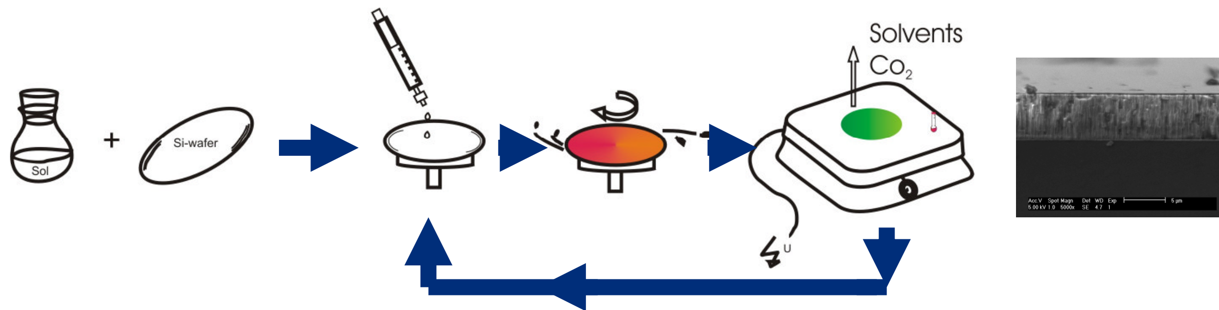

Fig. 1.11: Schematic of sol-gel processing. The coating and heating steps can be repeated to produce thick film.

Several drops of sol precursor are deposited onto the wafer surface. The hydrolysis is usually allowed to occur as the film is being deposited onto the substrate. Moisture in the atmosphere is used to supply water for the reaction. The reaction should proceed at significant rate implying that gelation will occur in a short period of time.

The heating of the PZT films on a hotplate is usually performed in one-step-process or two-step process. In the former the film is placed on a hotplate with crystallization temperature straight after spin-coating. The two step processes involves the intermediate step, usually referred to as pyrolysis, prior to crystallization. Upon heating first the organic residuals evaporate forming an amorphous solid. This solid is transformed into an intermediate pyrochlore phase at pyrolysis temperature between 300 and 470°C [82]. The intermediate phase is usually characterized as pyrochlore.

Pyrochlore is a ternary compounds with an $A_2B_2O_7$ stochiometry, where A is a larger and trivalent cation and B is a smaller and tetravalent cation, Fig. 1.12. The pyrochlore structure (Fd3m) is related to the fluorite structure and can be derived from the fluorite structure (Fm3m) by ordering the cation sublattice and creating ordered oxygen vacancies in such a way that coordination of the A atoms remains cubic, as in fluorite, but the coordination of the B cations decreases to octahedral. Ordering causes the pyrochlore unit cell to double with respect to the fluorite unit cell [70].

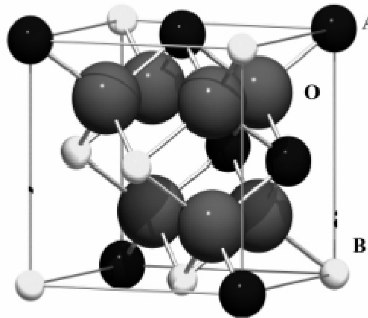

Fig. 1.12: Pyrochlore structure, taken from [70].

More detailed work on pyrochlore has revealed that there are actually two nanostructured pyrochlore phases forming during pyrolysis of PZT. One phase is amorphous and the other has the above mentioned fluorite structure [83-84]. Which one will form depends on the solution chemistry, Zr-to-Ti stochiometry, PbO stochiometry and underlying substrate technology [85]. The crystallization from pyrochlore-phases to perovskite is performed at temperatures above 500°C.

1.5.1.1 Spin coating

Sol-gel spin coating can be divided into 4 main stages [86]. In the first stage the liquid or a sol is dispensed onto the substrate. In the second stage the substrate is accelerated to its final desired rotational speed, Fig. 1.13a. This stage is usually characterized by aggressive fluid expulsion from the wafer surface by the rotational motion. Eventually, the fluid is thin enough to be completely co-rotating with the wafer and any evidence of fluid thickness differences is gone. Ultimately, the wafer reaches its desired speed and the fluid is thin enough that the viscous shear drag exactly balances the rotational accelerations. In the stage three, Fig. 1.13b, the substrate is spinning at a constant rate and fluid viscous forces dominate fluid thinning behavior [87]. This stage is characterized by gradual fluid thinning. Depending on the surface tension, viscosity, rotation rate, there may be a small bead of coating thickness difference around the rim of the final wafer. If the fluid thickness was initially uniform across the wafer, then the fluid thickness profile at any following time will also be uniform, leading to a uniform final coating (under ideal circumstances). In the fourth stage, Fig. 1.13c, the substrate is

spinning at a constant rate and solvent evaporation dominates the coating thinning behavior.

As the prior stage advances, the fluid thickness reaches a point where the viscosity effects yield only rather minor net fluid flow. At this point, the evaporation of any volatile solvent species will become the dominant process occurring in the coating. At this point the coating effectively "gels". As these solvents are removed the viscosity of the remaining solution will rise.

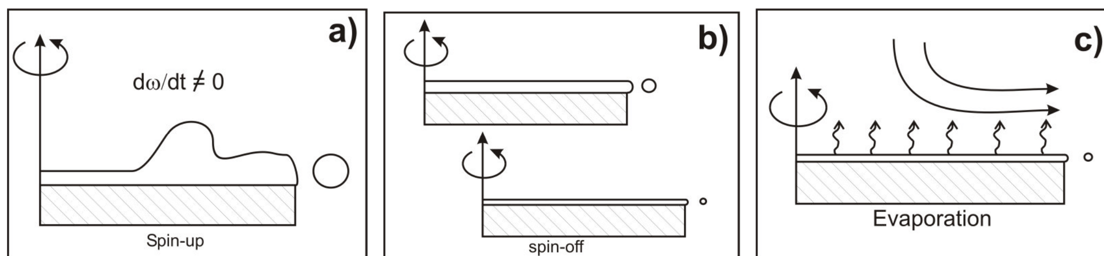

Fig. 1.13: Stages of spin coating technique. a) Spin up step, b) fluid spin-off stage, c) solvent evaporation stage after [85].

Stages 3 and 4 describe two processes - viscous flow and evaporation - that must be occurring simultaneously throughout all times. The final coating thickness is dependent on viscosity, spin rate and evaporation rate [88].

Some defects that can occur during spin coating include comets, striations and wafer edge effects [89]. Comets occur when relatively large solid particles impede the normal flow patterns of the solution on the spinning wafer. The presence of comets can be reduced or eliminated by working in cleaner environments and by filtering coating solutions as part of the dispense process. Striations are radialy oriented lines of thickness variation in the as-coated film, Fig. 1.14. Their occurrence is thought to arise because of evaporation driven surface tension effects. The early evaporation of light solvents can cause an enrichment of water and/or other less volatile species in the surface layer. If the surface tension of this layer is larger than the starting solution (and what still exists at deeper levels), then instability exists where the higher surface tension actually draws material in at regular intervals and the spaces in-between are more able to evaporate, and surface relief develops.

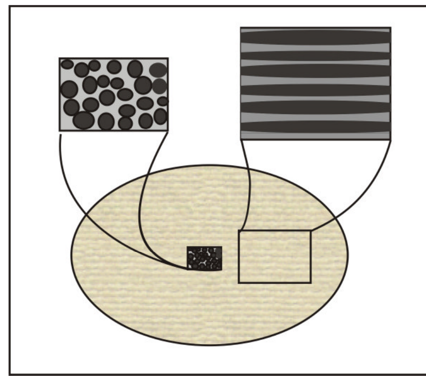

Fig. 1.14: Schematic diagram of striations on the wafer surface.

1.6 Thick sol-gel films

In this section the thick sol-gel film technology is going to be introduced. The film properties and the thickness limitation of these films will be given for comparison.

The definition of thick film components is not well established and depending on the application, thicknesses between 1 and 100 µm have been referred to as thick film. The films derived from sol-gel route without any additives have usually a single thicknesses below 0.1 µm [90] and thicker films are fabricated by repeating the sequence of spin-coating and heat treatment. The classification of thin and thick sol-gel derived films after the single layer thickness was made [91-93] or after total thickness regardless the single layer thickness [3, 94-96].

Various methods to increase the film thickness via sol-gel deposition were reported. They can be mainly classified into methods that use:

- modified sol-gel precursor
- composite method
- repeated sol-gel processes

to obtain either increased single layer thickness or total film thickness. Often the deposition of only one layer does not yield the required thickness and the coating procedure needs to be repeated. The single layer thickness in sol-gel technology is always limited through cracking of the films [97]. Depending on the sol-gel method this limit can sometimes be pushed to higher thickness but requires an appropriate heating profile [92, 98]. One major parameter in connection with spin coating is the viscosity of the sol. The viscosity needs to be increased to allow deposition of thicker layers. This can be done by addition of ethylene glycol [3] to the precursor. Further additives like polyvinylpyrrolidone (PVP) [99] or propylene glycol [100] were reported which can significantly increase the single layer thick but also introduce pores. The pore content reduces the density of the films and thus the dielectric and piezoelectric properties and the total performance of the film. Kozuka et al produced a 2 µm thick single layer by addition of PVP but found that the properties such film were rather poor due to pore content. Better properties were then reported for thinner films, e.g. for 0.75 µm thick films with the same method [101].

Similar reduction of properties with thickness was reported by Tu and Milne [102] who used a diol based PZT sol precursor. The 0.4 µm thick single layer film showed properties comparable to those films obtained via repeated coating of single layer from other work groups. As the film thickness was further increased, the remanant polarization was decreasing with increasing thickness but the permittivity was increased [102]. Only after the heating profile was modified were films with the 0.5 µm single layer thickness deposited and by repeating the procedure different film thicknesses were produced. Thus, a 10 µm film needed only 20 coatings. The ferroelectric properties were increasing with thickness. In films thicker than 10 µm no further increase was found and the ferroelectric properties were not dependent on thickness [92].

With the increase of total film thickness, Chen et al [3] observed an increase in the dielectric permittivity and remanant polarization. The coercive field was not sensitive to film thickness. The effective piezoelectric coefficient d_{33} was around 340 pC/N, which was higher than the value reported for undoped ceramic.

The use of **composite method** to produce thick sol-gel layers was reported by several authors [93, 103-105]. By mixing a PZT powder to the sol precursor an increased single

layer thickness between 1 to 3 µm can be achieved. The major drawback of the method is the porosity of the film which can be reduced by infiltration steps with pure sol precursor [103, 106]. The sintering aid Cu_2O-PbO was given to sol to increase the density of the film [106]. Through the choice of powder the properties of the film can be tailored. Tsurumi et al [105] used the method of [107] with the interfacial polymerization. The PZT film properties were much improved compared to composite methods and a surprisingly high $d_{33,f}$ =225 pm/V was measured.

Several authors fabricated thick films by **repeated coating** of thinner films [3, 94-96, 108]. The single layer thickness was between 130 nm [94, 109] and 330 nm [94]. The total thickness was between 2.7 µm [109] and 12 µm [3]. The films were dense and high dielectric and piezoelectric coefficients and ferroelectric properties.

An alternative method to spin-coating and dip-coating where the thickness is not limited by the viscosity of solution is the deposition via spraying of a sol precursor onto a substrate, while under active electrostatic field. Increased film thicknesses up to 0.6 [110] and 2µm [111] were reported.

Film fabrication using the electrophoretic deposition [112] is not related to the sol-gel method and a sol-gel deposition of photosensitive film [113] is only weakly related to sol-gel method. However, these methods are mentioned as the counterpart of sol-gel films that could possibly provide films with thicknesses in the range of several microns; the former by downscaling the powder size and the latter by upscaling. The minimal deposited thickness via electrophoretic deposition is 5 µm but the final annealing temperature needs to be increased to 900°C. The use of sol-gel method [114] either as a photosensitive film or to cast the sol into molds formed by photoresist after patterning with photolithography [115] could provide any thickness up to 23 µm but contain some surface cracking.

The properties of all available films and their thicknesses are summarized in Tab. 2. From these results it can be seen that e.g. the composite method aims to fabricate thick films in the thickness range which is required for conventional transducer application.

The other methods show the highest single thickness being 0.75 µm. Such films still yield good properties and when the thickness exceeds this limit, the properties of the film decays. The total thickness of such films is usually below 5 µm, except for two films. The ferroelectric and dielectric properties of such films are not reduced with increasing thickness. Their properties are comparable to the thin sol-gel films.

Tab. 1.2: Summary of the achieved film thicknesses using sol-gel and related methods. The properties of the films are as reported. Not all data was available for all films.

Method	PZT composition	Single layer	Total thickness	substrate	diel. const.	piezoel. coeff. d_{ij}[pC/N]	ferroelectric properties P[µC/cm²] E_c[kV/cm]
modified sol-gel [108]	PZT 45/55	0.33 µm	3.2 µm	steel			P_r=26 E_c=60
modified sol-gel [3]		0.25	12 µm		1450	$d_{33,f}$=340	P_r=26 E_c=31
sol-gel + PVP [99]		2 µm		silica glass			Pr=6.7 E_c=57.6
sol-gel + PVP [101]		0.75 µm		silica glass			P_r=24.6 E_c=96
1,2-diol route [92]		0.4 µm		Pt/Si	1100		P_r=33 E_c=46
diol route [102]		0.5 µm	10 µm	Pt/Si	950		P_r=37 E_c=33
composite [93]	PZT 48/48 + dopants	2 µm		Pt/Si	1800	d_{33}=70 e_{31} = 5 C/m^2	P_r =25 E_c=25
composite [103]		2.5 µm	20 µm				P_r =25 E_c=50
interfacial polymerisation [105]			23 µm		771	d_{33}=225 pm/V	P_r =33 E_c =70
sol-gel [98]		0.6 µm	5 µm				P_r = 24 E_c=38
sol-gel [95]	PZT 45/55		4 µm		1495		P_r=27 E_c=37
sol-gel [95]	PZT 52/48		4 µm		1545		P_r =25 E_c=28
sol-gel [95]	PZT 60/40		4 µm		1658		P_r =35 E_c=26
sol-gel [94]	PZT 45/55		3.3 µm		1055	d_{33}=54	
sol-gel [96]	PZT 50/50	0.13 µm	3.8 µm				P_r =53 E_c=70
sol-gel [109]		0.12 µm	2.7 µm			d_{31}=-132	
spray deposition [110]		0.6 µm		Al_2O_3	1430 1140	e_{31}=-8.9 C/m^2	P_r =20 E_c=60
electrophorese [112]			10 µm	Pt/Al_2O_3	750		P_s=43 P_r=33.6 Ec=21

From the Tab. 1.2 it can be seen that only few works were focusing on piezoelectric properties of the films and mainly dielectric permittivity and ferroelectric properties were reported.

1.7 Residual stress in PZT films

Residual stresses develop during sol-gel processing of piezoelectric thin films during the transformation of the metalorganic gel to the metal oxide (i.e. ceramic) on heat treatment. The processes in the film during deposition and heating can be considered in several stages:

(i) drying of solvent and pyrolysis of organics
(ii) structural rearrangement and densification
(iii) crystallization
(iv) cooling

The stress development in the thick PZT sol-gel film during processing was first characterized and described by [116]. Using the thermal gravimetric analysis the authors observed the evaporation and shrinkage of the sol-gel film and established microscopic and macroscopic models of the processes that take place and give rise to stress in the films. Thus it was found that the films with single layer thicker than 0.4 µm need an additional step of drying compared to thin films processed via two-step-process, or need a rapid firing and eventually annealing to compensate and avoid high stress accumulation and cracking. The stage of drying and firing was found to be most critical in the sol-gel processing of thick films and the resultant residual stress was attributed to the difference in dimensions of the film and the substrate after PZT crystallization. The first in-situ stress measurement during heating of single layer PZT film was performed by [11] followed by [117-118]. All authors showed a non-linear stress development in PZT during heating.

The total residual stress in the final polycrystalline film consists of intrinsic and extrinsic contributions. The intrinsic stress is induced by shrinkage and densification

during drying and firing, formation of intergranular stresses as anisotropic grain growth and by structural transformations at the Curie temperature. The intrinsic stresses due to shrinkage depend on relative rates of evaporation, viscous deformation and flow of liquid through the pores of the gel. Extrinsic thermal stresses are induced upon cooling due to the mismatch between the thermoelastic properties of the film with those of the substrate, while further extrinsic stress originates from lattice parameter mismatch between the film and the substrate [119-120]. If the stress in the film at any stage of the processing was too high, cracks occur. Cracking and delamination occur as a result of large tensile stress while compressive stress would force the film to buckle and thus delaminate from the substrate. In either way the film damage is inevitable and the film is wasted [121].

The residual stress in the sol-gel PZT film and its effect on PZT properties was extensively studied by several authors. However, in many cases the results were related to the film processing and thus only limited comparability between the results can be assessed. The reported stress results ranged from 100 MPa to couple of hundred MPa, depending on the substrate properties, PZT thickness and composition. The stress magnitude is also dependent on the characterization method. While i.e. the XRD and Raman spectroscopy stress characterization can determine the micro stresses that develop as a result of lattice defects, the curvature measurement focuses on macroscopic stress. Thus the stress results obtained by these two methods are only in rare cases correlating. Nevertheless, in all works a high contribution from the substrate to total stress was reported which was common to most of the investigation of stress origins in PZT films.

The residual stress affects the performance of PZT film. Tuttle et al reported that the sign of the stress during cooling through at Curie temperature influenced the orientation of the domain structure of the films [11]. Compressive stresses upon cooling through the Curie point resulted in domains with their *c*-direction and polarization vector normal to the film surface, while tensile stresses induced domains with their a-direction normal to the surface and with polarization vector in the plane. As a result, PZT films deposited on sapphire under compressive residual stress exhibited superior ferroelectric properties as compared to films deposited on silicon substrates under tensile residual stress.

Kweon et al [122] also found that the *c*-axis orientation content was related to the intrinsic stress generated during deposition of lead titanate films. The substrate stress was found to affect significantly the crystallographic orientation [123-124].

During the measurements of polarization or piezoelectric and dielectric properties of PZT ceramics under stress application it was observed that the applied stress greatly affected the PZT properties [125-127]. However, such results of the bulk ceramic are not transferable to PZT films. It is only logical to assume that the films, due to substrate constraint, will have other properties and will respond to applied stresses in a different way relative to the stress-free bulk ceramics [22]. Thus, in the bulk ceramics the dielectric constant is dependent on the applied stress [128] but in the films only a minimal influence by the applied stress was observed [129]. The remanant polarization and coercive field were reported to be more responsive to applied stress by several authors [129-132] and thus the coercitive field was reported to decrease with thickness and the remanant polarization was increasing with thickness. The applied stress can also induce depolarization and according to Franke [133] the stress-induced depolarisation in PZT thin films lay between 93 and 260 MPa. The residual stress has also an effect on the MEMS device processing. When the substrate underneath the film is removed the residual stress forces the film to bend as shown by Zhang et al [134]. Zhang et al studied the relationship of the residual stress in the stack Pt/PZT/Pt/Si and its effect on the fabricated cantilevers. Depending on the thickness of the underlying silicon layer the stress in the stack was enough to cause the cantilevers to bend. Only a careful stress analysis and required thickness of the underlying layer provided the parameters to balance the stress and to produce flat cantilevers.

1.8 Summary

It was shown that the piezoelectric films using PZT show excellent piezoelectric properties and have a great potential for MEMS applications. The sol-gel method yields thin films of very good quality. However, sol-gel method is usually correlated to thin films and to produce a thick film the individual coating steps and heating need to be repeated many times. This work is tedious and costly and at this stage not acceptable for

industrial applications. The devices using the PZT film as an active layer would require films in the thickness range between 1 and 10 μm. To produce a 1 μm film typically ten to fifteen coatings are still needed. The sol-gel derived films are throughout a considerable candidate for such application, especially since there is a lack of technologies that would be able to produce films in this thickness range. To drive the piezoelectric films towards the applications in MEMS the single layer thickness needs to be increased in order to reduce the number of processing steps in the way that is acceptable for industrial production.

The major limitation of the sol-gel method is that the single layer thickness cannot be increased easily. Only a careful analysis of the processes that are going on in the sol and the film and applying an appropriate heating profile can yield a thickness increase. Inappropriate heating can accumulate stress in the film making the films prone to cracking. The stress can be relaxed through pore formation but which will result in lower density and poor properties of the film. Such porous sol-gel derived films lose all the advantages that make sol-gel films very attractive.

The development of the residual stress in the film is inevitable while processing a sol-gel film on a substrate. It was shown that the residual stress can have an effect on the film orientation, phase content and the properties, and can have negative influence in MEMS fabrication. It was shown that also the thickness has an effect on the properties of the film and in thicker films the domain wall stabilization is less affected through substrate clamping. Thus, the film properties balance between the crystallographic orientation of the films, substrate clamping, residual stress and thickness.

1.9 Aim and the objectives of the study

Based on the previous review the following objectives were formulated:

1) **Increase in film thickness**

Single layer thickness is limited to below 0.1 μm due to cracking of the films during processing. To increase the single layer and total thickness the stress-related processes that take place in the film during heating needs to be

investigated. Some processing parameter need to be adapted, e.g. the viscosity of the sol precursor needs to be increased and the spin-coating needs to be adapted to the sol viscosity to yield thicker spin-coated films.

The heating profile for the processing of thick films which would minimize the stress development in the film plays the key role in the thickness increase. The best and appropriate investigation method of stress-controlled heating profile would be in-situ monitoring of stress as used by [11,117]. Unfortunately this method is not available and an alternative method must be used, e.g. the ex-situ curvature measurement after various stages of film processing. The parameters that affect the cracking in the film need to be characterized in order to avoid them. Hence, the gradual thickness increase with an appropriate heating profile followed by film characterization is the main objective.

The stress development in the films during multilayer deposition is also of great importance and would give insight into the maximum total thickness of the film that could be deposited via repeated spin-coating.

2) Film characterization

The so obtained thick films should be studied in terms of morphology and microstructure. The absence of cracks and pores should be evident. The grain growth and film orientation are essential for studies of film properties. It was shown in the review that the piezoelectric and dielectric properties have an intrinsic and extrinsic contribution. The intrinsic contribution to the electrical properties is purely dependent on the crystallographic orientation, and the extrinsic contribution depends on many other factors. Brooks et al [135] has shown that variation of the pyrolysis temperature or duration affects the crystallization and preferred orientation of the films. Thus, it would be necessary to find parameters which would enable fabrication of films with different orientation. Three PZT compositions will be studied within this work and the influence of the Zr-Ti stochiometry on the orientation is of great importance. Dependent on the sol precursor chemistry the preferred orientation can change during the multilayer film deposition as shown by Xu et al [17] and the orientation in the films needs to be characterized at different thicknesses of the

film to see if the preferred orientation is equal at any film thickness or in case it is not to detect any changes.

3) Piezoelectric and dielectric properties

From the point of view of piezoelectric application in MEMS the films should be characterized in terms of piezoelectric coefficients like d_{33}, d_{31} and e_{31} and the electromechanical coupling coefficients like k_{31}. It is of great importance to find the best piezoelectric properties of a film. The measurement of the d_{31} and k_{31} require cantilever design of the samples and will be a part of future work. As predicted by Du et al [19] the highest d_{33} coefficient in the films can be measured for [001] oriented film parallel to the polarization direction in tetragonal films. The highest $d_{33,f}$ is also expected for films with morphotropic phase boundary, as known from bulk ceramics [4]. Though the films are constraint to the substrate and there are more parameters which affect the d_{33} and e_{31} coefficients in the films than in the ceramics. These parameters need to be investigated.

The poling conditions must be adapted to thick films to yield the highest polarization and the best piezoelectric properties. The piezoelectric coefficients need to be studied in films of all three compositions and at different thicknesses. It was shown by several authors [3, 17] that in thicker films the domain wall movement is less affected by the substrate clamping and thus some extrinsic contribution is inhibited resulting in enhanced piezoelectric properties. Furthermore, the film deposition on different substrates would give different orientation and different properties of materials. To characterize and separte the inrinsic contribution from the extrinsic contribution to the piezoelectric properties the piezoelectric coefficient needs to be deterimined in PZT films with the same composition but different orientation. The determination of the dielectric constant of poled and unpoled films would allow the characterization of the extrinsic contribution of the 180° domain wall movements in the films.

4) Residual stress analysis

The residual stress in PZT film is dependent on many process related factors such as heating rate, film thickness, evaporation. In a film deposited on such substrate that consist of many different types of layers like platinum and silicon that have very different mechanical and thermal properties it can be expected that major stress will rise from the substrate. Thus, the substrate related stress development as well as the film related stress need to be characterized. It is also interesting to see if there are any differences in residual stress between the PZT compositions. The knowledge of relationship between the orientation and stress is of great importance. This can be studied e.g. if PZT films are deposited on different substrates. The phase development in PZT films with composition at the morphotropic phase boundary is dependent on the strain in the substrate, as shown by Li et al [13]. The stress characterization together with the phase characterization in such films would enable the control of phase development in PZT 52/48 films and tailoring the best piezoelectric properties.

Chapter 2: Experimental procedures: processing and characterisation of PZT films

2.1 Introduction to the Chapter

This chapter is divided into 3 main sections as film deposition methods, substrate preparation and film characterization methods which cover all the different aspects of films manufacturing and characterization. All experimental procedures used within the presented work including the processing conditions are given. Where pertinent, a short explanation of the background is given prior to the description of the experimental procedures.

2.2 Deposition techniques

2.2.1 Physical Vapour Deposition Techniques (PVD)

Physical vapour deposition techniques can be divided into three groups: sputtering, evaporation and ion plating. In this work only sputtering and evaporation methods were used.

2.2.1.1 PVD sputtering

Sputtering is an ablative plasma assisted method operated in high vacuum. A sputtering process is shown in Fig. 2.1. It utilizes ion bombardment with an inert gas such as Ar^+. The Ar^+ ions are generated by cold plasma. The sputtering relies on the transfer of physical momentum and kinetic energy from the incident particle (ions) to the surface atoms. The ion bombardment leads to structural changes in the near surface atoms and/or clusters of atoms by breaking the bonds and dislodging the surface atoms. Due to a considerable kinetic energy of some eV the sputtered atoms and ions move away from the target and condense on a substrate, located opposite to the target at distances between 50 and 500 mm.

Plasma discharge can be realized by DC or RF electrical field. The advantage of RF sputter sources is the possible deposition of non-conducting and semiconducting materials. The deposition rate is reduced significantly and cannot be compensated by higher electrical power supply. DC power supplies are able to provide more plasma energy [136-137].

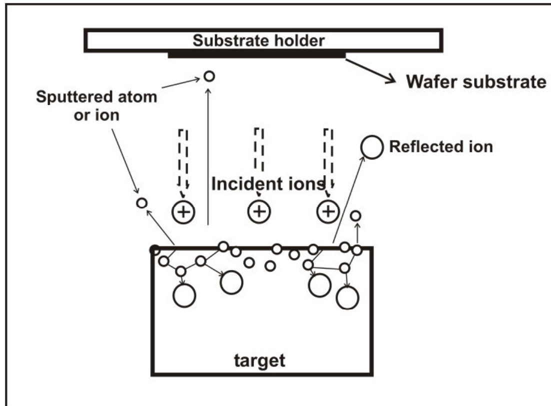

Fig. 2.1: The sputtering process shown condensates after schematically after [136].

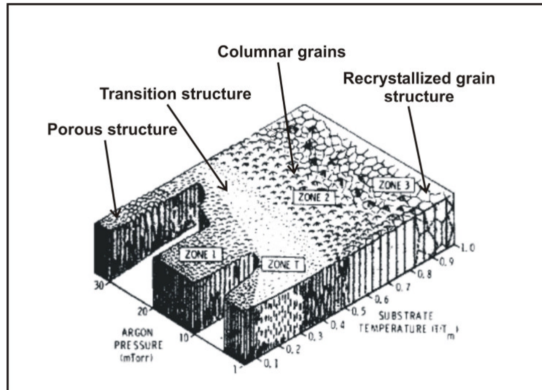

Fig. 2.2: Structural model of PVD Thornton et al [137].

A microstructure of thin PVD films is a function of substrate temperature, argon pressure, and ion energy. Based on these parameters the microstructure of PVD films was characterised by Thornton et al. [138], shown in Fig. 2.2. A polycrystalline structure is most likely to be created. Depending on the process conditions a high amount of defects like grain boundaries, pores and dislocations, vacancies, impurities and significant residual stress can be generated in the deposited thin films. A crystallographic texture of the thin films can be established through optimization of sputtering conditions [138-139]

In this study, PVD sputtering was used to deposit the bottom electrode on silicon and sapphire substrates. For the bottom electrode, first an 8 nm thick titanium adhesion layer was RF sputtered followed by an immediate platinum deposition. The thickness of platinum layer was 100 nm. Platinum was sputtered using DC power supply. Titanium adhesion layer was used to improve the adhesion between platinum and silicon oxide as platinum would not form good adhesion with silicon oxide layer and would peel off [140].

The deposition conditions are summarised in Tab. 2.1. This procedure was used to deposit platinum films with (111) orientation. Platinum substrates with different orientation (200) used in this study were supplied by TDK, Japan.

Tab. 2.1: PVD sputtering conditions for bottom electrode deposition.

	Ti deposition	**Pt deposition**
Power supply	RF sputtering	DC sputtering
vacuum before sputtering	< 6 x 10^{-7} Pa	< 6 x 10^{-7} Pa
Ar pressure	10 mTorr	10 mTorr
power	300 Watt	0.7 A, 450 V DC
sputtering rate and time	0.3 nm/second, 28 seconds	1.7 nm/second, 45 seconds
substrate temperature	room temperature	room temperature

2.2.1.2 PVD thermal evaporation

Thermal evaporation is also a vacuum-based PVD deposition technique in which a metal is heated to generate a metal vapour that can condense onto a substrate surface inside a vacuum chamber. For fabrication of high quality thin films a collisionless flight of particles has to take place from the vapour source to the substrate, so a vacuum of better than 10^{-5} Pa is required. The temperature needed is a function of vapour pressure of the material [136].

PVD thermal evaporation was used to deposit a circular top electrode needed for the measurement of electric properties of PZT films. A set of Au/Cr electrode dots was evaporated onto the film surface through stainless steel shadow mask with diameter 1 and 2 mm. Ideally the chrome adhesion layer was 10 nm thick and gold layer was 70 nm thick.

2.2.2 Preparation of sol precursor

All PZT films in this work were prepared by spinning sols on substrates. The each individual sol synthesis will be discussed in detail in the following sections.

2.2.2.1 Synthesis of PZT sol precursors

The route of PZT sol precursor preparation method is given in Fig. 2.3. It is a modified alkoxide sol route of [9], using lead acetate trihydrate, zirconium n-propoxide and titanium butoxide as precursors in a mixed solution of methanol (MeOH) and acetic acid (CH_3COOH).

Lead acetate trihydrate was dissolved in MeOH with stirring and heating. Zr and Ti precursors were firstly modified with acetic acid and then diluted with MeOH. Both solutions were mixed and heated under reflux for 2 h. When the solution was cooled to room temperature, ethylene glycol was added to stabilize the sol. Excess of 10 mol % Pb was added to the solution to compensate for the Pb loss during pyrolysis of the films. The concentrations of the solution were 0.4 M, 0.6 M, 0.8M and 1 M based on Pb. Three different sols with different Zr/Ti ratios were used:

- $Pb(Zr_{0.52}Ti_{0.48})O_3$
- $Pb(Zr_{0.40}Ti_{0.60})O_3$
- $Pb(Zr_{0.60}Ti_{0.40})O_3$.

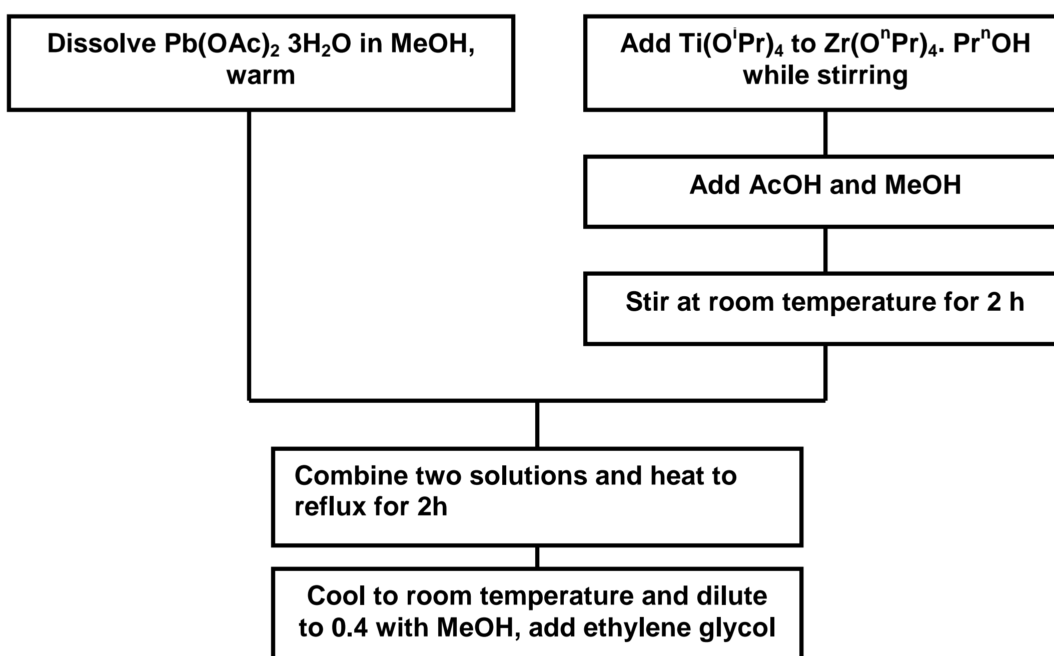

Fig. 2.3: Flow chart of the sol precursor production after [141].

2.2.2.2 Synthesis of $LaNiO_3$ and PbO sols

Pechini route was used to syntheses $LaNiO_3$ sol. $La(NO_3)_3$ and $Ni(NO_3)_2$ with equal moles were mixed and dissolved in citric acid and water. Ethylene glycol was added. The solution was then heated for 2 hours. The distillation was used to concentrate the solution to 0.1-0.2M. PbO sol was made by dissolving Pb 2-ethylhexanoate in ethanol.

2.2.3 Thermal oxidation

Silicon wafers with 450 to 600 nm thermal silicon oxide layer and polished surface were mainly used. However some of the wafers, especially 2" wafers and SOI wafers, were bare silicon wafers with some native silicon oxide on top. The thickness of the native silicon layer was probably in the range between 2 to 8 nm. To prevent a reaction of the bottom electrode with silicon which results in platinum and titanium silicide formation [142-143] together with the complete consumption of platinum, the bare silicon wafers were thermally oxidized in the furnace. The oxidation conditions were based on the diagram established by [144]. To grow a 700 nm thick silicon oxide layer the wafers were heated at 1200°C for 11 hours in a furnace with ambient air atmosphere.

2.3 Thick film processing

All steps of the sol-gel film preparation were performed in a clean room to avoid dust contamination in the samples. The substrates were prepared by the procedures described in the previous sections. The platinised wafers were spin cleaned with acetone and iso-propyalcohol and then treated in a barrel etcher in O_2 plasma atmosphere to eliminate any residual organics on the surface of the wafer. The process was performed at pressure lower than 2mbar for 5 minutes and the power of 20 W. The wafers with LNO as a bottom electrode were only treated in the barrel etcher. All the solutions were applied using a syringe with attached 0.2 μm inorganic filter and a spin coater. The standard deposition conditions were 3000 rpm spin-rate and 30 seconds spin-time.

Lower spin speeds e.g. 1500 rpm and 2000 rpm for 30 seconds were used to achieve thicker PZT films. LNO sol was spun at 4000 rpm for 40 seconds. In individual experiments other spin rates were employed and the spinning conditions will be given with the results.

Depending on wetting properties of the sol, either complete surface or a two third of the surface were covered with sol. The spun coated wet layers were dried, baked and crystallized by placing the samples on a hotplate with adequate temperature. The processing conditions for thick films evolved the usage of four different hotplates, each one with the different temperature, which were determined within this work. All PZT films were baked in sequence at 100°C, 300°C, 450°C and 550°C up to 600°C which involved the usage of four different hotplates. The holding time at each temperature varied between 1 and 10 minutes depending on the PZT composition, desired orientation and the single layer film thickness. The last used temperature was crystallisation temperature and had to be adapted to the each PZT composition. Films of the composition PZT 40/60 were crystallized at 550°C whereby films with higher zirconium amount needed higher crystallization temperature, as determined within this work.

After complete crystallization of one single layer the process of layer deposition and baking was repeated until the final thickness was reached.

2.4 Sample preparation for electrical characterization

Before any electrical measurements a set of top electrodes was deposited onto the films. A corner of each sample was wet etched to expose the bottom electrode. Two etching solutions were used called PZT etchant 1 and 2. The chemical composition of the first solution was 1% of hydrofluoric acid (HF) and 4% of hydrochloric acid diluted in water. The second solution was HNO_3 diluted in water (50%). Before any etching the rest of the film that should not be etched was covered by protective photoresist layer AZ 4562 and baked at 110°C for 2-5 minutes. The unprotected corner of the sample was dipped into the first solution for 10-20 second and then in the second solution for another 10-20 seconds. This process was repeated until a metallic platinum surface was clearly visible. The photoresist was removed with acetone.

2.4.1 Poling

To measure the electrical properties, such as piezoelectric coefficients, PZT films need to be poled. Contact poling and Corona poling were used in this work. To best pole the films, some poling parameters, such as field direction, field intensity, time and temperature etc., have been varied according to the film thickness and composition.

2.4.1.1 Contact poling

A DC electric field was applied to the bottom and top electrode via two probes connected to the poling rig power supply. The bottom electrode was at zero-potential. The poling was conducted at temperatures in the range between 90° and 200°C. The maximum poling voltage was 150 V and the maximum poling duration was 5 minutes. Only one sample or an electrode dot at the time can be poled with contact poling. Before the electric field was applied samples were left at the hotplate for up to one minute to allow the heat to equilibrate in the sample. After poling, the sample was immediately removed from the hotplate to cool down.

2.4.1.2 Corona poling

The setup of the Corona poling is depicted in Fig. 2.4. A sharp needle is suspended above a larger ground plate. The distance *d* between the tip of the needle and the ground plate can be in order of several centimetres. The sample is placed on the heated ground plate. The needle is connected to the high voltage supply. The principle of the Corona poling is the electron discharge at the sharp tip of the needle due to the strong electric field. The electrons are accelerated away from the sharp needle. In the vicinity of the needle the electrons collide with air molecules and ionize them. Farther away from the needle tip, where the electric field is decreasing with distance from the needle tip, the electrons decelerate and drift with relatively low energy that is not enough for ionization processes. A negative space charge is formed that decreases the electric field just in front of the sharp electrode. The ionized air will then collect on any insulator placed

between the wire and the ground plate. The charge will continue to build until equilibrium is met between the electro-forces of the plate and the environment.

The maximum applied voltage was around 12 kV. At first a low voltage was applied for 2 minutes, such as 5 kV. Then the poling voltage was switched off for 1 minute before the next poling period of 2 minutes at 8 kV was applied, followed by switching off of the field for 1 minute. Finally, the maximum voltage of 12 kV was applied for 2 minutes. The poling temperature was 130°C and the distance between the needle tip and the sample was 3 cm.

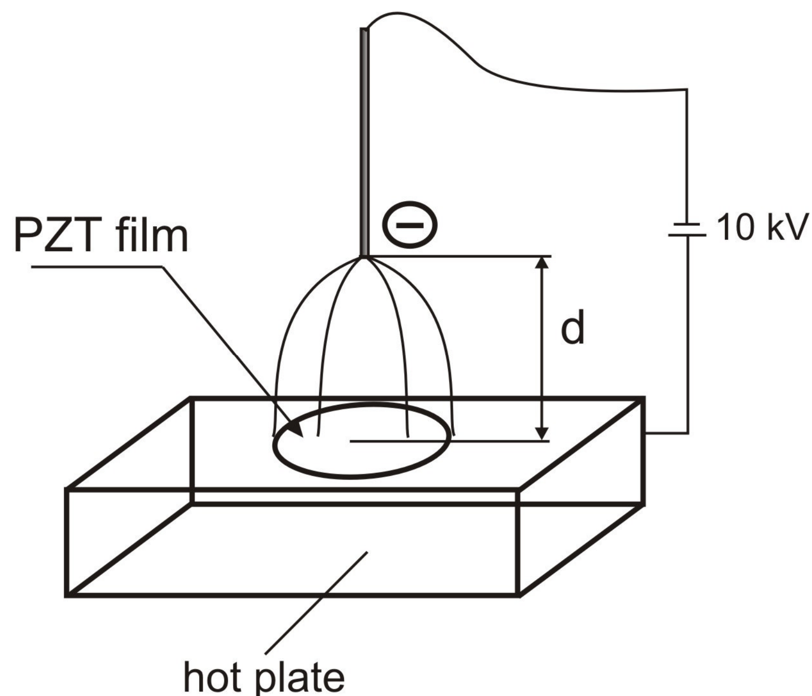

Fig. 2.4: Principle of corona poling.

2.5 Analytical techniques and methods

2.5.1 Analytical techniques for microstructure characterization

The microstructure of the films was analysed at different stages of the film processing.

2.5.1.1 Optical microscopy

Optical microscopy was used during film deposition to examine the film quality. The cracks and some spin-coating defects are ready visible with the bare eye if the sample is slightly tilted and held into the light. The optical microscope was used for examination purposes of microcracks, striations and buckling.

2.5.1.2 Scanning electron microscopy (SEM)

A focused electron beam is scanned over a specimen such that the interaction between the beam and the specimen excites various forms of radiation including backscattered electrons, secondary electrons, and x-rays, Fig. 2.5. The radiation is detected and analyzed to reveal information regarding the specimen's composition and topography. The contrast and resolution in SEM are functions of incident beam energy and intensity, and specimen properties.

Three different detectors were used to obtain information from the specimen, a secondary electron detector (SE), a back scattered electron detection system (BSE) and a high resolution detector (TLD). The secondary electrons have low energy and their detection is ideal for the examination of sample surface profiles. The contrast imaging with the back scattered electrons is dependent on specimen composition and atomic number, on the crystallite orientation and on electric polarity of the specimen [145].

Measurements of film thickness and grain structure were obtained using high-resolution cross-sectional scanning electron microscope (SEM) Phillips XL30 SFEG. Fracture cross-sections were prepared by scoring the back-side of the sample with a diamond stylus. The cross-section samples were mounted into specific sample holder for thin film examination. The grain size was also investigated in a top view, Fig. 2.6. Some samples were slightly etched with HF solution to reveal the grain boundaries structure.

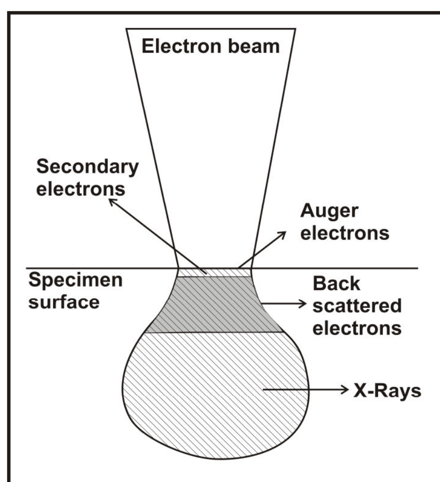

Fig. 2.5: Generation of radiation due to interaction of incident beam electrons with specimen atoms, in cross section.

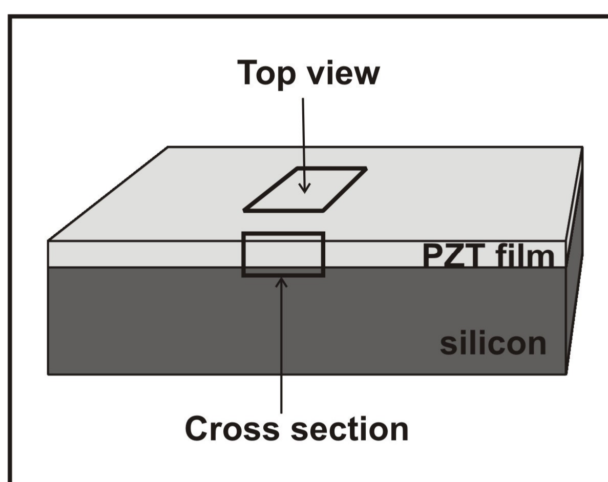

Fig. 2.6: Schematic diagram of sample examination directions.

2.5.1.2.1 Chemical composition analysis with EDX

EDX is a microanalytical technique that uses the characteristic spectrum of X-rays emitted by the specimen after excitation by high-energy electrons to obtain information about its elemental composition. It is often used in conjunction with SEM. The energy dispersive spectrum of generated x-rays, analysed with appropriate detection system, enables qualitative and quantitative analysis supposed the composition of the specimen is fairly known and artefacts can be excluded. The samples were analysed using the Phillips XL30 SFEG equipped with EDX detection system. The quantitative analysis including the ZAF correction [146] was performed using the software INCA™. Due to the penetration depth of the electron beam only films thicker than 1 µm were analysed where no signal was detected from the bottom electrode or the substrate.

2.5.1.3 Atomic force microscopy (AFM)

AFM operates by measuring attractive or repulsive forces between a tip and the sample [147]. In the AFM attractive or non-contact mode, the topographic images are derived from measurements of attractive van der Waals forces [148]. A sharp tip is scanned over

a surface with feedback mechanisms that enable the piezoelectric scanners to maintain the tip at a constant force (to obtain height information), or constant height (to obtain force information) above the sample surface.

In the constant force mode the tip hovers 50 - 150 Angstrom above the sample surface. Attractive Van der Waals forces acting between the tip and the sample are detected, and topographic images are constructed by scanning the tip above the surface. A small oscillation is given to the tip so that AC detection methods can be used to detect the small forces between the tip and the sample by measuring the change in amplitude, phase, or frequency of the oscillating cantilever in response to force gradients from the sample [149]. The imaging based on the constant force measurement is referred to as the tapping mode. Tapping mode imaging is implemented in ambient air by oscillating the cantilever assembly at or near the cantilever's resonant frequency using a piezoelectric crystal. The piezo-motion causes the cantilever to oscillate with a high amplitude (typically greater than 20 nm) when the tip is not in contact with the surface.

The grain growth in the platinum bottom electrode after various annealing steps was examined by AFM tapping mode. The surface structures of PZT films and of the platinum bottom electrode after PZT was etched away were investigated by means of AFM constant force and constant height mode.

2.5.1.4 X-ray diffraction (XRD)

The incident monochromatic beam is being diffracted on the specimen lattice planes obeying the Bragg's Law [150]:

$$n\lambda = 2d\sin\theta \qquad (2.1)$$

where n is the order of the reflection, λ is the wavelength of the incident beam, d is the lattice spacing and θ is the Bragg angle. Thus a characteristic diffraction pattern of each substance can be obtained if the substance is scanned in a 2θ–range. The obtained diffraction pattern is related to its crystallographic structure. The diffracted intensity is

dependent on various factors like the atomic and crystallographic structure, density, phase composition of the specimen and the instrumental set-up [151].

Measurements were performed using $CuK\alpha_1$ radiation at λ = 1.54056Å, using a Siemens AXS D5005 diffractometer with a Goebel mirror, and with a step size of 0.02°. All films were scanned in the range 2θ = 20° to 60° in which all peaks with high intensities are captured. The diffraction peaks were deconvolved with a profile fit functions, like Gaussian or Lorentzian function, after the background was subtracted. The program Peakfit™ was used. From the peak deconvolution the peak position, full width at half maxima (FWHM) and the integral intensity were obtained. These three peak characteristic parameters allow determination of several structural properties of the sample. The peak position allows the determination of the crystallographic lattice distance and thus the phase identification. The peak broadening due to small crystallite size can be determined if FWHM is analysed. The peak position in combination with the integral intensity allows determination of preferred crystallographic orientation of the polycrystalline specimen.

2.5.1.4.1 Qualitative phase analysis

The peak positions were compared with powder diffraction data files from PCPDF database regarding $Pb(Zr,Ti)O_3$, Pt, Si, $LaNiO_3$ files. PZT shows two crystallographic structures, a tetragonal and a rhombohedral phase. In the tetragonal structure the lattice parameters $a = b \neq c$ and thus two peaks for (100) and (001) lattice planes appear, which are close to each other, Fig. 2.7. This *a/c*-peak splitting is best observed on the (002)/(200) peak doublet. The rhombohedral phase in which $a = b = c$ the *a/c*-double peak can not be observed. However, rhombohedral structure is slightly tilted around the angle γ, $\alpha = \beta = 90° \neq \gamma$. The angle deviation is very small but it is sufficient to result in two non-equivalent (111) and (-111) lattice planes. In the XRD patterns this can be observed as peak doublet at the peak position (111), Fig. 2.8. If both phases are present, like in $Pb(Zr_{0.52}Ti_{0.48})O_3$, a maximum of 3 overlapping peaks at each position (111) and (002) can be observed, depending on the orientation of the film. The resolution of the laboratory XRD used in this work was sufficient to deconvolve three peaks; however,

the reproducibility of deconvolution was dependent on the film orientation and the intensity of the peaks.

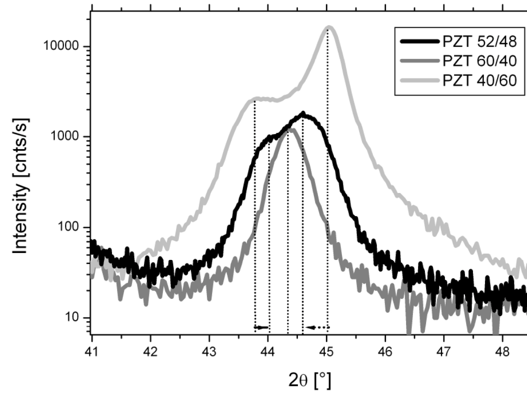

Fig. 2.7: Positions of (200)/(002) peaks in all three PZT compositions.

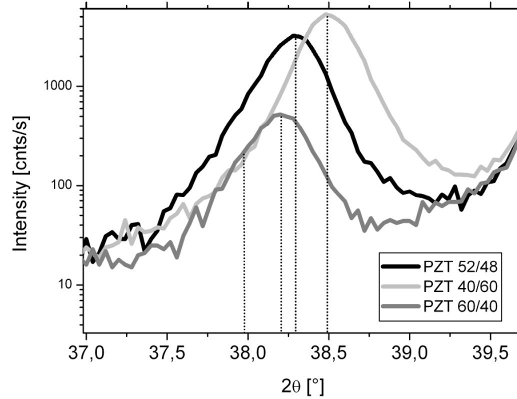

Fig. 2.8: Positions of (111) peak of all three PZT compositions.

The degree of crystallinity of the films could be analysed upon the detection of pyrochlore peak. Pyrochlore is an intermediate phase from which perovskite PZT is crystallized. Pyrochlore can be evidenced as a broad peak around $2\theta = 29.8°$ [135].

2.5.1.4.2 Crystallinity and preferred orientation

In a material with randomly oriented crystallites e.g. in a powder, the crystallites are randomly distributed within the specimen and all crystallite orientations are equally present. The lattice plane intensity will solely depend on the density and the atomic structure of the individual planes. Usually, in a thin sol-gel film on a substrate a preferred orientation of crystallites is found. Three types of texture are commonly observed:

- random, where no single orientation is dominant
- fibre-texture, where one orientation of the film grains is parallel to the growth direction, but the distribution is random about that direction and
- epitaxial, where the film orientation is fixed in three dimensions with respect to the substrate.

The deviation from random orientation and from the isotropy is a result of nucleation and crystal growth in thin films. Materials with preferred orientation exhibit anisotropy in their electronic and mechanical properties which are sometimes desirable.

The texture is usually investigated using X-ray diffraction pole figures [152], which depicts the relative orientation of crystalline grains in a material. In thin films where a columnar grain growth is evident and thus a fibre texture, the pole figure determination is not necessary. It is sufficient to determine the orientation of the crystallites by performing a θ - 2θ scan and compare it with a powder diffraction file of the same chemical composition. A deviation from random orientation is evident when the integral intensities are compared with the integral intensities of a powder sample from PCPDF files.

In PZT films the preferred orientation is usually calculated using the integral intensities of the (100), (110) and (111) peak:

$$I_{rel,(hkl)} = \frac{I_{(hkl)}}{I_{(100)} + I_{(110)} + I_{(111)}} \tag{2.2}$$

if no other peaks are detected.

2.5.1.4.3 Calculation of lattice parameters

From the peak position the lattice spacing d_{hkl} can be calculated using the Bragg Equation. Assuming a good calibration of the diffractometer and strain-free crystallites the calculated peak position should exactly match the peak position proposed by PCPDF file. If there is a noticeable deviation in the lattice spacing from the theoretical value this could be an evidence of microstrain in the specimen or a stochiometry deviation in solid solutions.

The lattice parameters *a* and *c* in tetragonal structure and their ratio are of interests as they indicate the degree of tetragonal splitting in different PZT compositions. They are determined from the (200)/(002) peak doublet as $a = 2d_{(200)}$ and

c = 2d$_{(002)}$. In the rhombohedral structure the a-lattice parameter is determined as a = 2d$_{(200)}$.

2.5.1.4.4 Crystallite size and microstrain

In ideal crystals the Bragg diffraction produces only a sharp line at exact angle θ_{hkl} where the double lattice spacing d_{hkl} matches exactly the wavelength λ of the incident beam. If the diffraction angle is in the vicinity of θ_{hkl}, the scattering of 1.1λ at some lattice planes, where incident beam is in-phase, is enabled. However, there is always a lattice plane in higher depth of the crystal that can extinguish this scattering where the incident beam is exactly out-of-phase. This extinction of in-phase and out-of-phase diffracted intensities allows only the occurrence of sharp lines. However, in samples with small crystallite size there is limited amount of lattice planes. When the incident beam is scattered on the lattice planes closer to the surface, in-phase scattering, it lacks the deeper lying lattice planes that could cause out-of-plane scattering. Due to the lack of deeper lying planes the extinction is suppressed and the incident beam is being diffracted but with much lower intensity than at exact Bragg angle. Thus, the crystallite size can be calculated from:

$$\tau = \frac{\lambda k}{B_c \cos\theta} \qquad (2.3)$$

Eq. (2.3) is called the Scherrer equation, where τ is crystallite size, k is a parameter between 0.8 and 1, B_c is FWHM.

The peak broadening can also occur as a result of microstress. Micro-stress is the stress due to accumulation of vacancies and interstitial atoms, shear planes, thermal expansion and contraction. In the material with microstress, tensile and compressive stresses can occur simultaneously. The micro-stress can be calculated after:

$$B_\varepsilon = 4\varepsilon \tan\theta \qquad (2.4)$$

where B_ε is the peak broadening due to the stain and ε is the strain. The crystallite size dependent broadening follows a cosθ−law while strain dependent broadening follows a tanθ-law. This is a key parameter which allows a separate determination of crystallite size and strain [153].

Prior to the calculation of peak broadening a calibration curve for instrumental broadening must be performed. This calibration curve must be performed on a certain powder such as LaB_6 which is stress-free and the grain size is above 5 µm so that no peak broadening contribution arises from the powder sample. A diffractogram of such sample contains sharp peaks and if broadening occurs, it is completely due to the instrumental broadening e.g. the axial divergence of the incident beam, the effect of flat specimen and the X-ray source image, limited through monochromator and focusing slits [154]. A powder diffraction file is determined for a standard material such as LaB_6. All detected peaks were deconvolved using the Pearson VII function. From all samples to be analysed the instrumental broadening is subtracted by:

$$B_t = B_{instrument} + B_{sample} \tag{2.5}$$

to obtains pure crystallite broadening from the sample B_{sample}. To determine the crystallite size and the strain, the Williamson-Hall plot was used. In the Williamson-Hall plot the B_{sample} is plotted against Bragg's Law 1/d where 1/d=2sinθ/λ for all diffracted lattice planes [155]. The slope of the plot is the strain ε and the crystallite size is given as the point of interception with y-axis for 1/d = 0.

2.5.2 Characterization of physical properties

2.5.2.1 Dielectric properties and capacitance measurement

The relative dielectric constant or relative permittivity is a complex material property consisting of a real part, the dielectric constant, and an imaginary part, the dielectric loss. It is a function of the ac-field frequency, Fig. 2.9, and temperature. Depending on

the excitation frequency, four different sources of polarization can be distinguished: the ionic, dipolar, atomic and electron polarization.

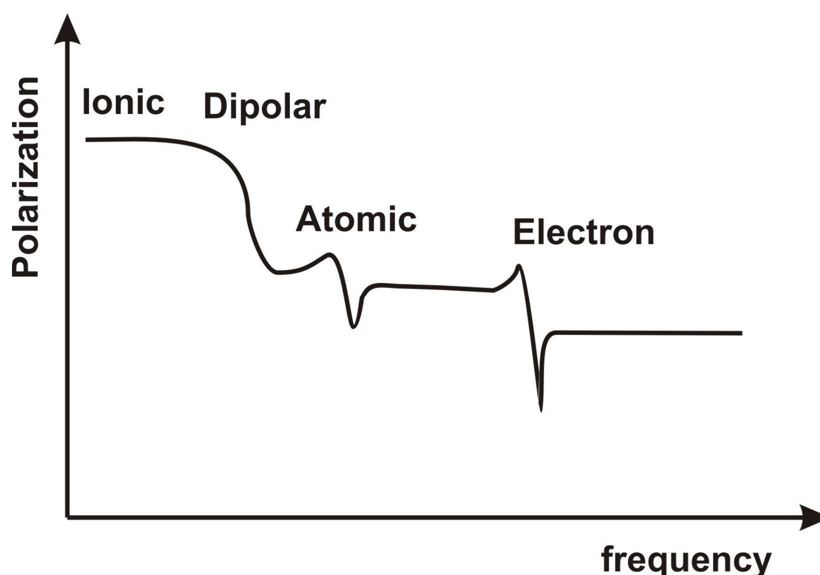

Fig. 2.9: Dielectric constant vs. frequency. In different frequency ranges a different polarization mechanism is active.

In the work described in this thesis, dielectric constants ε_r were determined by capacitive measurements from a Wayne Kerr impedance analyser connected to a probe station. Measurements were made at room temperature at 1 kHz, with dielectric loss tan δ measured simultaneously. In 2 films the dielectric constant was measured with increasing temperature ranging from room temperature to 200°C.

2.5.2.2 Ferroelectric polarization measurement

Polarization measurements, described in this thesis, were obtained using a standard Radiant Technologies RT66A ferroelectrics tester, which uses a modified Sawyer-Tower circuit. For polarization measurement at drive voltages greater than 20V, the RT66A was connected via the high voltage interface to a Trek voltage amplifier. This enabled polarization measurements to be made up to the breakdown limit. The Trek amplifier typically amplifies the drive voltage from the RT66A by a factor of 50 enabling the maximum voltage of about 1 kV. The high amplification factor also amplifies signal noise, which reduces the signal to noise ratio, resulting in noisy P-E

loops. The quality of data obtained was sufficient to determine the saturated polarization (P_{sat}), the remanant polarization (P_r) and the coercive field (E_c) from samples tested.

2.5.2.3 Determination of piezoelectric constants

Samples were prepared by etching the PZT film at the sample edge to expose the back electrode for the ground connection. The gold top electrodes with the diameters 1 and 2 mm were evaporated using a shadow mask. On the back of the wafer substrate a thin layer of conductive silver paint was applied and connected to the ground electrode. Piezoelectric measurements of $d_{33,f}$ and $e_{31,f}$ coefficients were performed using a Take Control Berlincourt Piezometer as described in [156].

2.5.2.4 Sheet resistivity measurements

The sheet resistivity measuring method consists of placing four probes on the surface of the material that make a contact along a line (Fig. 2.10). Current is passed through the outer pair of probes and the floating potential is measured across the inner pair. The resistivity can be calculated from the floating potential difference V between the inner and outer probes after [157]:

$$\rho = \frac{V}{I} 2\pi s \tag{2.6}$$

where I is the current through the outer pair of probes and *s* is an equipment parameter. Before each measurement the current is adjusted to the resistivity of a gold layer of known thickness. The current is set to a value I = 0.453 mA. The factor $2\pi s$ is implemented into this value. The sheet resistivity measurement is independent of the length and width of the continuous film and depends only on the film resistivity and the thickness of the film.

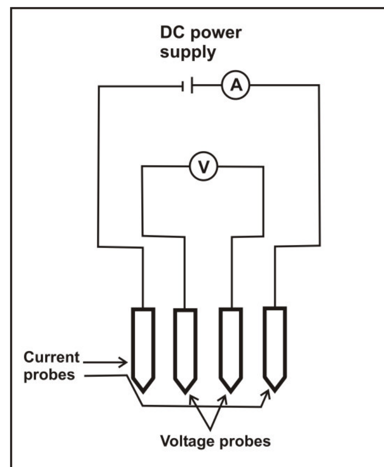

Fig. 2.10: Schematic of Four-Point-Probe after [157].

All measurements were repeated 5 times in the same sample area and an average value was taken.

2.5.3 Stress analysis

2.5.3.1 Townsend-Model for stress calculation

A substrate deposited with a film bends when cooling from higher temperature due to the thermal expansion mismatch between film and substrate and intrinsic residual stresses, Fig. 2.11.

A model based on Timoschenko's bimetallic beam [158] was chosen to analyse stresses after PZT film processing. In the following only some of the equations will be reproduced from Ref. [159]. A composite with number of layers i each with thickness t_i in which all layers are strained to have the same length d_0 at the initial state 1 shown in Fig. 2.12 [159]. The strain $\varepsilon_{i,0}$ is calculated as follows:

$$\varepsilon_{i,0} = \ln(\frac{l_0}{l_i}) \qquad (2.7)$$

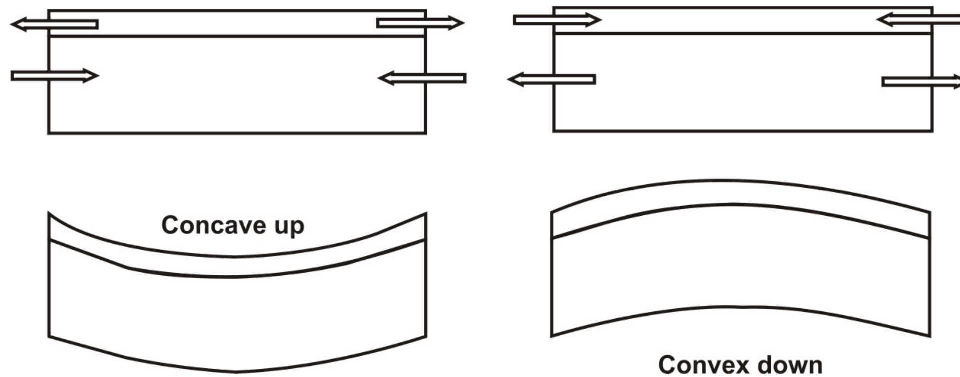

Fig. 2.11: Bending of the substrate due to film stress. Left: concave bending is due to tensile stresses in the film while convex bending (right) is due to compressive stresses in the film.

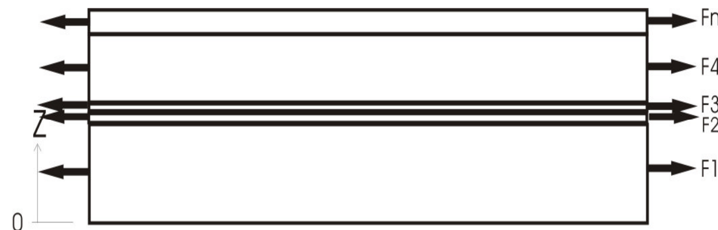

Fig. 2.12: A composite with n-layers. All layers are stretched due to force F to have same thickness.

The layered components are subject to end force and bonded together at the adjacent interfaces. This term can be interpreted as the lattice mismatch between layers. Such deformation produces strain which has to be compensated by an additional element of strain $\varepsilon_{i,F}$ so that the sum of end forces becomes null $\Sigma F = 0$. The total strain is:

$$\varepsilon_i = \varepsilon_{i,0} + \varepsilon_{i,F} \tag{2.8}$$

When the external forces in Fig. 2.12 are released, the composite will become bent, Fig. 2.13. An additional bending strain element must be added so that the net moment vanishes:

$$\varepsilon_i = \varepsilon_{i,0} + \varepsilon F + \varepsilon_{i,M} \tag{2.9}$$

$\varepsilon_{i,M}$ is produced by pure bending solution:

$$\varepsilon_{i,M} = (\pi - z)K \tag{2.10}$$

where π is the position of neutral plane, z is the coordinate distance normal to the linear dimension of the composite and K is the composite curvature.

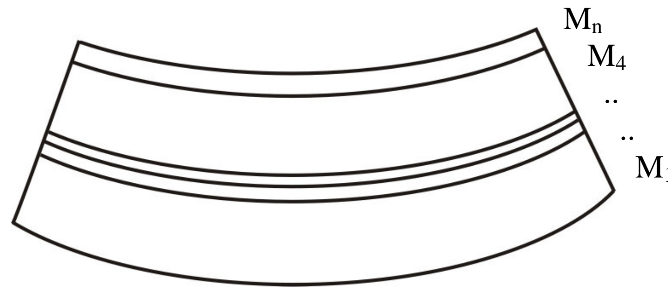

Fig. 2.13: After the force F is released, the compounds will bend due to the bending moment. This state would correspond to the film cooled down to room temperature if the film and substrate had the same length at processing temperature.

With Hooke's Law $\sigma = Y\varepsilon$ and the requirement of total moment to be null follows:

$$\sigma_i = Y_i \left[-\ln(l_i) + \frac{\sum_j Y_j t_j \ln(l_j)}{\sum_j Y_j t_j} + (\pi - z)K \right] \tag{2.11}$$

with Y_i as the Young's Modulus of the layer i for which the stress is calculated. To include the thermal inelastic strain $\alpha_i \Delta T$ one can write:

$$\ln(l_i) = \alpha_i \Delta T + \ln(l_{i,0}) \tag{2.12}$$

and the Eq. (2.11) becomes

$$\sigma_i = Y_i \left[-(\ln(l_{i,0}) + \alpha_i \Delta T) + \frac{\sum_j Y_j t_j (\ln(l_{i,0}) + \alpha_i \Delta T)}{\sum_j Y_j t_j} + (\pi - z) K \right] \tag{2.13}$$

The Eq. (2.13) allows stress calculation of all layers in a composite with different Young's Moduli. The same model also allows the calculation of the wafer curvature after:

$$K = \frac{\Delta T \sum_i Y_i \gamma_i \frac{t_i}{2} \left[-\alpha_i + \frac{\sum_j Y_j t_j \alpha_j}{\sum_j Y_j t_j} \right]}{\sum_i Y_i t_i \left[\left(\frac{\pi t}{2} - \frac{t^2}{3} \right) + (t - \pi) \frac{\gamma_i}{2} - \frac{1}{12} \left(3\gamma_i^2 + t_i^2 - t^2 \right) \right]} \tag{2.14}$$

where $\gamma_i = \sum \beta_{ij} t_j$ and $\beta_{ij}=-1$ for j<i, 0 for j=i and 1 for j>i. The neutral plane π for composite layers with different Young's moduli is calculated after:

$$\pi = \frac{t}{2} - \left(\frac{\sum_i Y_i \gamma_i \frac{t_i}{2}}{\sum_i Y_i t_i} \right) \tag{2.15}$$

2.5.3.2 Determination of wafer curvature by surface profilometry

All measurements of the wafer curvature were conducted using the Dektak Surface Profilometer, and performed always along the same line across the wafer (Fig. 2.14) using a self designed and constructed jig to assure the accuracy of the measurement. The scan length was always higher than 50% of the total diameter of the wafer. From

the profile the radius of curvature can be calculated in every single point of the profile using:

$$R(x) = \frac{(1 + y'^2)^{\frac{3}{2}}}{y''} \qquad (2.16)$$

where *y* is a polynomial function of at least 4th order applied to the curvature profile. *y'* and *y''* are first and second derivate of the function *y*. From the radius of curvature the stresses were calculated using the Townsend formula Eq. 2.13.

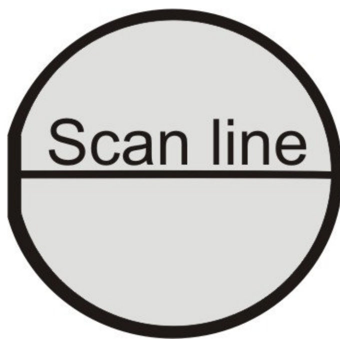

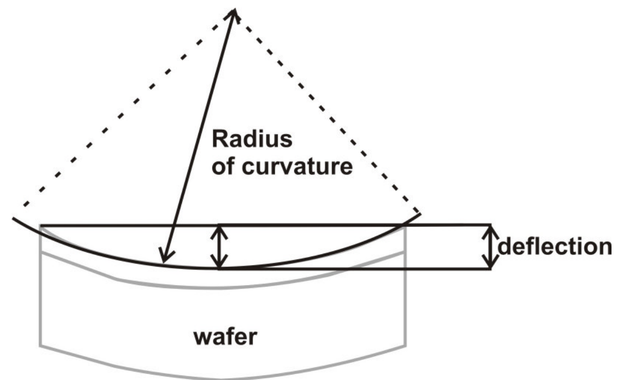

Fig. 2.14: Wafer with the primary flat and the scan direction for wafer deflection measurement.

Fig. 2.15: Maximum deflection at the centre of the wafer

The relationship between the curvature and the deflection d (Fig. 2.15) at the wafer centre for shallow parabolas can be approximated after:

$$d = \frac{r^2}{2 \cdot R} \qquad (2.17)$$

where r is the radius of the wafer and R is the radius of curvature [160].

In some results, where stress calculation was not possible, it was more appropriate to give the deflection at the centre of the wafer instead of the wafer

curvature. Maximum deflection was the peak value of the wafer deflection, found usually in the centre.

Chapter 3: Results and discussion

3.1 Introduction to the Chapter

The following chapter is divided into five main sections:

- The thick film processing
- Preferred orientation of sol-gel derived PZT films
- The residual stress in sol-gel derived PZT films
- Microstructural characterization
- The electric properties of the PZT films.

The first section begins with the investigation of stress-related processes in the sol-gel films during heating. Following from these investigations an appropriate heating profile was established which allows fabrication of thickness increased sol-gel films.

An extensive study on stress relaxation mechanism in the platinum/silicon substrate was conducted and will be discussed. The processing of PZT films on different bottom electrode types will be mentioned. This section concludes with the characterization of stress-related processes in the films in all PZT compositions and requirements on sol-gel processing to produce a thick PZT film.

The second section, the **preferred orientation,** outlines the characteristics of preferred orientation of the thickness increased PZT films that were deposited after the heating profile from section one. The changes of orientation with thickness and orientation and growth of each composition will be discussed. The aim of the study was to mainly characterize the PZT growth on Pt(111)/Si substrate. Some films were deposited on other substrates and will be introduced in this section.

The fourth section **microstructural characterization** focuses on the determination of lattice parameters in PZT films and discusses the origin of lattice parameter distribution. The determination of morphology including the grain size analysis will be introduced in this section.

The third section, the **residual stress,** focuses on the modeling and characterization of residual stress of PZT films deposited on Pt/Si substrates. The limitation and the preliminary stress characterization will be introduced first, followed by the stress results on Pt/Si substrate. The residual stress in the PZT films deposited on other substrates than Pt(111)/Si and its effect on the film orientation will be discussed.

The last section, the **electric properties** of the PZT films outlines the dielectric and piezoelectric properties of the PZT films with different composition and thickness, orientation and stress. The extrinsic contribution to the dielectric properties will be characterized, followed by the hysteresis loop measurements at different temperatures. This section concludes with the observation of the PZT film microstructure of different compositions related to domain formation.

3.2. PZT thick film processing

3.2.1 Increase of single layer thickness

Thicker single layer can be obtained either by increasing the sol concentration or by decreasing the spin speed. Higher thickness can be obtained when higher concentrated sol together with low spin rate is used. The relationship between the coating thickness and spin speed for 0.6M concentrated sol is depicted in Fig. 3.1. The relationship between the spin rate and layer thickness of a diluted solution depends on the spin speed [161] after:

$$t = k\omega^{-p} \tag{3.1}$$

with t as the thickness of the spin coated layer, k the constant depending on the evaporation rate, the viscosity the diffusivity and the molecular weight of the solvent. Bornside et al [161] found that the thickness of such solution depends inversely on the square root of the spin speed and thus has a value of 0.5. Here, p=0.42 was found which is a close match to the theoretical value. The maximum spin rate for each sol concentration is given in Tab. 3.1. The spin rates in Tab. 3.1 were the lowest applicable

spin rates which would give the maximum thick and crack-free single layer for an individual sol concentration.

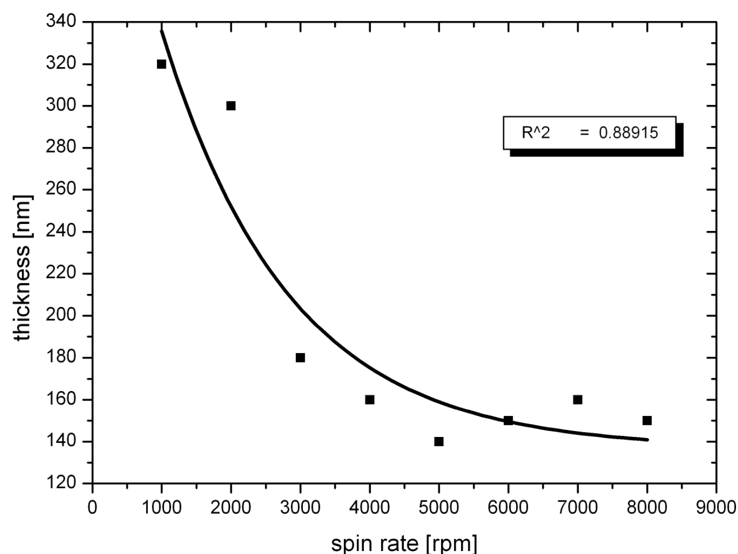

Fig. 3.1: Relationship between spin speed and layer thickness of 0.6 M concentrated sol.

Tab. 3.1: Spin-coating parameters used for different sol concentrations with the maximum obtainable crack-free layer thickness.

sol concentration	spinning conditions	film thickness
0.4 M	1500 rpm, 30 seconds	140 nm
0.6 M	1000 rpm, 30 seconds	320 nm
0.8 M	2000 rpm, 30 seconds	300 nm
1 M	3000 rpm, 30 seconds	500 nm

3.2.2 Investigation of key processing parameters

The processing conditions for thick PZT films were derived from thin film processing where a single layer was around 70 nm thick. Thin film processing involves 2 temperatures to crystallise the thin film, a pyrolysis temperature around 300°C and a crystallization temperature around 550°C. When the thickness was increased to 200 nm per layer it was found that the films cracked at a total thickness of 1 µm, Fig. 3.2. Such critical thickness associated with film cracking and above which it is not possible to deposit a crack-free film is usually observed in sol-gel derived films [91, 162].

It was assumed that the film cracked because of high uncontrolled stresses in the films. Hence, it was significant to investigate the stress evolution due to the change of thickness in the sol-gel films in order to find the processing parameters for crack-free thick films. A combination of ex-situ wafer curvature measurement for stress detection, thickness and XRD measurement to monitor the structural changes in the film was performed after defined heating cycle.

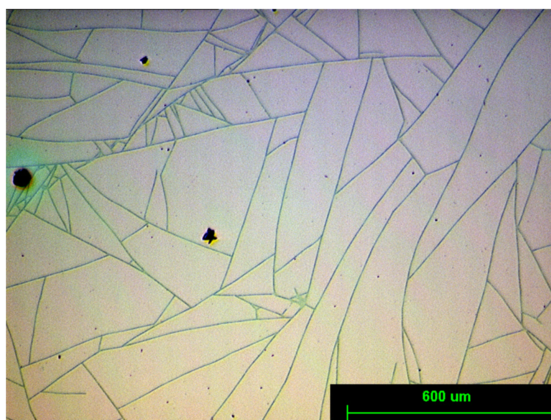

Fig. 3.2: Cracks in 1 µm thick film baked at 2 temperatures 300°C and 550°C for each layer.

A single layer of 0.6M concentrated PZT 40/60 sol was spin coated onto a platinised silicon substrate at the spin rate of 1500 rpm for 30 seconds. The film was stepwise heated at temperature. The starting and finishing temperatures were 100°C and 550°C respectively, with a step interval of 25°C. At each temperature the film was heated for one minute, and then cooled down to room temperature to perform the film analysis. Then the film was heated for another minute at the same temperature. This is referred to as one cycle at a temperature. After each heating step the film was cooled down to room temperature to perform the film analysis. After one such cycle the film was treated at the next higher temperature and the same analysis was performed again.

As a stress-related measurement parameter the wafer deflection was chosen. The deflection measurement results after each heating step cooled down to room temperature are depicted in Fig. 3.3. The positive deflection values stand for convex wafer deflection while negative values stand for concave wafer shape.

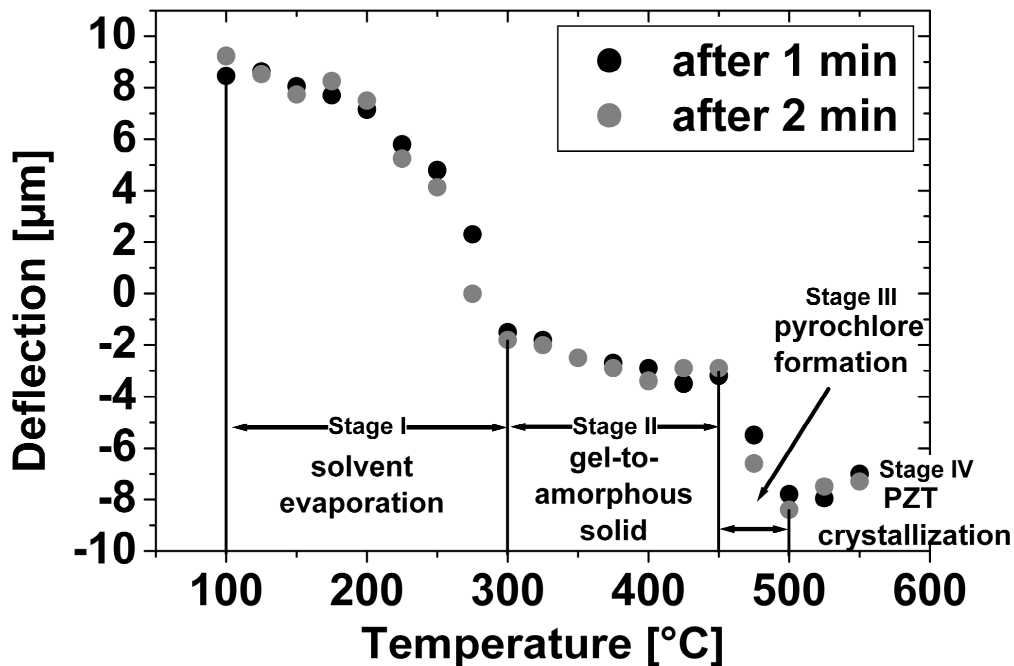

Fig. 3.3: Wafer deflection in the temperature interval of 200 nm thick PZT40/60 sol-gel film deposited onto a 2" platinised silicon substrate.

The measured deflection showed the same values after the first and second treatment at the same temperature, within the accuracy of the measurement, except at temperatures 275 °C and 475°C. This exception will be mentioned in the following paragraphs. From Fig. 3.3 it was observed that the deflection is not increasing linearly with temperature but has four different progression regimes. Depending on the progression regimes the deflection was then divided into four corresponding temperature stages. Those were between 100°C and 300°C, 300° and 450°C, 450°C to 500°C and above 500°C.

Before the sol deposition the wafer had a convex shape with the deflection around 9 µm. During the film processing the shape of the wafer changed to concave. In the first temperature range between 100° and 300°C the deflection progression showed a parabolic regime. Starting with 100°C the wafer was losing the strong convex bow and becoming flatter after each additional temperature treatment. A zero deflection was measured at 275°C showing a flat wafer. At 300°C a concave bending was measured.

In the temperature range between 300°C and 450°C, a moderate linear deflection increase was observed, from -2 to -3 µm. In the temperature range between 450°C and

500°C, a steep linear deflection increase was found. In the last temperature range above 500°C, the wafer deflection was linearly decreasing with temperature having the final value of -7 µm.

Thickness reduction was determined after each processing step, Fig. 3.4. Four different spin speeds were used to deposit the films with the sol of 1M concentration. The films spun with rates of 1500 rpm and higher showed starting layer thickness between 1 and 1.5 µm. The film thickness has been gradually reducing during the film processing. The largest shrinkage for all film thicknesses was found between 100°C and 300°C. Above 300°C the films were shrinking linearly. Similar results indicating major thickness and volume reduction below 300°C and a linear weight loss above this temperature were reported by [78, 118, 163-165]. The strong thickness decrease below 300°C can be attributed to the solvent evaporation in the wet film. The resulting thickness of all films was between 450 and 550 nm.

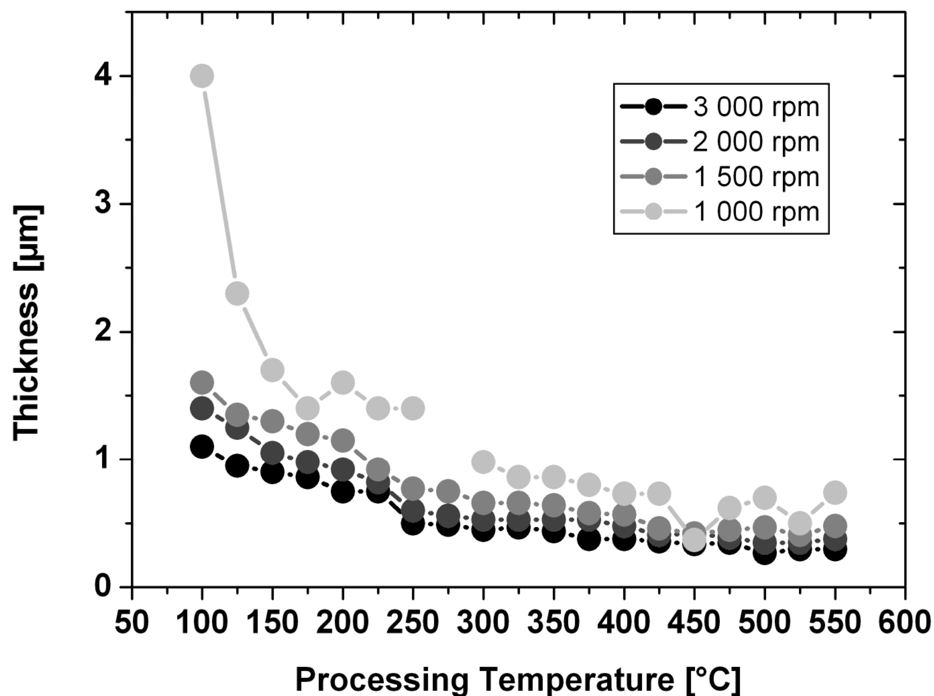

Fig. 3.4: Thickness reduction during film processing 1 M concentrated sol solutions deposited at 4 different spin speeds.

The film spun with 1000 rpm showed more than double starting layer thickness when compared with the other spin rates. The final thickness was 750 nm which was nearly double the value of other film thicknesses. This film experienced large thickness reduction during the thermal treatment, having the final thickness of only a quarter of its initial spun-on thickness. All other films experienced a loss of at least half of the initial film thickness. The real loss was probably higher as the first thickness measurement was performed after the temperature treatment at 100°C. During this first baking at 100°C, some colour changes could be observed indicating thickness reduction in the films.

Fig. 3.5 and 3.6 show the XRD patterns of the film at temperatures above 450°C. XRD was performed only on the film treated above 300°C. Between 300 and 450°C a small flat hump was found at around 2θ=30°, similar to the one in the XRD pattern at 450°C. Thus the XRD results below 450°C are not given here. At 475°C this broad peak disappeared and instead a sharper peak at 29.8° was observed, Fig. 5. This peak was clearly identified as a pyrochlore peak [135]. No other peaks except the Pt peak were observed at this temperature. At the next higher treatment temperature 500°C (Fig. 3.6) some perovskite PZT peaks were observed. The pyrochlore peak showed lower intensity. After the final treatment at 550°C perovskite PZT peaks had higher intensity and the pyrochlore peak was not detected meaning that pyrochlore was completely transformed to perovskite.

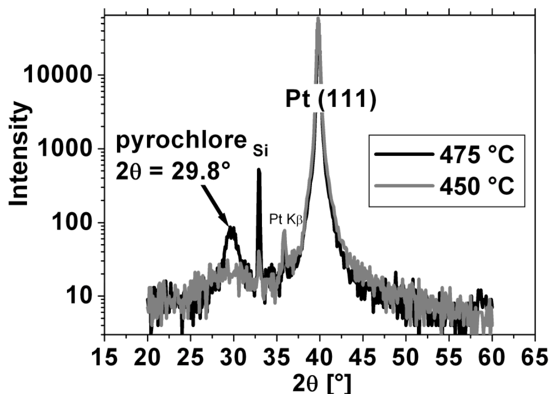

Fig. 3.5: XRD patterns of PZT 40/60sol-gel sol-gel films treated at 450°C and 475°C.

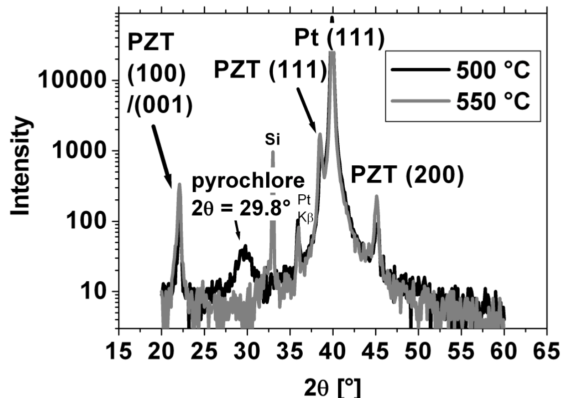

Fig. 3.6: XRD patterns of PZT 40/60 films treated at 500°C and 550°C.

From the deflection results (Fig. 3.3), the thickness reduction results (Fig. 3.4) and the XRD results (Fig. 3.5 and 3.6) it was possible to identify the ongoing processes in the sol-gel film in each temperature range.

In the first temperature range between 100 and 300°C the large thickness shrinkage and large deflection increase indicated high volume loss and tensile stresses in the film. In this temperature range the film was experiencing the transformation from sol-to-gel where various reactions take place i.e. evaporation of the different organic substances like solvents and $COOH^-$ and water [116]. The decomposition of most of the organic substances was reported to take place in the temperature range between 250°C and 350°C [166] and around 330°C [78]. Because of the high substance loss the film tends to shrink. However, due to the substrate constraint this is not entirely possible and the film forces the substrate to change its bending curvature. The reduction of initial high compressive (convex) curvature towards zero-deflection values is the indication of increasing tension in the film. Garino et al [129] reported residual tensile stress of 200 MPa after the film has been treated at 350°C and increased tensile stress in this temperature range was also reported by [116-117].

Above 300°C the wafer had a concave shape indicating tensile stress. In this temperature range, between 300 and 450°C, the magnitude of the deflection and shrinkage increase was relatively small and it corresponds to the transformation of gel-to-amorphous solid, as no peaks were observed in the XRD patterns. In this range probably the residual organics including CO_2 were evaporating, and also a decomposition of stronger bridging ligands is taking place in this temperature range [165, 167].

The deflection of the film thermally treated between 450° - 500 ºC showed high deflection increase for around 4 μm. Based on the XRD results this temperature range was attributed to the pyrochlore formation, which was reported to take place between 430°C and 550°C [78], or around 450°C [166]. The pyrochlore formation of slightly modified sol was found between 400 and 420°C by [168]. The deflection results imply that the pyrochlore formation was inducing large tensile stresses probably due to the change of the thermal expansion coefficient of pyrochlore. Such high tensile stresses during pyrochlore phase formation were reported earlier by [117, 129]. However, there

might be other contributions to the stress at this temperature which will be mentioned in the following subsection.

When the thermal treatment temperature was further increased to 500°C and above, the deflection started to decrease and reached a final value of -7 μm. This last temperature range was attributed to the pyrochlore-perovskite transformation or crystallization of PZT film. The tensile stress was partially relaxed after the transformation of pyrochlore to perovskite. In-situ stress measurements performed by Spierings et al [117] have shown a stress decrease above 450°C. In this work, it is likely that the stress relaxation due to the crystallisation into paraelectric cubic phase itself and also due to the phase transition at Curie temperature.

Based on the measurement of deflection in the single layer a temperature profile for thermal treatment of each single layer was established. A profile with four-temperature processing stages was used. These temperatures were 100°C, 300°C, 450°C and 550°C, corresponding to the starting points of four temperature ranges of deflection change. The thermal treatment at 100°C did not follow from the above findings of optimized processing conditions. It was chosen in order to allow a stepwise evaporation of the solvents and organics.

The thermal treatment of the PZT films from room temperature to high temperature is associated with the following changes in the film: evaporation of the solvent, burn-off of organic contents, pyrochlore formation and the transformation of pyrochlore to perovskite. Each of these changes induces a certain amount of stress. If the amount of simultaneously induced stress is very high, the films tend to crack. By choosing the above temperature profile, each individual process is being separated from the others, e.g. the first process in the film is allowed to finish before the next one can start. Thus the amount of stress induced at one time is limited and controlled. If the films are fired at other temperatures than indicated in Fig. 3.3, all processes in the film would simultaneously happen or would overlap, giving rise to high stresses. The film would crack easily like observed in Fig. 3.2.

As mentioned earlier, the wafer deflection values after thermal treatment for 1 or 2 min at the same temperature were almost the same except at 275 ºC and 475 ºC. At the latter two temperatures the change of deflection is too large to be attributed to the measurement error. The same deflection values at all other temperatures after the

thermal treatment for one and two minutes show that all stress related processes were finished already after 1 minute of thermal treatment. If the samples were treated at the same temperature for longer than one minute, no significant change was found. At 275°C and 475°C the changes in the film were not as fast, and the ongoing processes in the film needed longer time to complete. It is likely that the evaporation processes at 275°C needed more time to complete. The pyrochlore to perovskite transformation is likely to be another process needing more time to fully crystallize the film. This result gives some indication about the required minimum baking time for the PZT sol-gel films. Similar fast PZT film processing and crystallization was found by [169] where annealing times up to 1 minute were sufficient to crystallize PZT films.

3.2.3 Stress related deflection development in multilayer film deposition

To investigate the deflection development during repeated film deposition a similar method as described in the previous chapter was employed. The PZT sol was spin-coated and treated in sequence at the four chosen temperatures, at 100°C, 300°C, 450°C and 550°C. After each completed treatment, e.g. 1 minute at the 100°C, the film was cooled down and the deflection was measured. The film was then processes at the following temperatures until one layer was completely crystallised. A next layer was then deposited and the same cycle of heating and deflection measurement was applied. This was repeated until a film with the desired thickness was deposited. In Fig. 3.7 the deflection results are depicted. The film was deposited on an as-sputtered platinised silicon substrate. The initially compressive deflection was turned to tensile as soon as the film was treated at 300°C. A further deflection increase was found after the treatment at the next temperature. A tensile deflection reduction was found after the final anneal as already observed in the Fig. 3.3 from the previous subsection.

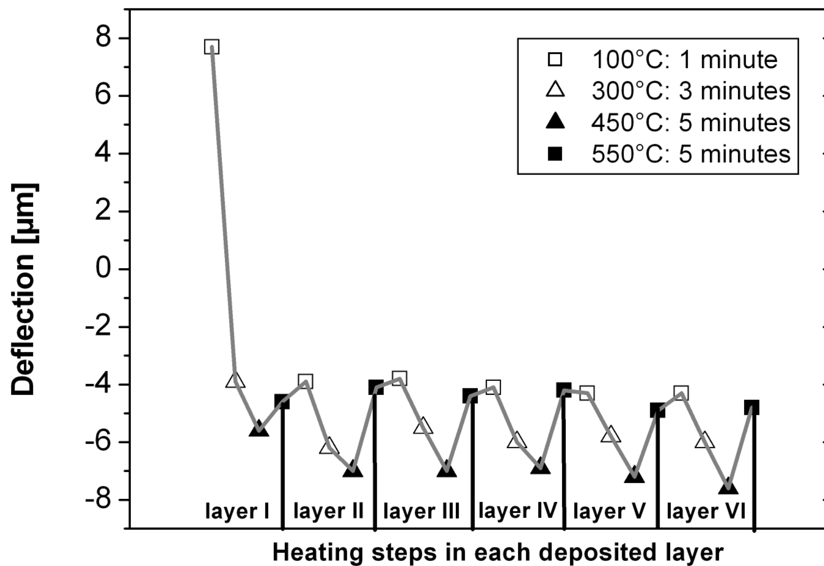

Fig. 3.7: Development of deflection in multilayer PZT films. The deflection was determined after each heating step, after the film was cooled down to room temperature.

The amount of the deflection was dramatically reduced after the processing of the first layer. The high deflection change during the processing of the first layer corresponds to the results obtained from deflection measurements of a single-layer. In all the following layers cyclic deflection behaviour was found. Although the stress in the films varies during processing and a large deflection increase was found at some stages, the total residual stress after the crystallization of each individual layer, (black squares) did not increase much with each additional layer. The cyclic behaviour of the deflection corresponds to the results of Park et al [164] who performed in-situ deflection measurement during multilayer deposition. Park et al found that all subsequently deposited multilayers showed the same stress profile upon heating and also nearly same residual stress.

This procedure of film processing that was used to produce the film in Fig. 3.7 was adopted for all films to produce crack-free and dense films.

The difference in the deflection of the first and all subsequent layers suggest that there was other contribution to the stress in the first layer besides those from the film.

3.2.4 The effect of the platinised silicon substrate on the total wafer bending

As-deposited platinum bottom electrode usually encounters compressive stress, as reported by [170-171]. The stress state is dependent upon several factors like argon pressure during RF sputtering and the deposition temperature. The intrinsic compressive stress can be released when the as-sputtered platinum layer is heated to the maximum processing temperature. However, after annealing large tensile stress formed [117]. Usually, tensile stress is found after cooling down to room temperature. During platinum annealing the defects in the microstructure related to the sputtering process can be healed and the stresses change from compressive to tensile. Spierings et al [117] observed such relaxation of intrinsic stress in platinum that occurred regardless if PZT was deposited on top of platinum or not, and also regardless the atmosphere or if at first lower annealing temperature was employed. Once the sample was heated to the maximum temperature, the compressive stress relaxed and platinum showed tensile stress in the range of 940 MPa. The stress did not change upon further repeated heating in the same temperature range. Hence, the wafer deflection is not only the result of intrinsic film stresses due to film shrinkage, and the extrinsic stresses due to the thermal expansion mismatch between the PZT film and the substrate layers, but also a result of the relaxation processes in the platinum bottom electrode.

The crystallographic texture of platinum film after sputtering was usually (111) texture. In Fig. 3.8 a rocking curve of the as-sputtered and annealed platinum (111) peak is depicted. Gaussian fit of the rocking curve showed a higher intensity for annealed platinum. The full width of half maxima (FWHM), a value indicating the degree of columnar texture, was reduced from 4.95 of as-deposited Pt to 3.31 of annealed Pt. This shows an enhancement of platinum columnar (111) texture after annealing.

To characterise the processes in platinum electrode during annealing and to characterize the contribution of platinum relaxation to the wafer deflection, platinised silicon substrates were annealed at 550°C for different period of time. The microstructural changes were analysed by means of XRD and the AFM tapping images. Fig. 3.9 shows XRD $\theta-2\theta$ scans around the Pt(111) peak of all annealed samples. A

peak shift to higher 2θ angles could be observed. An increase in intensity amplitude in annealed platinum was obvious.

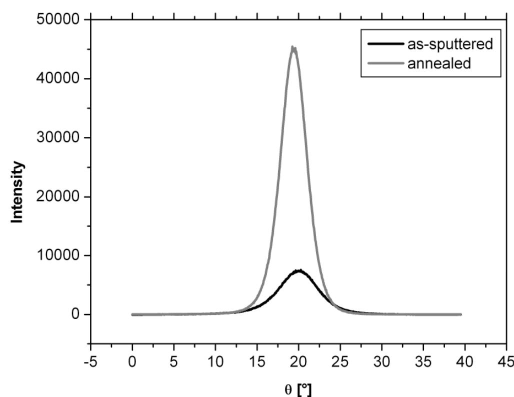

Fig. 3.8: Rocking curve of as-sputtered and 10 minutes annealed platinum

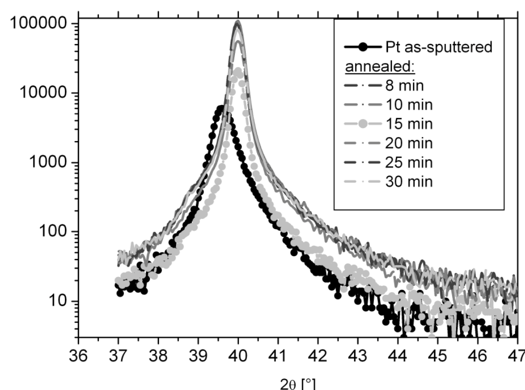

Fig. 3.9: XRD patterns of as-sputtered and annealed platinum, logarithmic scale

Fig. 3.10 depicts the AFM tapping images of platinum surface of as-sputtered and annealed platinum for 8, 10, 15, 20 25 and 30 minutes. To determine the grain size from the AFM images a mesh of 10 parallel, equidistant horizontal and vertical lines was drawn across the image and the grain size of the grains along these lines was determined. Then the average grain size was built. In images where 2 grain sizes were distinguishable the grain size of the majority of small grains was determined separately and their average was built. The results of the grain size analysis of the same samples by means of XRD are given in Fig. 3.11 and compared against the grain size results determined using AFM images. Before annealing, the grain size was fairly uniform between 10 and 14 nm (Fig. 3.10), or 20 nm (Fig. 3.11). After 8 min annealing (Fig. 3.10b), a mixture of the grains with the size between 20 and 33 nm and the clusters with no distinguishable grain boundaries were observed. The diameter of these clusters was larger and it was probably composed of several smaller grains. The XRD results revealed a grain size around 93 nm. Fig. 3.10c shows the grain structure of platinum after annealing for 10 minutes. This image, although having a low quality, quite clearly displays two different grain sizes, the smaller grain size between 36 and 51 nm and larger grains at around 110 nm. After 15 minutes annealing, Fig. 3.10d, the large grains with approximately grain size of 110 nm, similar to the grain size in Fig. 3.10c. There were some small grains visible for the first time. Those small grains were estimated to

have the grain size of around 14 nm. A mean value around 70 nm was determined from Fig. 3.11. After the next annealing interval, Fig. 3.10e, more small grains were visible. Their grain size lay between 14 and 33 nm. The size of bigger grains could not be estimated as the grain boundaries were not clearly visible but the XRD results showed a grain size around 75 nm. After 25 minutes annealing the grains looked more uniform between 49 and 69 nm, Fig. 3.10f with some smaller grains. After 30 minutes annealing, it could be distinguished between large grains, in the order of 80 nm could be distinguished with small grains around 28 nm, Fig. 3.10g.

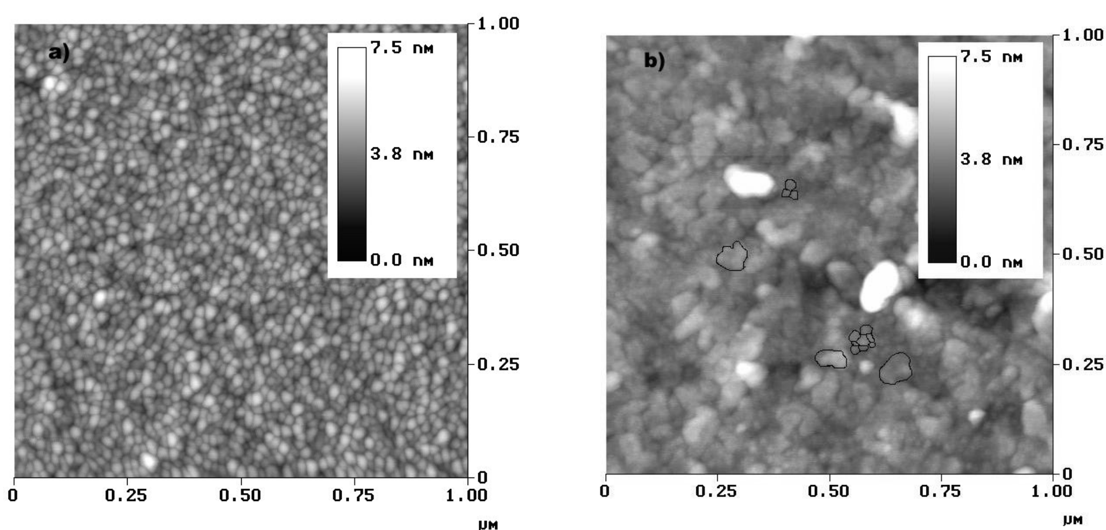

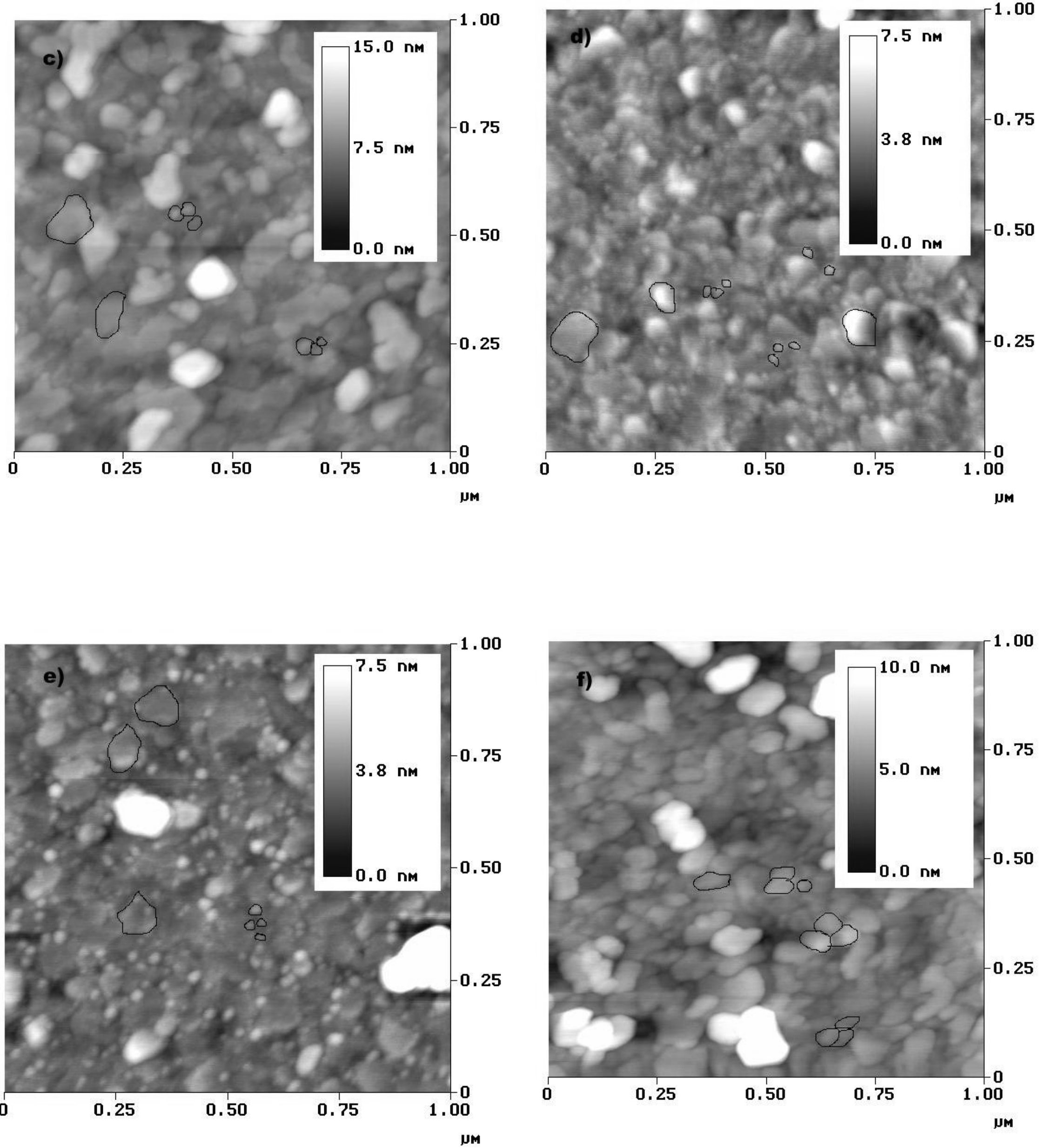
c)
15.0 nm
7.5 nm
0.0 nm
d)
7.5 nm
3.8 nm
0.0 nm
e)
7.5 nm
3.8 nm
0.0 nm
f)
10.0 nm
5.0 nm
0.0 nm
0
0.25
0.50
0.75
1.00
µm

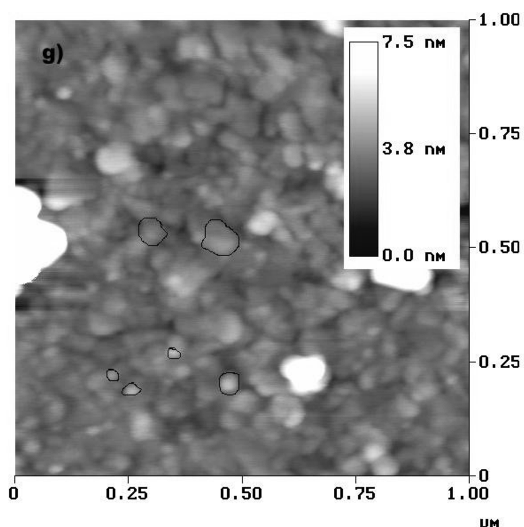

Fig. 3.10. a) to g): AFM images of platinum surface after various annealing times. Some of the grains were highlighted.

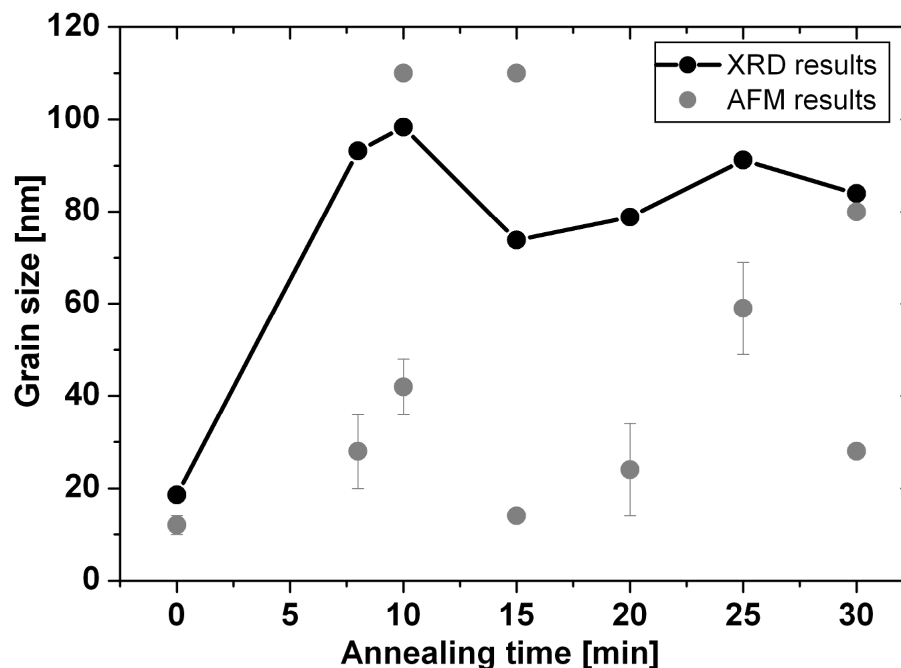

Fig. 3.11: Grain size of Pt calculated from XRD results from Fig. 3.9 together with the AFM results.

As shown in Fig. 3.10 and 3.11 the grain structure of platinum is changing during annealing at 550°C. At first the grain growth occurs. The initial grain size has been

nearly doubled and some large grains reach a considerable size of 110 nm. After only 15 minutes annealing, a recrystallization was observed where small grains were forming out of large grains. This means that some of the grains reached a critical thickness and that the energy level was high enough to initiate the recrystallization which would lower the total defect density [172]. If platinum was further annealed the recrystallized grains would grow. A resulting microstructure would be the one observed in Fig. 3.10g, where a coexistence of small grains resulted from the recrystallization and large grains unaffected during the recrystallization can be found.

The critical thickness could be estimated to be around 110 nm which corresponds closely to the thickness of the platinum layer. When the grains reach 100 nm size it means that they have same diameter and the same height, reaching from the silicon-platinum interface to the platinum top surface. At this stage only a lateral growth would be possible. However, the lateral growth does not seem to appear and instead, a recrystallization occurs when the grain diameter reaches the same value as its length.

The grain size determined from the XRD results showed slightly different results as determined from the AFM images. This is because the AFM, being a visual method, allows a distinction of between various grain sizes, whereas in the XRD all grain sizes contribute to the intensity of the same peak and to its broadening. Thus the results by XRD give a grain size value of the majority of the grains.

A recrystallization of platinum was reported by several authors [173-175], mostly in connection with hillock formation. The hillock formation is believed to be inhibited by the diffusion of titanium atoms through platinum layer. However, the hillock size was reported to range between 0.5 µm [117, 176] and 2-3 µm [175] and to form if the thickness of the titanium adhesion layer was thicker than 10 nm with 100 nm thick platinum layer. If the thickness of the titanium layer was reduced below 10 nm, like in this work, the recrystallization and the surface roughness increase could still be found but in much smaller range. In case of thinner titanium layer the grain size of recrystallized platinum was only 100 nm [175] and thus more corresponding to this work. A titanium thickness dependent grain growth of platinum was also reported by Nam et al [177]. The hillock formation is believed to be the stress relaxation mechanism due to large compressive intrinsic stress.

To investigate the role of titanium in platinum/titanium bilayer on the stress and the recrystallization of platinum, the deflection of platinum was studied after the same temperature regime as for PZT films, Fig. 3.12. Three substrates, each with 100 nm thick platinum, but with different thickness of titanium adhesion layer were heat treated. The substrates I, II and III contained 0, 8 and 16 nm thick titanium adhesion layers, respectively. Substrates I and III were treated at each temperature for two minutes in the whole temperature range. The substrate II was heated for 5 minutes at each temperature.

All three deflection curves showed similar behaviour of descending deflection in the temperature range below 300°C. The substrate I showed linear deflection decrease in the total temperature range. The deflection was compressive at all points and decreased for only 3 µm in total temperature range. A moderate linear deflection increase without any significant change of the wafer curvature was found. The results suggest that there was no stress-related platinum recrystallization in this platinum film, although the thermal treatment time should have been sufficient for the platinum recrystallization.

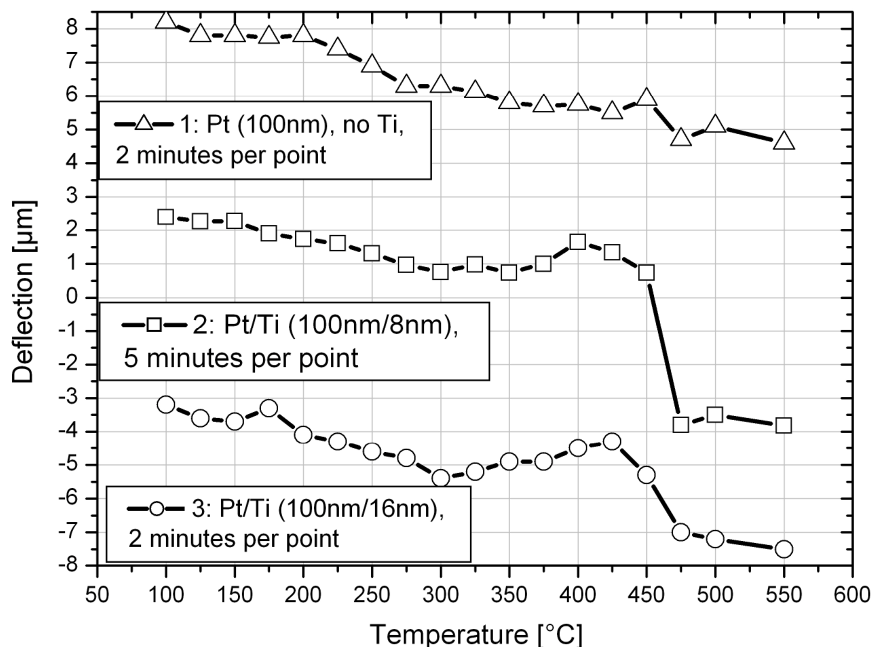

Fig. 3.12: Deflection in platinised silicon layer with different titanium thickness.

The deflection of substrate II showed a linear compressive deflection decrease until 350°C. Above this temperature and up to 400°C the deflection increased slightly. In the temperature range between 400°C and 475°C, the deflection changed abruptly from compressive to tensile and increased significantly for about 6 µm in this temperature range. Above 475°C, the deflection was nearly constant, indicating tensile stress. Assuming that the annealing time was sufficient for platinum to recrystallize, the temperature around 450°C can be concluded as the recrystallization temperature.

The substrate III showed similar deflection progression like substrate II. The initial concave wafer shape was due to silicon substrate. After platinum deposition the wafer deflection was less concave meaning that compressive stress was introduced through sputtering. An increase in tensile stress was observed above 300°C. In the temperature range between 450°C and 475°C a large tension increase was found.

The linear decrease of stress with temperature like in substrate I was reported by Kweon et al [176] who performed in-situ wafer curvature measurement on platinum layer on silicon without the titanium adhesion layer. When the titanium adhesion layer was present a different stress behaviour was found, more similar to substrate II. At first a moderate linear stress increase with temperature was found followed by a much steeper stress increase between 400°C and 570°C. Above 570°C a stress relaxation was observed. The stress increase in the temperature range was attributed to the titanium diffusion through platinum layer.

Stress progression in substrate III correlates to the results reported by Spierings at el and Chung et al [117, 178]. The results of Spierings et al and Chung et al showed also a stress increase with temperature, but before the appearance of major stress increase above 400°C, there was a stress relaxation between 300°C and 450°C. This stress relaxation was quite similar to that observed in substrate III and was attributed to partial diffusion of titanium though platinum. Like in this work, in all results in the mentioned literature a stress relaxation accompanied with recrystallization and hillock formation was evidenced. A change of stress from compressive to tensile was found around the maximum annealing temperature. Upon cooling down to room temperature the tensile stress increased linearly and was attributed to thermal stress between platinum and silicon. At room temperature tensile residual stress was around 1 GPa

[117, 176]. The stress relaxation and recrystallization was attributed to the interdiffusion of titanium through platinum layer.

From the results in Fig. 3.12 a titanium related platinum recrystallisation can be concluded. If no titanium was present, platinum would not recrystallise in the given time frame and the stress state would still be compressive. With titanium layer present, the recrystallisation occurred at around 450°C and the process was faster if the titanium layer was thicker.

The interdiffusion in solids can be usually investigated by means of X-ray spectroscopy. However, this method was not available and instead, the sheet resistivity measurements were conducted simultaneously to the deflection measurement after annealing. The measurement was performed on substrate III from Fig. 3.12 and on a film with 4 nm thick Ti layer. The results are presented in Fig. 3.13.

Assuming that the total thickness of the bilayer does not change with annealing, and that the grain size increase has only little influence on the sheet resistivity, the total conductivity should remain constant in the whole temperature range. The influence of the grain growth should moreover reduce the resistivity because the grain growth reduces the fraction of the grain boundaries. Pure platinum is a very good conducting material with very low resistivity around $1.06x10^{-5}$ Ωcm. The resistivity of Ti is slightly higher, around $4.5x10^{-5}$ Ωcm [179]. The total initial resistivity at room temperature (Fig. 3.13) was higher than that of the pure platinum indicating the structural defects in platinum and possibly some contribution of Ti adhesion layer. In the bilayer with only 4 nm titanium the resistivity decreased slightly after annealing indicating some healing of the defects. A very different behaviour was found in the bilayer with 16 nm titanium. During annealing the resistivity increased exponentially indicating diffusion processes in the layer. The resistivity increase can be attributed to titanium diffusion though platinum.

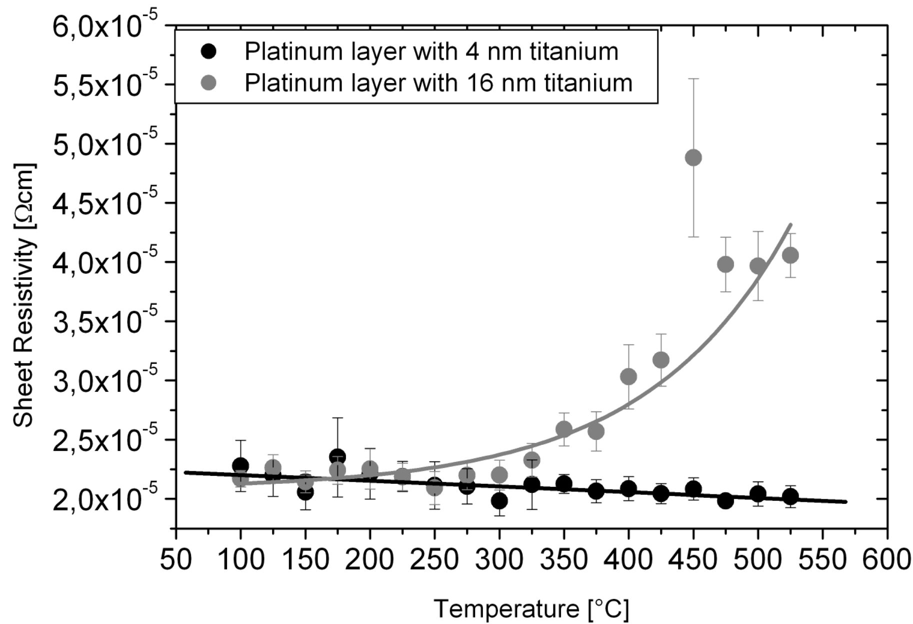

Fig. 3.13: Sheet resistance in platinum layer with different titanium thickness. Platinum layer was 100 nm in both samples.

The driving force for the titanium interdiffusion is believed to be the high affinity of titanium to form oxides. The titanium diffusion was reported to start at temperatures as low as 150°C [180]. At annealing temperature as high as 650°C some dissociation of SiO_2 can take place and some oxygen atoms may out-diffuse. This oxygen dissolves in the region of the metallic bilayer metal films where it can react with titanium to form TiO_{2-x}. The high partial pressure of oxygen and the strong affinity between Ti and oxygen seems adequate to cause its short circuit-diffusion along the platinum grain boundaries. Considering the low solubility and diffusion rate of oxygen in platinum, the diffusion of titanium is more likely to occur. The thermodynamical driving force for the diffusion of titanium seems to be the formation of a reduced TiO_{2-x} phase at the interface [175]. At high temperatures and oxygen partial pressure titanium interstitials are the most likely defects to dominate the diffusion mechanism in a reduced TiO_{2-x} layer compared with well reacted TiO_2 layer [181].

The oxidation of Ti to TiO_2 and the thermal stability of the TiO_2, once it is formed, supports the idea of stable stress after platinum recrystallisation. Thus the following scenario can be concluded: The platinum recrystallisation is inhibited through both, the large compressive stress and the tendency of titanium to form titanium oxides.

The kinetics of the recrystallisation is triggered by the titanium content. Once the platinum is recrystallised and titanium completely oxidized the stress state is stable in the bottom electrode, and does not change upon further thermal treatment.

The platinum recrystallisation will most likely affect the PZT film processing. The initiation of the platinum recrystallisation at 450°C overlaps with the temperature at which the pyrochlore formation was found. It was observed earlier that in the PZT film in the temperature range between 450°C and 475°C large tensile stresses occur. According to the recrystallisation findings in platinum this large deflection increase between 450° and 475°C can not be contributed to pyrochlore formation alone. More likely, this large tensile stress is the sum of the platinum recrystallisation induced by titanium and the stress related to the pyrochlore formation. Although some contribution of pyrochlore to the tensile stress cannot be excluded completely, its contribution to stress is probably far less than previously assumed.

3.2.5 Stress related wafer deflection and processing of sol-gel PZT films on different substrates

To further investigate the effect of substrate stress on the total stress of the PZT film and to characterise the amount of deflection resulted only from PZT film shrinkage, one single PZT layer was deposited on a pre-annealed platinised silicon substrate and another was deposited on $LaNiO_3$ – coated (LNO) silicon substrate.

Before the PZT deposition, LNO was deposited using the sol-gel method. The total thickness of LNO was 70 nm and the LNO was completely crystallized. The films were treated after the same temperature treatment as described in subsection 3.2.2 and the deflection was measured.

Fig. 3.14 shows the deflection results after 2 minutes treatment. For comparison reasons the already discussed result from Fig. 3.3 was included. The results on LNO/Si showed a linear deflection increase between 100°C and 300°C followed by an abrupt change of deflection from convex (compressive) to concave (tensile) at 325°C. This temperature range was attributed to the decomposition of organic substances. Above 375°C a linear deflection increase was found again.

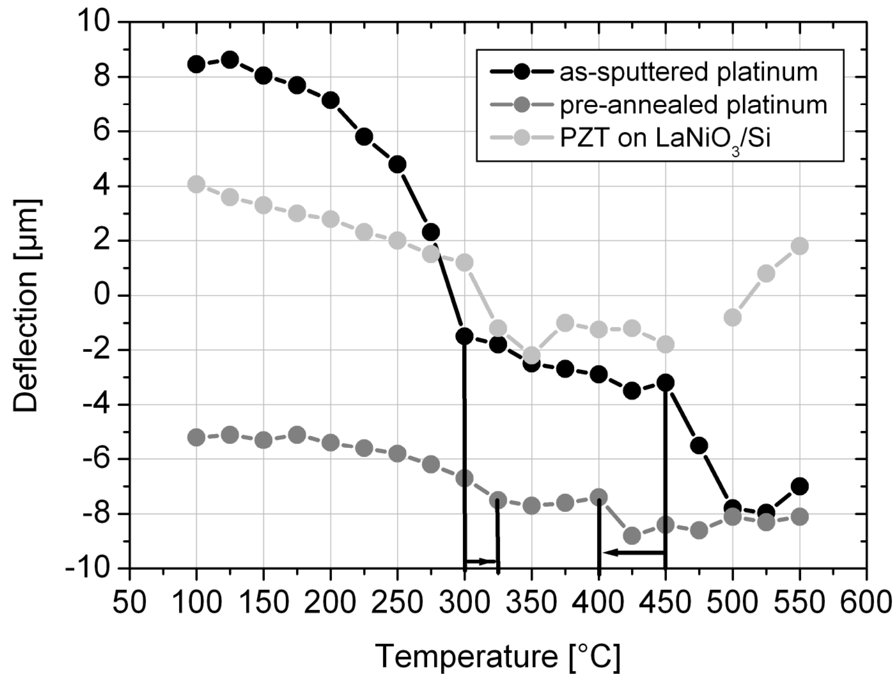

Fig. 3.14: A comparison of wafer deflection of PZT films on three different substrates.

The deflection measured at 450 °C showed both, tensile and compressive peak and was omitted from the results as not being clear. Above 500°C the tensile deflection was decreasing and the wafer became compressive again, mostly likely as a result of film crystallization. The total deflection difference from the first to the last measurement point was only 2 µm although the PZT film went through a cycle of deflection with maximum values of in total 6 µm. The strong deflection increase related to pyrochlore formation could not be observed for PZT on LNO. The lack of such strong deflection increase supports the idea that this strong increase was mostly due to platinum recrystallisation. In general, similar stress profiles for each film-related process of PZT film deposited on LNO and the platinum substrate were found. The major difference was the deflection introduced from the substrate. While platinum electrode contribution was significantly to the total deflection the effect of LNO/Si substrate on the total stress was minimal. LNO is an oxide ceramic film and once crystallized, no big microstructural changes can be expected in the film under further thermal treatment. Hence, a lower deflection contribution from LNO than from platinum can be expected.

The platinised Si wafer was annealed at 600°C for 10 min prior to PZT deposition. The stress in platinum changed from compression to tension. A single PZT

layer was then deposited on the pre-annealed platinum. When platinum was annealed the sign of the stress after annealing was purely the product of thermal expansion mismatch between platinum layer and silicon wafer. A PZT layer was deposited on such substrate and thermally treated like the previous film. On pre-annealed platinum the wafer bending was concave at any time of the film processing. The magnitude of the deflection on pre-annealed substrate was much lower than it was on as-sputtered platinum, and the difference from the beginning to the end of the film processing was only 3 µm. This is five-times lower compared with the film processed on non-annealed substrate. The temperature stages identified earlier on as-sputtered platinum could be identified although the regions were not as pronounced as on the non-annealed substrates. The parabolic shape of the first region could be observed as well as the second and the fourth linear regions. The deflection increase at pyrochlore formation was much smaller than on as-sputtered platinum supporting the hypothesis that the major deflection at 450°C stems from the platinum recrystallisation as this substrate was fully recrystallised before PZT deposition. Thus, the small deflection increase can be mainly attributed to the pyrochlore formation.

All temperature regions were slightly shifted e.g. the end of sol-to-gel transformation region was found here at 325°C and the starting point of pyrochlore formation was found as low as 400°C. The former shift of the temperature range was so small that it could have been caused by the experimental error. The latter temperature shift was too large to be attributed to the experimental error. It is more likely that this shift was caused by enhanced pyrochlore formation on a pre-annealed substrate at lower temperature. The crystallisation temperature was also found to be lower. The shift of the crystallization temperature to lower temperatures could be obtained in presence of the Ti buffer layer on top of platinum as reported by [185].

The stress, and thus the deflection, induced by the PZT film on the pre-annealed substrate were very small. In the PZT film on pre-annealed substrate also lower deflection contribution from platinum was found. This confirms the assumption that once the microstructural changes in platinum were completed, the stress in the substrate was only a product of thermal expansion mismatch between platinum and silicon.

This result indicates that although the major deflection and stress impact come from the substrate, the PZT stress contribution is clearly stated through the non-linear

shape of deflection progression. The change of deflection before and after PZT processing was around 3 µm.

After the different stages in the PZT sol-gel processing were identified, it could be concluded that the processes occurring in the film were strongly stress related. Very high stress contribution was arising in platinised silicon substrates. The investigation of relaxation processes in platinum substrate and deflection analysis on a pre-annealed substrate enabled a control of substrate related stress contribution. Thus, it was possible to separate the substrate induced stress and the stress arising from the film.

3.2.6 Deflection in single layer of three PZT compositions on platinum during sol-gel film processing

Fig. 3.15 shows the single layer deflection of PZT films at various compositions. All processing parameters for all PZT compositions were the same, as described in subsection 3.2.1, except the thickness of platinum bottom electrode. PZT 60/40 and 52/48 were deposited on a substrate containing 200 nm thick platinum layer whereas PZT 40/60 was deposited on 100 nm thick Pt layer.

In all three compositions similar deflection values were found after processing for 1 and 2 minutes were found. However, at 200°C and 475°C for PZT 52/48 and at 425°C for PZT 60/40 different deflection values were obtained after 1 and 2 min. of heat treatment. This effect was explained before and shows that the 1 minute long thermal treatment is not sufficient to complete the stress-related processes in the film at indicated temperatures.

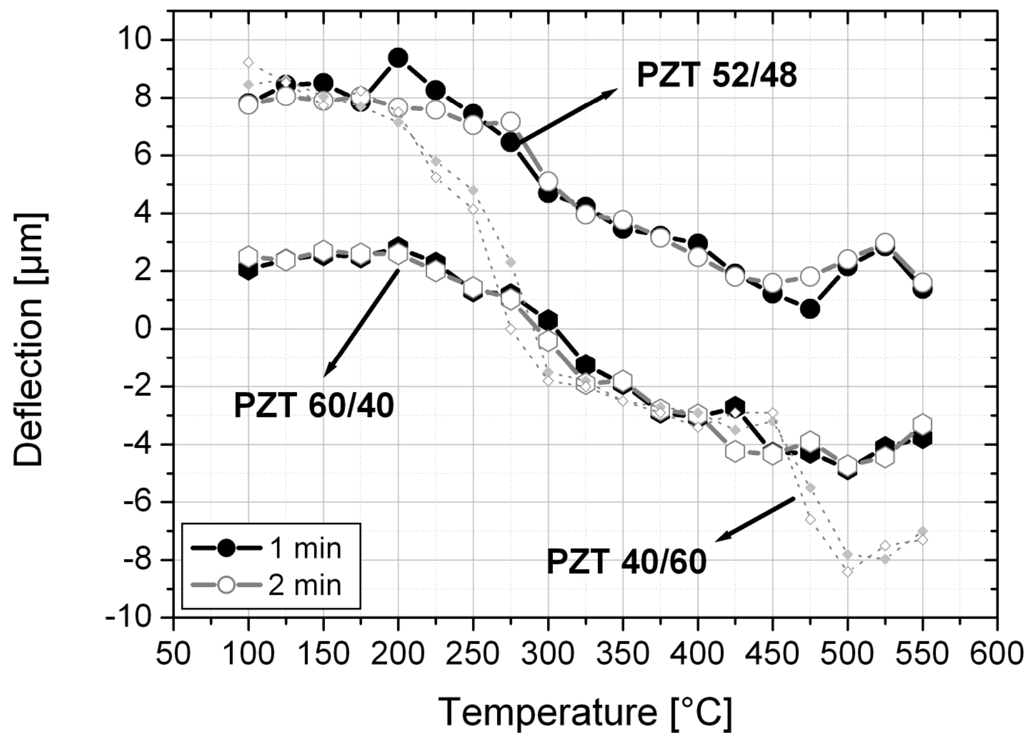

Fig. 3.15: Single layer deflection in three different PZT compositions with the same sol concentration. The Pt electrode thickness was 200 nm for PZT 52/48 and PZT 60/40 and 100 nm for PZT 40/60.

As discussed in the previous sections, in PZT 40/60 the steps between the stages were very clear so that it was very easy to distinguish between individual stages. Comparing the deflection curves of PZT 52/48 and PZT 60/40 with the previously discussed curve for PZT 40/60 it becomes obvious that the curves measured on PZT 52/48 and PZT 60/40 showed slightly different behaviour. The first temperature interval between 100°C and 300°C or stage I could be easily identified for PZT 52/48. Above 300°C the deflection was linear increasing. The next characteristic temperature was 475°C. This temperature can be attributed to the pyrochlore formation temperature. Above 475°C the deflection was linear decreasing. The latter temperature interval can be contributed to the stage IV or the crystallization of PZT.

Similar deflection progress was found for PZT 60/40. The first stage was found to be between 100°C and 325°C. Between 325 ºC and 470°C linear deflection progress was observed. Above 500°C the deflection was decreasing due to the formation of perovskite PZT.

The major difference between the deflection progression for PZT 52/48, PZT 60/40 and PZT 40/60 is the platinum thickness. In thicker platinum the recrystallisation was probably slower than in thinner platinum layer and thus no crystallization could be observed. In section 3.2.3 the recrystallisation of 100 nm thick platinum was found to start at the point where the grain diameter reaches 100 nm. In case of thicker platinum layer, the recrystallisation may not necessarily need to start at 100 nm. Following the assumption of cubic-like crystallites, the recrystallisation should start when grain diameter reaches 200 nm, and for this process more time would be needed than 10 minutes. Thus, the kinetics of platinum recrystallisation plays an important role. It could be observed from Fig. 3.15 that the deflection of PZT 52/48 in the whole processing interval remains compressive. This can be explained as follows: the stress relaxation of platinum is dependent on time and temperature, and thus the energy input. Assuming it is a linear relationship between energy input and the stress relaxation, it can be easily shown that for a double thickness of platinum a double time at the same annealing temperature is needed to reach the same state of stress relaxation as for the thinner layer. The longer time is needed for titanium to diffuse through the double thickness of platinum. This serves only as an example and the real relationship between platinum relaxation and energy is probably more complicated. However, if one considers the deflection difference of all PZT compositions between 100°C and 550°C, based on Fig. 3.15, one would find that the total deflection on 200 nm shows roughly only half of the deflection values for PZT on 100 nm thick platinum. The deflection difference for 40/60 is around 16 µm whereas the deflection difference for PZT 52/48 is only 7 µm and for PZT 60/40 only 6µm. Thus, the contribution of platinum was much lower for PZT 60/40 and PZT 52/48, and the curves were not as pronounced as for PZT 40/60 where platinum recrystallisation occurred clearly. This does not mean that the total residual stress in PZT films would be smaller on thicker platinum. Quite the opposite would be the case. Once the platinum is relaxed higher residual stresses in platinum would be found, having larger impact on PZT stress.

Although the characteristic processing stages were less clear for PZT 52/48 and PZT 60/40 on thicker Pt, it was still obvious that the deflection was not decreasing

linearly with processing temperature and that some of the processes in the films could be identified, like the evaporation stage and the crystallization stage.

All films reported in this study were treated at the same temperatures. The crystallization of PZT 60/40 and PZT 52/48 was found to start at lower temperatures than in PZT 40/60 but these films needed longer to fully crystallize. A Zr-Ti stochiometry dependent pyrochlore formation was reported by Schwartz et al [85]. Accordingly, pyrochlore forms preferably in zirconium rich PZT compositions. Also, dependent on the sol precursor chemistry and the hydrolysis ratio, the pyrolysis temperature can be shifted to lower temperatures. Thus, the pyrochlore formation would start earlier or at lower temperatures in Zr-rich films followed also by crystallization at lower temperatures. However, this does not imply that the crystallization is also completed earlier than in PZT 40/60 films. Zirconium has higher melting point than titanium and thus the Zr ion mobility is lower than the mobility of Ti ions. The Zr rich films need longer time to crystallize or the temperature needs to be increased to achieve good crystallinity at acceptable rate. Sufficient crystallinity was achieved only if the films were crystallized at T=630°C instead of 550°C. The PZT 60/40 needed at least 10 minutes at crystallization temperature to fully crystallize one 200 nm thick single layer. To crystallize one 200 nm thick PZT 52/48 layer 5 minutes at 630°C or 10 minutes at 550°C were enough.

3.2.7 Summary of the section and future work

The processing of thickness-increased sol-gel films was investigated. A combination of analysis techniques was employed. The stress development was monitored via ex-situ wafer deflection measurement after various processing steps. It was found that crack-free films could be fabricated if a specific heating profile was applied and the heating of the sol-gel film was so conducted that the stress peaks are avoided. Films up to 5 µm thick were obtained by repeated deposition of 200 nm thick single layers. The maximum single layer thickness was increased to 500 nm and a 2.5 µm film was fabricated by only 5 repeated coatings.

A high stress development was observed in the platinised substrate and was further investigated. A more detailed analysis revealed a platinum recrystallisation. This

recrystallisation was probably based on the same mechanism like hillock formation but had one huge difference to hillock formation. The recrystallised grains were much smaller and the recrystallisation did not result in the damage of the film. Nevertheless, the pyrochlore formation in the sol-gel film was dependent on the substrate properties and if such recrystallised platinum substrate was used for PZT film deposition, the pyrochlore was forming at lower temperatures. The deposition of a single PZT layer caused the wafer deflection of around 3 µm. Every subsequently deposited PZT layer caused only minimal incremental deflection increase.

All the stress related investigations in PZT sol-gel films were conducted on films with single layer thickness of 200 nm using the 0.6 M concentrated sol. The same deflection measurement was done also on single layers spin-coated with 0.8 M and 1 M concentrated sol. The results were very similar to the results obtained for 0.6 M sol and were omitted here. There was no major deflection increase in films produced with 0.8 M and 1 M sol. However, some other, probably more important developments were noticed in thick films.

In films thicker than 400 nm per single layer it was observed that cracks appear mainly at the drying stage of the films or when the first deposited layer was not fully crystallized. It was also observed that the delamination occurs frequently when depositing films with increased thickness. The high stress during drying is likely to get stronger than the adhesion between Pt/Ti and silicon and thus the platinum electrode delaminates, Fig. 3.16.

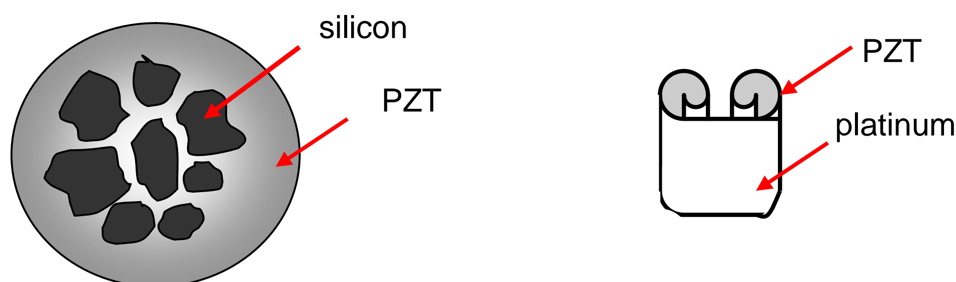

Fig. 3.16: Planar view of the damaged film through delamination (left) and a delaminated patch (right).

Thus, the delamination occurs at the weakest point of the composite. This delamination was also a result of high tensile stress. A film/substrate failure associated with compressive stress results frequently in buckling of the film along with cracking. If the compressive stress in the film cannot be withstood by the platinum adhesion, the platinum delaminates and results in the buckling of the film. These observations need to be considered in future to further increase of the film thickness. Processing of sol-gel films with increased single layer thickness has shown that, once the key processing parameters were known, it was possible to deposit easily films up to 300 nm thickness on a 2″ substrate. Films with larger thickness were only deposited onto substrates smaller than a 2″ wafer. The limiting parameter in the deposition of thicker films e.g. ticker than 400 nm were drying cracks as reported by Yi et al [116]. The reason for drying cracks is very simple. The processing related thickness reduction between the spun-on sol layer and the fully crystallized PZT layer was immense. It is easy to imagine that the thicker the layer, the more solvents need to be removed. Also, the thicker the film, the longer the way of material transport from the bottom of the layer to the top layer. If the heating is too fast, large amount of solvents tries to evaporate and high pressure within the film is building up which then leads to cracking. To avoid the drying cracks a controlled heating is required, e.g. with an appropriate heating rate. A rapid thermal annealing (RTA) would be a method of choice for such annealing. If the film is processed using the RTA for drying it is probably better to transfer the whole processing from hot plates to RTA process. The results from this section can be easily transferred and adapted in the RTA process, only small optimization of the heating rate would be necessary.

3. 3. Crystallographic Orientation of PZT thick films

3.3.1 Introduction to the section

The following section outlines the orientation and crystal growth of PZT films with different compositions. All films were prepared using the processing procedure reported in section 3.2. The preferred orientation and growth of the PZT films on silicon (100) substrates with different types of electrodes will be reported. Some films were deposited on sapphire substrates and the orientation of these films will also be discussed.

3.3.2 Film morphology

All analysed films were crack-free. To evidence if the films were porous some films were polished. A cross section of one polished film is depicted in Fig. 3.17. The white particles are debris from the polishing paste. The surface of the film is smooth and no pores could be observed. The areas in the film surface that might seem like long pores, marked in black square in Fig. 3.17, are most likely broken out grains. Because these areas look like columnar grains it is likely that some of the grains were broken out of the sample through grinding and polishing.

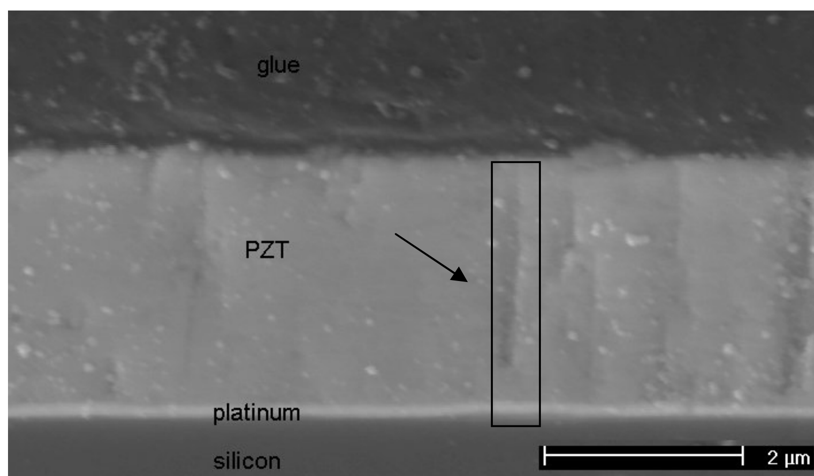

Fig. 3.17: Polished cross section of a 3 µm thick PZT 52/48 film.

A typical surface of PZT sol-gel films is presented in Fig. 3.18. The surface of PZT films was usually smooth with some black dots. These dots were probably impurities as a result of dust particles in the clean room. Their number can increase with each additional coating.

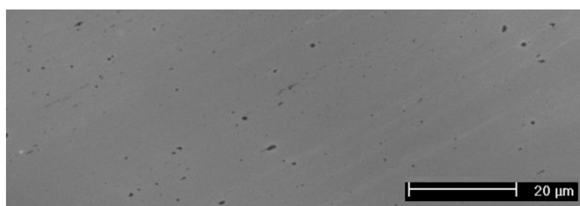

Fig. 3.18: Typical surface morphology of PZT films.

An example of fracture section for one PZT 52/48 film is depicted in Fig. 3.19. A detailed microstructure analysis will be given in Section 3.5.

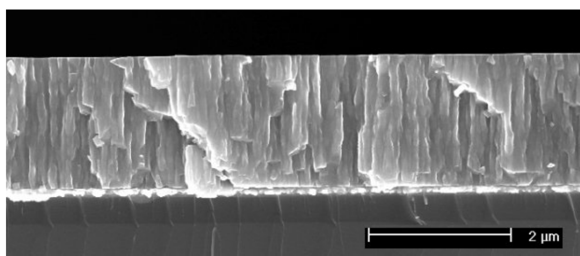

Fig. 3.19: Fracture section of PZT 52/48 films.

3.3.3 Crystallographic orientation of PZT films on Pt(111)

The crystallographic growth and orientation were examined in all three PZT compositions. A set of samples for each PZT composition was produced using different thermal treatment parameters. The sample batches had following names: PZT 40/60-Pt(111)/Si-3µm-10, PZT 60/40-Pt(111)/Si-3µm-6, PZT 52/48-Pt(111)/Si-2µm-10. The full sample list is given in Appendix A. The orientation of the films with the thickness of 1µm, 2µm and 3µm was analysed except for the set of PZT 52/48 samples. The orientation of the latter set was examined only at the thickness of 2 µm but was extended with results of the individual samples where orientation at such thicknesses

was analysed. The results of phase analysis and characterization on PZT 40/60 and PZT 60/40 served as a base for the phase characterization of PZT 52/48 films. The details of the phase analysis are given in Appendix B.

3.3.3.1 Tetragonal PZT 40/60

Ten samples were fabricated using the heating profiles for thick films, section 3.2.2. The heating period at each temperature was varied and the heating profile of each sample was different. The XRD patterns of one such PZT 40/60 film at three different thicknesses were shown in Fig. 3.20. The peaks were identified and attributed to the tetragonal PZT. No pyrochlore was detected and thus all films were well crystallised.

In the set of 10 PZT 40/60 films the strongest peaks were those belonging to the (001)/(100) and (111) lattice planes. The preferred orientation can be clearly indicated when the diffractogram of a film is compared with a powder diffractogram data, Fig. 3.21. Instead of determing a diffraction data on a PZT powder the readily available powder diffraction file 33-0784 for tetragonal PZT from the PCPDF database was used. The randomly orientated PZT yields highest diffracted intensity of (110) oriented crystal planes, attributed to 100% intensity. All other planes have a percentages of the (110) diffracted intensity. The diffracted intensities in the film were different than in the powder and the highest intensities were found for (100) and (111) lattice planes while (110) peak was only weakly present. This simple comparison shows that the PZT films were strongly textured. Also, the determination of X-ray diffracted intensities in different positions and rotation of the sample showed same diffraction files (not shown here) stating the columnar texture in the films.

The integral intensities of 1μm, 2μm and 3μm thick films were normalised and their percentages are given in Tab. 3.2 for each film. The single layer thickness for all films was 200 nm/layer. Some of the given intensities do not add up to 100% which means that this difference goes back to the diffracted intensity of (110) peak. Three films with initially preferred (111) orientation, marked in grey, three films with mixed orientation and 4 films with (100) preferred orientation in 1 μm thick films were obtained. In the peak doublet (001)/(100) much higher relative diffracted intensity of (100) peak than of (001) peak was found.

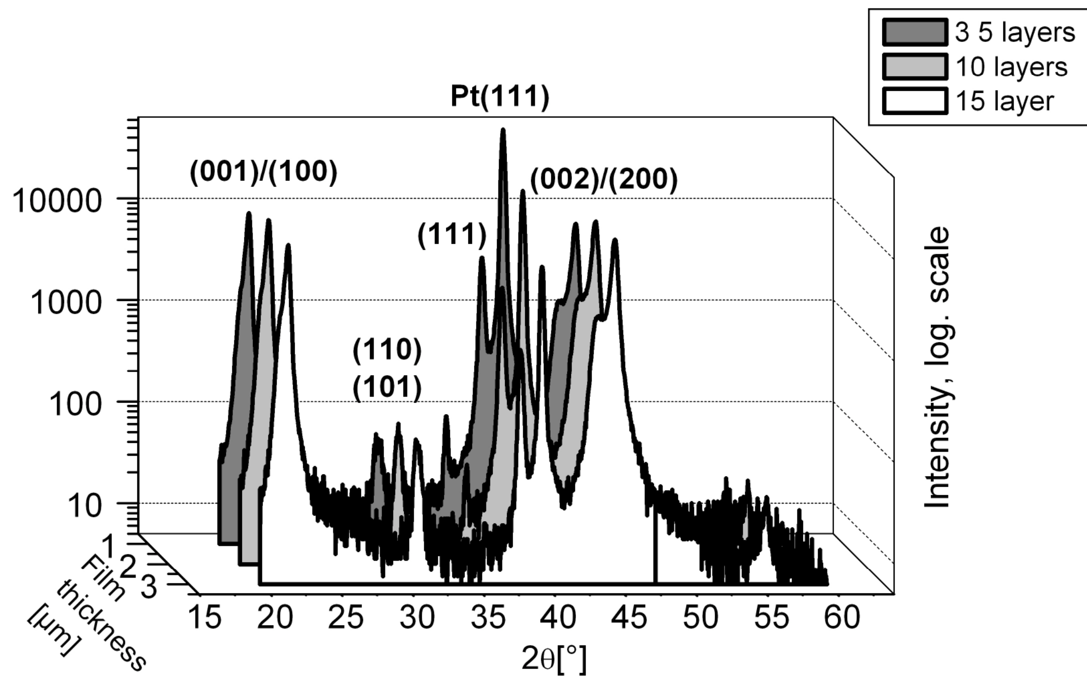

Fig. 3.20: Diffractograms of one PZT 40/60 film at three different thicknesses.

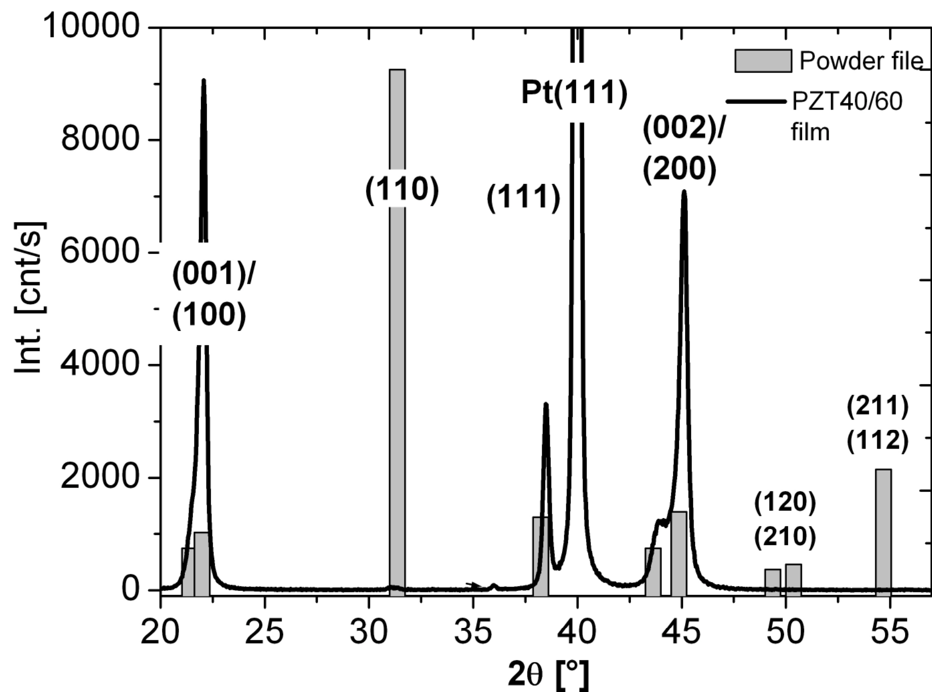

Fig. 3.21: Comparison of diffractograms for a PZT powder and for the PZT film.

The intensity ratio (100) to (111) was changing with thickness in all films. Lower diffracted intensity of (111) lattice plains was detected in 3 µm thick films, compared to the (111) intensity of 1 µm thick films, and the diffracted intensity of (100) lattice plains was much stronger in 3 µm thick films, Fig. 3.22.

Tab. 3.2: Relative peak intensity for all appearing peaks in PZT 40/60 films, in percent. The processing parameters for each film are attached ahead the orientation results.

processing parameters		orientation with thickness in percent				processing parameters		orientation with thickness in percent			
T[°C]	t[min]	**film1**	1 µm	2 µm	3 µm	T[°C]	t[min]	**film 6**	1 µm	2 µm	3 µm
100	1	(001)	2	26	8	100	1	(001)	1	1	10
300	5	(100)	97	73	78	300	1	(100)	10	22	27
450	2	(111)				450	5	(111)	88	75	60
550	5					550	5				
		film 2						**film 7**			
100	1	(001)	2	8	3	100	1	(001)	5	6	9
300	5	(100)	8	12	25	300	3	(100)	28	49	61
450	5	(111)	89	76	68	450	5	(111)	67	40	22
550	3					550	5				
		film 3						**film 8**			
100	1	(001)	13	22	11	100	1	(001)	42	13	13
300	5	(100)	67	65	81	300	3	(100)	46	74	80
450	2	(111)	19	12	6	450	2	(111)	12	11	5
550	1					550	2				
		film 4						**film 9**			
100	1	(001)	16	8	35	100	1	(001)	10	17	22
300	5	(100)	61	76	54	300	3	(100)	88	80	76
450	5	(111)	23	16	8	450	2	(111)	2	2	1
550	5					550	5				
		film 5						**film 10**			
100	5	(001)		9	10	100	1	(001)	5	10	8
300	5	(100)		83	78	300	3	(100)	55	65	80
450	2	(111)		8	11	450	5	(111)	37	21	8
550	3					550	2				

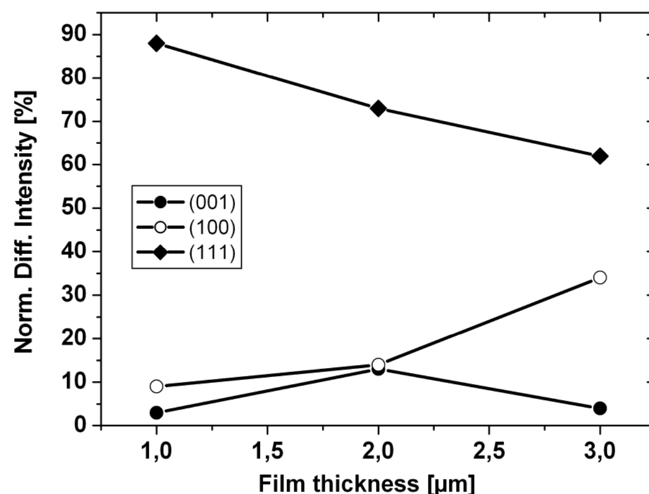

Fig. 3.22: Typical decrease of (111) orientation, here in (111) PZT 40/60 oriented film (film 6).

This can be explained if the preferential crystal growth is considered. At the interface of PZT film to the platinum electrode the nucleation of PZT is influenced the by lattice match of pseudocubic PZT (111) with lattice spacing $d_{(111)PZT}$=0.2237 nm to the Pt(111) with lattice spacing $d_{(111)Pt}$=0.2265. The nuclei would occur at the platinum-film interface according to the lattice match between PZT(111) and Pt(111) lattice planes. Other nucleation mechanism can take place only if (111) nucleation is suppressed. In thicker films a longer period is required for the growth of the interface-nucleated grains to consume the amorphous matrix during the transformation. If the film is transferred to next higher temperature before the amorphous phase was totally consumed through interface-nucleated grain growth an occurrence of other, more energetically intensive nucleation events is possible. These other events result in grains of other orientation such as (100) [163]. The nucleation of (100) on Pt(111) is probably more energetically intense on Pt(111) but the grain growth of (100) plains has much lower activation energy than the growth of (111) lattice plains [184]. Thus, some (100) nuclei can be formed and the faster grain growth of (100) oriented nucleation sites results in a mixed orientation within the first layer. In all subsequently spin-coated PZT layers the already present PZT serves as nucleation sites and the growth behaviour is continued. However, once the (100) nuclei formed on the nucleation sites provided by the previously coated PZT, they grow faster through thickness than (111) oriented grains. When the (100) grains reach the top surface of the PZT layer they can continue to grow in lateral

direction. In cubic crystals the (100) and (001) directions are equivalent. Thus with each additional coating the (100) grains grow slightly larger in lateral direction and suppress the growth of (111) oriented crystallites. After coating of 15 layers the change of intensity ratio of (100) to (111) oriented crystallites can be significant. The cross-section of such thick films with change of orientation with thickness is schematically depicted in Fig. 3.23. A higher intensity for (100) is therefore picked up by the XRD in thicker films.

The change of orientation and the dominance of (100) orientation with thickness were reported by [3, 94-95, 185] and for PZT 45/55 [186].

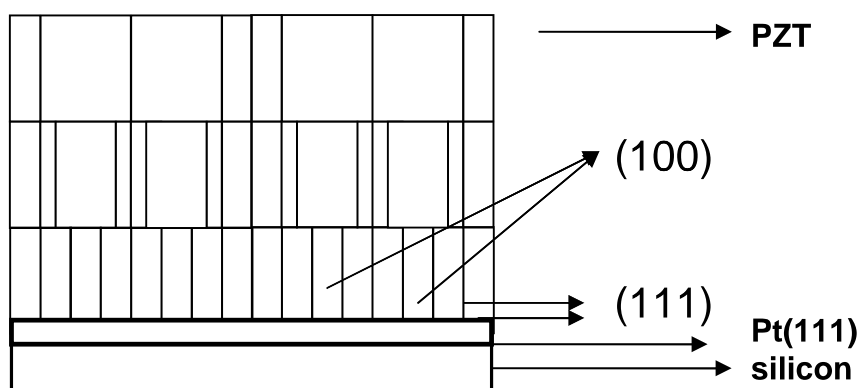

Fig. 3.23: A schematic cross section of a PZT film with thickness dependent change of orientation.

Some indication of the change of orientation was observed in all films, Fig. 3.24, where a strong columnar grain growth occurred. The cross section of the films was prepared by the fracture of the film. Because the fracture occurs at interfaces with weakest bonding, such as grain boundaries, the single columnar grains are well pronounced. In all films with columnar grain growth deposited on tensile substrate another feature was observed. In some columns a horizontal fracture also occurred as if some of the columns were broken. Such fracture could result from cracks or pores but the fracture surface would possibly be much rougher if the fracture was due to pores. The fracture due to cracks was excluded as the crack propagation, if any, was usually observed through thickness and no cracks were observed in-plane of the film.

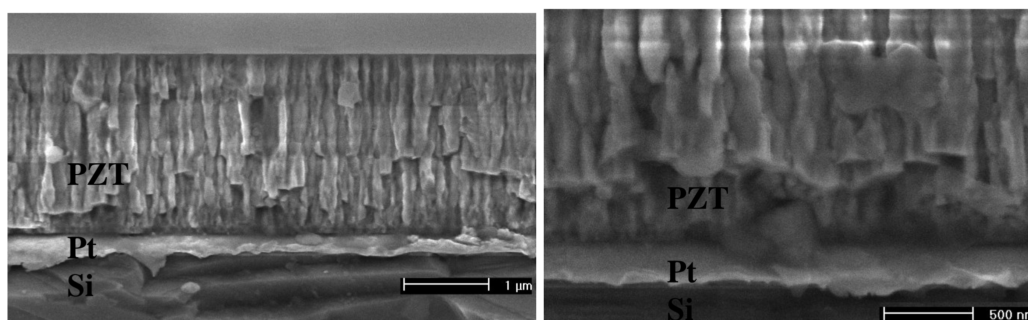

Fig. 3.24: Fracture through columnar grains, possibly due to change of orientation with thickness. 10 layers each 200 nm thick were deposited on platinised silicon substrate.

It is thus more likely that e.g. (111) oriented grains were grown next to the electrode but further away from the electrode, and in much thicker PZT layers, a nucleation of (100) on (111) grains occurred, or the lateral growth of (100) suppressed the growth of (111) grains. An interface between (100) and (111) oriented grains would be less stable and fracture could appear along the interface much easier.

The usage of four temperatures in the film processing makes it more difficult to draw any conclusions between the processing conditions and the resulting preferred orientation of the film. According to Schwartz et al [85] the degree of hydrolysis in the sol-gel film can reduce the pyrolysis temperature and also the crystallization temperature. This implies a relationship between the film orientation and the drying time at 300°C. However, no indication of drying time influence on the orientation was observed.

The pyrolysis time at the pyrochlore formation temperature T=450°C seems to have more influence on the film orientation. The 1 µm thick films held for only 2 minutes at this temperature showed very high diffracted intensity of (100) peak. These films were No. 1, 3, 5, 8 and 9 from Tab. 3.2. All other films were held for 5 minutes at 450°C and had significantly stronger (111) orientation. These results suggest that the treatment period at 450°C has most influence on the film orientation, and variation of the treatment time can result in films of different orientation. The obtained results correspond to the results of Liu and Phule [187] who obtained (111) oriented PZT 40/60 films when the films were treated at 300° (2 min), 400°C (30 min) and 600-700°. If the thermal treatment at 400°C was skipped the films were (100) oriented. The authors argued that the temperature treatment at 400°C is related to pyrochlore formation and

(111) orientation, as shown by other authors [78]. Heat treatment at 400°C would lead to pyrochlore formation and preferred (111) orientation. Furthermore, the authors claimed that the perovskite formation of Ti rich sol like PZT 40/60 preferably transforms without the intermediate step of pyrochlore formation. In this case preferably (100) oriented films were obtained if the films were immediately crystallized after drying. The use of lower pyrolysis temperature by Liu and Phule than in this work is likely to be due to the usage of different sol precursors as the difference in sol precursor chemistry can alter the pyrolysis temperature.

3.3.3.2 Rhombohedral PZT 60/40

A batch of 6 samples, each with different orientation, was obtained. The diffractograms of one PZT 60/40 film at three different thicknesses are shown in Fig. 3.25. The films were treated at the temperatures 100°C, 300°C, 450°C and 630°C between one and ten minutes. In the diffractogram of the 1 µm thick film a small pyrochlore peak was observed, indicating uncompleted crystallization. To fully crystallize the films the 1 µm thick films were annealed for another 40 minutes at 630°C. Afterwards all films were fully crystallized. The processing conditions of all subsequently deposited layers were sufficient to fully crystallize the films except for film No. 1 and 5. These latter two films needed another annealing for 40 min at 630 °C when 3 µm thickness was reached. The need of longer crystallization time and higher crystallization temperature were attributed to the higher zirconium content of the PZT 60/40 films.

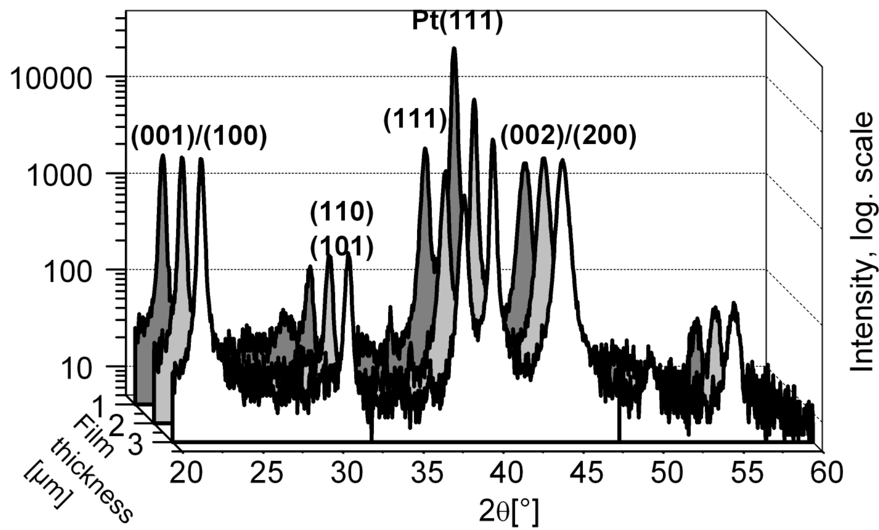

Fig. 3.25: Diffractograms of one PZT 60/40 film at three different thicknesses.

The peaks were identified in all films as belonging to the rhombohedral PZT. The results of normalized integral intensities together with the processing details for each film are given in Tab. 3.3.

Tab. 3.3: Normalized integral intensities for all detected peaks in PZT 60/40.

T [°C]	**t [min]**	**Orientation with thickness, in percent**				**T [°C]**	**t [min]**	**Orientation with thickness, in percent**			
			1 µm	**2 µm**	**3 µm**				**1 µm**	**2 µm**	**3 µm**
film 1						**film 4**					
100	**1**	**(100)**	4	6	7	100	1	**(100)**	10	14	18
300	**3**	**(110)**	14	22	34	300	5	**(110)**	5	8	10
450	**5**	**(111)**	56	62	38	450	5	**(111)**	83	76	65
630	**2**	**(211)**		8	16	630	10	**(211)**			
film 2						**film 5**					
100	**1**	**(100)**	45	41	47	100	1	**(100)**	20	12	12
300	**3**	**(110)**	13	18	20	300	5	**(110)**	17	41	47
450	**5**	**(111)**	42	31	20	450	5	**(111)**	40	21	12
630	**10**	**(211)**		8	10	630	5	**(211)**		20	23
film 3						**film 6**					
100	**1**	**(100)**	42	51	59	100	1	**(100)**	11	11	13
300	**3**	**(110)**	3	6	7	300	5	**(110)**	8	23	31
450	**10**	**(111)**	53	43	30	450	10	**(111)**	72	53	34
630	**10**	**(211)**				630	5	**(211)**		11	17

The thickness dependent change of orientation was observed also in PZT 60/40 films. The diffracted intensity of (111) lattice plains was lower in thicker films and was in correlation to PZT 40/60 films, Fig. 3.26. However, a major difference between PZT 40/60 and PZT 60/40 films was found. The increase of diffracted intensities with thickness was found not only for (100) lattice plains but also for (110) and (211) lattice plains. Also, the degree of (111) orientation in PZT 60/40 films was much higher than in PZT 40/60 films, although the lattice match between the rhombohedral phase (111) ($d_{(111)}$ = 2.2367Å) and Pt(111) ($d_{(111)}$ = 2.265Å) is lower than between the tetragonal PZT (111) to Pt(111).

Following the argument of the nucleation and crystallization of PZT 40/60 from previous sub-section all PZT 60/40 films were treated for at least 5 minutes at 450°C. This would be sufficient for pyrochlore to form and yield (111) orientation. Also, the stochiometry of the sol precursor was different. Schwartz et al [85] suggested that in Zr-rich films the pyrochlore formation is more favoured than in Ti-rich films. The crystallization temperature was also increased and some films were exposed to an additional annealing step. All these factors affect the film orientation. The high degree of (211) and (110) orientation is most likely the result of the temperature increase that was sufficient to activate the nucleation and growth of (211) and (110) lattice plains.

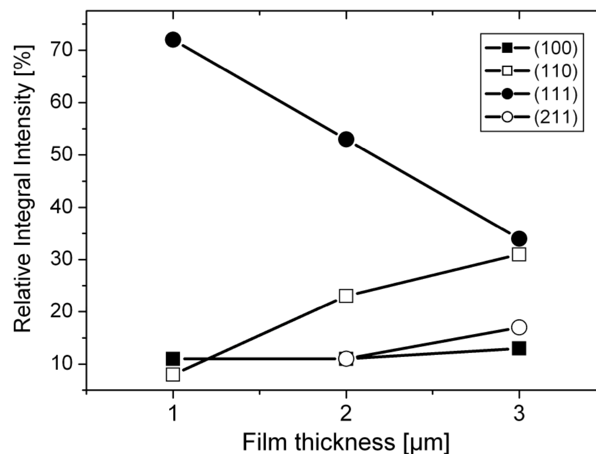

Fig. 3.26: Thickness dependent change of orientation.

3.3.3.3 Phase characterization and orientation of PZT 52/48

The thickness dependent change in orientation was observed also in PZT 52/48 films. The films at three different thicknesses were compared, Fig. 3.27. The diffracted intensities of the film presented in Fig. 12 and two other films are summarized in Tab. 3.4. All films showed a high fraction of (111) intensity which decreased with increasing thickness. A moderate intensity increase of (100) lattice plains with thickness was noticed. A higher fraction of (110) and (211) orientated crystallized in thicker films than 1 µm was found.

These orientation results are comparable to the orientation findings of Zr-rich PZT 60/40. The fraction of the (100) oriented rhombohedral phase was very high in films below 1 µm but decreased with increasing thickness. The intensity of (111) oriented peaks showed very high fraction of tetragonal phase in this orientation. These results can be related to a better lattice match of the tetragonal (111) lattice plains to the Pt(111) lattice plains.

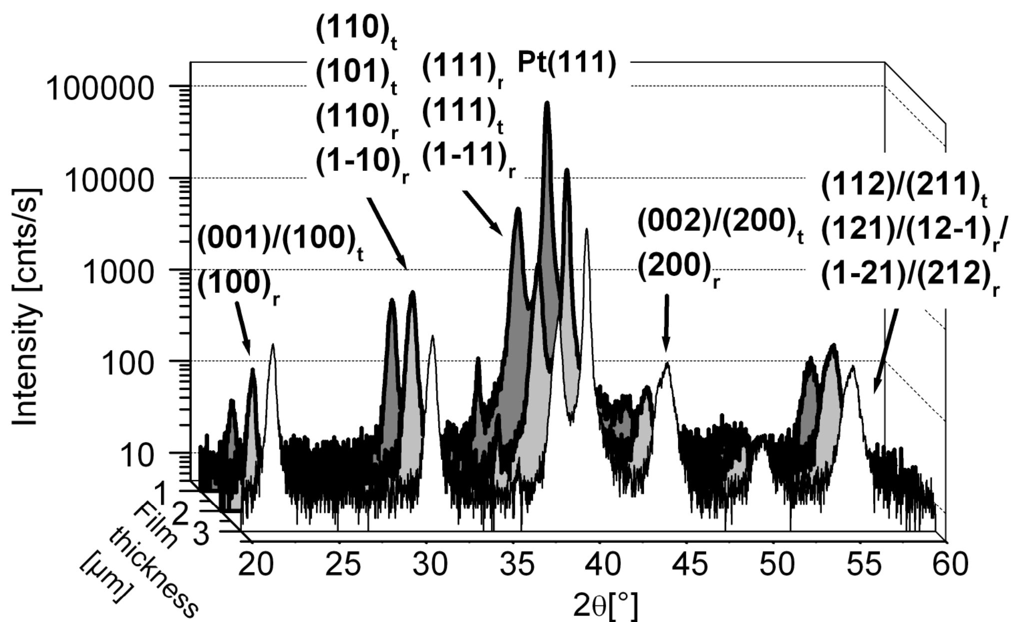

Fig. 3.27: Diffractorgrams of a PZT 52/48 films at three different thicknesses.

Tab. 3.4: Relative intensity and phase content at different thicknesses in three PZT 52/48 films.

	Relative intensity in %				% rhombohedral phase	
film thickness	**(100)**	**(110)**	**(211)**	**(111)**	**(100)**	**(111)**
film 11						
0.8 µm	40		9	51	70	29
1.28 µm	48		6	46	59	23
1.76 µm	61		5	34	67	35
2.24 µm	69		5	26	61	24
film 12						
1µm µm	1	9	2	88		33
2µm µm	3	28	16	53		25
3µm µm	16	20	32	32	56	55
film 13						
0.91 µm	40		2	58	41	37
1.69 µm	21	47		32	3	28

Further work regarding phase content and orientation analysis were carried out on a batch of 10 samples. All samples were 2 µm thick. The results of the phase characterization and the orientation are summarised in Tab. 3.5. Where no tetragonal peak split into (001)/(100) peak doublet was observed the samples were assumed to be pure rhombohedral. The peak (110) showed considerable intensity in some of the films but was not considered in the analysis because each phase, the tetragonal and the rhombohedral phase, has two peaks at this position and it was not possible to resolve this peak into 4 individual peaks. Thus, only peak groups (100) and (111) were considered in the phase analysis and their ratios were built. In three films (samples 4, 5 and 9) only the rhombohedral phase was found. Since the peaks (002)/(200) intensities were too low to be deconvolved, the tetragonal phase cannot be entirely excluded, as these films may contain some tetragonal phase, but in other orientations rather than (100), e.g. in (110). The results show that in most samples with two phases the tetragonal phase content was at least 50% or more, based on (111) and (100) peak groups analysis. The values around 50% seem to be reasonable considering the Zr/Ti ratio of around 50/50 and stress-free samples. Other Zr/Ti ratios suggest a presence of different strain in the films, according to the strain dependent phase formation in PZT

with MPB composition [188-189]. Similar ratio around 50% was found by [95] for PZT thin films.

The given values of predominant orientation show that (100) orientation was found only in two samples (Nr. 2 and 6) in both phases, and a mixture of (100) in one phase and (111) in the other phase was present in 2 samples (Nr. 3 and 10). (111) orientation was dominating in all other films. A predominant (111) orientation in PZT 52/48 films was also reported by [78].

Tab. 3.5: Phase content and orientation of PZT 52/48 films.

	phase content in [%]		**orientation**	
sample nr.	**tetragonal**	**rhombohedral**	**tetragonal**	**rhombohedral**
1	56	44	(111)	(111)
2	67	32	(100)	(100)
3	60	40	(100)	(111)
4		100		(111)
5		100		(111)
6	48	52	(100)	(100)
7	70	30	(111)	(-111)
8	53	47	(111)	(-111)
9		100		(111)
10	67	32	(111)	(100)

3.3.4 The effect of post-annealing on the orientation of the PZT films

A diffractogram of a 3 µm thick film is depicted in Fig. 3.28. The film was processed using the usual processing parameters and was annealed at 650°C for 30 minutes. The diffractograms show exactly matching peaks before and after annealing. The more detailed analysis of the films was carried out. The results of compared relative integral intensities of all peak groups are summarised in Tab. 3.6. Only total values for one group of peaks are given. After comparing the peaks in their shape and intensity amplitude it was concluded that there was no noticeable change in phase content or in orientation. All peaks had the same shapes before and after annealing and their intensities were very close to each other, as given in Tab. 3.6. The difference between some of the values in Tab. 3.6 is within the accuracy of the method and a spread of 5% is reasonable. From the results on Fig. 3.28 and Tab. 3.6 it was concluded that once the

films were fully crystallized, the orientation and the phase content were not changing significantly during further annealing.

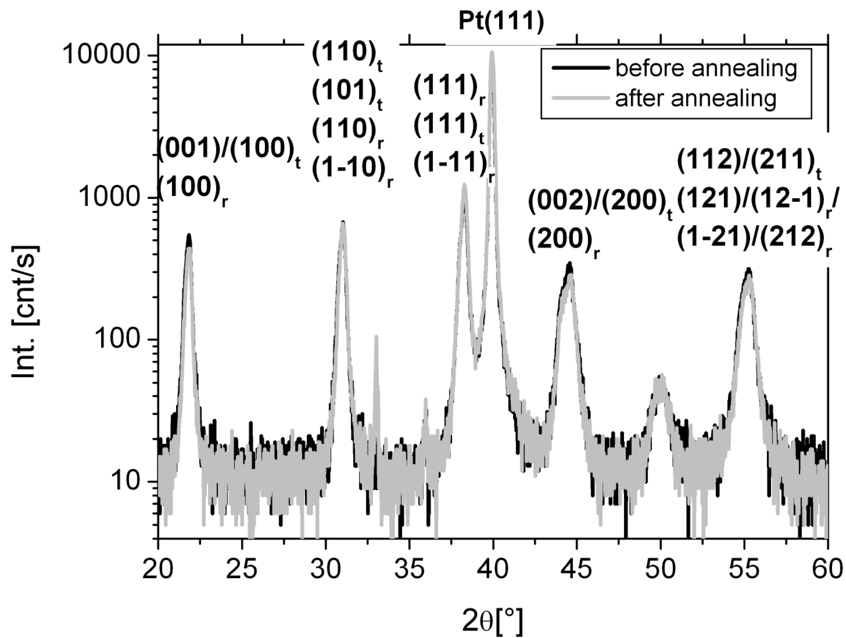

Fig. 3.28: A diffractogram of a 3µm thick film before and after final annealing step.

Tab. 3.6: Intensities of all peak groups before and after annealing step in percent of the total intensity. Sample: PZT 52/48-Pt(111)/Si - 3 µm -film 12.

	1µm		2µm		3 µm	
	not annealed	annealed	not annealed	annealed	not annealed	annealed
(100)	0.5	0.5	3	4	16	13
(110)	8.7	10.5	28	34	20	20
(111)	87.5	85	53	44	32	34
(200)			3	9	19	17
(211)	3.3	4	13	14	19	16

3.3.5 The effect of PbO buffer layer

The effect of PbO buffer layer on the orientation of PZT 52/48 film was investigated by XRD and the results are shown in Fig. 3.29. An approximate 40 nm thick PbO layer was spin coated by sol-gel technique on a platinised silicon substrate and crystallized prior to PZT deposition.

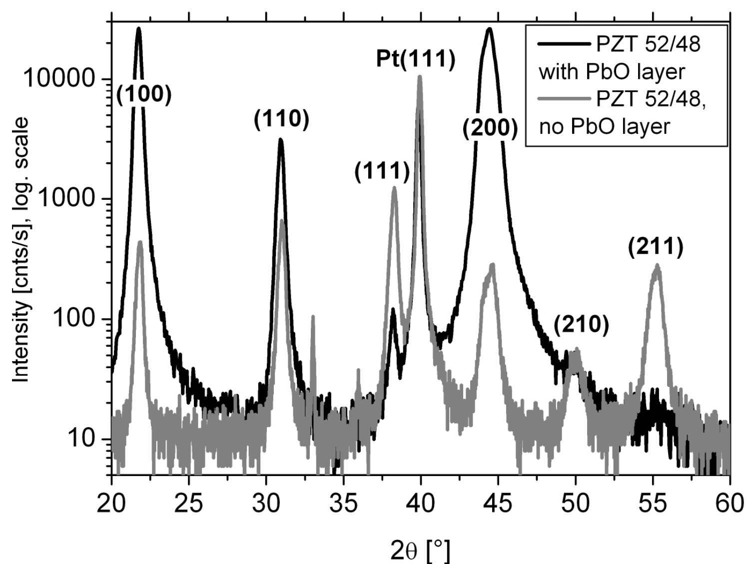

Fig. 3.29: A comparison of two PZT 52/48 3 µm thick films, with and without PbO buffer layer. Sample: PbO/Pt(111)/Si/3"- 3 µm-film 14.

The intensities of two 3 µm thick PZT 52/48 films deposited on platinised silicon substrate with and without PbO buffer layer were compared. The PZT film with PbO buffer layer had a 90% content of (100) preferred orientation. This is the highest degree of (100) texture found in PZT 52/48 films on Pt (111). This result correlates to the reported promotion of PZT (100) nucleation on Pt (111) due to PbO buffer layer [78, 199]. The origin of (110) peak of whether it was due to bubbles formation in PZT film or due to the PbO (110) orientation cannot be concluded here.

3.3.6 The effect of single layer thickness on orientation

Two PZT 40/60 films having the different single layer thickness were processed under identical conditions. The total thickness was 2 µm for Film 1 after the deposition of 10 layers and 1.8 µm for Film 2 after only 6 layers. Thus, the Film 1 having the single layer thickness of 200 nm was compared to the films with 300 nm thick single layers. The results of the orientation showed a higher degree of (110) orientation in Film 2, Tab. 3.7. The nucleation of (110) grains in PZT films on Pt can only take place on the interfaces to bubbles in the films [191] meaning that the thermal treatment in the film with thicker single layer was too fast and longer time at each temperature is needed. The

influence of single layer thickness on the orientation of PZT 52/48 films was not as obvious. Possibly the orientation and the phase selection in PZT 52/48 is more complex than in pure tetragonal PZT. The orientation of two PZT 52/48 films processed under similar conditions is summarized in Tab.3.7. Film 1 had 160 nm/layer thickness and total thickness around 2.2 µm. The single layer thickness of the second film was 200 nm/layer and the total thickness around 2 µm.

Tab. 3.7: Influence of the single layer thickness on the orientation.

	single layer thickness			
	PZT 40/60		PZT 52/48	
	film 11	film 12	film 11	film12
(100)	21%	12%	69%	74%
(111)	52%	45%	26%	25%
(110)	26%	43%		

3.3.7 Crystallographic orientation in 5 µm thick films

One 5 µm thick PZT 40/60 film (film 13, Appendix A) and two 5 µm thick PZT 60/40 films (films 7, 8, Appendix A) were deposited onto Pt(111)/Si substrates. The applied thermal profile was chosen to support (111) orientation in PZT 40/60 films, and (100) orientation in PZT 60/40 films, respectively. All films showed high degree of (100) orientation at 5 µm thickness. The degree of (100) orientation was 70% in PZT 40/60, and 85 % and 90% in two PZT 60/40 films. The predominant orientation in such thick films can be attributed to the faster growth of (100) crystallites compared to crystallites of other orientation as discussed in previous sections.

3.3.8 Effect of the bottom electrode on the orientation of thick PZT films

PZT films were deposited on substrates such as Pt(200)/Si, silicon with LNO as the bottom electrode and on platinised sapphire substrates. In the following sub-sections the orientation of such films will be discussed.

3.3.8.1 PZT 52/48 on $LaNiO_3$/Si substrate

The diffractogram of LNO on silicon is depicted in Fig. 3.30. The LNO film was around 75 nm thick and was fully crystallized after final annealing at 560°C for at least 5 hours. A random orientation was found. The film resistivity was ρ= 8.8 x10 $^{-4}$ Ωcm and thus sufficient to be used as bottom electrode. The resistivity was comparable to the resistivity of LNO reported in Ref. [96] .

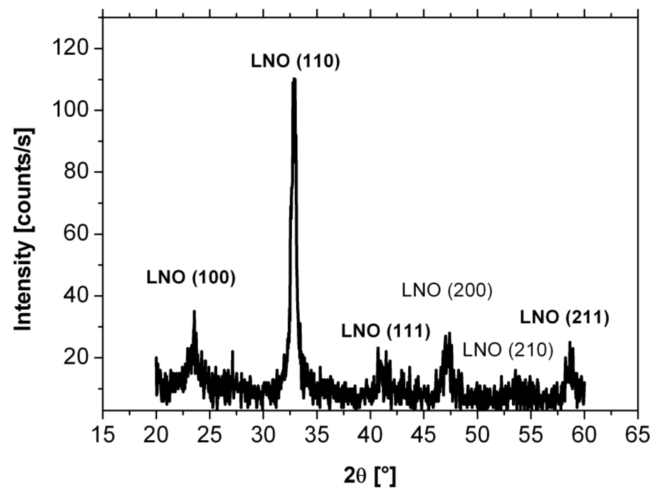

Fig. 3.30: A diffractogram of crystalline LNO bottom electrode.

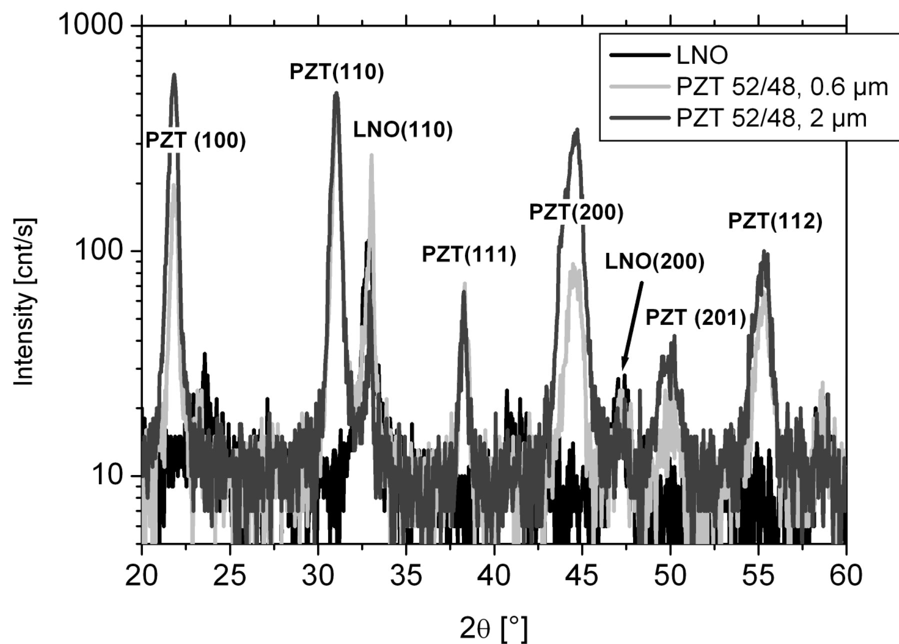

Fig. 3.31: Diffractograms of PZT 52/48 films deposited on LNO/Si substrate (film 16).

The diffractogram of a PZT 52/48 film, at two different thicknesses, deposited on such LNO substrate is depicted in Fig. 3.31. The peaks of LNO were detected in both PZT films in Fig. 3.31 although their intensities were weaker due to the PZT film deposition. LNO has a perovskite structure like PZT and the lattice spacing of LNO to PZT is similar. Evidence for this is the 2θ−viscinity of the same (hkl) peaks of LNO and PZT in the XRD pattern. A more detailed orientation analysis was carried out on 4 PZT 52/48 films at different thicknesses, Tab. 3.8.

Tab. 3.8: Integral intensities of PZT on LNO/Si, in percent.

Sample name	film 15		film 16		film 17		film 18
Thickness / Orientation	1 µm	2.4 µm	0.6 µm	2µm	0.8 µm	2 µm	2 µm
(100)	28	52	22	44	35	22	65
(110)	48	30	55	37	50	13	25
(111)	5	3	6	3	2		
(120)	5	4	2	4			5
(211)	12	10	15	12	13	50	5

The intensities are given as a sum of all peaks regardless of the phase to which they belong. A tetragonal peak split was found in all films thicker than 1 µm. Film 16 showed some rhombohedral content. High diffracted intensities were picked up at the lattice planes (100) and (110) in all films. Some intensity originating from (211) lattice planes was found in the Film 17. The orientation selection in PZT films deposited on LNO is different to the previously discussed orientation on Pt(111). At first, the LNO was deposited on amorphous silicon oxide layer. The amorphous layer does not provide any nucleation sites for LNO and only the nucleation mechanisms with high activation energy can take place, like surface nucleation (LNO surface) or homogeneous nucleation. Whatever the nucleation mechanism was, the lack of the nucleation sites at the interface is likely to result in a random orientation. The crystallization time was in deed very long for LNO, around 5 hours at 550°C. Because of the good lattice match between LNO and PZT the LNO grains serve as a nucleation site for PZT. Thus, thinner PZT films exhibit random orientation similar to LNO layer. In thicker films the favourable growth of (100) lattice planes would out rule the growth in any other

direction and, as discussed in earlier section, the diffracted intensity of (100) was much stronger in films of final thickness.

3.3.8.2 PZT on Pt(200)/Si(100) substrate

All three PZT compositions, PZT 40/60, PZT 60/40 and PZT 52/48, were deposited on Pt(200)/Si substrates. The Pt(200) substrate consists of expitaxial matching layers on silicon in order to obtain a (200) orientation of sputter deposited platinum. The diffractograms of each PZT film is depicted in Fig. 3.32. All films were 2 μm thick.

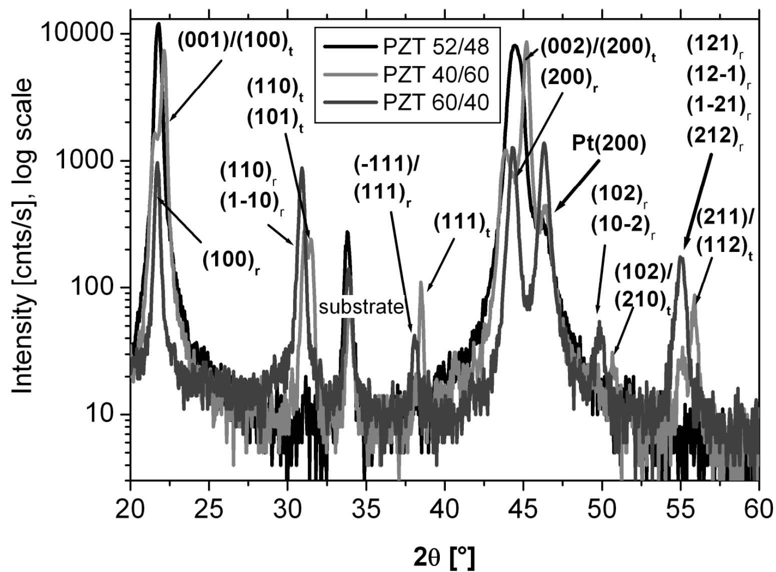

Fig. 3.32: Diffractograms of PZT 52/48 (film 19), PZT 40/60 (film 14) and PZT 60/40 (film 9) on Pt(200)/Si.

The diffractogram of PZT 52/48 exhibited a (100) texture. Although no clear, (200) peak splitting was observed the broad nature of this peak allows an assumption that both tetragonal and rhombohedral phases were present. A phase content of around 30% was found for rhombohedral phase. In this film a very good matching between the substrate orientation and PZT orientation was found. However, PZT 40/60 and PZT 60/40 films on Pt (200) showed a dominant (100) orientation though some other peaks were found. The content of (100) orientation was around 92% for PZT 40/60 and around 80% for PZT 60/40. It must be noted that some of the PZT 40/60 films deposited on Pt(111)

substrate showed higher (100) intensity than the film on Pt(200). PZT 40/60 films have shown strong tendency to nucleate and grow with (100) orientation on Pt(111) so it is more surprising that on Pt(200), where better conditions are given for (100) orientation, a lower degree of (100) orientation was obtain.

Despite the good lattice match between PZT (200) d_{200}=2.018 and Pt (200) d_{200}=1.96 some other nucleation mechanisms were also taking place apart from the interface nucleation on Pt (200). In PZT 60/40, this was the highest degree of (100) orientation found in only 2 µm thick PZT 60/40 films.

3.3.8.3 Effect of the sapphire substrate (Al_2O_3) on the PZT film orientation

The sapphire substrates were employed to study orientation of PZT films on a substrate with different mechanical and thermal properties than silicon. PZT 52/48 and PZT 40/60 films were deposited onto platinised (012) oriented sapphire (single crystal Al_2O_3) substrates. One PZT 40/60 film was deposited on a (006) oriented sapphire substrate without any bottom electrode.

The diffractograms of 1.1 µm and 1µm thick PZT 52/48 and PZT 40/60 films, respectively, are depicted in Fig. 3.33. A well pronounced (200) peak split was found in both PZT compositions on sapphire. In PZT 52/48 a double (111) peak was found indicating the presence of the rhombohedral phase. In both PZT films the orientation was a mixture of (100) and (111) orientation, Tab. 3.9.

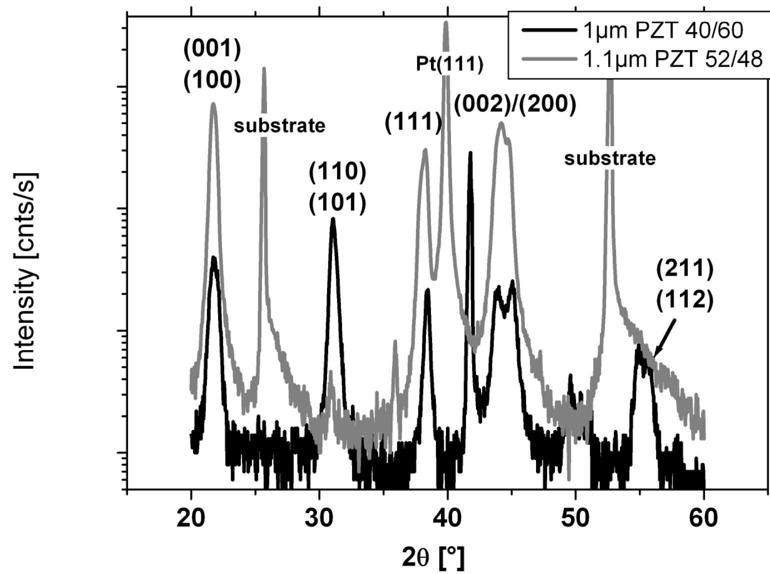

Fig. 3.33: Two 1µm thick PZT 52/48 and PZT 40/60 film on sapphire substrates.

The diffractograms of two PZT 40/60 films on sapphire with and without Pt layer are depicted in Fig. 3.34. The PZT 40/60 film deposited on (006) oriented sapphire substrate showed predominant (110) orientation along with some (100) and (111) peaks. The ratios of intensities of in-plane (100) and out-of-plane (001) domains were equal on a sapphire substrate with and without Pt.

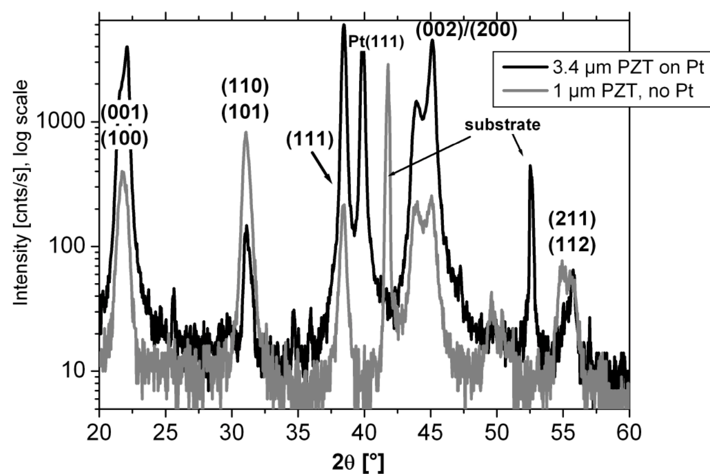

Fig. 3.34: Two PZT 40/60 films deposited on sapphire substrate with and without Pt(111) electrode.

Tab. 3.9: Integral intensities (in percent) of PZT films on sapphire substrates.

PZT composition	PZT 40/60 (film 15)	PZT 40/60 (film 16)	PZT 52/48 (film 20)
substrate	Pt(111) /sapphire	sapphire, no Pt	Pt(111)/ sapphire
(100)	54	31	70
(110)		50	
(111)	43	10	30
(211)		8	

3.3.9 Chemical analysis of PZT films

The element analysis by means of EDX analysis was performed on three samples from each sample and sol batch. For each film at least 3 measurements on different spot were performed. The results are summarized in Tab.3.10. The ratio Zr/Ti was matching the intended sol composition Zr/Ti ratio for all films, within the accuracy of the measurement. All films were Pb deficient and the highest lead deficiency was found in PZT 60/40 films possibly due longer processing time.

Tab. 3.10: Results of the chemical analysis in PZT films with different composition.

	Pb in atom-%	Zr in atom-%	Ti in atom-%
PZT 40/60	94±3	40±2	60±2
PZT 52/48	90±3	50±2	50±2
PZT 60/40	90±4	60±3	40±3

3.4 Residual stress analysis

3.4.1 Introduction to the section

This section focuses on the analysis of residual stress in PZT films with different compositions. The stress model and the experimental data collection will be further explained, along with the limitation of the analysis. The residual stress was calculated for all PZT compositions and will be introduced and origin of the residual stress will be discussed. The effect of stress on the orientation will be shown.

3.4.2 Preliminary Characterizations

Full characterization of anisotropic wafer bending and the limitation of the measurement technique were given in Appendix C. Here, only a short summary is given.

Due to the anisotropy of the (100) silicon single crystal it is expected that the wafer bending is not uniform in different directions of the wafer. Also the primary and the secondary flat of the wafer have some influence on the deformation of the wafer. To compare the stress in different wafers the geometry of the sample and the direction of the measurement is very important. In all analysed films a 2” or 4” wafers were used and the curvature was measured in all wafers in the same direction. According to the anisotropy of the Young’s Modulus of (100) silicon all calculations were performed using the Young’s Modulus along the [1-10] direction. Thus the following stress results are only valid for circular wafers with the measurements in [1-10] silicon direction.

3.4.2.1 Initial consideration

The residual stress calculation with the Townsend-Model requires the measurement of the wafer curvature before and after the stress was introduced in order to calculate the difference in the stress introduced through processing. If the initial deflection was zero and the wafer was flat, then only the deflection measurement after the processing is sufficient.

In sol-gel films the stress builds up during heating of the films and also upon cooling down after the crystallization. Thus, two kinds of stresses can exist, the processing stress and the residual stress due to thermal contraction upon cooling. The stress that is built up during heating can be completely different to the stress built up during cooling down of the film, especially as some stress can be relaxed upon paraelectric-ferroelectric transition at the Curie temperature.

The stress development upon heating was investigated in section 3.2.2 and it was shown that tensile stress increases in the film up to the point where crystallization occurs. After the crystallization a stress relaxation was found. The stress analysis in the following section focuses on the stress that builds up after the crystallization or during cooling down the film to the room temperature. There are few reasons for the choice of limitation of the stress analysis. First of all and as seen from Section 3.1 the thermal stress in platinum is much larger than the stress in the PZT film upon heating. After the film crystallization the material properties of all layers, the film and the substrate are known and are available. Furthermore, it is expected that the stress in the temperature range from the crystallization and upon cooling is linear, apart of the stress relaxation at Curie temperature. As it will be seen later on the thermal expansion coefficients this is not quite true but can be sufficiently approximated. Up to this point, all required parameters for the stress calculation are known except of the wafer curvature at the crystallization temperature. Because no in-situ measurements were available some conclusions were deduced from the measurements in Section 3.2.

On the measurements of annealed platinum it was observed that the tensile residual stress in the substrate, after platinum recrystallisation, was only due to the thermal expansion mismatch between platinum and silicon. The same results were shown by Spierings et al [117]. This means that platinum reaches the same length as silicon at the annealing temperature, through the process of recrystallisation. This is in analogy to the bimetallic beams on which the Townsend model was based. This finding suggests that the substrate is flat at the crystallization temperature. Once platinum recrystallised the stress state in the substrate was stable and repeated annealing at the same temperature did not affect the stress state.

By choosing the annealing temperature to be the same as the crystallization temperature of PZT, it is assured that the wafer curvature with deposited PZT will be

flat or nearly flat at the crystallization temperature. This assumption seems far fetched at first. However, any deviation from the flat wafer will be due to the shrinkage of the PZT film during heating up. In Section 3.2 it was shown that whatever the stress was during heating the stress decreased upon the perovskite crystallization because of the large thermal expansion coefficient of the perovskite phase that is similar to that of platinum. Also, the deflection measurement in the multilayers has shown that each PZT layer goes through a cyclic stress state but after the crystallization only small total stress increase was observed. Thus, the largest part of the PZT film shrinkage must have been relaxed at some point, most likely at the crystallization and the Curie point. Also if any strain is existent in the film at the point where the film is able to undergo structural changes it seems very likely that the film strain energy will contribute towards the creation of an equilibrium microstructure of the film whereby the strain energy can be annihilated. However, the measured deflection during multilayer film deposition in the stress analysis will be first simulated using the curvature calculation (Eq. 2.14). If there was any deviation from the assumed condition it was noticed by comparing the curvature calculation and curvature measurement. The curvature calculation and comparison of the experimental to the theoretical values enables a more detailed analysis of the residual stress in PZT films.

Before any residual stress results can be given the stress in the substrate and the influence of the substrate must be characterized first. Also, the influence of the material coefficients such as TEC and Young’s Moduli on the wafer curvature needs to be investigated.

3.4.2.2 Stress in as-sputtered platinum

After sputtered platinum layer the wafers always showed an increase of compressive deflection of 1.25 ± 0.5 µm in average (on 2″wafer), in reference to the initial substrate bending. This value was determined from 18 experiments on the silicon wafers with the same thickness. It can vary slightly from sample to sample depending on the sputtering conditions and the chamber pressure, as the pressure can increase during the deposition process and thus some variations in the microstructure from sample to sample can be obtained. The change of deflection after platinum annealing varied between 1 to several

microns. This value is dependent on the thickness of all layers, e.g. Ti, Pt and SiO_2 layers and the annealing temperature. However, the deflection simulation showed the residual thermal stress in platinum was always around 980 MPa.

It must be noted that different Young's Modulus of platinum was used for the stress calculation. On the annealing experiments on platinum it was observed that there was some titanium diffusion through platinum. The total Young's Moduli of pure Ti is around 110 GPa [179] and of pure Pt around 170 GPa. It is reasonable to think that the Young's Modulus of the titanium/platinum bilayer is different from that of platinum. This can become clear when titanium diffusion into platinum layer is considered. From the simulation of the platinum deflection during annealing it was found that the value of 270 GPa matches much better the experimental deflection than the Young's Modulus of 170 GPa of pure platinum. When alloying pure metals usually their strength is increased. Work of Biggs et al [192] showed a significant increase in mechanical hardness of platinum when it was alloyed with 4-5 weight-% of titanium. Because there is a proportional law between the hardness and the mechanical strength in metals the increased Young's modulus was justified simply by the interdiffusion of titanium into platinum layer.

3.4.2.3 Curvature simulation

The experimental data was collected after silicon oxidation, platinum deposition and after crystallization of each new deposited PZT layer. The experimental data for PZT 60/40 film together with the curvature simulation is depicted in Fig. 3.35. To point out that the experimental data for each PZT composition was different the experimental data of PZT 40/60 was also included. PZT 40/60 and PZT 60/40 films were deposited on comparable substrate and both have single layer thickness of 200 nm/layer showing that the incremental deflection was much smaller for PZT 40/60 than for PZT 60/40.

To find the starting point for stress calculation of PZT film, the experimental data from PZT film deflection was fitted linearly. The deflection value based only on the thermal stress in the substrate before PZT deposition was calculated and in the example in Fig. 3.35 it was 2.1 μm. A curvature calculation was carried out based on a model of 4 layers: Si, SiO_2, Pt/Ti and PZT. The calculated curvature data was then

compared with the experimental data and the initial point for PZT stresses was determined by subtracting the initial substrate bending. Thus, if the experimental curve was shifted along the y-axis by subtracting the initial wafer bending, the experimental data would overlap with the calculated data. Only then the stress calculation was carried out. If the calculated data was not parallel to the experimental data, the parameters in the calculation were varied to find the best fit and then analysed. The results of the analysis will be mentioned where such fitting was necessary.

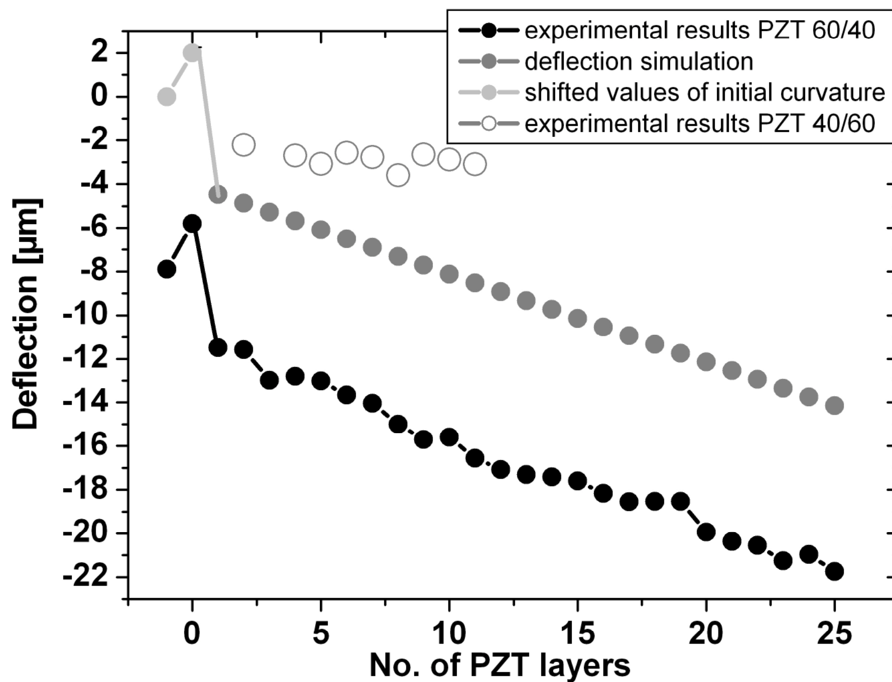

Fig. 3.35: Measured deflection in the substrate and the PZT film together with the calculated deflection for PZT film

When calculating stresses based on the measurements of wafer deflection the initial curvature of the wafer had to be considered. Neglecting the initial bending of the substrate would result in different stress values. The maximum error in PZT film stress calculation can be up to 10 MPa if the wrong deflection was used.

3.4.2.4 The parameter variation

The stress calculation with the Townsend-Model relies on many parameters which can only be obtained experimentally. Here, the values reported in the literature were used, although the parameters vary from source to source. To minimize the errors caused by introducing incorrect parameters such as thermal expansion coefficients (TEC) and Young's modulus, the curvature was calculated after Eq. (2.14) for each set of experimental data. The modelled curvature was then compared with the experimental curvature. The influence of taking different literature parameters on the deflection modelling was observed. The results are depicted in Fig. 3.36 to 3.43. For more clear result presentation the deflection was depicted instead of curvature. One parameter was changed at a time while the others were fixed at their literature values. The Young's Modulus of platinum was determined in the previous section. The parameters such as wafer size and thickness and layer thickness were measured and were input into the calculation.

It was found that the strong variation of TECs of silicon oxide and platinum shifted the curve only slightly along the y-axes and thus had only minor influence on the total curvature. The major impact of TEC variation was found between silicon and PZT and depending on the TEC ratio of silicon and PZT, the curvature could be either tensile or compressive. Hence, the curvature is highly influenced by the TEC ratio of Si and PZT and a small variation has a large impact.

The variation of Young's Modulus of platinum and silicon oxide again shifted the curve parallel along the y-axes showing only slight influence on the total curvature. The variation of Young's Modulus of PZT and silicon was more significantly influencing the starting point and the inclination of the curvature progression.

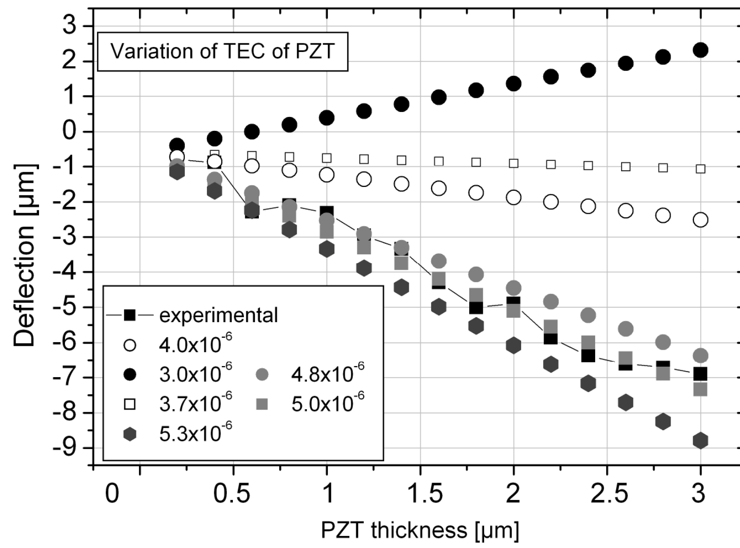

Fig. 3.36: Influence of the Thermal Expansion Coefficients (TEC) variation of PZT on the total deflection of the 4-layers structure.

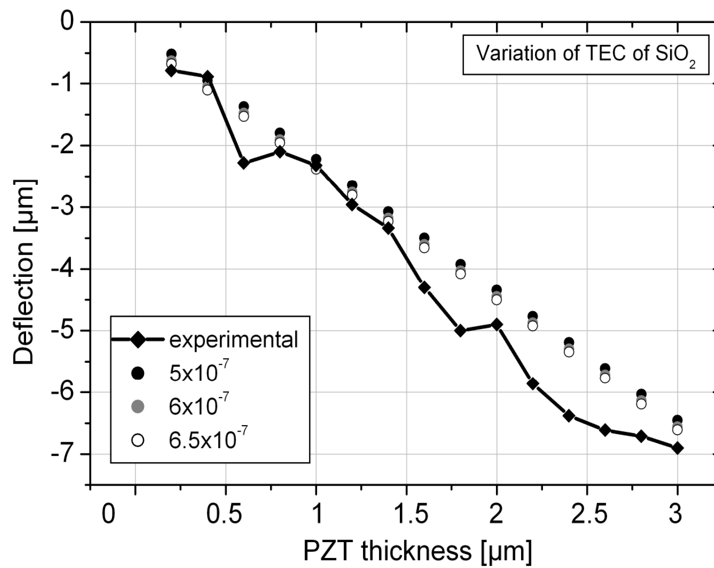

Fig. 3.37: Influence of the Thermal Expansion Coefficients (TEC) variation of SiO_2 on the total deflection of the 4-layers structure.

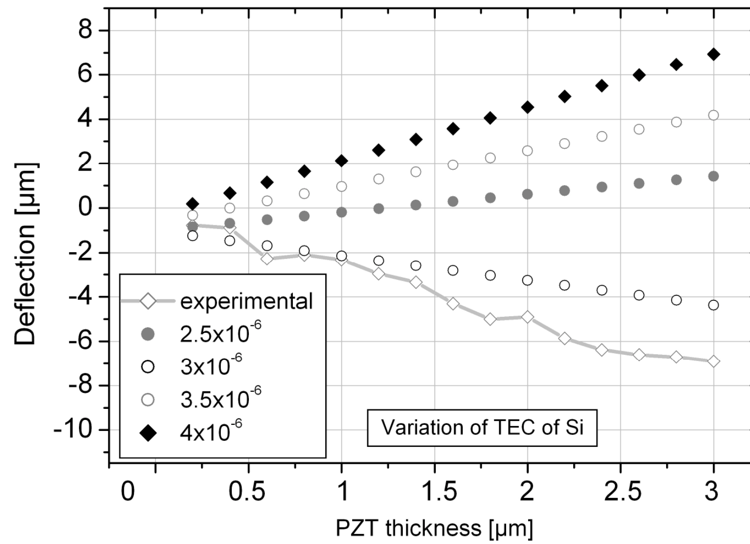

Fig. 3.38: Influence of the Thermal Expansion Coefficients (TEC) variation of Si on the total deflection of the 4-layers structure.

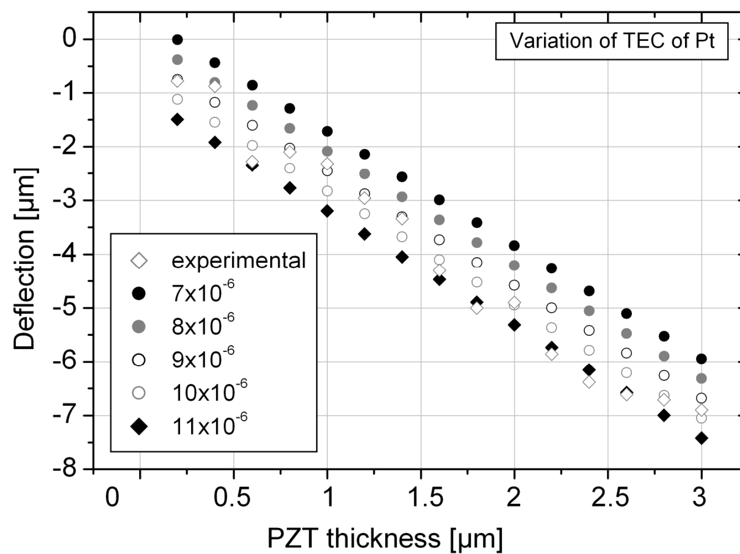

Fig. 3.39: Influence of the Thermal Expansion Coefficients (TEC) variation of Pt on the total deflection of the 4-layers structure.

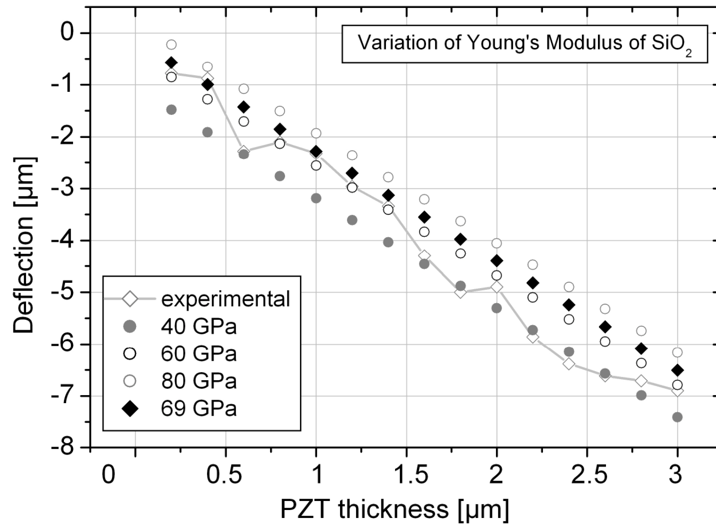

Fig. 3.40: Influence of the Young's Modulus variation of SiO_2 on the total deflection of the 4-layers structure.

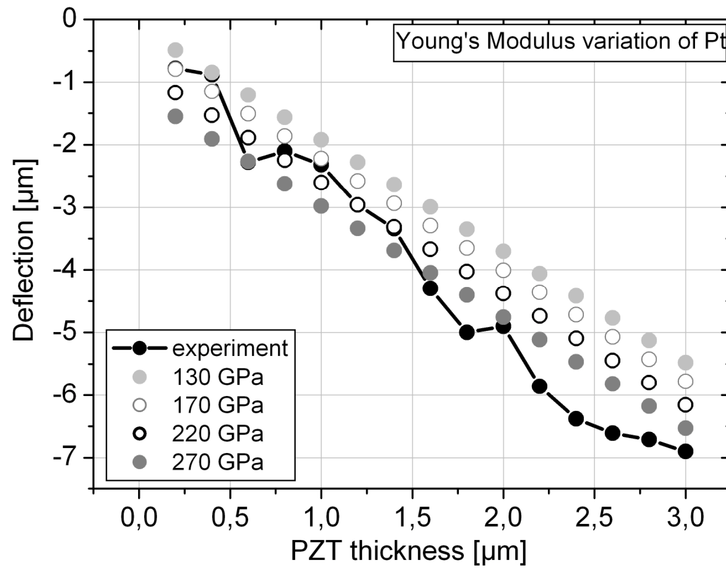

Fig. 3.41: Influence of the Young's Modulus variation of Pt on the total deflection of the 4-layers structure.

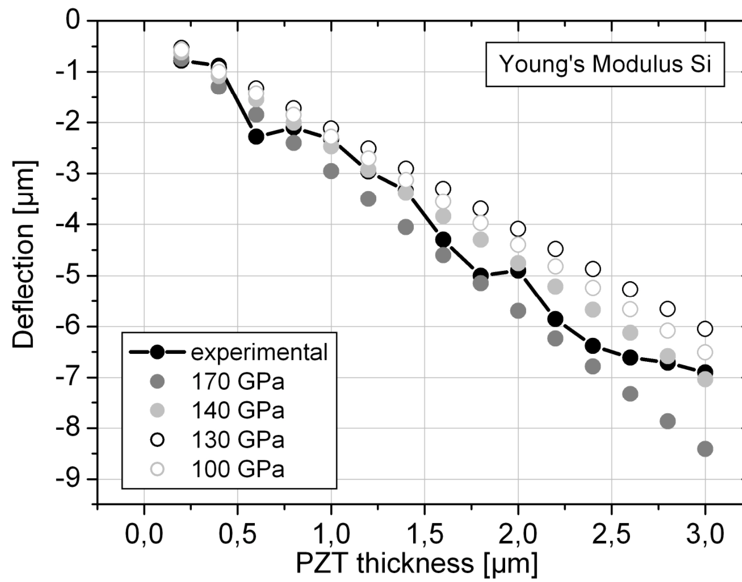

Fig. 3.42: Influence of the Young's Modulus variation of Si on the total deflection of the 4-layers structure.

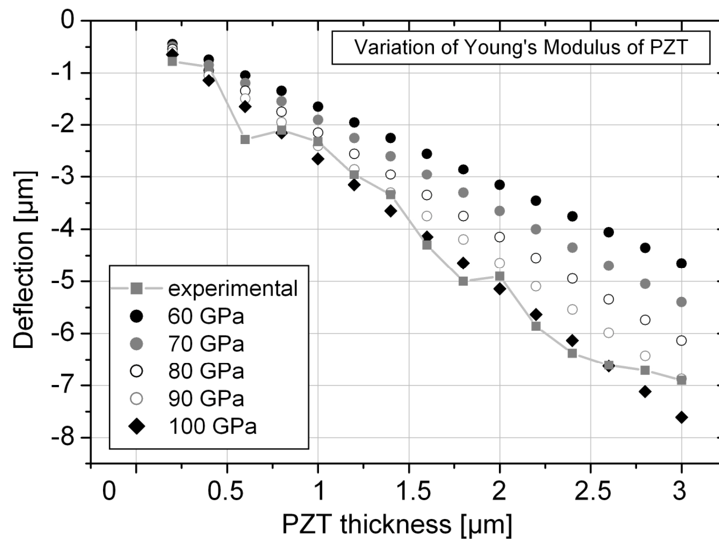

Fig. 3.43: Influence of the Young's Modulus variation of PZT on the total deflection of the 4-layers structure.

Finally, the values that were used in the calculation are summarized in Tab. 3.11. The values for the TEC of PZT are different for each PZT composition and additionally the TEC changes upon paraelectric-ferroelectric transformation at the transition temperature. For all PZT compositions the TEC is non-linear with temperature. Fig.

3.44 shows an example of the thermal strain of rhombohedral PZT with temperature, after [193]. The TEC of PZT can be calculated at each temperature as the inclination of the curve in Fig. 3.44. For other PZT compositions the strain-temperature can vary considerably.

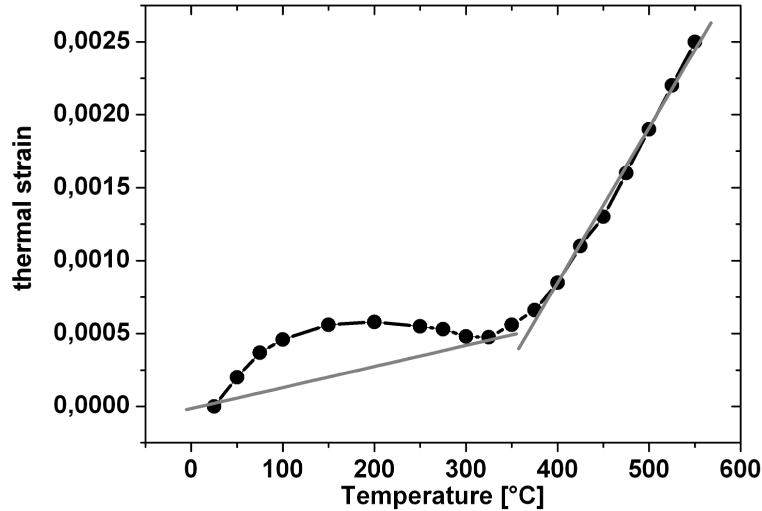

Fig. 3.44: Thermal strain of PZT 60/40 vs.temperature, reproduced from the dilatometry results from [193].

To simplify the stress calculation the weighted average TEC values of paraelectric and ferroelectric phases were calculated. The transition temperature was taken from [4]. The TECs of the paraelectric and the ferroelectric phase α_{para} and α_{ferro} were taken from the literature, Tab. 3.11. The weighted average TEC for each composition was calculated after:

$$\alpha_{PZT} = \alpha_{para} \cdot \frac{(T_a - T_c)}{\Delta T} + \alpha_{ferro} \frac{T_c}{\Delta T} \tag{3.2}$$

with the annealing temperature T_a and the Curie or transition temperature T_c. The calculated TECs are summarized in Tab. 3.11 and were used to calculate curvature and fit it with the experimental results.

Tab. 3.11: Parameters used in the stress calculation

Layer	average TEC [1/K]	Young's Modulus [GPa]	T_a [°C]	T_c [4] [°C]	TEC para. phase [1/K]	TEC ferro. phase [1/K]
silicon (100)	$3.6x10^{-6}$ [135]	170 [194] <110> direction				
silicon oxide	$5.5x10^{-7}$ [195]	69 [195]				
platinum/ titanium	$9x10^{-6}$ [178]	290, 170 GPa [179]				
PZT 40/60	$3.7x10^{-6}$	85 [196]	550	370	$9.4x10^{-6}$ [11]	$2.1x10^{-6}$ [11]
PZT 52/48	$5.3x10^{-6}$	85 [196]	630	390	$8x10^{-6}$ [197]	$1.9x10^{-6}$ [197]
PZT 60/40	$4.7x10^{-6}$	85 [196]	630	430	$1x10^{-5}$ [193]	$2.5x10^{-6}$ [193]

3.4.3 Residual stress in PZT films with different composition

The calculated residual stresses in all four layers for a PZT 60/40 film are depicted in Fig. 3.45. The stress in silicon layer was calculated at the bottom of the layer and was compressive in the range between -1 and -4 MPa with increasing PZT film thickness. Values in the range of several MPa were also found by [198]. The stress in silicon oxide layer was compressive between -131 and -133 MPa. The reason for compressive stress in SiO_2 layer is because its TEC is one order of magnitude lower than that of Si or Pt.

In platinum layer, tensile stresses were found. Taking the Young's Modulus of Pt/Ti layer as determined in previous section (270GPa), the calculated stress was around 990 MPa. This value matches exactly the residual stress in platinum of 988 MPa determined by [117, 176, 199-200]. In the PZT 60/40 film the tensile residual stresses were found to be around 62 MPa. In all layers, the stress was found to increase with PZT film thickness. In all films on platinised silicon substrates such stress relation was found.

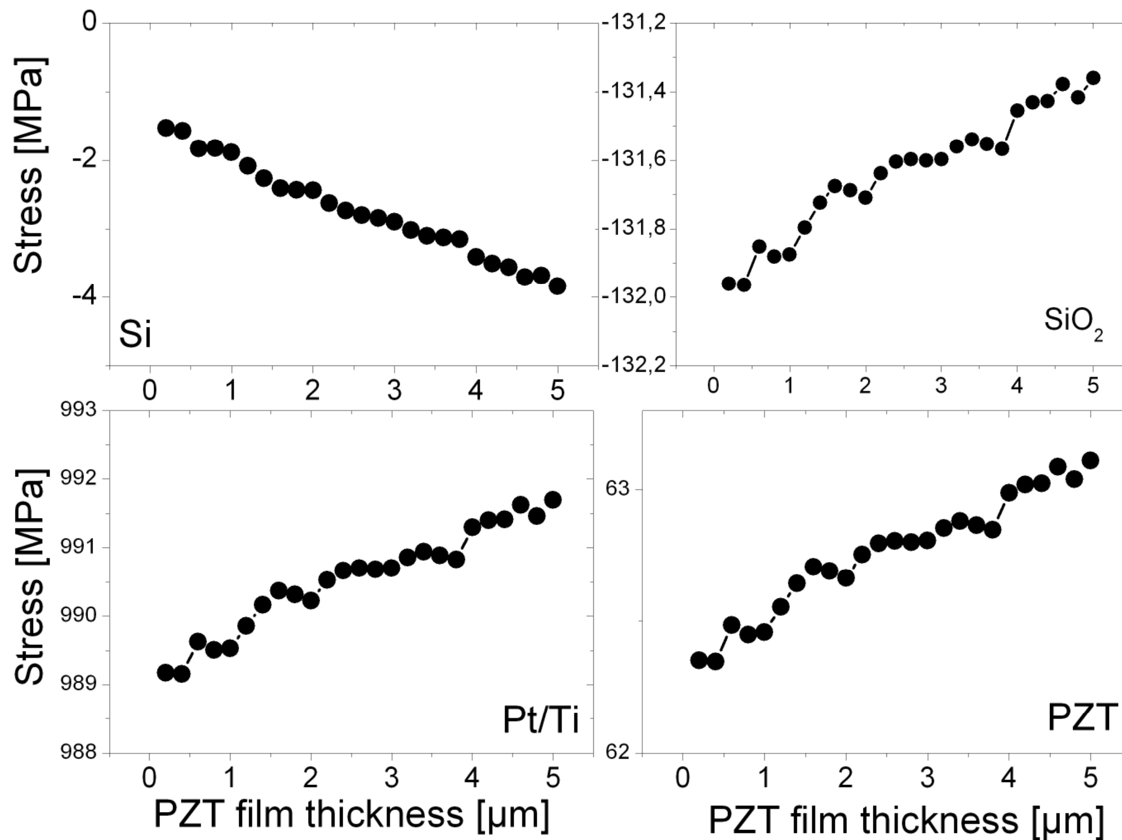

Fig. 3.45: Residual stress in a PZT 60/40 film with increasing film thickness. 25 layers with 200 nm single layer thickness were deposited and the wafer curvature was measured (at room temperature) after crystallization of each layer. Sample: PZT 60/40-Pt(111)/Si/2" - 5 µm - film 6.

In PZT 40/60 film similar stress progression, like for PZT 60/40, was found in all layers, Fig. 3.46. The major difference between the PZT 60/40 and PZT 40/60 is the lower annealing temperature for PZT 40/60 films and its lower TEC. It was expected that the stress in all layers would be lower when lower temperature was used. Very low stresses in PZT 40/60 films were found. The deflection in such films was found to remain more or less stable and did not increase noticeably with increasing thickness. The low stress values in PZT 40/60 film are correlated to the low thermal expansion mismatch between PZT and silicon.

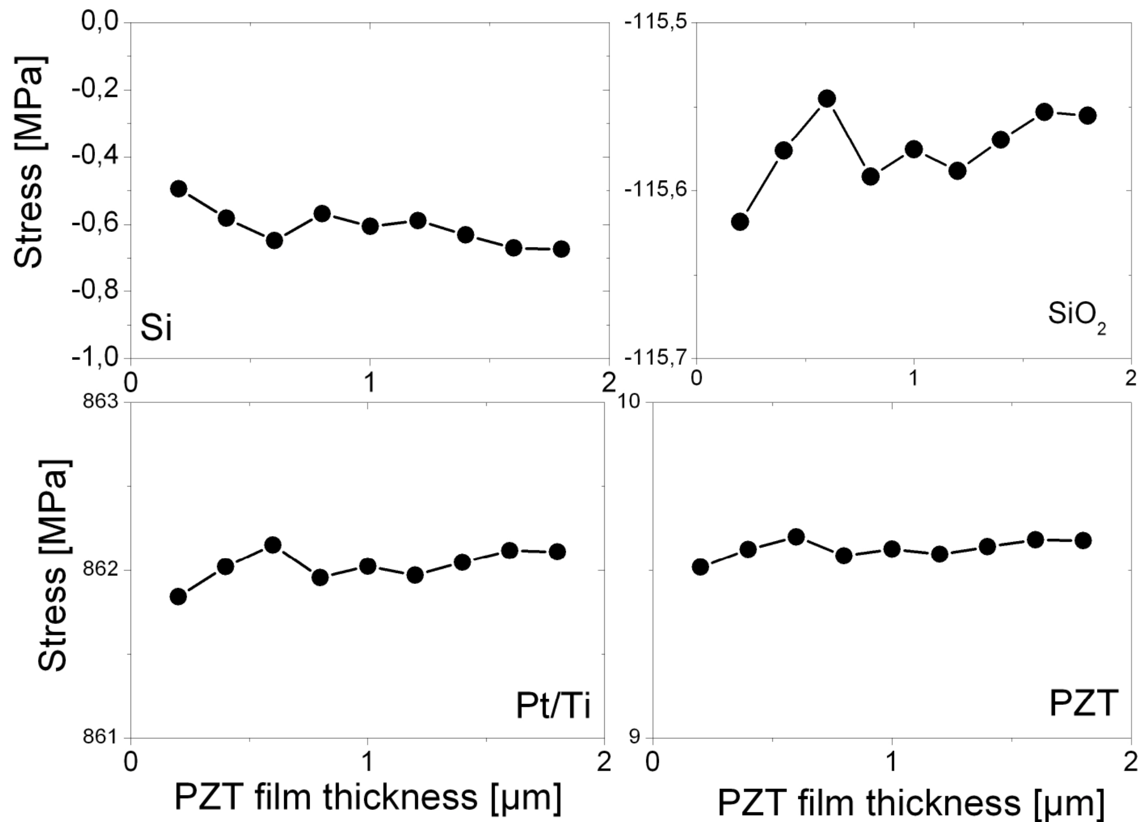

Fig. 3.46: Residual stress in PZT 40/60 film with increasing thickness. 10 layers were deposited onto 2" platinised silicon substrate, each layer was 200 nm thick. Sample: PZT 40/60- Pt(111)/Si/2" - 2 µm film 11.

In the processing of PZT 52/48 films, the same crystallization temperature was used as for PZT 60/40 films and thus similar values for all substrate layers of PZT 52/48 and PZT 60/40 were found, Fig. 3.45 and 3.47. The residual stress in PZT 52/48 was in average around 90 MPa and comparable to the values reported in [132, 178, 201] which were between 100 and 144 MPa. Slightly higher values between 133 and 197 MPa in PZT 52/48 films of different thickness up to 1.8 µm were reported by [134]. Higher stresses were reported for PZT 52/48 and lower for PZT 40/60 in [200, 202].

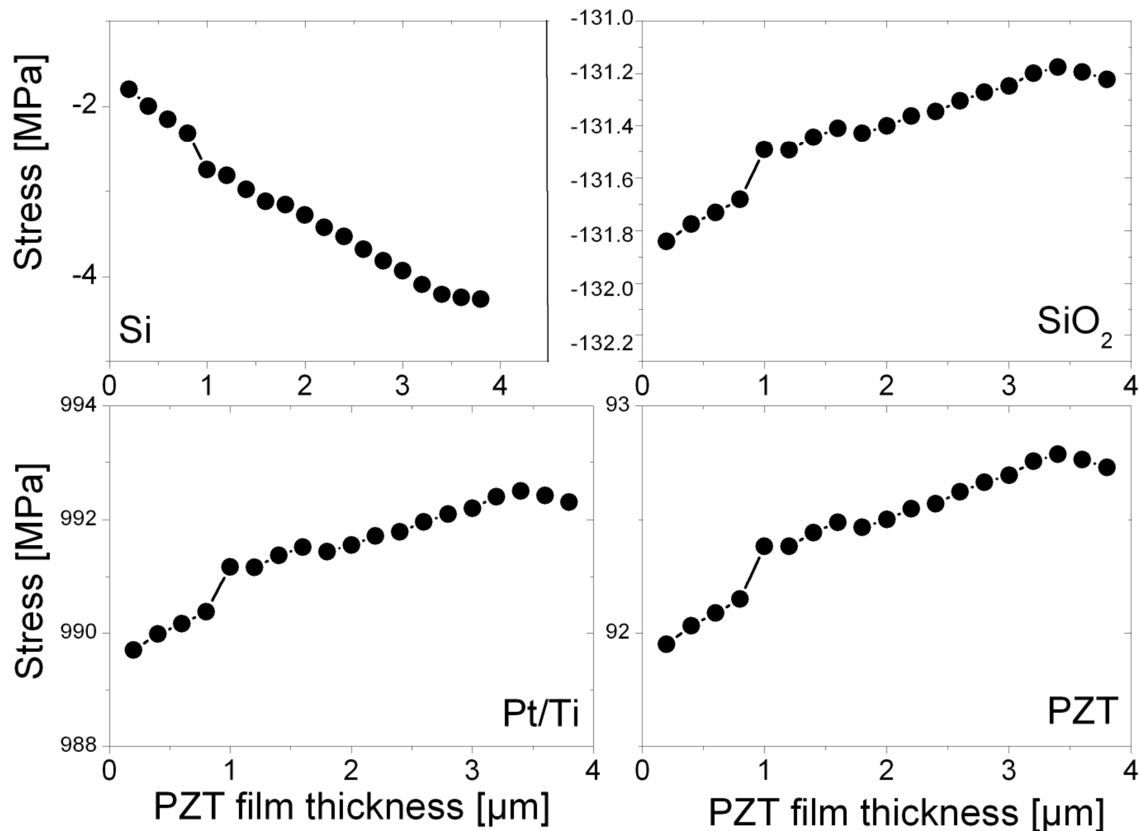

Fig. 3.47: Residual stress in PZT 52/48 film with increasing thickness. 20 layers were deposited onto platinised silicon substrate; each layer was 200 nm thick. PZT 52/48-Pt(111)/Si/2”- 2 µm - film 21.

In all films on platinised silicon substrate tensile stresses in PZT films and in the platinum layer were found. Silicon and silicon oxide showed compressive stress. Relatively low stresses were found in PZT films when compared with the platinum/titanium stress. The amount of PZT stress brought into the composite structure was significantly low. A closer look at the high residual stresses in platinum layer reveals that the major wafer curvature was introduced through platinum and only small amount was due to PZT film. However, when PZT was deposited on such substrate, the stress from the underlying layers must not be neglected as it will strongly influence the stress in the PZT film, especially if devices need to be fabricated from using such films and the silicon substrate needs to be thinned.

The PZT 52/48 composition exhibited highest stress values of all PZT compositions. The TEC of PZT 52/48 was the highest of all PZT compositions, which means that this PZT film shows the largest shrinkage when cooled down from the

crystallization temperature. The crystallization temperature was also higher than for PZT 40/60 films, which means that the thermal strain in PZT 52/48 is higher. Although the crystallization temperature of PZT 60/40 was the same as for PZT 52/48 the pure rhombohedral composition has lower average TEC meaning that the thermal shrinkage of PZT 60/40 is lower than of PZT 52/48.

3.4.4 Residual Stress and film orientation

The residual stress was calculated in one previously mentioned PZT 52/48 film which was deposited on 2“ platinised silicon wafer with a PbO buffer layer (film 14). The degree of (100) orientation in this 3 µm thick film was around 88% with rhombohedral phase content of around 15%. One other PZT 52/48 film, also mentioned earlier, was deposited onto a 3“Pt(200)/Si substrate (film 19), and was completely (100) orientated. The fraction of the rhombohedral phase was 33 %. The residual stresses in these two PZT 52/48 films were determined to be 17 and 19 MPa, respectively. The deflection increase with PZT film layer deposition was very low in both films. To fit the calculated data to experimental data the TEC had to be significantly decreased and was closer to the films with pure tetragonal phase. On the other hand, the second parameter that could have been varied in Eq. (2.14) was the Young’s modulus of PZT. Only a reduction of the Young’s Modulus of PZT to 30 GPa for both films delivered same curvature and eventually the same stress. Such low stresses in PZT 52/48 film can only be due to the high (100) orientation as the stiffness of PZT films is anisotropic and varies for different orientations. In contrast, a 3 µm thick PZT 52/48 film deposited on a comparable substrate had mixed orientation and the residual stress around 56 MPa. This film was crystallized at 550°C hence had the lower stress than in the film shown in Fig. 3.46. Those results suggest strong relation of residual stress and orientation in PZT 52/48 films.

Two 5 µm thick PZT 60/40 films were deposited (films 7 and 8). One was to 85% predominantly (100) oriented and the other was 90% (100) oriented. The stress difference between these two films is around 1 MPa.

The relationship between the orientation and the stress in particular in PZT 52/48 can be explained on the anisotropic TECs of the tetragonal ferroelectric phase.

Cook et al [203] measured the TEC of PZT 48/52 ceramics before and after poling and reported large discrepancy of the TEC between poled and unpoled films. The thermal strain was dependent on the polarization direction, and was largely negative in direction parallel to the polarization direction and was strongly positive in the direction perpendicular to the polarization direction.

According to Cook et al the TEC in (100) direction is around $\alpha_a = 4.7 \times 10^{-6}$ K^{-1} and in (001) direction around $\alpha_c = -6.6 \times 10^{-6}$ K^{-1} in the temperature range between room temperature and 350°C. According to the latter values a schematically representation of the thermal contraction in (001) direction and expansion in (100) direction of tetragonal unit cell during cooling is given in Fig. 3.48a. In a PZT film on a substrate consisting of the mixed (100) and (001) orientation the thermal contraction is depicted schematically in Fig.3.48b. For simplification the expansion or contraction of the crystallites is depicted only in one direction.

In (100) oriented crystallites or *a*-domains an in-plane thermal expansion during cooling can be observed, in respect to the XRD measurement direction. In (001) oriented crystallites or *c*-domains the thermal in-plane contraction can be observed during cooling. According to the anisotropic TECs determined by Cook et al, the thermal expansion is larger than thermal contraction. Thus, the fraction of (001) to (100) oriented crystallites dictates the total thermal strain. In respect to the substrate contraction during cooling, either total tensile or compressive strain occurs below the transition temperature. Above the transition temperature the TEC is likely to be isotropic due to cubic crystallographic structure of paraelectric phase. Due to large positive TEC of the paraelectric phase, PZT film shrinks faster than the substrate and thus tensile stress accumulate in the film above the transition temperature. This stress can be up to 100 MPa at the transition temperature as calculated with Townsend model. Thus the total residual stress at the room temperature is the difference between the thermal contraction above the transition temperature and the thermal expansion or contraction, dependent on the ratio of *c* to *a* domains, below the transition temperature.

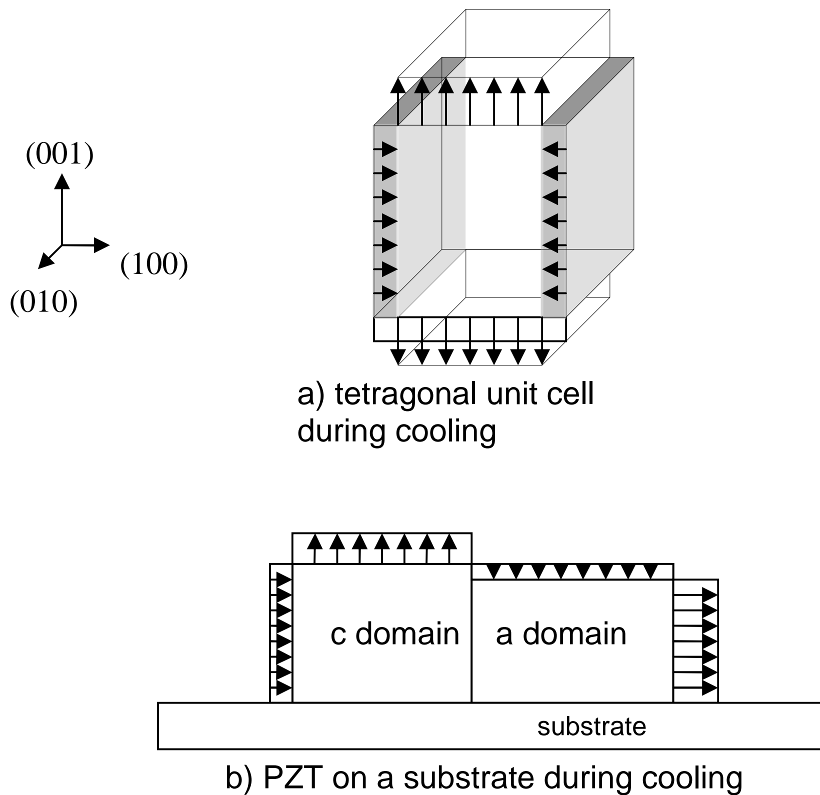

Fig. 3.48: a) Thermal deformation of the unit cell in tetragonal PZT. The same contraction as in (100) direction is found also in (010), not shown in the figure. b) Thermal deformation of *a* PZT film with a and *c* domains during cooling.

The fraction of *c* to *a* oriented domains can alter the total thermal expansion or contraction of the films. The average TEC for an isotropic film can be calculated as

$$\alpha = \frac{2\alpha_a + \alpha_c}{3} \quad (3.3)$$

according to the fractions of 1/3 of each domain orientation in tetragonal film [201].

In the PZT 40/60 films the fraction of *c*-domains was always around or below 30% and thus the anisotropic thermal expansion was not noticeable. Furthermore, such domain orientation indicates the tensile stress at the transition temperature according to Tuttle et al [11] and is in agreement with the residual stress calculations in this work.

In PZT 52/48 films there is more complex relationship between the orientation and stress due to tetragonal and rhombohedral phase coexistence. Thus, the paraelectric (100) oriented PZT 52/48 can transform into rhombohedral (100) and tetragonal (100)

and (001) at the same time. The phase ratio and tetragonal split are both dependent on the strain at the transition temperature, according to the phase-field simulations [13], and already small strain deviation can result in very different ratio of the tetragonal c- to a-domains or the ratio of the tetragonal (100) oriented to rhombohedral (100) oriented phase.

In contrast, in (111) oriented tetragonal films the domain formation also takes place at the transition temperature from paraelectric to ferroelectric phase but the efficient in-plane relaxation is far less than in (100) oriented films. According to the angle between the lattice plane vectors [100] and [111] of 54.7° (Fig. 13) the efficient in-plane strain $\varepsilon_{(111)}$ that can be accommodated in (111) oriented film by the domain formation is

$$\cos\alpha = \frac{\varepsilon_{(111)}}{\varepsilon_{(100)}} \Rightarrow \varepsilon_{(111)} = \cos\alpha \cdot \varepsilon_{(100)} = \cos(54.7) \cdot 0.028 \approx 0.016$$

and thus much smaller in [111] than in [001] direction. The unit cell distortion due to the phase transition from cubic to tetragonal crystallographic structure and its effect on the (111) lattice planes is depicted in Fig. 3.49. As it can be observed in Fig. 3.49 the tetragonal distortion causes a tilt of the (111) lattice planes together with some changes in the in-plane dimensions of the (111) lattice plane. It can be easily seen in Fig. 3.49 that there is a radial in-plane symmetry of the tilt of (111) crystallites caused by the tetragonal distortion. As can be seen from the projection of the (111) planes before and after the phase transition the amount of the in-plane dimension changes is rather small. Compared to the strain in the *c*-direction the effective in-plane strain in (111) oriented film is smaller. Thus, less in-plane strain can be accommodated in (111) oriented films due to the tetragonal distortion.

In the rhombohedral films there is no such increase or decrease in unit cell dimensions like in tetragonal PZT so that the effect of stain relaxation is likely to be much smaller than in tetragonal films. However, the thermal expansion coefficients are needed for more detailed analysis which was unfortunately unavailable. However, there is also some difference of the thermal expansion coefficients of the pure rhombohedral and tetragonal phase.

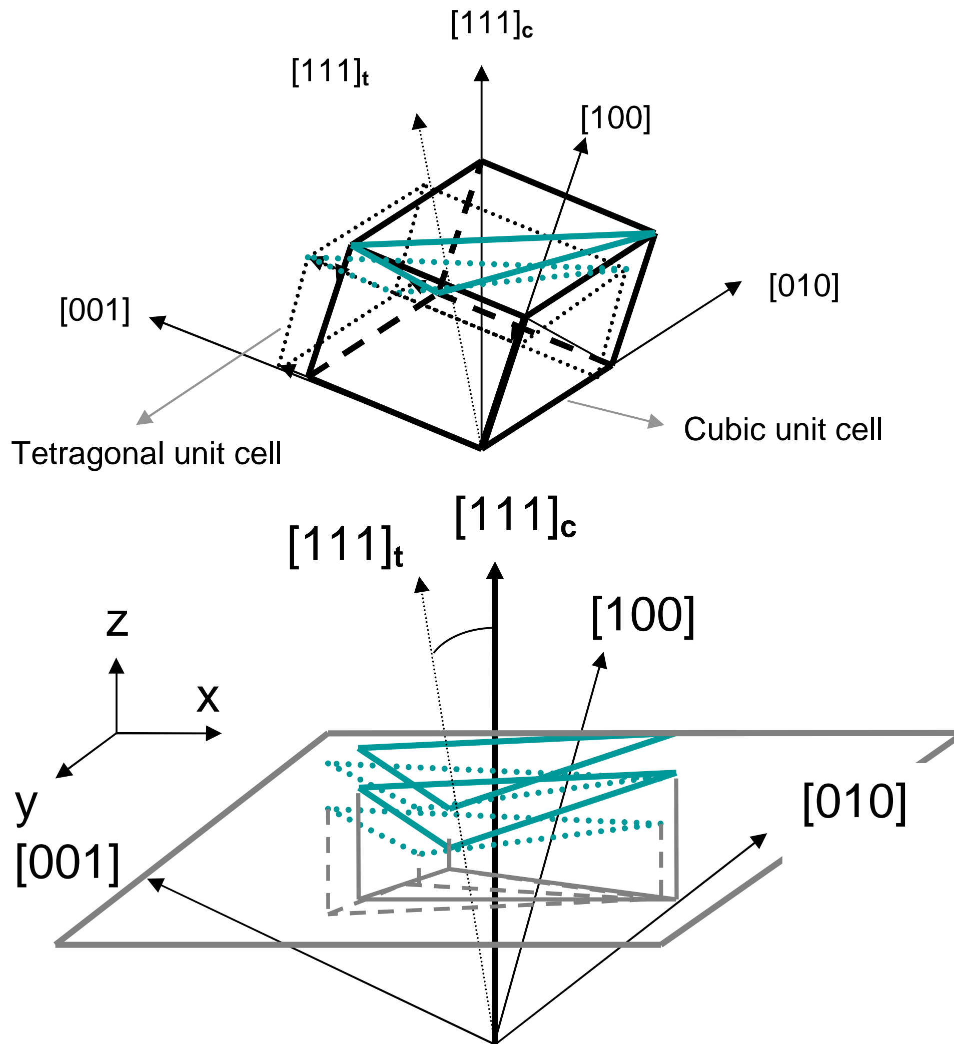

Fig. 3.49: The phase transition from cubic to tetragonal (above). The elongation of the unit cell in c-direction and the contraction in a-directions are depicted. The lattice plane (111) is highlighted with blue colour. Below: the influence of the tetragonal distortion on the lattice planes (111) whereby only the lattice planes (111) are extracted from the upper picture. The dimensions of the cubic and tetragonal (111) lattice planes are depicted in-plane of the film and their dimensions are projected into the plane of the film with the orthogonal coordinates x,y,z.

The thermal contraction of $PbTiO_3$ is an average -5.3x10^{-6} K^{-1} while the thermal expansion of $PbZrO_3$ phase is 8.4x10^{-6} K^{-1}. The $PbZrO_3$ has an orthorhombic crystallographic structure which is a different structure to the rhombohedral PZT. Although in the mixture of two phases the thermal expansion can be quite different, only within certain limits it may explain why the lowest stress was found in the

tetragonal Ti-rich phase and highest stress in the rhombohedral phase, supposed both films have same orientation.

3.4.5 Stress on compressive substrate

The orientation of PZT 40/60 films was investigated on two compressive substrates. One film was deposited on platinised silicon substrate where firstly a 100 nm thick platinum layer was deposited on the back of the wafer (Sample PZT 40/60 Pt(111)/Si/Pt/2" - 2 µm film 17). The substrate was annealed to induce tensile stresses on the back. The tensile stress on the back of the wafer acted as a compressive stress to its front. Then the 100 nm thick platinum bottom electrode was deposited on the front side, having the compressive stress, followed by a deposition of 2 µm thick PZT 40/60 film. The stress calculation cannot be performed because the top electrode platinum had large intrinsic compressive stress that was not allowed to relax and to heal the defects due to the sandwiched position of this layer between PZT and silicon. The simulation of curvature required large assumptions about the properties of the bottom platinum electrode. Hence the deflection wafer results are given, Fig. 3.50, showing compressive deflection after a 2 µm film was deposited. It must be noted that the incremental deflection is unusually large for PZT 40/60. Though, platinum's tendency to heal the defects is very high so that some thermal expansion and change towards tensile stress could be expected every time when PZT was being crystallized so that the compressive stress was eventually lowered after 2 µm film deposition. This is also equivalent to 10 cycles at temperature with total heat treatment of more than 150 minutes. However, when this substrate was heated during PZT processing, the platinum on the back would tend to expand and force the wafer to straighten. But since the platinum underneath PZT was compressed it built a major constraint in the bending. Thus, the total wafer bending was not able to reach the state of flat wafer at the crystallization temperature and the PZT deposited on such substrate was grown under compressive stress.

The orientation of such grown PZT 40/60 film showed predominant (111) orientation, Tab. 3.12 film 1. A comparison of this film with a film deposited under identical conditions but on a platinised silicon substrate under tensile stress (film 2)

shows that on the tensile substrate (100) orientation was obtained. The samples were compared at the same thickness.

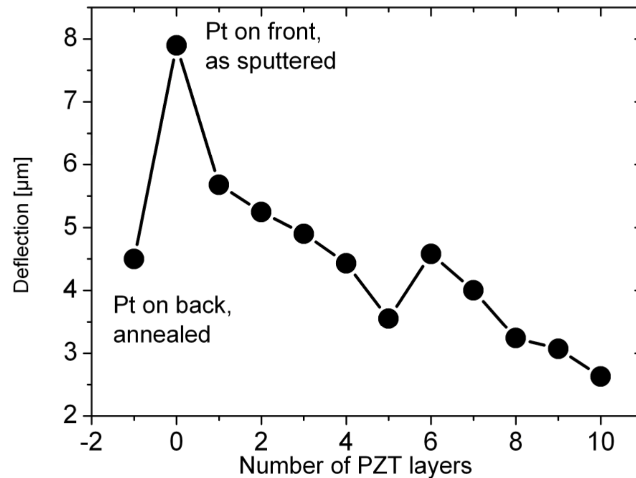

Fig. 3.50: Measured deflection in the PZT 40/60 film with platinum layer on the back.

Tab. 3.12: Orientation of the PZT 40/60 film deposited onto compressive and tensile substrates under the same processing conditions, 2µm thick.

Samples	(100)	(111)
Film1 Compressive	16%	83%
Film2 Tensile	87%	11%

Another PZT 40/60 film was deposited onto a sapphire substrate with Pt/Ti (111) as a bottom electrode (film15). Due to the higher thermal expansion of sapphire to PZT, compressive stresses can be expected in PZT film. The residual stress results are depicted in Fig. 3.51 that has shown very high compressive stress in PZT. The thermal expansion coefficient of sapphire is much larger than of silicon, around $5.8x10^{-6}$ K^{-1}, and the mismatch of the thermal expansion coefficients between platinum and sapphire is thus lower than that of platinum and silicon. Hence the lower stress in platinum was obtained. However, the residual compressive stress found in PZT does not mean that the film was under compressive stress during pyrochlore formation and PZT crystallization. The thermal expansion coefficient of paraelectric PZT is around $9.4x10^{-6}$ K^{-1} and thus

higher than in sapphire and platinum immediately before the crystallization temperature. Depending on the amount of shrinkage of PZT before the pyrochlore formation temperature it is possible that PZT was in tension and not necessarily in compression at this temperature in the early stages of the film deposition. Such change of initial tensile stress which changed to compressive upon cooling was reported by [11] for PZT 40/60 deposited on Pt/MgO substrate. MgO has also the thermal expansion coefficient higher than silicon.

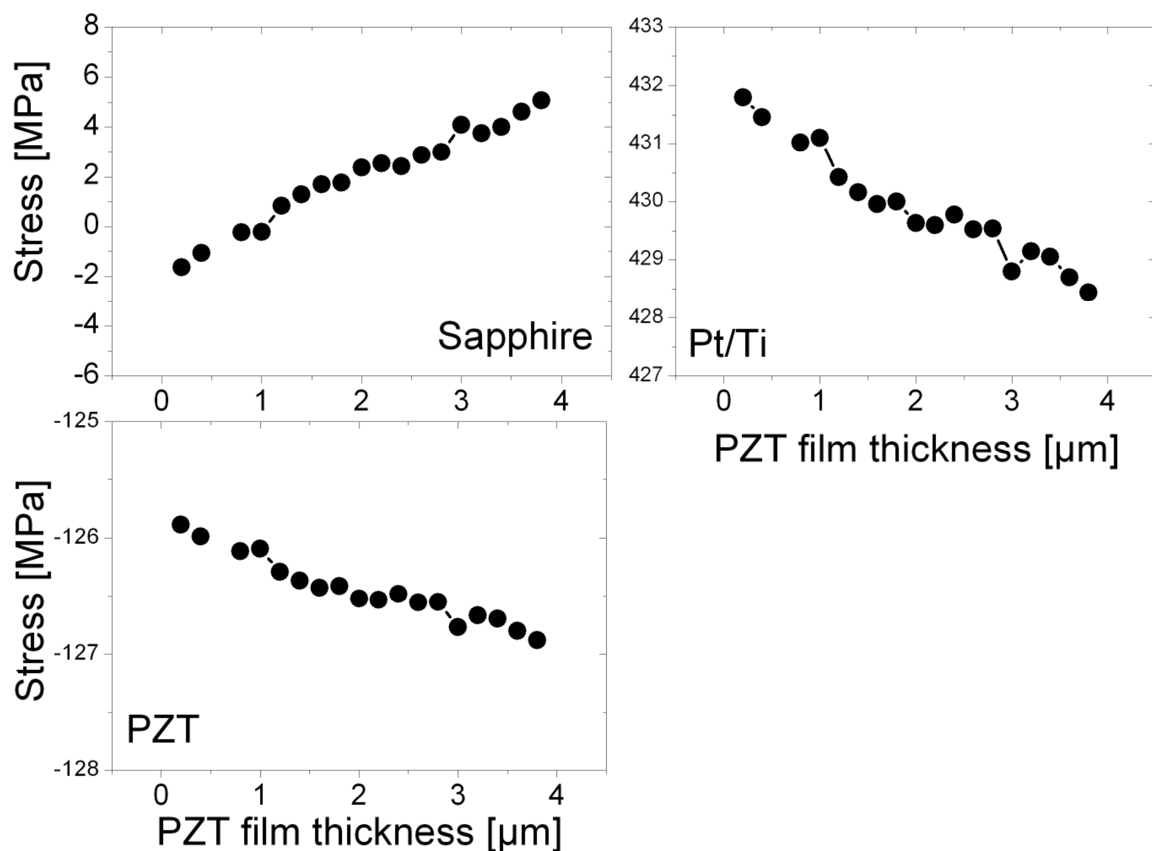

Fig. 3.51: Residual stress in PZT 40/60 film deposited on platinised sapphire substrate.

The orientation of a 3.4 μm film shows higher relative intensity of (111) peaks when compared with a 3 μm thick film grown under the same conditions but on platinised silicon substrate (PZT 40/60-Pt(111)/Si-3μm-film 4), Tab. 3.13. On Pt/Si substrate the tensile stress dominates. The substrate stress influence on the orientation was reported by [11, 123, 205] and used to produce highly oriented films. Obtaining the different

orientation in films on substrates with tensile or compressive stress was also reported by [124] for PZT 70/30 where preferably (111) orientated films were obtained on tensile and (100) orientated films on compressive substrates. The nucleation and orientation mechanism is dependent on many factors such as sol chemistry and thermal profile and thus the orientation on tensile substrate may differ. However, it is interesting to note that when the stress state was changed the orientation changed although all processing parameters were the same.

Tab. 3.13: Orientation of PZT 40/60 films deposited onto a tensile and compressive substrate.

Sample	(100)	(111)
Pt/Si, tensile	89%	8%
Pt/sapphire, compressive, film 15	54%	44%

The effect of the stress on the crystallographic orientation was showed on the example of PZT 40/60 films. The films deposited on compressive substrates showed much higher (111) orientation than the films deposited on tensile substrate. The effect of the substrate on the orientation is well known and was reported by several authors [11, 123-124, 206]. However, the direct influence of the stress on the orientation is not explained in this connection, possibly because the orientation selection of different PZT compositions on Pt(111) is not quite understood. Also, the sol chemistry seems to play an important role [207]. It is generally believed that Pt (111) promotes PZT(111) growth [135] and that the sol-gel crystallization involves a formation of an intermediate quasi-amorphous pyrochlore phase $Pb_2Ti_2O_{7-x}$ prior to perovskite transformation. Thus, the PZT nucleation seems complex and depends on both substrate and annealing profile [178-135].

There have mainly been two reported mechanisms on the nucleation of PZT on platinum. These include (1) the occurrence of intermetallic phases $Pt_{5-7}Ti$ [78] and Pt_3Pb [208] that act as an intermediate phase to improve the lattice match between PZT (111) and Pt (111) and (2) The use of seeding layers, like PbO, to support (100) nucleation [190] with an appropriate pyrolysis temperature [169]. The oxidation of Ti to TiO_2, stemming from the titanium adhesion layer, was reported but the results are less clear.

In some cases the TiO_2 supports (111) growth [209], in others it seems to promote (100) nucleation and growth [210-211].

In addition to the observed effect of long annealing time at pyrochlore formation temperature to promote (111) orientation there might be other effects to stabilize one certain nucleation mechanism. In the PZT 40/60 films where high (100) orientation was obtained under tensile stress, the (111) orientation was obtained if the substrate properties were different. There are two contributions to the stress in the film, one from the structural changes in the film itself and the other from the substrate expansion at the temperature. The substrate expansion will again affect the stress in the film. By introducing a new substrate the stress in the film was changed, and different orientation resulted. Due to the stress difference other stress compensation mechanisms can become active. Thus, it is quite possible that on the compressed substrates the Pt_3Pb phase was formed to minimize the lattice mismatch of PZT to Pt and so to promote (111) orientation. Another possibility for different orientation could be the changed kinetics of the Ti outdiffusion and platinum recrystallisation which in turn would have different effect on the PZT nucleation. However, the nucleation concerns only the first PZT layer and as it was shown in section 3.3 the orientation can change with thickness. Unfortunately the orientation of the films deposited on compressive substrate was not determined at different thicknesses and so it may be speculated if the (100) orientation increased with thickness in the films with compressive stress. The high degree of (111) orientation at 2 μm and 3.4 μm suggests a partial suppression of (100) growth. Thus it is possible that due to tensile strain during crystallization the lateral growth of (100) grains is supported while under compressive strain it can be suppressed in favour of the (111) crystallite growth.

3.4.6 Wafer size influence

When PZT was deposited onto larger wafers a higher stress was found in the PZT film. If a 2μm film was deposited on a 2” wafer the residual stress around 10 MPa was found. The deposition of the same sol under equal conditions but on a comparable 4” substrate resulted in the film having the 33 MPa residual stress. The orientation of these films together with another film deposited on a quarter of a 4” wafer (after cutting) substrate

(see film 2, Tab. 3.2 section 3.3.1) is summarized in Fig. 3.52 and Tab. 3.14. Some difference in the orientation of the films due to wafer size was noticeable.

All films were 2 µm thick PZT 40/60 films with 200 nm per single layer. The substrates were Pt(111)/Ti/SiO_2/Si with the same SiO_2 thickness for all films. Except for the wafer size, and thus the stress in the substrate, all the processing parameters were the same. The sample deposited on a quarter of a wafer had initially the same curvature as a 4”wafer.

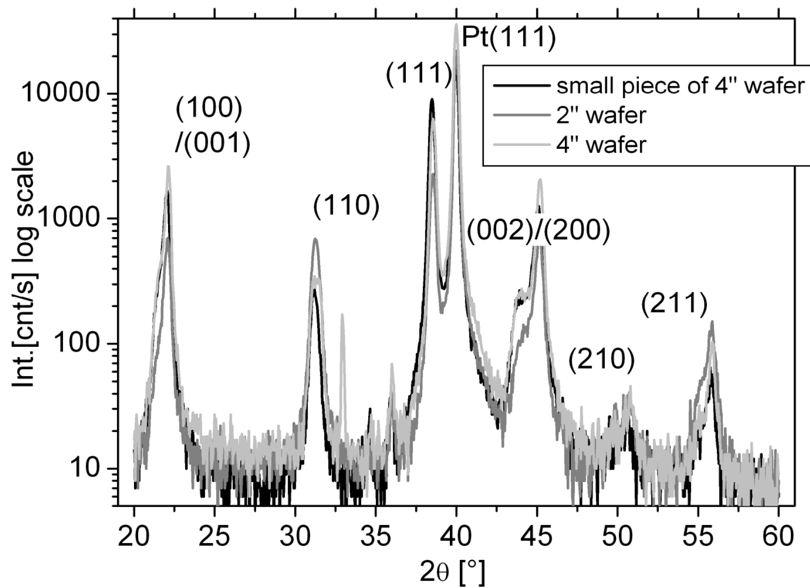

Fig. 3.52: Diffractograms of PZT 40/60 films deposited onto platinised silicon wafers of different size.

Tab. 3.14: Orientation (in percentage) of PZT 40/60 films processed under the same conditions but deposited onto different wafer size. All films were 2 µm thick.

	piece of 4” wafer (film 2)	4" wafer (film 18)	2” wafer (film 11)
(100)	20%	30%	21%
(111)	76%	60%	52%
(110)	3%	6%	26%

The influence of the wafer size on stress and eventually on the orientation leads to another restriction when reproducing the film orientation. The sample size, which influences the stress in the substrate, together with the initial curvature of the substrate, is another suggestion of stress influence on the nucleation and crystallization of the PZT film. From the considerations of e.g. length or width of the sample it can be derived that the thermal stress in the comparable substrates is the same. The length of the spin-coated PZT layer is equal to the length of the Pt/Si substrate at room temperature. For length of platinum d_{Pt} after recrystallization it was found that

$$d_{Pt,600}=d_{Si}+\alpha_{Si}\Delta T d_{Si}$$

at the crystallization temperature. α_{Si} is the TEC of silicon and ΔT is the temperature range between crystallization temperature and room temperature. At the room temperature the substrate shrinks and

$$d_{Pt,RT}=d_{Si}+\alpha_{Si}\Delta T d_{Si} - \alpha_{Pt}\Delta T d_{Pt,600}.$$

The length difference, or more precisely the thermal mismatch, between silicon and platinum creates the wafer bow. Thus the curvature of the wafer should be the same on the same substrate types regardless the wafer size, which is in contradiction to the experimental results. This indicates that there are other effects of the substrate bending on the stress and eventually on the orientation of the film. The anisotropic wafer bending of the silicon wafer is possibly different in wafers of different size as the ratio of the wafer diameter to the wafer thickness is different. Furthermore, the measurement was performed along one line across the wafer which might not be sufficient for stress analysis when comparing circular wafers of different sizes.

3.4.7 Stress controlled phase formation

The phase formation in PZT 52/48 in strain dictated as shown by [13]. Usually values around 50% in average of tetragonal to rhombohedral phase were found (section 3.3). In

the following example first a 1.1 μm thick PZT 52/48 film was deposited on one side of a double side polished wafer. This film is referred to as Side A film and was under tensile stress (films 22 and 23). After the film deposition was completed a 100/8 nm thick Pt/Ti bilayer was deposited on the back of the wafer followed by the PZT film deposition of 0.9 μm PZT 52/48 film. Thus the back of the wafer was under compression as the tensile stress from the Side A acted as compressive stress on the film from the Side B. The compressive stress in Side B was probably gradually reduced which in turn reduced the tensile stress on the Side A. The XRD patterns of the (200) and (111) peaks are displayed in Fig. 3.52. The XRD results of PZT 40/60 and PZT 60/40 films are included for comparison. In the film deposited under tension a broad peak at (111) and (200) positions can be seen, indicating a peak doublet and peak triplet, respectively. The rhombohedral and tetragonal phases are evident. In the film grown on a compressive substrate only one peak can be observed at the (111) peak position and two peaks at the (200) peak position. The lattice parameters and the phase content are summarized in Tab. 3.15. Both films had preferred (100) orientation. A degree of 75% was found in film on side A and 83% was found in film on Side B. The calculated lattice parameters clearly indicate a phase coexistence of the tetragonal phase with the c/a-ratio 1.02 and rhombohedral with lattice parameter a=0.4074nm. The tetragonal split is thus higher than the usually found ratio of 1.015 in PZT 52/48 but lower than in the pure tetragonal films. The c/a-ratio in tetragonal films is around 1.027. In contrast, the film on Side B showed only one (111) peak and thus no indication of phase co-existence. Nevertheless, two peaks were identified at the (200) peak position. These two peaks, if belonging to the tetragonal phase, would have too small c/a-ratio of around 1.006. The lattice parameter d=0.4077 shows good match to the rhombohedral phase. However, the lattice spacing of the other peak d=0.4052 does not match the tetragonal phase. Also, for a complete identification of the tetragonal phase another peak is missing. According to the phase-field simulations the stable phases in the PZT films under low strain, tensile or compressive, are the tetragonal, rhombohedral and orthorhombic phase. Except for the orthorhombic phase the film on Side A showed a phase mixture of the rhombohedral and tetragonal phase. On the Side B only the rhombohedral phase was found, and an unidentified peak. It can be speculated if this not identified peak belongs to the orthorhombic phase or the a-domain oriented tetragonal

phase. However, the results correlate to the phase-field simulations. The results are reported in [189].

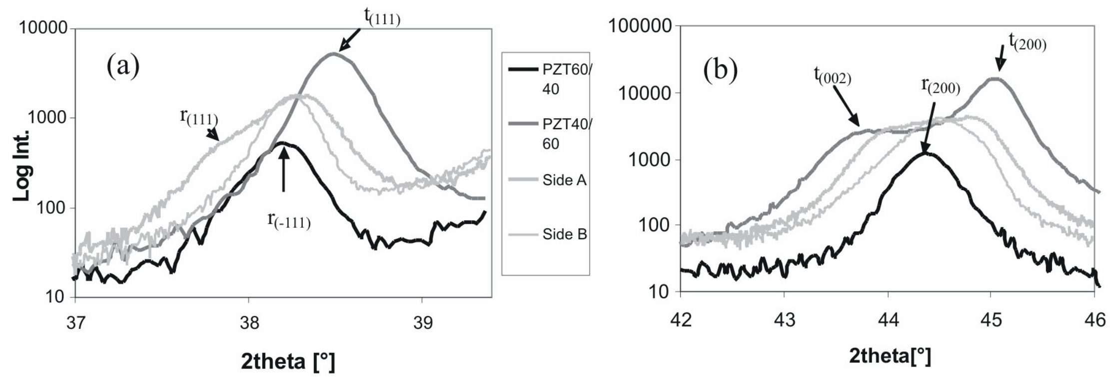

Fig. 3.53: Diffractograms of the films with change in phase content due to stress. The diffractograms of PZT 40/60 and PZT 60/40 films are included.

Tab. 3.15: Lattice parameter for PZT52/48 films on Side A and Side B.

	Lattice parameters		Phase content	
	Side A	Side B	Side A	Side B
(1-11)r	0.2364	0.2352	0.06	0.17
(111)t	0.2347		0.19	
(002)t	0.4117		0.26	
(200)r	0.4074	0.4077	0.38	0.73
(200)t	0.4036	0.4052	0.37	0.27

3.5 Microstructural characterization

3.5.1 Lattice parameter of PZT films with different compositions

The average lattice parameters of all PZT films from the sample batches PZT 40/60-Pt(111)/Si-3μm-10, PZT 60/40-Pt(111)/Si-3μm-6 and PZT 52/48-Pt(111)/Si-2μm-10 are summarized in Tab. 3.16. The tetragonal split was calculated for all PZT films containing the tetragonal phase and the relation of lattice parameter *c* to *a* was given as *c/a*-ratio. For the rhombohedral phase the lattice parameter *a* is given. The standard deviation was calculated for all sample batches. The tetragonal lattice parameter *c* increased with thickness in PZT 40/60 films. The tetragonal lattice parameter *a* was higher in the 3 μm thick films than in films with lower thickness. The *c/a*-ratio in films above 1 μm was in average 1.027 and corresponds to the *c/a*-ratio of the bulk PZT 40/60 composition [97, 213].

In rhombohedral PZT 60/40 films the lattice parameter *a* was slightly lower than reported values for the bulk ceramics of the same composition and was decreasing with thickness [213]. The tetragonal lattice parameter *a* and *c* in the PZT 52/48 films were both much smaller than those in pure tetragonal film. The smaller tetragonal unit cell is typical for PZT 52/48 films and c/a-ratio corresponds to the c/a-ratio of bulk ceramic reported by [21-214]. The lattice parameters of the rhombohedral phase were lower than the lattice parameters of the pure rhombohedral phase.

A factor that can influence the lattice parameter measurement is the intensity of the peaks (200)/(200) in the tetragonal phase and (200) of the rhombohedral phase. The intensity of such films is considered with low degree of (100) orientation and films with lower thickness, e.g. 1 μm thick films. The higher uncertainty in latter films reflects in the high standard deviation determined for 1 μm thick PZT 40/60 and PZT 60/40 films. In all films thicker than 1 μm the standard deviation was smaller, most likely due to higher degree of (100) orientation. The lattice parameters of the rhombohedral phase and tetragonal phase in PZT 52/48 quite similar and thus the diffracted intensities of all three peaks are very close to each other.

The measurement uncertainty from the step size 0.04° equals to $4x10^{-5}$ nm for all samples. The uncertainty of peak position after performed peak fit was different for all

films. The peak fit according to the program PEAKFIT™ was around or better than $r^2=0.99$. The lowest error $1.7x10^{-5}$nm was determined for rhombohedral lattice parameter in PZT 60/40 films and for the (200) lattice parameter in PZT 40/60 films. The lattice parameter (002) in PZT 40/60 had higher error around $1.7x10^{-4}$nm. The highest uncertainty was found in PZT 52/48 films. The error is estimated to be around 0.001 nm.

The variation of lattice parameters in the films was mostly due to strain. It is assumed that all films from the same batch in Tab. 3.16 had same initial state of stress as for all films similar substrates were used. However, as seen in the previous section, some residual strain or stress deviation due to different film orientation can be expected in samples from the same sample batch. Strain differences are possible between the films of different compositions. A strain related discussion will follow in next paragraph.

Tab. 3.16: Lattice parameter of PZT films deposited in Pt(111)/Si substrates.

	c [nm]	**standard deviation c**	**a [nm]**	**standard deviation a**	**c/a-ratio**	**standard deviation c/a**	**literature value [nm]**
PZT 40/60, 1 µm	**0.4111**	0.0026	**0.4017**	0.00015	**1.023**	0.0067	**c=0.4146 a=0.4036 c/a=1.027**
PZT 40/60, 2 µm	**0.4127**	0.00048	**0.4017**	0.00024	**1.027**	0.0013	
PZT 40/60, 3 µm	**0.413**	0.00049	**0.402**	0.00049	**1.027**	0.0007	
PZT 60/40, 1 µm			**0.4081**	0.000461			**0.409 [213]**
PZT 60/40, 2 µm			**0.4080**	0.000134			
PZT 60/40, 3 µm			**0.4076**	0.000109			
PZT 52/48, 2 µm tetragonal phase	**0.410**	0.0011	**0.404**	0.0013	**1.015**	0.0039	**c/a=1.014 [213]**
PZT 52/48, 2 µm rhombohedral phase			**0.405**	0.0025			**a=0.4064 [213, 215]**

The unit cell parameters were determined for all PZT films and samples in this work. Some of PZT 40/60 films on different substrates are summarized in Tab. 3.17. All PZT 40/60 films in Tab. 3 have different state of stress and stress results are given for some of the films. The diffracted intensity of (100) lattice planes was determined for all films from Tab.3.16 and 3.17 as

$$I_{rel,(100)} = \frac{I_{(100)}}{I_{(100)} + I_{(110)} + I_{(111)} + I_{(001)}} \quad (3.4)$$

The relationship between the *c/a*-ratio and the relative diffracted intensity of (100) lattice plains is depicted in Fig. 3.54. At lower (100) percentages and thus higher (111) diffracted intensity the tetragonal split was lower in the films. The PZT 40/60 films grown on compressive substrate and with predominant (111) orientation showed higher tetragonal split than the PZT 40/60 films deposited onto tensile substrate.

Tab. 3.17: Lattice parameters of PZT films deposited on various substrates.

		full sample name	**c [nm]**	**a [nm]**	**c/a-ratio**	**literature value [nm]**
film 11	10MPa	PZT 40/60 -Pt(111)/Si/2" - 2 µm film 11	**0.4082**	**0.4013**	**1.0170**	**c=0.4146**
film 14		PZT 40/60 Pt(200)/Si/3" - 2 µm film 14	**0.4123**	**0.4010**	**1.0284**	
film 15	-130MPa	PZT 40/60 Pt(111)/Al2O3/3" - 3.4 µm film 15	**0.4116**	**0.4015**	**1.0252**	**a=0.4036**
film 16		PZT 40/60 -Al2O3 - 1.2 µm film 16	**0.4120**	**0.4026**	**1.0234**	
film 17		PZT 40/60 Pt(111)/Si/Pt/2" - 2 µm film 17	**0.4074**	**0.4016**	**1.0145**	**c/a=1.027**
film 18	33MPa	PZT 40/60 -Pt(111)/Si/4" - 2 µm film 18	**0.4100**	**0.4011**	**1.0222**	
film 19		PZT 40/60 Pt(111)/SOI/4" - 2 µm film 19	**0.4099**	**0.4015**	**1.0207**	

The relationship between the relative intensities of (001) to (100) peaks and the *c/a*-ratio was analysed. The results are given in Fig. 3.55. The majority of PZT 40/60 films had the fraction of *c* domains around 30% or 0.3, hence the most of the results are accumulated in the (001)/(100) ratio range between 0.1 and 0.4. The films of the (001)/(100) ratio above 0.6 were deposited on compressive substrates. A trend between the predominantly (100) oriented PZT 40/60 films and the c/a-ratio could be observed. At low (001)/(100) ratios the *c/a*-ratio matches the values of PZT 40/60 films around 1.027. With increasing fraction of (001) domains the tetragonal split becomes lower. The films within the black circle in Fig. 3.55 had predominant (111) orientation and the

results showed different relationship to the *c/a*-ratio. It is assumed that there must be a different relationship between *c/a*-ratio and fraction of (100) domains in such films. However, due to low number of (111) oriented films no conclusions can be made between (111) oriented films and the *c/a*-ratio and more work is needed.

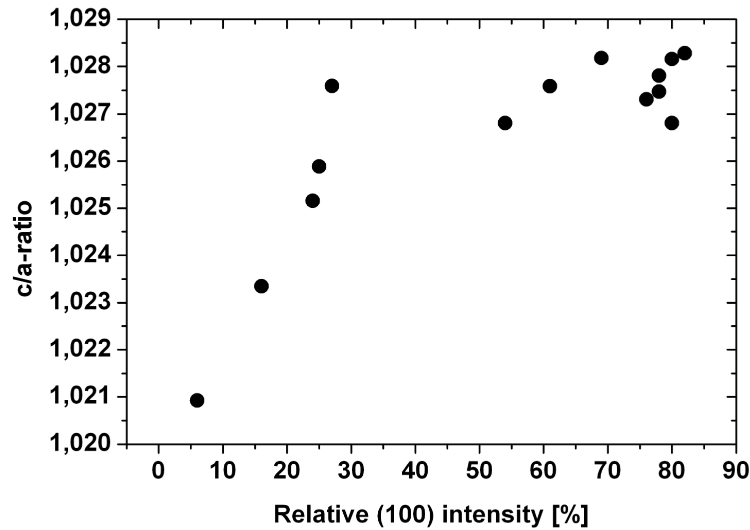

Fig. 3.54: *c/a*-ratio in PZT 40/60 films with increasing (100) relative intensity.

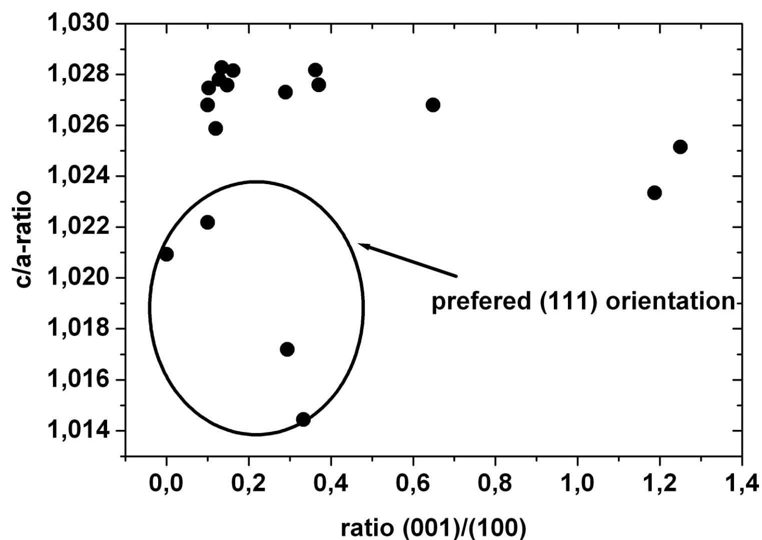

Fig. 3.55: c/a-ratio in PZT 40/60 films with the relative fraction of (001) to (100) domains.

As seen in the previous section the strain in the PZT films is mostly due to difference in thermal expansion between the film and the substrate. Taking the anisotropic expansion of PZT into account, the following model can be established, Fig. 3.56. According to the results from previous section, the thermal contraction of a PZT film of the mixed (100) and (001) orientation is depicted schematically in Fig. 3.56.

The (100) oriented crystallites or a-domains, in respect to the XRD measurement direction, a thermal expansion in-plane during cooling can be observed. In (001) oriented crystallites or c-domains a thermal in-plane contraction can be observed during cooling. According to the anisotropic TECs determined by Cook et al, the thermal expansion is larger than thermal contraction. Thus, the fraction of (001) to (100) oriented crystallites dictates the total thermal strain. In respect to the substrate contraction during cooling either total tensile or compressive strain occurs in the film below the transition temperature. With superimposed e.g. compressive stress the crystallites are under in-plane pressure, and if total stress is tensile than crystallites are in-plane elongated. However, in the XRD measurement the out-of-plane direction is considered. The relationship between the in-plane strain to the out-of-plane strain is related through the compliance tensor and for this specific case it is the compliance s_{13} that relates the in-plane strain to the out-of plane stress $\sigma_3=\varepsilon_1 s_{13}$. The s_{13} for tetragonal PZT is $s_{13}=-4.98 \times 10^{-12}$ Pa^{-1} and for rhombohedral PZT $s_{13}=-0.93 \times 10^{-12}$ Pa^{-1} [216]. On the sign of s_{13} for both, tetragonal and rhombohedral structure can be seen that tensile in-plane strain induces compressive out-of-plane stress. Thus, in PZT films with tensile in-plane strain the lattice parameters *c* and *a* will be smaller and in PZT films with compressive in-plane strain the lattice parameters will become greater. The in-plane strain affects both lattice parameters *a* and *c* equally as the film is free to expand or contract into the out-of-plane direction. Thus, the *c/a*-ratio is a good indication for in-plane stress.

With the derived relationship between the thermal strain and fraction of (100) orientation in the film, and earlier derived relationship of strain in (111) films, the *c/a*-ratio dependence on the fraction of (100) films can be explained, Fig. 3.54. The larger the fraction of *a*-domains in tetragonal films the higher is the in-plane compression. The in-plane compression will result in the out-of-plane displacement and thus increase the out-of-plane lattice spacing. The smaller the fraction of (100) the larger the tensile strain

between the substrate and the film resulting in out-of-plane displacement and thus a decrease of lattice spacing. With increasing content of (001) oriented crystallites the compressive strain is reduced and the out-of-plane is less in tension or can even become compressive, resulting in lower *c/a*-ratio.

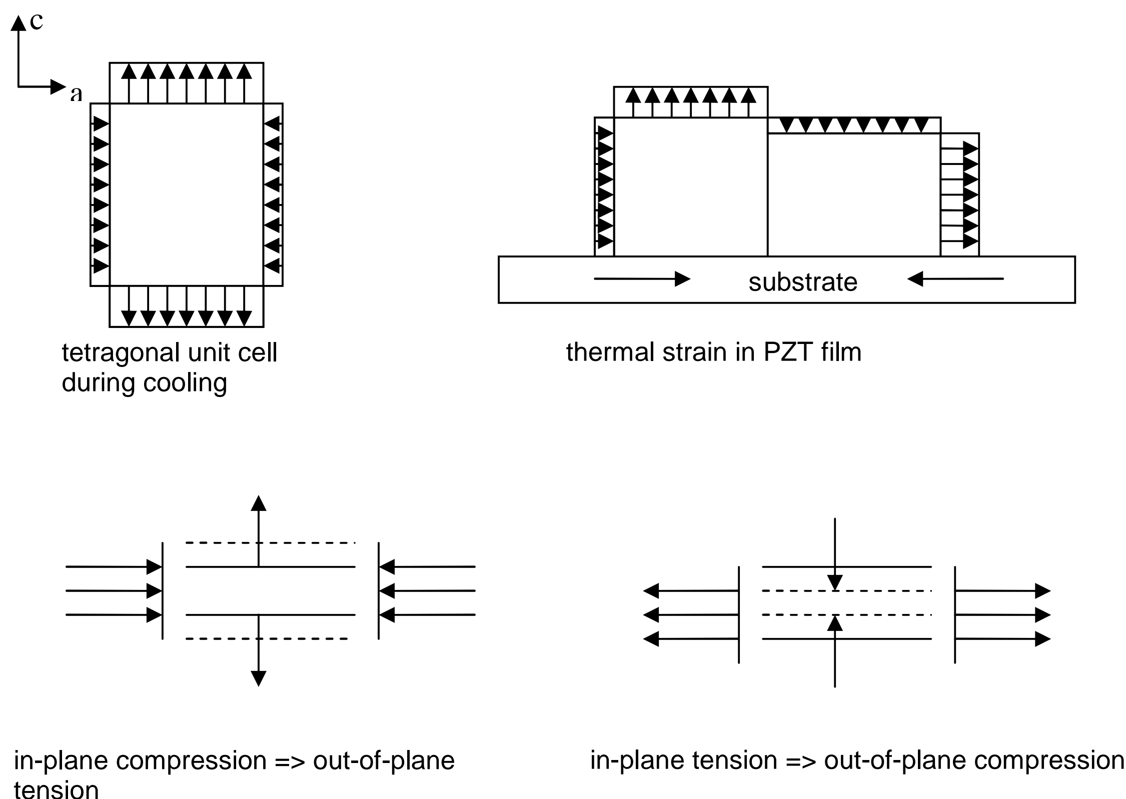

Fig. 3.56: Thermal expansion or contraction in PZT films due to thermal expansion mismatch between PZT film and substrate and the effect of in-plane strain on the lattice spacing.

The *c/a*-ratio of the tetragonal phase and lattice parameter *a* of the rhombohedral phase in PZT 52/48 films deposited on different substrates are summarized in Tab. 3.18. A strong variation of tetragonal lattice parameters on different substrates was found. The *c/a*-ratios of all PZT 52/48 films from Tab. 3.16 and Tab. 3.18 deposited on platinised substrates with the phase content of the (100) oriented rhombohedral phase is depicted in Fig. 3.57. The relative intensity of the rhombohedral phase (100) was calculated as

$$I_{rel,(100)R} = \frac{I_{(100)R}}{I_{(100)T} + I_{(110)} + I_{(111)T} + I_{(111)R} + I_{(001)T} + I_{(100)R}}. \qquad (3.5)$$

The indices T and R refer to the detracted intensity of tetragonal and rhombohedral phase respectively. The intensity of (110) peaks was determined as total intensity regardless of the phase as this intensity was usually below 5 % for most of the films deposited on Pt/Si substrates.

The *c/a*-ratios in the PZT 52/48 showed large scattering and thus the results showed no clear dependence with the relative intensity fraction of tetragonal (100) or (001) oriented domains. The large scattering of the results is partly due to lower resolution of (100) peak group in PZT 52/48 film as mentioned earlier. The *c/a*-ratio trend with total (100) diffracted intensity from peaks $(100)_t$, $(001)_t$ and $(100)_r$ showed similar behaviour in Fig. 3.57. In PZT 52/48 films with very low degree of (100) orientation large tetragonal split was found. The *c/a*-ratios were well above the observed average *c/a*-parameters in PZT 52/48. As the degree of (100) orientated crystallites increased, the tetragonal split was decreasing and *c/a*-ratio in these films was closer to the average *c/a*-ratio around 1.015. In films with predominant (100) orientation ($(100)_r$ above 0.5) the tetragonal split was lower. The results were fitted with parabolic law. Due to large uncertainty in the determination of lattice parameter in PZT 52/48 films it is possible that also a reversed power function could be fitted and thus more accurate experimental results are needed. More accurate results could be obtained if the step size was reduced and time per step was increased.

The lattice parameter *a* of the rhombohedral phase versus the relative intensity of (100) oriented rhombohedral phase is displayed in Fig. 3.58. However, in connection with the results in Fig. 3.58 it can be observed that as the tetragonal lattice parameters increase the rhombohedral lattice parameter *a* decreases, in dependence of the relative rhombohedral (100) diffracted intensity. The lattice parameter *a* of the rhobohedral phase shows smaller scattering around the average value than the lattice parameters of the tetragonal phase. In the range of the rhombohedral (100) between 20 and 40% there seems to be equilibrium strain state where the c/a-ratio is around its average values and also the rhombohedral lattice parameter a is closer to its reported values. Due to low

number of rhombohedral PZT 60/40 samples no further analysis of lattice parameters was possible in these films.

Tab. 3.18: Lattice parameters determined for PZT 52/48 films deposited on different substrates.

stress	full sample name	tetragonal phase			rhombohedral	literature value [nm]
		c [nm]	a [nm]	c/a-ratio	a [nm]	
60 MPa	PZT 52/48-PbO/Pt(111)/Si/3"- 3 µm-film 14	0.4117	0.4035	1.0203	0.4032	
	PZT 52/48-LNO/Si- 2.4 µm-film 15	0.4115	0.4067	1.0190	0.4038	
	PZT 52/48-LNO/Si- 2 µm-film 16	0.4114	0.4004	1.0275	0.4058	
	PZT 52/48-LNO/Si- 2 µm-film 17	0.4102	0.4045	1.0139	0.4076	
	PZT 52/48-LNO/Si- 2 µm-film 18	0.4099	0.4033	1.0164	0.4066	
19 MPa	PZT 52/48-Pt(200)/Si/3"- 2 µm-film 19	0.4094	0.4041	1.0131	0.4077	
	PZT 52/48-Pt(111)/Al_2O_3/3"- 1.1 µm-film 20	0.4121	0.4043	1.01928	0.4088	**c/a=1.014 [213]**
17 MPa	PZT 52/48-Pt(111)/Si/2"- 3 µm-film 24	0.4111	0.4055	1.0140	0.4076	**a=0.4064 [215]**

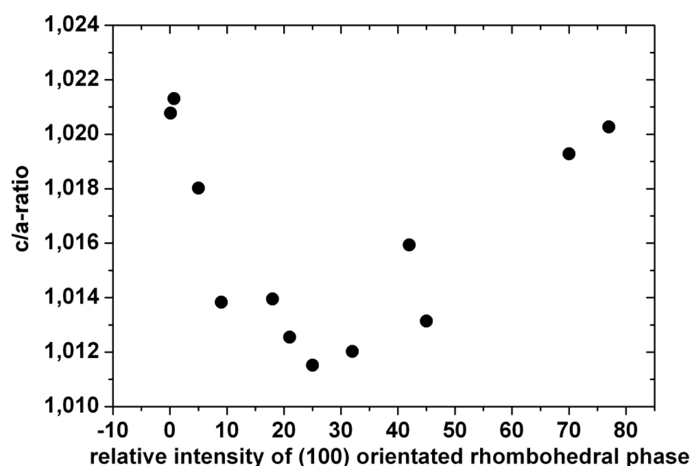

Fig. 3.57: Relationship between the tetragonal c/a-ratio and rhombohedral phase content in (100) orientation.

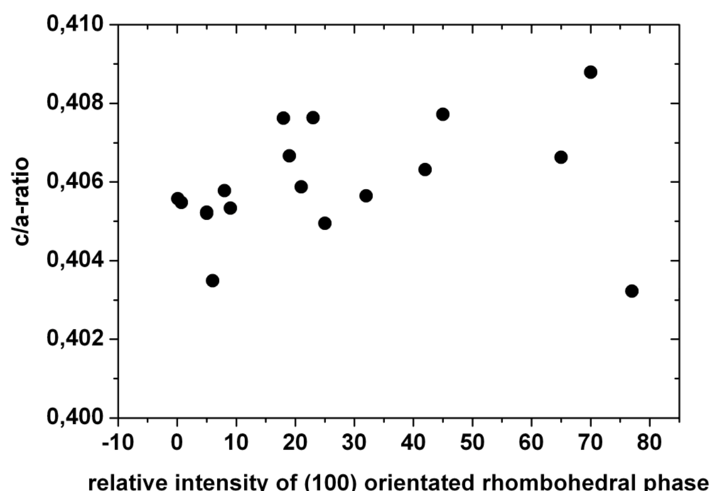

Fig. 3.58: Relationship between the rhombohedral lattice parameter *a* and rhombohedral phase content in (100) orientation.

In PZT 52/48 films the relationship seems to be more complex. According to the phase-field calculations at first the tetragonal phase is formed and at lower temperatures the formation of rhombohedral phase occurs. The (100) oriented paraelectric crystallites can transform into (100) and (001) tetragonal crystallites or into rhombohedral (100) crystallites. Thus, there are more variables in strain development than in pure tetragonal phase. The values of *c/a*-ratio and rhombohedral lattice parameter *a* close to the literature values were observed in the range between 20% and 40% (100) oriented rhombohedral phase. However, a more detailed analysis in the PZT 52/48 films is needed and is a subject of further work.

3.5.2 Crystallite size of PZT films with different compositions

In the following section the analysis of the microstructure of the PZT films with different compositions will be introduced. Some of the cross section images were captured using the back scattered electron detection mode (BSE). In all images PZT films on Pt(111)/Si substrates are depicted, and it will be pointed out if other substrate was used.

The crystallite size of PZT films of all compositions coated on Pt(111) and Pt(200) are summarized in Tab. 3.19. The grain size was determined using the

Williamson-Hall plot and Scherrer equation. An example of best obtainable Williamson-Hall plot is depicted in Fig. 3.59.

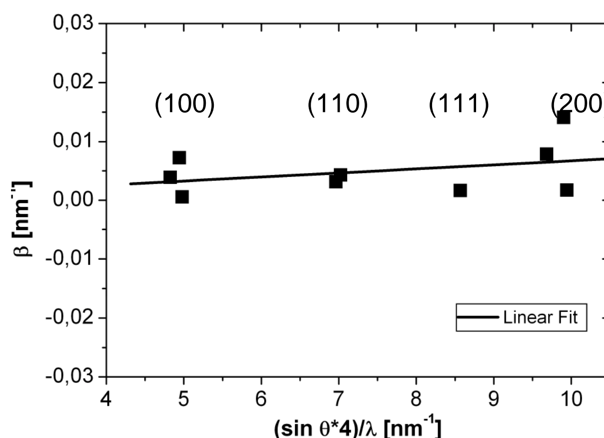

Fig. 3.59: Williamson-Hall Plot for a PZT 52/48 film.

However, in all films crystallites of two different sizes were observed e.g. one small grain size around 50 nm and large grain sizes above 200 nm. Besides, in predominately (111) oriented films there was not a sufficient number of peaks for linear regression. Thus the results obtained with the Williamson-Hall plot were not accurate and the Scherrer formula was applied. The results obtained with the Scherrer formula do not consider strain in the crystallites and, dependent on the strain, it can happen that the crystallite sizes determined on (001) and (002) lattice planes do not match although the diffracted intensity stems from the same crystallites. This phenomenon is due to the fact that at lower 2θ-angles in the XRD the peak broadening is mostly due to the crystallite size. With increasing 2θ-angles the strain contributes stronger to the peak broadening. Furthermore, the penetration length of the incident beam differs at different 2θ-angles and thus the peak broadening can appear larger for (200) than for (100) as the same crystallites are detected under a different angle. The Williamson-Hall plot is thus more appropriate for such analysis but could not be performed with satisfactory results as the films were strongly textured and had distribution of grain size.

The crystallite size was determined for all films from sample batches PZT 40/60-Pt(111)/Si-3µm-10, PZT 60/40-Pt(111)/Si-3µm-6 and PZT 52/48-Pt(111)/Si-2µm-10 and the average results are summarized in Tab. 3.19 for all compositions. In

addition, the crystallite size of PZT films of all compositions deposited on Pt(200)/Si is given.

In the films on Pt(111) substrates large difference between the crystallite size with (200) orientation and crystallite sizes of other orientations was found for all PZT films. The crystallite size of (200) showed also much larger spread than all other crystallites. The crystallite size of (200) of PZT 40/60 correlates roughly to the single layer thickness in these films indicating that the (200) oriented crystallites grow through the thickness of the coating whereas crystallites of other orientation are much smaller. This result correlates to the previously mentioned faster grain of (100) oriented lattice planes compared to crystallites of other orientation. The crystallite size of (200) or (100) oriented crystallizes of the compositions PZT 52/48 and PZT 60/40 is somewhat smaller than of PZT 40/60 composition, it, however, showed largest crystallize size among all crystallites of different orientations.

Tab. 3.19: Crystallite size in all PZT compositions on Pt(111)/Si and Pt(200)/Si.

PZT on Pt(111)/Si	grain size in [nm] of the crystallites with the (hkl) orientation							
	$(001)_T$	**$(100)_R$**	**$(100)_T$**	**$(1\text{-}11)_R$**	**$(111)_T$**	**$(002)_T$**	**$(200)_R$**	**$(200)_T$**
PZT 40/60	33±6		25±2		93±10	11±2		210±84
PZT 52/48				49±10	95±19	81±42	138± 132	109±86
PZT 60/40		130±18		89±32			31±3	
PZT on Pt(200)/Si	grain size in [nm] of the crystallites with the (hkl) orientation							
	$(001)_T$	**$(100)_R$**	**$(100)_T$**	**$(1\text{-}11)_R$**	**$(111)_T$**	**$(002)_T$**	**$(200)_R$**	**$(200)_T$**
PZT 40/60	30		100			20		330
PZT 52/48						16	40	102
PZT 60/40		109		49			45	

In PZT 40/60 films the crystallite size of (001) or (002) oriented crystallise was much smaller than in PZT 52/48 films. There is probably some crystallite size dependent phase transition. Also, all (002) peaks in the PZT 40/60 films had very strong peak broadening, Fig. 3.60, and a good peak fit was obtained only when a Pearson function

was applied. This function can be applied to non-symmetric peaks and peaks with very broad tail. Such peak shape was found for all (002) peaks in PZT 40/60 films deposited on platinum substrate. The non-symmetry and strong broadening is an indication of large defect density due to dislocations and mechanical twinning [153]. Thus, the small crystallite size is possibly an indication of domain formation as domains are equivalent to mechanical twinning in crystals.

The crystallite size in PZT 40/60 film deposited on Pt(200)/Si substrate shows similar crystallite size distribution as PZT 40/60 films deposited on Pt(111)/Si. PZT 52/48 showed also much larger crystallite size of the tetragonal (200) oriented crystallites. The tetragonal (002) and rhombohedral (200) oriented crystallites showed more similar crystallite size to the substrate. The crystallite size of (200) oriented crystallites in PZT 60/40 film on Pt(200) substrate showed much better correlation to the crystallite size of the substrate.

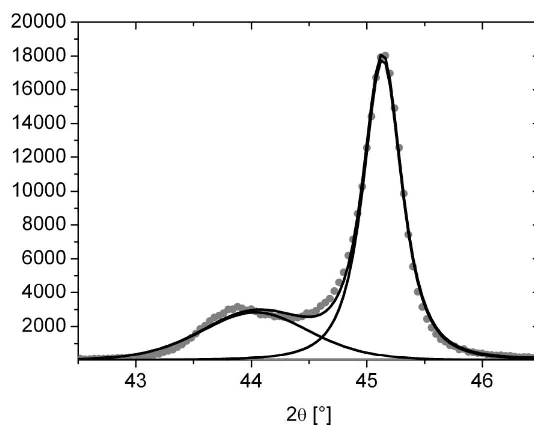

Fig. 3.60: Peak broadening found in PZT 40/60 films on (002)/(200) peak doublet indicating very small crystallite size.

The grain size of PZT films deposited on different substrates is summarized in Tab. 3.20. Both PZT compositions, PZT 40/60 and PZT 52/48 showed smaller grain size on different substrates.

Tab. 3.20: Crystallize size of PZT films deposited on various substrate.

PZT sample	grain size in [nm] of the crystallites with the (hkl) orientation						
	$(001)_T$	**$(100)_T$**	**$(1\text{-}11)_R$**	**$(111)_T$**	**$(002)_T$**	**$(200)_R$**	**$(200)_T$**
PZT 52/48 on LNO/Si	35±12	46±13	53	19	21±8	57±34	35±8
PZT 52/48-PbO/Pt/Si-3µm -film 14	49				18	20	
PZT 52/48-Pt/Si2“-3µm-film 24	165	92	75	95	26	35	20
PZT 52/48-Pt/Al_2O_3-1.1µm-film 20	43	48	41	51	22	53	34
PZT 40/60-Pt/Si/4“-2µm-film18	36			81	22		110
PZT 40/60-Pt/SOI/4“-2µm-film 19	20	58		64	17		50
PZT 40/60-Pt/Si/2“-2µm-film17	22	85		72	46		55
PZT 40/60-Pt/Si/2“-2µm-film 11	20	20		43	16		17
PZT 40/60-Pt/ Al_2O_3/3“-3.4µm-film15	20	94		90	25		90

3.5.3 Morphology of PZT film

The typical surface and cross section of a tetragonal film is depicted in Fig. 3.61. Two different films are depicted. The surface image was captured in the BSE mode. The brightness contrast was increased and thus the areas with lower density appear dark. The grain shape of PZT 40/60 films had a square-like shape which is typical for the grain growth of the cubic or tetragonal crystals. It could be distinguished between 2 grain sizes in all PZT 40/60 films. As can be observed in Fig. 3.61 there are few grains with grain size between 500 and 800 nm but the majority of the grains was much smaller.

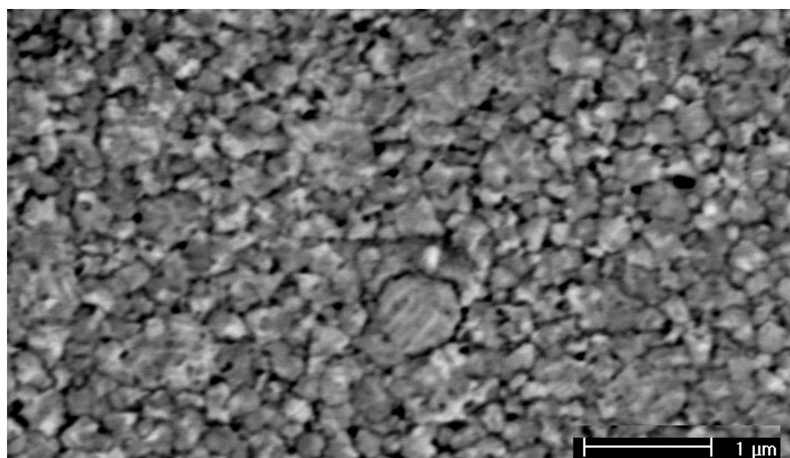

Fig. 3.61: Surface of a PZT 40/60 film The brighter areas within individual crystallites were related to domain in the topographic mode and will be discussed at later point.

The maximum calculated grain size in PZT 40/60 on Pt(111) was around 200 nm attributed to crystallites with (200) orientation. The crystallites of other orientation such as (001) and (111) were much smaller. As the crystallites with (100) or (200) orientation grow much faster than crystallites with other orientation it can be assumed that the large crystallites are (100) oriented crystallites due to their lateral growth once the (100) crystallites consumed the complete amorphous matrix through thickness. Thus the large grains in Fig. 3.61 can be attributed to (200) crystallites.

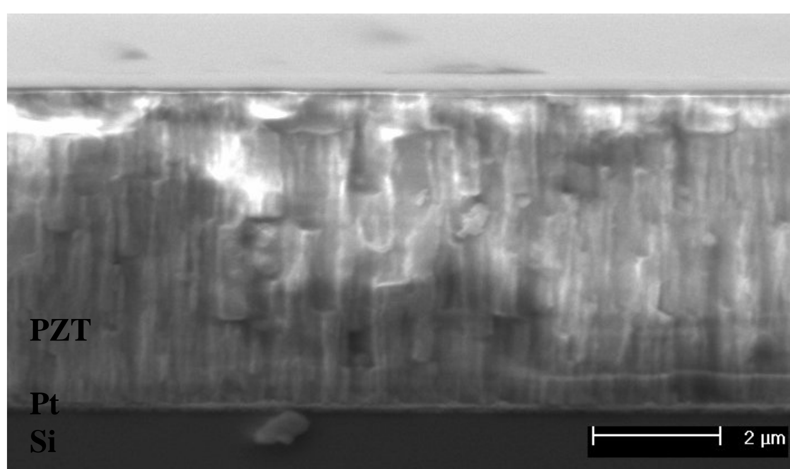

Fig. 3.62: Typical fracture section of PZT 40/60 films

The cross section image shows columnar structure which was typical for PZT 40/60 films, Fig. 3.62. The average grain size of the columns was between 100 and 200 nm. Also, some large grains were observed that probably correspond to (100). Some charging of the film was inevitable.

The typical surface morphology of the PZT 60/40 films is depicted in Fig. 3.63. The morphology of PZT 60/40 films was much different compared to that of PZT 40/60 films. The rhombohedral PZT was found to be a rather unusual grain shape consisting of highly curved and interlocked grain boundaries. Thus it was difficult to estimate the grain size for such grain morphology. It was mentioned in previous section that PZT 60/40 films were very mainly (111) oriented and its orientation was found to correspond better to the platinum orientation than in PZT 40/60 films. Thus such grain structure could be a result of the grain growth on platinum. In Fig. 3.64 the surface of platinum after recrystallisation is compared to the surface image of PZT 60/40. The large dark areas were related to residual pyrochlore or lead deficient and zirconium rich areas in the surface of zirconium rich films as reported by Reaney et al [217]. These areas could not be crystallized. Etching of PZT films revealed similar residual features on platinum surface as shown by Spierings et al [117, 174] after etching the PZT that crystallized with the rosette structure, Fig, 3.65. However, this residual phase was not detected with the XRD.

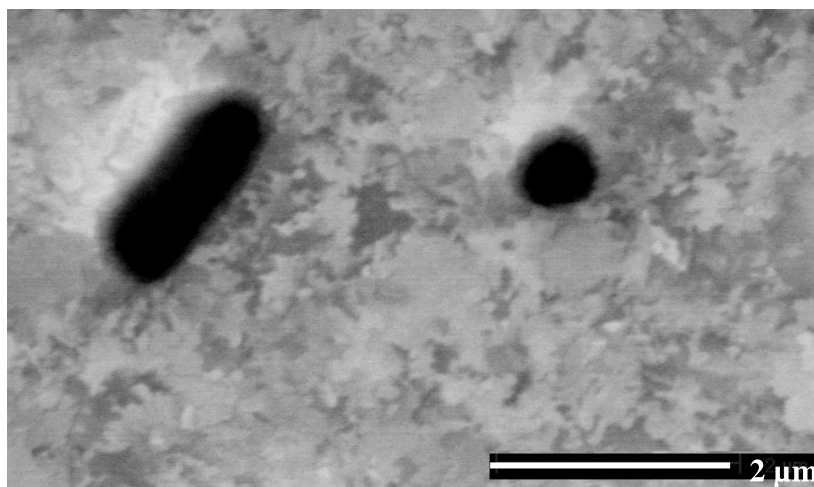

Fig. 3.63: Typical surface morphology of PZT 60/40 films, BSE contrast.

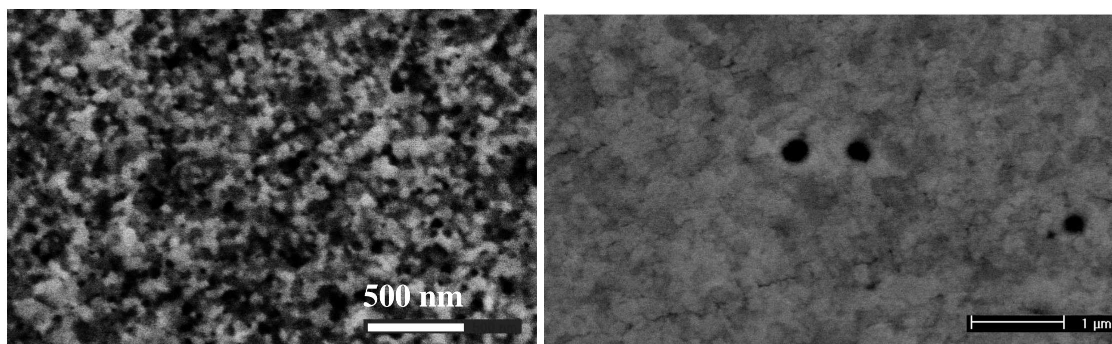

Fig. 3.64: Surface images of recrystallised platinum (left) and PZT 60/40 film (right). Both images are captured in BSE contrast.

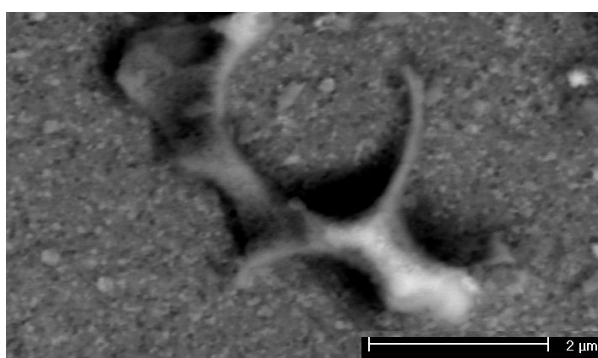

Fig. 3.65: Residual not crystallized phase of PZT 60/40 films on platinum surface after etching away the PZT film.

The fracture cross section of PZT 60/40 films was also less regular than e.g. in tetragonal films and in some grains a fracture along inclined boundaries occurred, Fig. 3.66 and 3.67. No columnar grain growth was found in PZT 60/40 films. The PZT 60/40 film in Fig. 3.66 was etched before examination. The smaller picture is an enlargement of a smaller area marked with the black square. In this enlarged picture the individual coatings can be observed with the single layer thickness around 200 nm. Much smaller grains within these layers can be distinguished which correlate in size to the grain size results determined with the Scherrer Eq.(2.3) The image of in Fig. 3.67 was taken using the BSE mode and reveals the structure of the film. The same area of the sample was imaged in the SE mode, Fig. 3.68, showing that the dark areas in the Fig. 3.67 are not pores. Some inclined fracture surfaces which are usually not observed using the secondary electron detector.

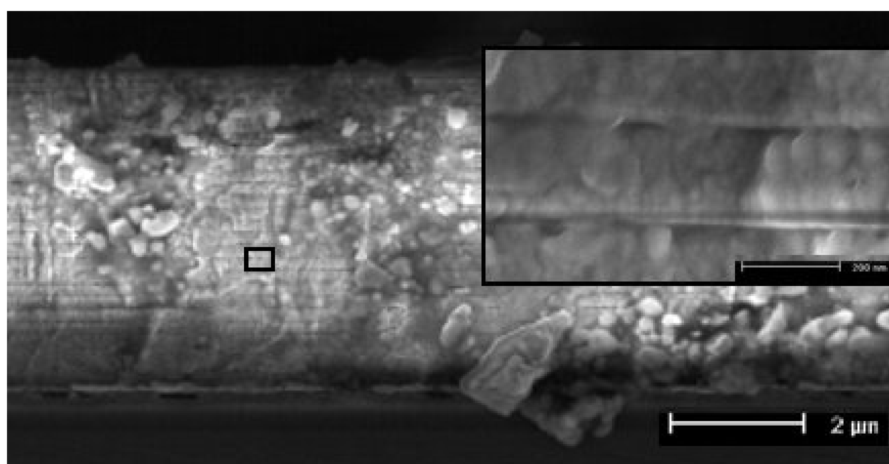

Fig. 3.66: Fracture section of PZT 60/40 film, etched with HF before examination.

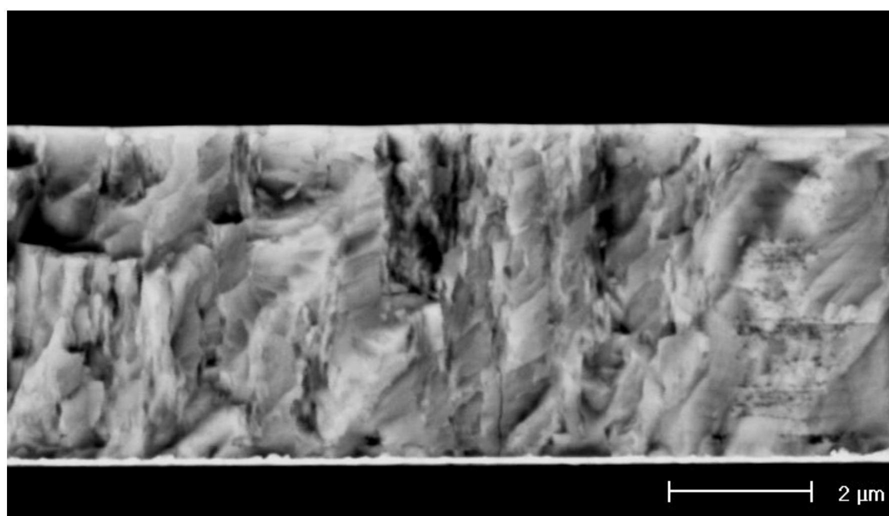

Fig. 3.67: Fracture section of a PZT 60/40 film viewed with BSE contrast.

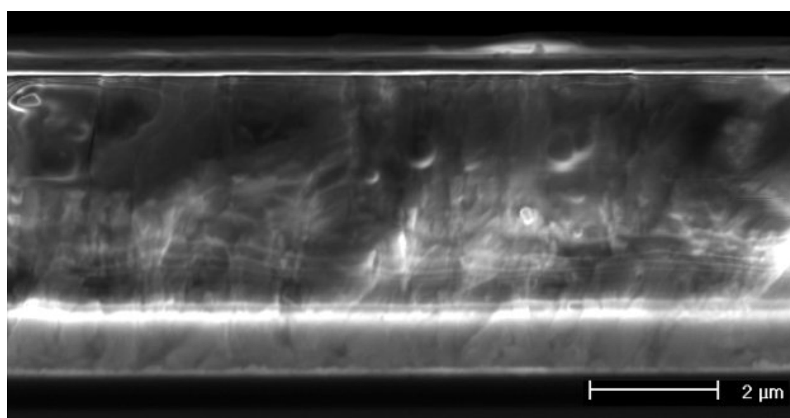

Fig. 3.68: Same sample area as Fig. 3.67 viewed with SE contrast.

In PZT 52/48 the different microstructure was observed if the film was grown on compressive stress rather than tensile stress, Fig. 3.69 and 3.70. These two films were deposited on the same double side polished wafer. The film deposited under tensile stress was referred to the Side A film and the film on the back of wafer was deposited under compressive stress and was referred to as side B film. The details of the film processing, stress and phase formation were discussed in section 3.4. In Fig. 3.69 the image contrast was inverted to reveal better the grain boundaries and the structure of the film. The dark areas that look like pore were actually charged particles on the surface of PZT and appeared white in the original image. The microstructure of PZT 52/48 grown under tensile stress, Fig. 3.69, consisted mostly of square-like grains with sharp grain boundaries that were attributed earlier to the tetragonal phase. The fraction of tetragonal phase in this film was 80%. The amount of (100) orientation was around 84%. Some smaller grains with grain boundaries similar to those from Fig. 3.63 were found in the film and were contributed to the rhombohedral phase, within the white border. It cannot be said for sure if within the white border only rhombohedral phase was existent and if all other grains were belonging entirely to the tetragonal phase. The high fraction of the tetragonal phase supports this hypothesis but it would be rather unusual if the phase distribution would be localized.

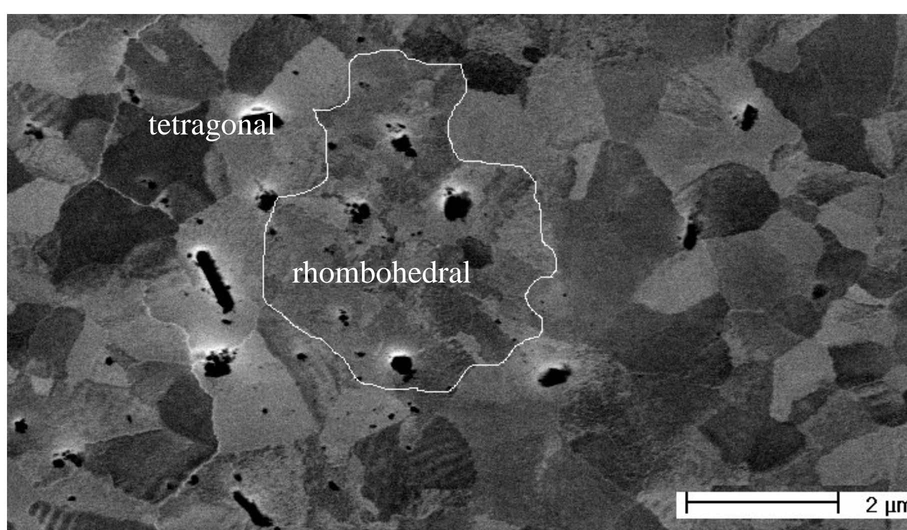

Fig. 3.69: Surface morphology of PZT 52/48 grown under tensile stress.

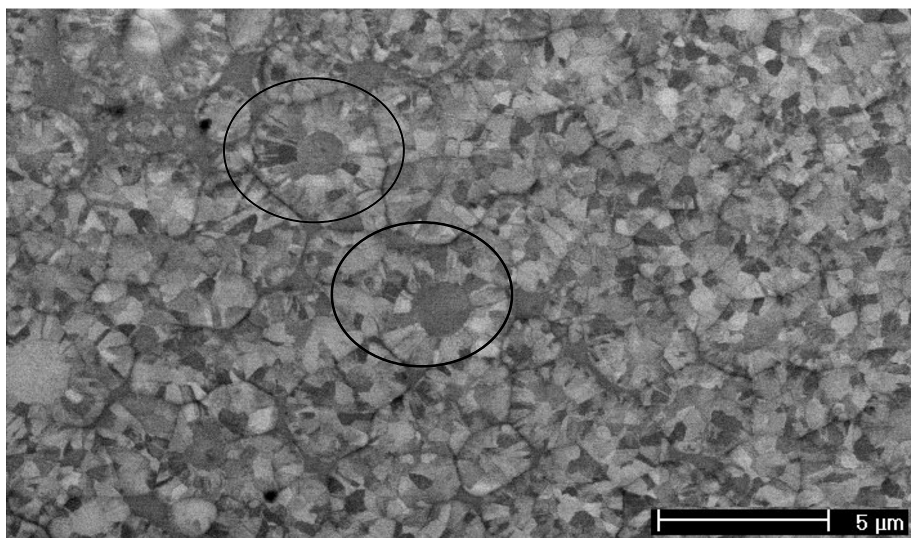

Fig. 3.70: Surface image of a PZT 52/48 film deposited onto compressed substrate.

In the PZT 52/48 film grown under compressive stress, Fig. 3.70, very large grains with diameter of several microns were observed within which much smaller dark and bright areas were formed. Four different shades of grey can be distinguished and two variations of such large grains were found, the ones that looked as if they had a circular nucleus around which the areas of different contrast was radially formed, and such which did not have such nucleus. The circular grains were reminiscent of the rosette structure where the centre of a rosette was not fully crystallized [218]. The morphology of PZT 52/48 films showed high sensitivity to stress in the film, and different grain growth can be observed in PZT 52/48 films with different stress. This is in agreement with the observations of stress influenced nucleation and crystal growth from the previous section.

The fracture section of PZT 52/48 films showed largest variations. Depending on the phase content the columnar grain structure similar to PZT 40/60 films can be found, Fig. 3.71, or such grain structure more similar to PZT 60/40s where individual grains cannot be distinguished, Fig. 3.72.

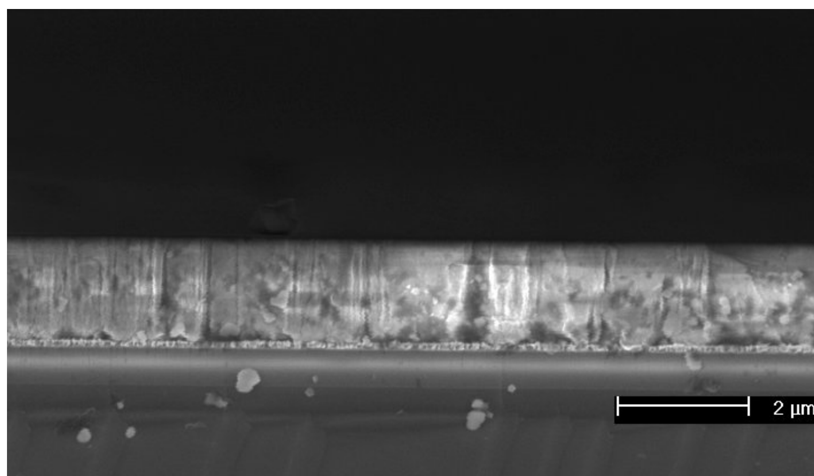

Fig. 3.71: Fracture section of PZT 52/48 film grown under tensile stress.

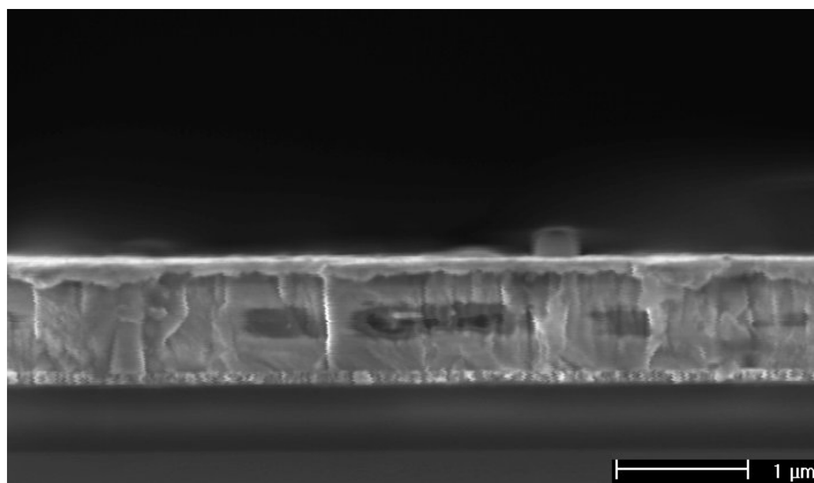

Fig. 3.72: Fracture section of PZT 52/48 film grown under compressive stress.

3.6 Electrical properties of PZT films

3.6.1 Introduction to the Section

This section outlines the electric properties of the films. The piezoelectric coefficients, the dielectric constant and the ferroelectric properties were determined. Some experiments were conducted in the way that the extrinsic and intrinsic contribution to the dielectric constant and piezoelectric coefficients can be separated. The intrinsic contribution originates from the response of the single domains and is thus related to the film orientation. The extrinsic contribution has different origins which will be discussed for each sample set. Such separated analysis can provide important information about the influence of the grain size, preferred orientation, the film thickness, and the mechanical boundary conditions on the intrinsic responses, the domain structures, and domain wall motion in these films. The microstructure of the films was introduced and related to the electric properties and domain formation in the films. The poling conditions for thick films were investigated.

3.6.2 Dielectric properties

The dielectric constant was measured for all films from the sample batches PZT 40/60-Pt(111)Si-3µm-10, PZT 52/48-Pt(111)Si-2µm-10 and PZT 60/40-Pt(111)Si-6 on which the orientation of the PZT films with different composition on Pt(111)/Si was studied. The film orientation with more detailed analysis is given in Section 3.2. The average dielectric constant was given for all PZT films with different composition in Tab. 3.21. The dielectric constant was measured at 1 kHz.

Tab. 3.21: Dielectric constant of PZT films deposited on Pt(111)/Si and Pt(200)/Si.

Pt(111)/Si	**PZT 60/40**	**PZT 52/48**	**PZT 40/60**
thickness	3 µm	2 µm	3 µm
ε	860 ± 150	1025 ± 25	540 ± 20
tan δ	below 0.04	below 0.02	below 0.02

The highest dielectric constant on Pt(111) was found in PZT 52/48 films, followed by PZT 60/40 and PZT 40/60 films. This is not surprising as the PZT 52/48 comprises the rhombohedral and the tetragonal phase and has thus 14 equivalent polarization directions. The rhombohedral phase has 8 equivalent polarization directions and the tetragonal phase has 6 equivalent polarization directions. According to the calculations of Du et al [19], the maximum obtainable intrinsic dielectric constant in tetragonal films is 499 in the direction perpendicular to the polarization and thus for in-plane oriented *a* domains. In the rhombohedral compositions slightly higher dielectric constant can be expected than in tetragonal film, around 530, also for the direction perpendicular to the polarization direction. Thus all dielectric constants exhibit values higher than the intrinsic dielectric constant indicating some contribution from the domain wall movements [219]. The domain wall movements in PZT films that contribute to the dielectric constant are 180° domain wall oscillations. Non-180° domain wall movements in PZT films with thickness below 5 µm are usually not mobile due to substrate clamping as observed by Xu et al [17]. To determine the fraction of extrinsic contribution the films were poled and the dielectric measurement was repeated after poling. The dielectric constant for PZT 40/60 films is depicted in Fig. 3.73 before and after poling.

The dielectric constant was lower in PZT 40/60 films after poling. The decrease was an average 15% and is consistent with the values reported by Xu et al [17]. It was observed that the dielectric constant after poling had values below 500 which reflect the intrinsic dielectric constant of predominantly (100) oriented films. The dielectric loss tan δ, a parameter indicating the difference of phase angle to 90° between the current and voltage of an ideal capacitor, decreased in the PZT 40/60 films after poling, Fig. 3.73, indicating lower loss in films when the polarization is more uniform polarization.

During poling the 180° domains are easy to switch so that the contribution of 180° domain wall movements can be removed. The switching of non-180° domains during poling in films of such thickness is less likely to occur due to substrate clamping. The switching of the 90° domains in tetragonal films can be evidenced if XRD measurement was performed on the (002)/(200) peak doublet before and after poling. If the diffracted intensities of the (002) and (200) peak differ after poling, it means that 90° domain switching occurred. Unfortunately, due to small electrode size and the

poling conditions, the sample size was too small for any reliable measurements. However, if some switching during poling occurred it would result in higher fraction of the (001) oriented domains and would thus lower the dielectric constant as the dielectric constant in the (001) direction is lower than for (100) oriented films.

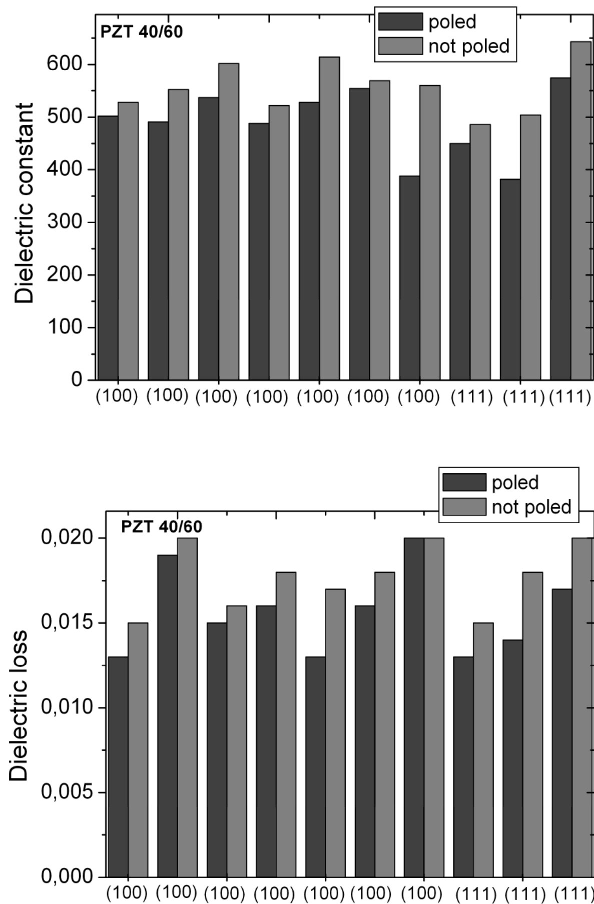

Fig. 3.73: Dielectric constant (above) and loss (bottom) of PZT 40/60 film with different orientation before and after poling.

The dielectric constant of PZT 60/40 films ranged between 600 and 1000 and was thus much higher than the dielectric constant of PZT 40/60 films although the intrinsic dielectric constant in rhombohedral films is only slightly higher than in the tetragonal films. The difference between the measured and intrinsic dielectric constant of the PZT 60/40 films shows higher extrinsic contribution to the dielectric constant in rhombohedral films compared to the tetragonal films. The measured dielectric constant of PZT 60/40 films correlates to the values reported by Kalpat and Uchino [220] for

sputtered PZT 70/30 films. Values such as 1050 for (100) oriented films and around 900 for (111) films were reported. Due to small difference in the structure and the composition of the PZT 70/30 to the PZT 60/40 some small deviation of the dielectric constant must be considered. However, this deviation is likely to be small.

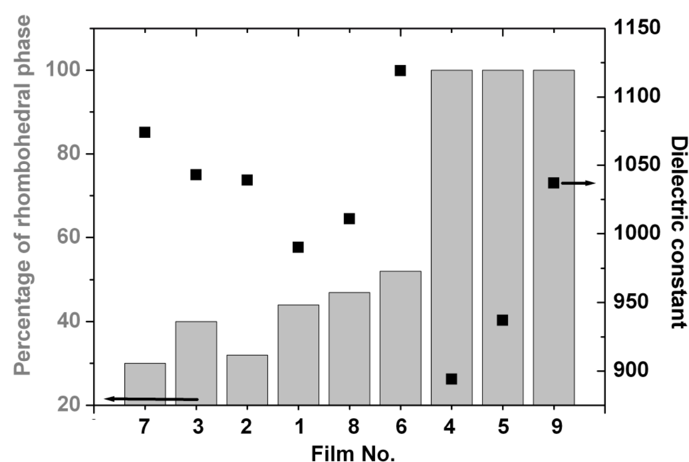

Fig. 3.74: Dielectric constant of PZT 52/48 film with different orientation and rhombohedral phase content.

The dielectric constant of the PZT 52/48 films was between 900 and 1100 on Pt(111)/Si, Fig. 3.74. From this sample batch only 3 films were predominately (100) oriented, all other films showed predominant (111) orientation. All films, regardless the orientation, exhibited similar dielectric constant, although the orientation dependent variation of the dielectric constant in PZT 52/48 films was expected [3, 120]. However, some minor influence of the phase content was observed. The dielectric constant was found to be lower in films with pure rhombohedral phase. The PZT films at the morphotropic phase boundary have an additional extrinsic contribution to the dielectric constant. In films with phase coexistence the phase boundary motion can take place. Thus, the lower dielectric constant in the PZT 52/48 films, where only rhombohedral phase was evident, can be attributed to the lack of the tetragonal phase and the phase boundary motion. Indeed, the dielectric constant on the PZT 52/48 films containing only the rhombohedral phase is quite similar to the dielectric constant of the pure rhombohedral films. In summary, all the values from Tab. 3.21 agreed well with those reported by Chen et al [3] who determined the orientation-dependent dielectric constants of PZT 40/60, PZT

60/40 and PZT 52/48 films to be between 500 and 650, between 800 and 1000 and between 850 and 1100, respectively.

3.6.2.1 Dielectric Properties on different substrates

The dielectric constant of the 2 µm thick films deposited on Pt(200)/Si was determined and summarized in Tab. 3.22. To compare the dielectric constant of PZT films on different substrates, the already discussed values of the films on Pt(111)/Si are included.

Tab. 3.22: Dielectric properties of PZT films on Pt(200)/Si substrates. The results from Tab. 3.21 are included for comparison

Pt(111)/Si	**PZT 60/40**	**PZT 52/48**	**PZT 40/60**
thickness	3 µm	2 µm	3 µm
ε	860 ± 150	1025 ± 25	540 ± 20
tan δ	below 0.04	below 0.02	below 0.02
Pt(200)/Si	**PZT 60/40 (film 9)**	**PZT 52/48 (film 19)**	**PZT 40/60 (film 14)**
thickness	2 µm	2 µm	2 µm
ε	890 ± 80	1240 ± 60	865 ± 20
tan δ	below 0.04	below 0.02	below 0.02

On Pt(200)/Si all films have shown an increase in the dielectric constant. The strongest increase was exhibited by the PZT 40/60 and PZT 52/48 films. The dielectric constant of PZT 40/60 films was much larger on the Pt(200) substrate than on Pt(111) substrate although the majority of the films from the batch PZT40/60-Pt(111)Si-3µm-10 had similar degree of (100) orientation as the PZT film deposited on the Pt(200) substrate. The PZT 52/48 film on Pt(200) substrate was (100) textured and thus higher intrinsic contribution to the dielectric constant can be expected, compared to the mainly (111) oriented PZT 52/48 on the Pt(111) substrate. In the PZT 52/48 film on the Pt(200) substrate both phases, the tetragonal and the rhombohedral, were found, and thus some contribution of the phase boundary motion can be expected. In the PZT 60/40 films only slightly higher dielectric constant on the Pt(200) substrate was observed compared to the films on Pt(111). The film on Pt(200) substrate had predominant (100) orientation and according to the results of Kalpat and Uchino [220] a much higher dielectric constant would be expected than it was found for this film.

The dielectric constant of PZT 52/48 films on LNO/Si substrate was around 1170 and thus higher than on Pt(111)/Si. The dielectric loss was also slightly higher, around 0.04, Tab. 3.23. A much smaller dielectric constant around 600 of PZT 50/50 on LNO/Si was reported by [96]. It should be noticed that Hu et al determined this value at 10 kHz instead of at 1 kHz so that some frequency dependent reduction of the dielectric constant must be included. Also, the thickness of the PZT layer was not mentioned. The resistivity of the LNO reported by Hu et al [96] is comparable to this work.

Tab. 3.23: Dielectric constant and loss of films deposited on different substrates than Pt/Si.

Film	Substrate	thickness	dielectric constant	dielectric loss
PZT 52/48, film 15	LNO/Si	2.4 µm	1170±50	0.04
PZT 40/60, film 15	Pt/Al_2O_3	3.4µm	570±20	0.028
PZT 40/60, film 17	Pt/Si/Pt	2 µm	560±30	0.028

The dielectric constant of the PZT 40/60 films grown under compression was 570±20 and 560±30 for the 3.4 µm thick film on Al_2O_3 substrate and for the 2 µm thick film on Pt/Si substrate. The loss was around 0.028 in average for both films. These values correspond to the values found in PZT films grown under tension and thus showed no influence of the residual stress on the dielectric constant. Such a low response, below 2 %, of the dielectric constant in PZT films when compressive or tensile stress was applied, has been reported by several authors [19, 129, 132] and marks a difference between the films and bulk ceramics. The bulk ceramics were found to respond readily to the applied stress and exhibit lower dielectric constant with increasing compressive stress [221-222]. The low response to stresses of the dielectric constant in films can be contributed to the inactivity of non-180° domain wall motions due to clamping of the film to the substrate.

The dielectric constants of PZT 52/48 films showed an increase with increasing film thickness, Tab. 3. Such increase with thickness was reported by [94] in PZT 45/55 films, where the clamping in thinner films is stronger and thus reduces the dielectric constant. The substrate clamping is lower in thick films and higher permittivity can be observed only in thicker films.

In 5 μm thick PZT 40/60 and PZT 60/40 films an increase of dielectric constant was found compared to 3 μm thick samples, Tab. 3.24. The results suggest that in thicker films higher contribution of 180° domain wall motion can be found and are in good agreement with the results reported by Xu et al [17].

Tab. 3.24: Dielectric of PZT 52/48 films at different thicknesses, sample PZT 52/48-Pt(111)/Si - 3 μm -film 12.

thickness	1 μm	2 μm	3μm
dielectric constant	800± 50	1025 ± 25	1080 ± 30

Tab. 3.25: Dielectric constant of 5μm and 4μm thick films.

5 μm films	dielectric constant
40/60, film 15	630±17
60/40, film 7	1070 ± 15

3.6.2.2 Measurement of the dielectric constant in a temperature range

The dielectric constant was measured in a temperature range between room temperature and 200°C on two different films. One PZT 52/48 film deposited on Pt(200) substrate and one PZT 40/60 film deposited on Pt(111) substrate were employed. The measurement results are displayed in Fig. 3.75. In the temperature range up to 200°C the dielectric constant of PZT 40/60 and PZT 52/48 was increasing linearly due to divergent permittivity towards the Curie temperature. In the measured temperature range the dielectric constant of PZT 52/48 increased for 32% and for 46% in the PZT 40/60 film. Similar behaviour and corresponding values for PZT 52/48 were reported by Wolf et al [223] and Zhang et al [224]. Wolf et al [223] also reported the dielectric constant for PZT 40/60 which was lower than that of PZT 52/48 and its increase was around 20%. The diagram of PZT 52/48 showed a typical non-linear increase. In the temperature range between 100 and 120 °C the slope of the curve changed and was much steeper above 120°C. Such behaviour was reported by several authors [123, 223].

A small thermal hysteresis between heating up and cooling down curves was observed in PZT 52/48. It is possible that at increased temperature some diffusion occurred as the heating was very slow and took approx. 1 hour to reach 200°C. The

higher dielectric constant after cooling suggests that there was some structural re-arrangement in PZT film most likely related to the domain wall de-pinning which would enhance further domain wall motion. The decrease of the dielectric loss of PZT 52/48 in this temperature range and lower dielectric loss after heating, Fig. 3.76, supports the idea of domain wall de-pinning.

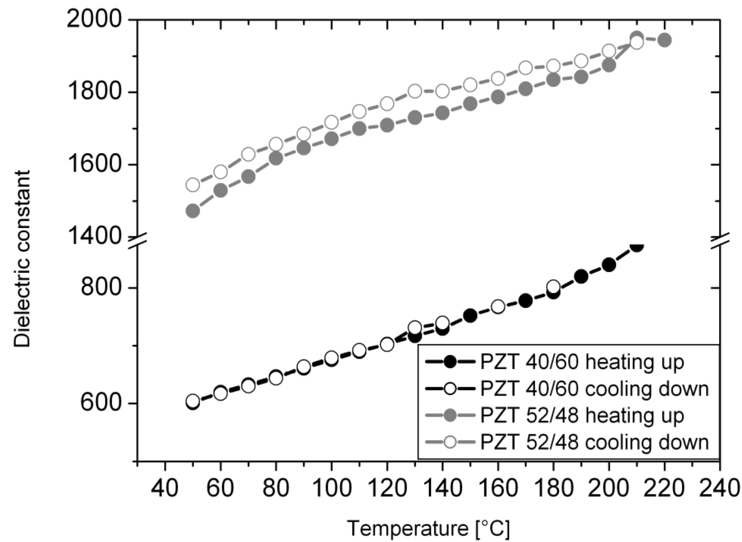

Fig. 3.75: Dielectric constant of 2µm thick PZT 52/48 and PZT 40/60 during heating and cooling. Samples: PZT 52/48-Pt(200)/Si/3”- 2 µm-film 19, PZT 40/60-Pt(111)/Si/2” - 2 µm film 11.

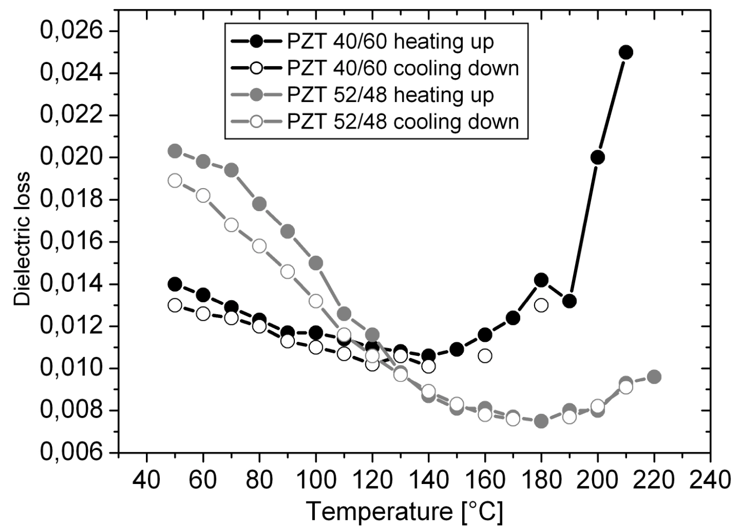

Fig. 3.76: Dielectric loss of 2µm thick PZT 52/48 and PZT 40/60 during heating and cooling.

Another possible explanation for the hysteresis and higher dielectric constant would be a higher phase boundary motion contribution after heating. It could also explain why such hysteresis was not observed in PZT 40/60. However, the domain walls might be stronger pinned in PZT 40/60 films.

The dielectric loss showed some sensitivity to temperature and decreased with increasing temperature up to 140°C for PZT 40/60 or 180°C for PZT 52/48, Fig. 3.76. The temperature dependence of the dielectric loss was reported by Zhuang et al [225] in ceramics and by Xu et al in PZT films which peaked in the temperature range between 200 and 250K. However, the temperature sensitivity of the dielectric loss is not quite understood. The peak position and shape depend on the activation energy of the domain wall motion of each phase and thus a different peak can be found for PZT 52/48 and PZT 40/60.

3.6.3 Ferroelectric hysteresis of PZT films in the temperature range between 20°C and 170°C

The ferroelectric properties were determined for all PZT compositions because of the relationship between the intrinsic polarization, the $d_{33,f}$ and the remanant polarization, although the knowledge of ferroelectric properties is usually not required in piezoelectric applications. The characterization of the ferroelectric properties was necessary as a support and expansion to the piezoelectric properties to precisely define these and to complete the PZT film characterization.

The ferroelectric hysteresis loop was determined in a temperature range for all samples having the same thickness and similar stress state. The hysteresis was measured at 90, 130, 150 and 170°C for most of the samples. It was observed that for most of the films the maximum saturated polarization P_s was reached at a driving voltage of 160 kV/cm although some films exhibited even higher saturated polarization if the field could be further increased. Thus, all PZT 40/60 films were compared at the driving voltage of 160 kV/cm, and the PZT 60/40 at 200 kV/cm.

An example of (100) and (111) PZT 40/60 films is given in Fig. 3.77. All (111) oriented films exhibited higher remanant polarization P_r and higher coercive field than the (100) films.

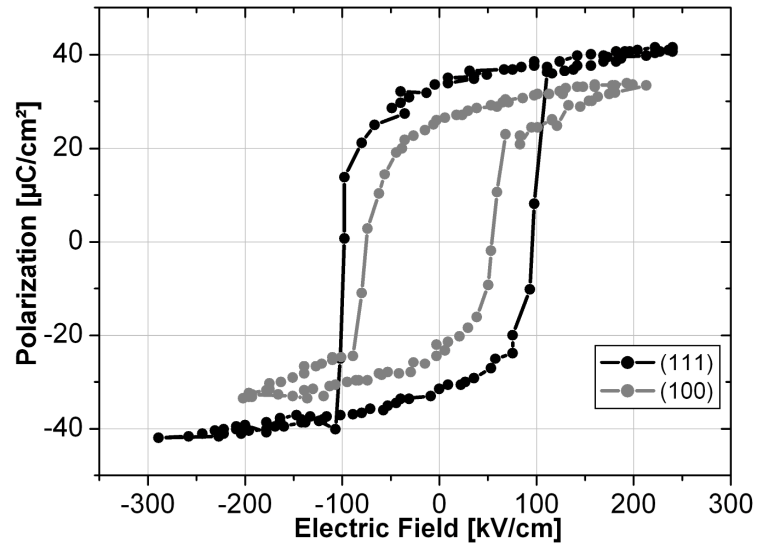

Fig. 3.77: Hysteresis loop of (100) and (111) oriented PZT 40/60 films. Driving field was 160 kV/cm for both films.

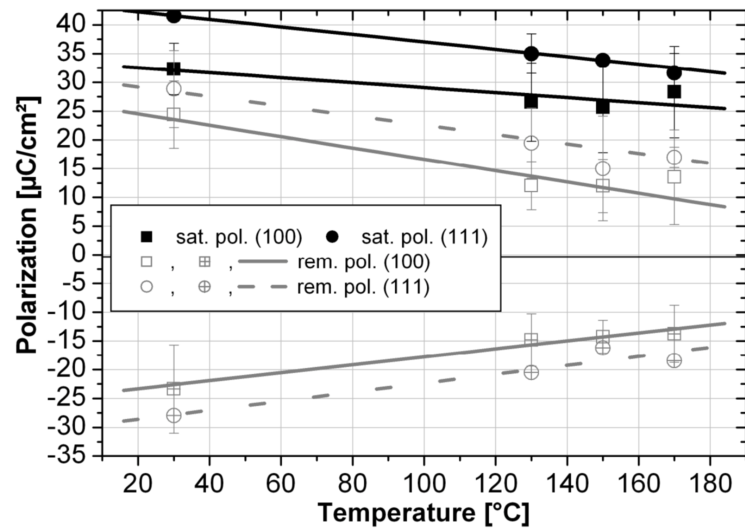

Fig. 3.78: Temperature dependent polarization in PZT 40/60 films. Driving field was 160 kV/cm for all films.

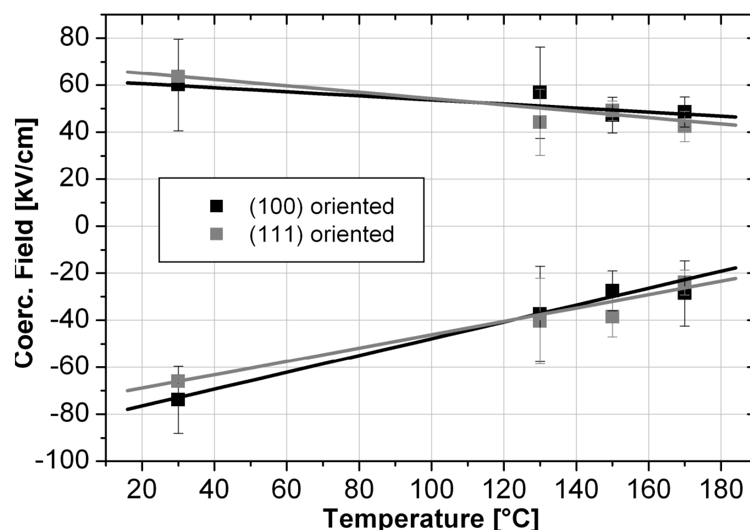

Fig. 3.79: Temperature dependent coercive field in PZT 40/60 films at driving field 160 kV/cm.

The changes of the saturated and remanant polarization for all (100) and (111) oriented PZT 40/60 films with increasing temperature are depicted in Fig. 3.78. The remanant polarization (P_r) was much lower than the saturated polarization for both films, around 20% at room temperature. For both orientations the saturated polarization decreased in the measured temperature range. A decrease of the saturated polarization for 12% was found in (100) oriented films and around 24% in (111) oriented films. The decrease of the remanant polarization with increasing temperature was around 43% and this decrease was more in (100) oriented films than in (111) oriented films, the latter was about 41%. Higher decrease of the remanant polarization than the saturated polarization with increasing temperature was found in (100) oriented films. Bruchhaus et al. reported similar results for sputter deposited PZT 40/60 films whereby the P_r and E_c had only 55% of their room temperature values when measured at 125°C [226].

The influence of the temperature on the coercive field (E_c) in PZT 40/60 films is depicted in Fig. 3.79. All films have shown a decreased E_c with temperature indicating an easier domain wall motion with increasing temperature. An asymmetry in the decrease of the coercive field with temperature was found. The negative coercive field was initially much larger than the positive coercive field and its decrease was much more than the decrease of the positive coercive field when temperature increased. In the

measured temperature range (20 – 180 ºC), the positive E_c decreased for 20% and 33% in (100) and (111) oriented films respectively, while the negative E_c around 63% in both (100) and (111) oriented films.

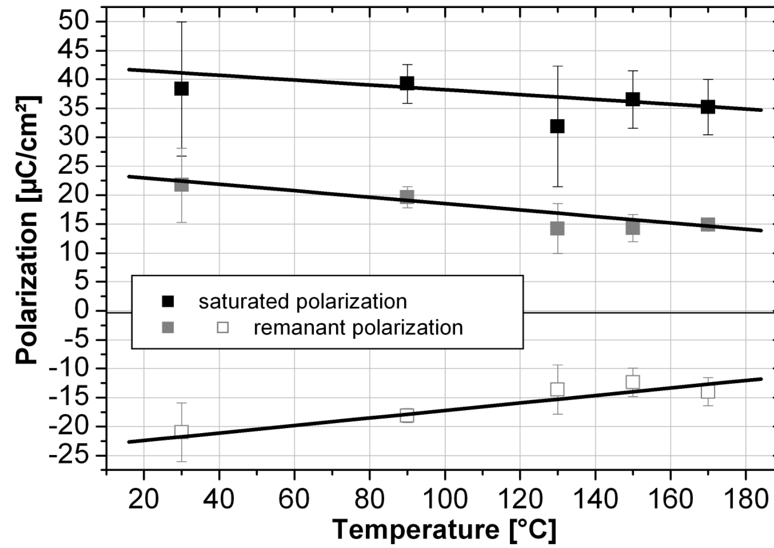

Fig. 3.80: Temperature dependent polarization in PZT 60/40 films at driving field 200 kV/cm. The P_s was equal to -(-P_s).

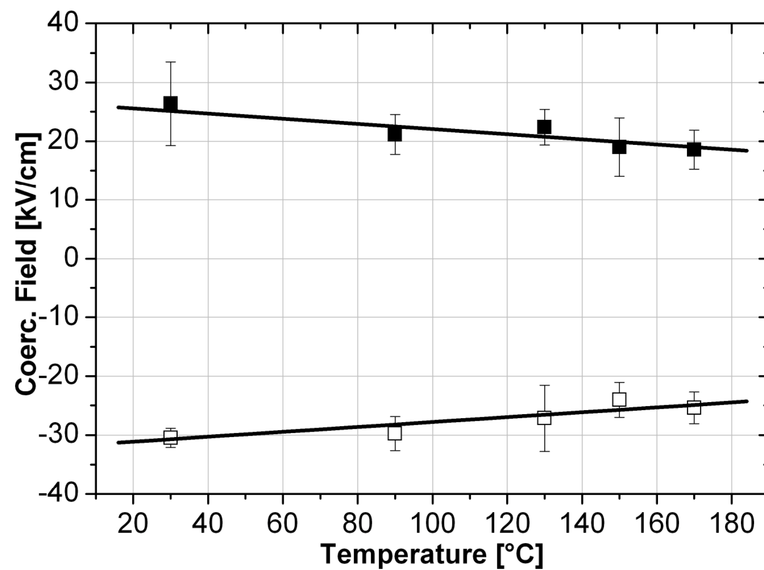

Fig. 3.81: Temperature dependent coercive field in PZT 60/40 films. Driving field was 200 kV/cm for all films.

The saturated and the remanant polarization of PZT 60/40 decreased for 13% and 33% respectively, in the temperature range, Fig. 3.80. The negative and positive terms of the remanant polarization were symmetric. The positive coercive field decreased for 30% and negative for 17%, Fig. 3.81, when temperature increased to 180 ºC. The coercive field shifted to the negative side in all the temperature range.

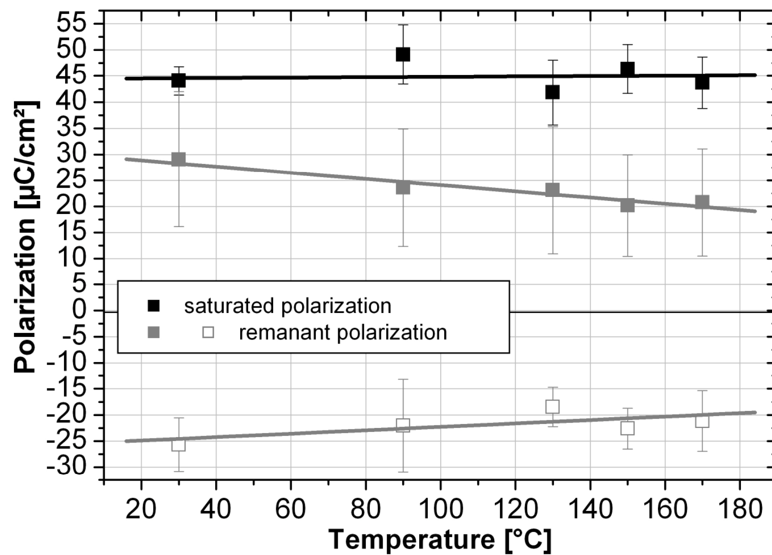

Fig. 3.82: Temperature dependent polarization in PZT 52/48 films. The P_s was equal to -(-P_s).

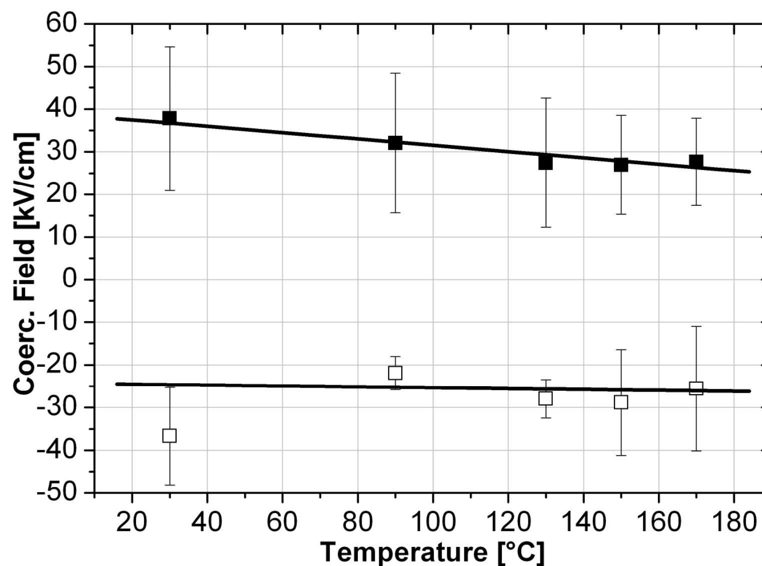

Fig. 3.83: Temperature dependent coercive field in PZT 52/48 films at driving field 200 kV/cm.

The saturated polarization of PZT 52/48 remained constant with temperature, Fig. 17. At room temperature the negative and positive remanant polarizations had the same value but decreased with temperature. The positive remanant polarization decreased for 29% and the negative for 18%. The positive coercive field was larger than the negative at room temperature and decreased 27% with increasing temperature while the negative coercive field remained constant in the temperature range, Fig. 3.83.

The P_s, P_r and E_c values of all films together with the decrease percentage in the temperature range are summarized in Tab. 3.25.

Tab. 3.25: Summary of ferroelectric properties of all films in the temperature range 20°C to 170°C.

PZT	P_s	ΔP_s	$+P_r$	$\Delta +P_r$	P_s-P_r	$-P_r$	$\Delta -P_r$	$+E_c$	$\Delta +E_c$	$-E_c$	$\Delta -E_c$
40/60 (100)	32	12%	24	43%	38%	-23	41%	60	20%	-74	62%
40/60 (111)	41	24%	29	41%	30%	-28	34%	64	33%	-66	64%
60/40	38	8 %	22	32%	42%	-21	33 %	26	30 %	-31	17 %
52/48	44	0 %	29	29 %	36%	-26	18 %	38	27 %	-37	0 %

Highest saturated polarization at room temperature was found in PZT 52/48 films followed by (111) oriented PZT40/60 and PZT 60/40 films. (111) oriented PZT 40/60 films and PZT 52/48 films exhibited highest values of remanant polarization. The lowest decrease in the temperature range was found for PZT 60/40 films.

In all films the remanant polarization was lower than saturated polarization, PZT 60/40 films showed the largest difference between P_s and P_r, indicating large fraction of domains switching back when the field was removed. The highest remanant polarization at room temperature was found in (111) oriented PZT 40/60 and PZT 52/48 films. In PZT 52/48 and (111) oriented PZT 40/60 some asymmetry in the negative and positive remanant polarizations was found in the temperature range.

The saturated and remanant polarizations in PZT 40/60 were strongly dependent upon orientation with lower values in (100) films. The PZT 40/60 films had a relatively low fraction *c* domains so that only a small amount of (001) domains contributed to the polarization. Higher polarization would be expected in (001) oriented films and thus in the direction parallel to polarization.

The coercive field was highest for (111) oriented PZT 40/60 films and lowest in PZT 60/40 films with PZT 52/48 films in between. In all films an asymmetry of the coercive field was found which increased with temperature. Such asymmetry of the coercive field indicates aging of PZT as known for PZT ceramics [198]. The aging is associated with the accumulation of defects which pin and hinder the domain wall motion and is referred to as aging of the ceramics. The accumulation of defects causes a depolarization fields which then biases the coercive field and shifts into one certain direction. A shift of the hysteresis into one direction is referred to as imprint.

A model for aging or imprint of the coercive field in the PZT films was developed by Grossmann et al [227-228]. According to Grossmann et al, a thin interfacial layer is formed between PZT and bottom electrode. Due to defects in this interfacial layer a large electric field arises. This field is compensated by another electric field in the surface layer pointing into the direction of the polarization and can cause emissions of Frenkel-Poole (electron-hole) charges from the electrode into the film or lead to charge separation in the surface layer. If these charges become trapped, an evolution of internal bias will occur leading to a shift of the hysteresis loop. The field in the surface layer is proportional to ferroelectric polarization. Additionally, a linear increasing temperature dependence for charge separation was suggested, whereby the thickness of the interfacial layer can increase with temperature. Such behaviour was observed for all PZT films and thus all films had an interfacial layer. The origin of this layer can be easily explained on the lattice mismatch between PZT and Pt. A fairly good lattice match is realized for all PZT compositions of (111) orientation and Pt. All crystallites with other orientation than (111) have no lattice match to platinum and thus there must be an interfacial layer which would improve the adhesion and nucleation between PZT and platinum. Accordingly, in films that showed high orientation discrepancy to the substrate texture like (100) oriented PZT 40/60 films on Pt(111) the interfacial layer can be expected to be stronger present, e.g. thicker. The thickness of such layer affects the domain wall movements and switching behaviour.

A typical shape change of the hysteresis for all PZT films measured at room temperature and at 170°C is depicted in Fig. 3.84. The initially square-like hysteresis loops of PZT 40/60 at room temperature became round at 170°C. At room temperature

the hysteresis loop of the PZT 52/48 film shows a more quadratic shape similar to that of (100) oriented PZT 40/60 but with lower coercive field. At increased temperature the loop of PZT 52/48 looked more similar to the PZT 60/40 films, also depicted in Fig. 3.84, suggesting that the rhombohedral phase responses easier to external field and temperature.

The remanant polarization of all films in this work was higher than that reported by Wolf et al [223] for 2 or 4 µm thick PZT films. A comparable values of P_r of the PZT 60/40 films were reported by [75, 196], although much higher value for E_c=78 were found [75]. A lower P_r and a higher E_c of PZT 60/40 and 52/48 were reported by [229-230]. Tuttle et al [206] reported orientation dependence of polarization in PZT 40/60 films but not of the coercive field. A constant P_s with temperature of PZT 52/48 was reported by [17] in the temperature range between 50 and 300 K while the remanant polarization was decreased in the same temperature range. Similar coercive field values around 60 kV/cm were reported for PZT 40/60 and PZT 52/48 by [165].

The comparisons of hysteresis loops of 5 µm thick films and 3 µm thick films are depicted in Fig. 3.85. Only PZT 40/60 showed increased remanant polarization at nearly the same coercive field with thickness. The other two PZT compositions exhibited similar (PZT 60/40) or even lower (PZT 52/48) ferroelectric properties than thinner films. It was reported that the remanant polarization increases with thickness until a saturated value is reached [196]. Above this value the remanant polarization shows no dependence on thickness. Remiens et al [231] reported such behaviour of sputtered PZT films, where above 0.7 µm saturation in polarization was found. According to this, the films in this work were much thicker and have already reached the saturated polarization so that no change can be found with thickness. The increase of P_r and P_s for PZT 40/60 must thus have other reasons. It is possible that the increased polarization in 5 µm thick PZT 40/60 film is related to the thickness of the interfacial layer. In thinner films the thickness relation between the film and the interfacial layer is lower than in thicker films. Thus the thicker films would be less sensitive to the effects of the interfacial layer and the non-180° domain wall movement would be enhanced.

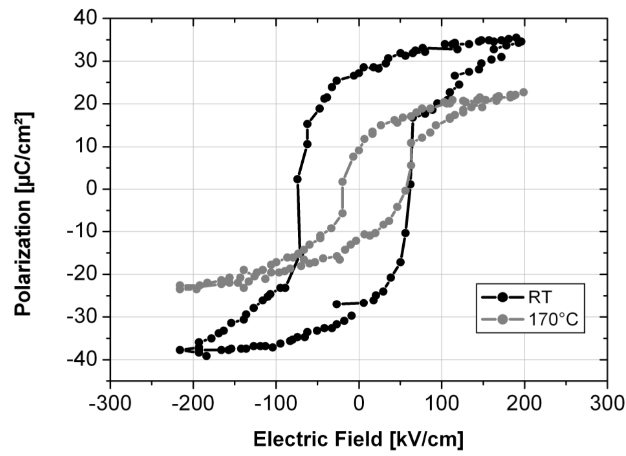

a)

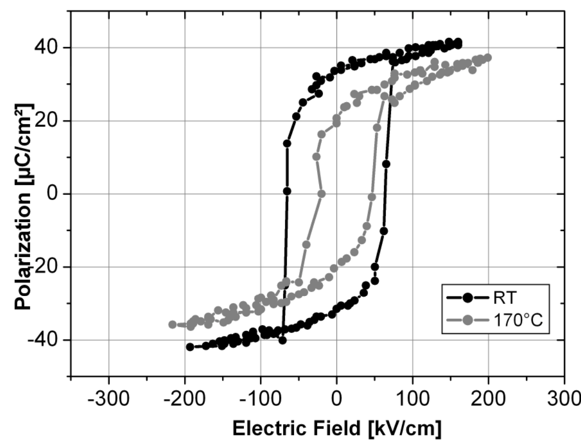

b)

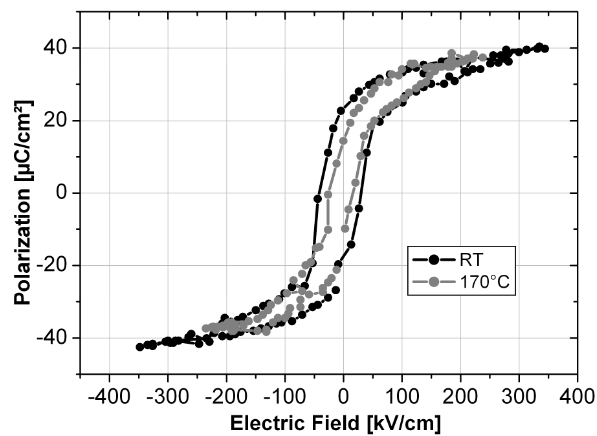

c)

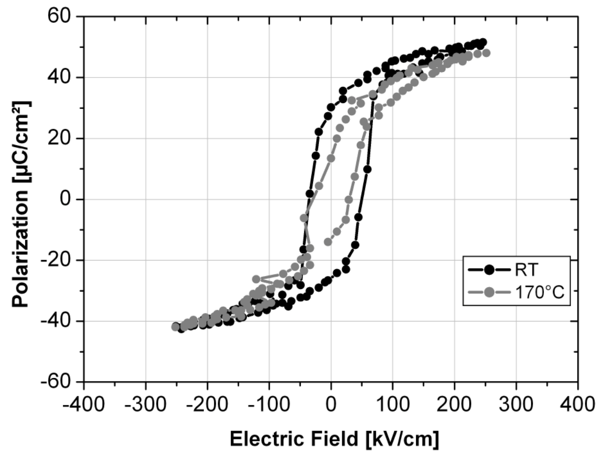

d)

Fig. 3.84: Comparison of hysteretic loops at room temperature and at 170°C of PZT 40/60 a) with (100) and b) (111) orientation, c) PZT 60/40 and d) PZT 52/48. All loops compared at the same driving field.

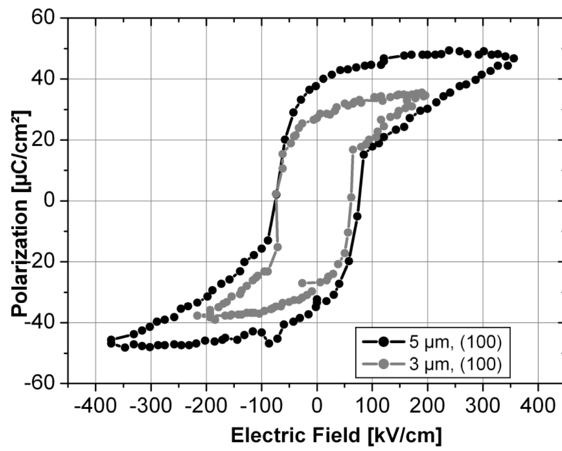

a)

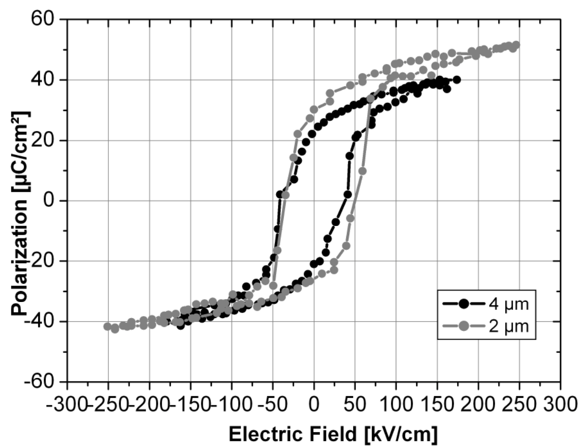

b)

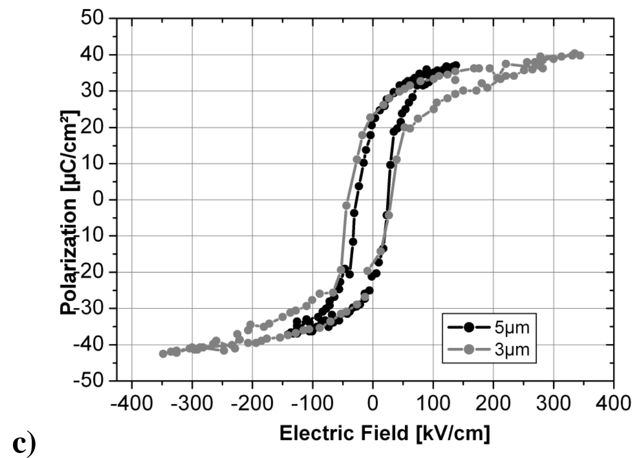

Fig. 3.85: Hysteresis loops of 5 µm PZT films compared to 3 µm films, at room temperature. a) PZT 40/60, b) PZT 52/48, c) PZT 60/40. The driving field for all compared films was equal.

The remanant polarization and coercive field of 3.4 µm and 2 µm thick PZT 40/60 films with compressive residual stress compared against the (111) oriented 3 µm thick films are depicted in Fig. 3.86 and 3.87. The (111) oriented PZT 40/60 film was chosen because highest polarization was found in this films at comparable thickness and because the compressed films also exhibited preferred (111) orientation.

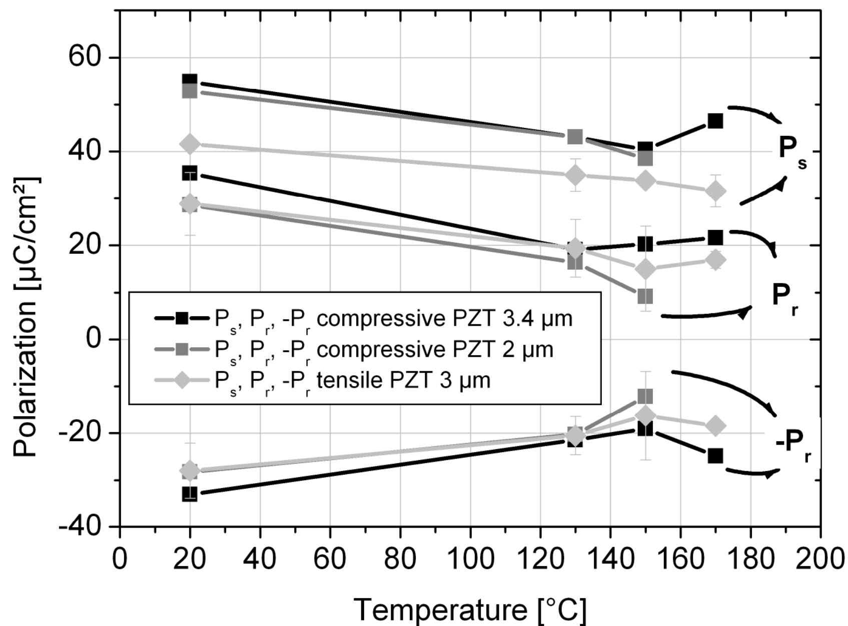

Fig. 3.86: Temperature dependent polarization of PZT 40/60 films with compressive residual stress (film 15, film 17) compared with a 3µm thick and (111) oriented PZT 40/60 film under tensile stress at RT (film 2).

The saturated polarization of the compressive films was higher than that of the tensile films. The remanant polarization of the 3.4 µm film showed highest values while 2 µm compressive and 3 µm tensile films showed the same values. A decrease of polarization with increasing temperature was found in all films. The higher difference between the P_s and P_r in the 2 µm film suggests that more domains switch back in this film than in other films when the electric field is removed. This film is also highly (111) oriented like 3µm thick film so that the contribution of the orientation to the difference can be excluded. The 3.4 µm film has only slightly higher thickness than 3 µm and a bit lower content of (111) orientation but it exhibited much higher polarization than the 3µm thick film under tension.

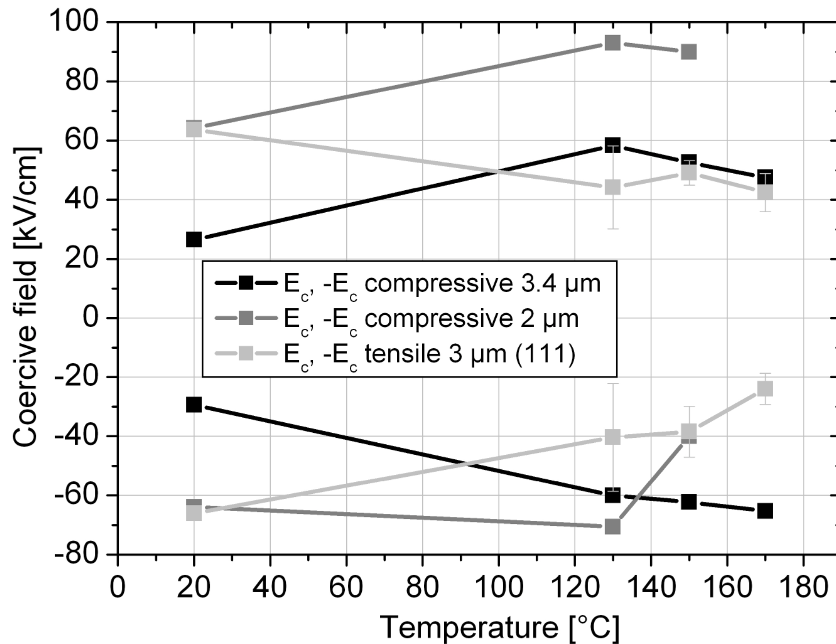

Fig. 3.87: Temperature dependent coercive field of PZT 40/60 films with compressive residual stress (films 15 and 17) compared with a 3µm thick and (111) oriented PZT 40/60 film under tensile stress at RT (film 2).

The results correlate to the reported results that films grown under compressive stress exhibit higher saturated and remanant polarization than the tensile [129, 205, 232] possibly due to the stabilization of (001) domains under compression [132]. However, the compressed films in this work were (111) oriented and it is likely that other factors are responsible, such as the enhanced domain wall mobility in compressed films.

At room temperature the coercive field E_c of the compressive 3.4 µm film was much lower than usually found for PZT 40/60, and the E_c of the 2 µm film was similar to that of 3µm thick film. However, in contrast to PZT 40/60 films under tension, it was found that the coercive field increases in compressed films. This can be explained in terms of thermal stress and thermal expansion. PZT films, under tension at room temperature, reduce the tensile stress upon heating due to thermal expansion. Thus, the stress between the film and the substrate is reduced and it hinders less the domain wall motion in the films. For the consideration of the compressed films a more detailed analysis is needed. On sapphire e.g. the film is under compression while the platinum and PZT are under tension. The thermal strain of PZT 60/40 is depicted in Fig. 3.88 as the diagram for PZT 40/60 was not available. However, the results of Cook et al [203] show similar diagram for tetragonal PZT 48/52.

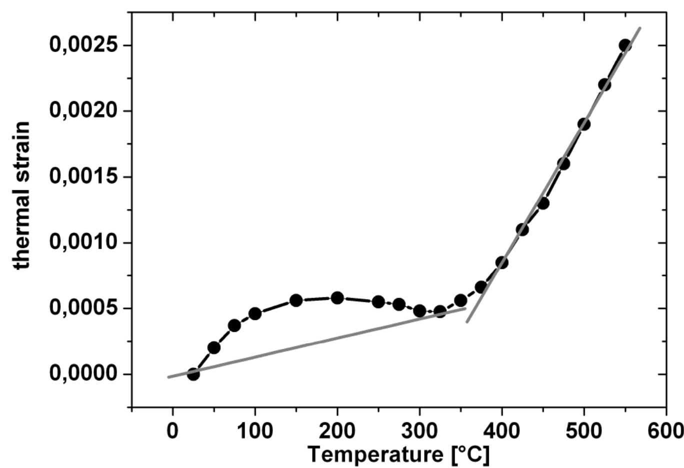

Fig. 3.88: Thermal strain of PZT 70/30. Diagram reproduced from Fig. 3.44.

The TECs of Pt and sapphire are around 9x10-6 and 5.8x10-6 respectively. Upon heating PZT up to 100°C PZT has a TEC around 5x10-6 and thus quite similar to sapphire. Because PZT is already under compression the additional expansion forces the film to higher compression. Above 100°C the TEC of PZT decreases and becomes lower than the TEC of sapphire. Thus, the compressive stress in PZT can be lowered as the thermal expansion of sapphire is now higher than of PZT. The E_c results of PZT on sapphire showed higher values for the coercive field at 130°C but above this

temperature the coercive field decreased again. The increase of the compressive stress in the films must stabilize the domain wall motion. The higher coercive field in the 2 µm thick film than in the film on sapphire can indicate that this film was under compressive stress and the interfacial layer was slightly thicker as only the 2 µm film showed an asymmetry of the coercive field.

3.6.4 Contact Poling of PZT films

The films were poled under various conditions and the $d_{33,f}$ was measured as an indication of the degree of the poling in the film. The poling conditions that were found to give the highest $d_{33,f}$ were then applied to the films of the same composition and thickness.

In contrast to thin films it was found that thicker films need lower field and much shorter time to fully pole. Contact poling of thin films was usually conducted at 130°C but showed rather poor results in thick films, especially in PZT 40/60 films. To find the best poling conditions for PZT 40/60 films the poling duration, electric field and poling temperature were varied, Fig. 3.89.

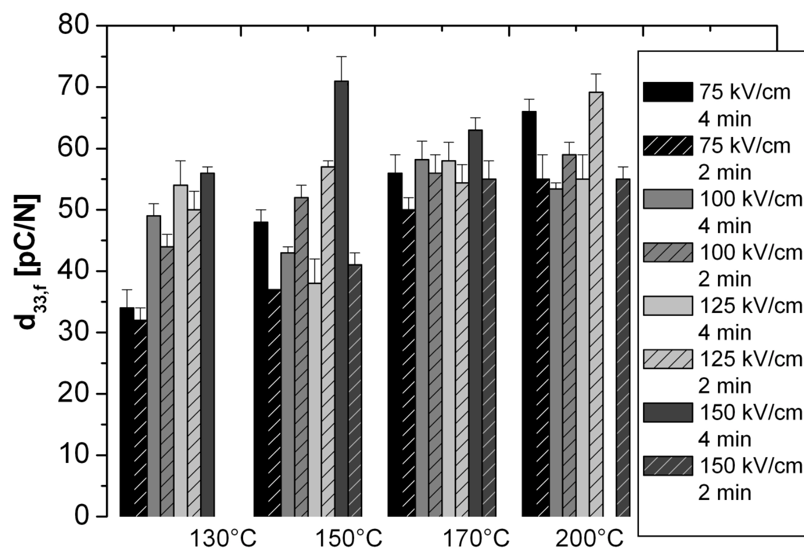

Fig. 3.89: Poling conditions and measured $d_{33,f}$ for a 2 µm PZT 40/60 film.

It was observed that the $d_{33,f}$ of PZT 40/60 was higher if poling took place at higher temperature while the electric field was constant. The longer poling e.g. 4 minutes instead of 2 minutes showed also better results at most of temperatures and fields except for two measurements at 150°C and at 200°C. The poling temperature of 200°C was probably too high and led to breakdown if the films were poled for longer than 2 minutes. By increasing the temperature to 200°C at the same poling duration and electrical field it was possible to increase the $d_{33,f}$ from 35 to 65 pC/N. The film breakdown was observed at electric field of 150 kV at 130°C. If the temperature was not increased this would be the highest obtainable value. However, poling at higher temperatures showed that this was not the highest possible $d_{33,f}$ for this film and values up to 70 pC/N were obtained. The best values were obtained when films were poled either at 150°C, 150 kV/cm for 4 minutes or at 200°C, 125 kV/cm for 2 minutes. Hence, all other PZT 40/60 films were poled at those two conditions and were compared. The most films showed better results at the latter poling condition.

In PZT 60/40 films the increase of poling temperature to 200°C had the opposite effect and lowered the $d_{33,f}$. It was found that the rhombohedral films were best poled at temperature as low as 90°C and 130°C but at the same field, Fig. 3.90. In Fig. 3.90 two films were compared, film 1 had slightly higher degree of (100) orientation than film 2. The poling duration was 2 minutes for all poling trials. For film 1 the increase of poling temperature from 90° to 130°C led to the same values at lower fields like at lower temperature and higher field. Film 2 showed best $d_{33,f}$ values when poled at 130°C and 120 kV.

A comparison of the poling effect on the PZT 40/60 and PZT 52/48 thick films is depicted in Fig. 3.91. The increased temperature and higher field enhanced the $d_{33,f}$ in PZT 40/60 film while it led to the breakdown of the PZT 52/48 film. The best $d_{33,f}$ values for PZT 52/48 films were found at 130°C at 115 kV/cm. This poling condition is quite similar to that of PZT 60/40 films indicating the relationship of the phase content and thus the Zr/Ti ratio onto the poling conditions. It was observed that the tetragonal and rhombohedral films have contradictory behaviour in terms of poling temperature. Both films exhibit best $d_{33,f}$ values at the same electric field strength e.g. 90 kV/cm. The poling temperature for tetragonal films need to be raised up to 200°C while rhombohedral films were fully poled already at 130°C and tend to break down at higher

temperatures. This explains the difficulties to fully pole PZT 52/48 films where both phases were present and a compromise between the two contradictory poling conditions must be found.

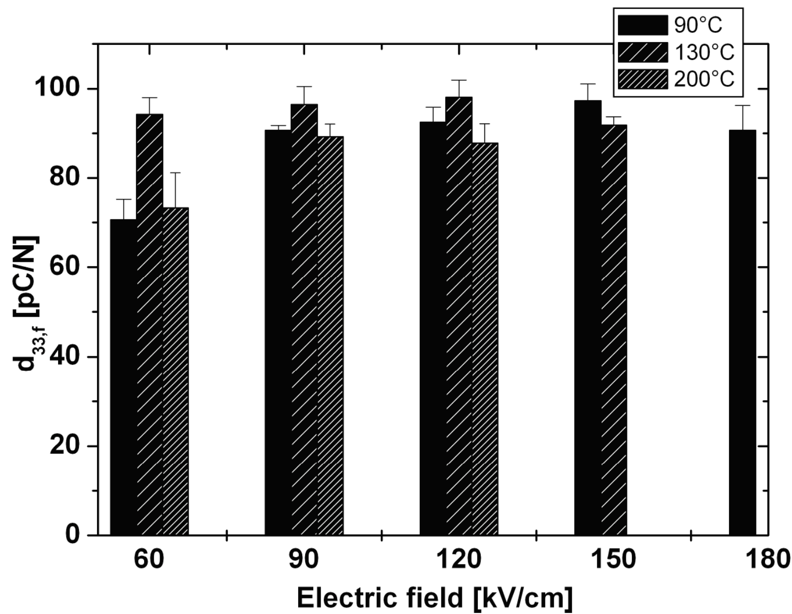

Fig. 3.90: Poling conditions and measured $d_{33,f}$ for 5 µm PZT 60/40 films.

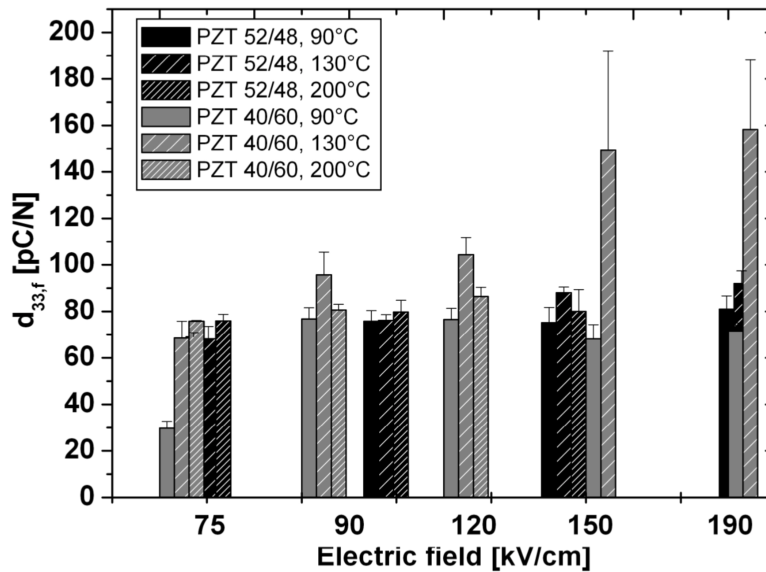

Fig. 3.91: Comparison of the effect of poling conditions on the $d_{33,f}$ of 5 µm PZT 40/60 and 4 µm PZT 52/48 film and measured $d_{33,f.}$

The need of higher temperatures and stronger electric field to fully pole PZT 40/60 indicates the thermal and electric activation of non-180° domains for which the activation threshold is much higher than in PZT films containing the rhombohedral phase. Due to strong clamping to the substrate and the high strain that is induced during *a* to *c* domains switching, the 90° domain switching is usually limited. As already shown in the previous section, the tensile strain is reduced upon heating and possibly the threshold for switching gets lower with lower strain. Thus more 90° domains can switch and higher $d_{33,f}$ is exhibited. The 180° domain usually do not contribute to the piezoelectric properties as there is no strain involved into 180° domain wall oscillation.

The poling was also conducted on PZT 40/60 films with compressive residual stress, Fig. 3.92. The highest $d_{33,f}$ values were obtained for PZT 40/60 when this film was poled at 200 °C. The field strength showed some minor influence and showed only slightly higher values when very high field was applied. This sample could also withstand large electric fields without dielectric breakdown. The compressive PZT 40/60 film on sapphire showed similar tendency towards high fields, Fig. 3.93.

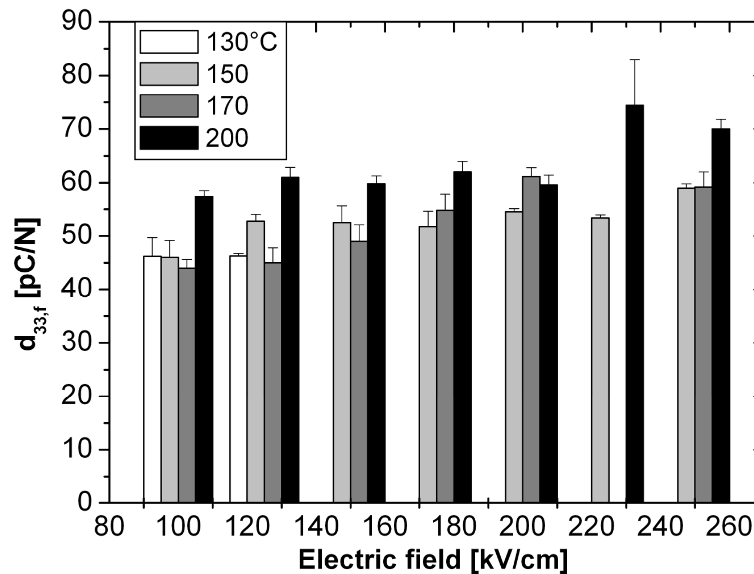

Fig. 3.92: Poling conditions and $d_{33,f}$ of a compressive 2 µm PZT 40/60. Poling time was 2 min.

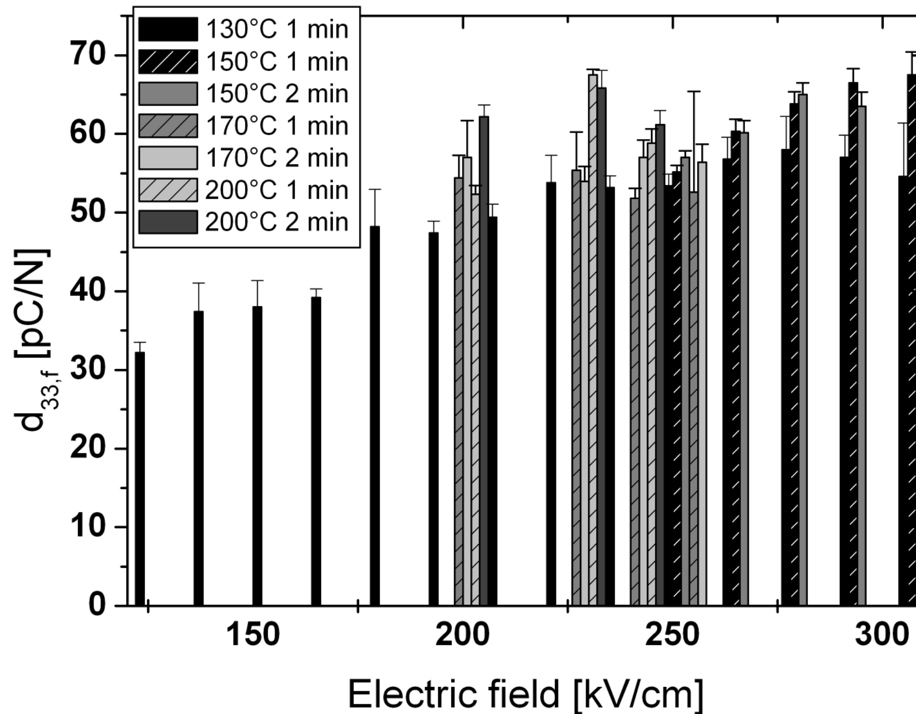

Fig. 3.93: Poling conditions and $d_{33,f}$ of compressed PZT 40/60 on Pt/Al_2O_3 substrate.

The highest properties were obtained when the film was poled at fields around 200-250 kV/cm and 200°C or above 280 kV/cm and at 150°C. The enhancement of $d_{33,f}$ due to increased temperature was obvious especially at electric fields above 260 kV/cm and at 130°C where a saturation of $d_{33,f}$ was found. When the field was increased at the same temperature the $d_{33,f}$ was found to decrease. In contrast, when the temperature was increased above 130°C and the field was above 260kV/cm a much higher $d_{33,f}$ was measured. This is also an indication of thermally activated non-180° domain switching but in comparison to films with tensile stress the activation field for out-of-plane to in-plane domain switching must be much higher in films with compressive residual stress. The need of higher field and temperature correlates to the increased coercive field with increased temperature in these films as observed on the hysteresis loop measurements. The films with compressive residual stress showed dielectric breakdown only at very high fields at the temperature 200°C indicating that films with compressive stress can withstand much higher electric field without dielectric breakdown.

3.6.5 Piezoelectric properties

The piezoelectric effect consists of two parts, the intrinsic and the extrinsic piezoelectric effect. The intrinsic effect refers to the homogeneous unit cell deformations caused by the electric field, and the extrinsic effect represents the elastic deformation caused by the motion of non-180° domain walls (partially domain switching) and the interphase interfaces [16].

The average and orientation related piezoelectric coefficients $d_{33,f}$ and $e_{31,f}$ of all PZT compositions for 3 µm thick films (2 µm for PZT 52/48) are summarized in Tab. 3.26. All films had the same single layer thickness. It was observed that in individual compositions the highest $d_{33,f}$ coefficients were obtained in (100) oriented films and the lowest $d_{33,f}$ was found in (111) oriented films. The films with mixed orientation consisting of (100) and (111) orientation exhibited $d_{33,f}$ in order between the highly (100) and (111) oriented films. The highest $d_{33,f}$ was observed in (100) PZT 52/48 films, followed by PZT 40/60 and then by PZT 60/40 films.

Due to the polarization axis in (001) direction this is reasonable for (001) oriented tetragonal films. However, the films in this work were mainly (100) oriented. Thus significant switching must have occurred in the (100) oriented films during poling or the extrinsic contribution was higher in these than in (111) oriented films. In rhombohedral films the polarization axis lies along (111) directions but the highest $d_{33,f}$ can be expected along the pseudo-cubic (001) direction [19-20, 233]. The higher $d_{33,f}$ of the PZT 52/48 corresponds also to the reported values [234] and the phase boundary motion is an additional contribution to the $d_{33,f}$ responsible for highest $d_{33,f}$ in films with morphotropic boundary composition.

Tab. 3.26: Piezoelectric coefficients of 2µm and 3µm thick PZT films.

	PZT 60/40	PZT 52/48			PZT 40/60		
thickness	3 µm	2 µm			3 µm		
orientation	mixed	(100)	(111)	(100)/(001) +(111)	(100)	(111)	(100)/(001) +(111)
$d_{33,f}$ [pC/N]	-63 ± 3	-91 ± 5	-70 ± 4	-80 ± 5	-78 ± 4	-67 ± 1	-75 ± 7
$e_{31,f}$ [C/m²]	8.3 ± 1	10.5 ± 0.3	8.5 ± 1	9.1 ± 1	9.8 ± 0.4	8.9	8.2 ± 0.4

Corresponding to the $d_{33,f}$ values, the highest $e_{31,f}$ was similarly found for (100) oriented films. Values up to 10.5 were obtained for (100) oriented PZT 52/48 films and were all much higher than $e_{31,f}$ of sputtered PZT films of similar thickness reported by [231]. Similar $e_{31,f}$ values of sol-gel films to this work were reported by [185].

The $d_{33,f}$ of PZT films of all compositions deposited on Pt(200)/Si substrate was similar to the values measured in (100) oriented PZT films of all compositions on Pt(111)/Si, Tab. 3.27. This is reasonable as the PZT films deposited on the Pt(200) substrate were mainly (100) oriented. All films were 2µm thick. The tetragonal PZT exhibited slightly lower value on Pt(200) than on Pt(111) although the same degree of (100) orientation was detected. The lower $d_{33,f}$ of the PZT 40/60 film on Pt(200) substrate is likely to be due to lower thickness of the film.

The rhombohedral film showed higher value on Pt(200) than on Pt(111) due to higher degree of (100) orientation. In PZT 52/48 films same $d_{33,f}$ was found on both substrates. In all films $e_{31,f}$ was found to be slightly higher on Pt(200)/Si than on Pt(111)/Si. Higher $e_{31,f}$ coefficient in PZT 52/48 film on Pt(200) can be related to lower tensile stress in this film, as seen in section 3.3.

In PZT 40/60 and PZT 52/48 films with increased single layer thickness but comparable total thickness, the $d_{33,f}$ was found to be in the same range for all films of one composition, Tab. 3.28. The higher $d_{33,f}$ of the PZT 52/48 film with 130 nm single layer thickness was due to higher degree of (100) orientation in this film. The lower $d_{33,f}$ in the film with 500 nm single layer thickness was due to incomplete crystallization as some residual pyrochlore was found in that film.

Tab. 3.27: Piezoelectric coefficients of PZT films deposited on Pt(200)/Si substrate.

	$d_{33,f}$ [pC/N]	$e_{31,f}$ [C/m²]	fraction of c-domains (002)/((002)+(200))
PZT 40/60, film 14	70	9.55	22%
PZT 52/48, film 19	92±2	11.4	46% tetragonal (002) 50% rhombohedral
PZT 60/40, film 9	74		

Tab. 3.28: $d_{33,f}$ in films with increased single layer thickness but similar total thickness.

single layer thickness	**$d_{33,f}$ [pC/N]**		**total thickness [µm]**	
	PZT 52/48	PZT 40/60	PZT 52/48	PZT 40/60
130 nm	105	-	2	-
200 nm	91	78	2	2
300 nm	-	85	-	2
500 nm	-	60	-	2.60

The $d_{33,f}$ of 5µm thick films fabricated via repeated coating of 200 nm thick single layer are given in Tab. 3.29. The 5 µm films showed increased $d_{33,f}$ of all PZT compositions. The highest increase was found in PZT 40/60 film which was close to the theoretically predicted value of 169 pC/N [19]. The highest values were measured if high field and increased poling temperature was used which probably enabled the non-180° domain switching. The $d_{33,f}$ of 5 µm thick films for the compositions of PZT 40/60 and 60/40 were higher than the corresponding bulk compositions and their $d_{33,f}$ coefficient increased 40% and 100% for PZT 60/40 and PZT 40/60, respectively, when compared with 3 µm thick films. The $e_{31,f}$ of the 5 µm PZT films was slightly higher than that of the 3µm thick films for all three investigated compositions.

Tab. 3.29: Piezoelectric coefficients $d_{33,f}$ and $e_{31,f}$ of 4 and 5 µm thick PZT films.

Sample / thickness	$d_{33,f}$ [pC/N]	$e_{31,f}$ [C/m²]
PZT 40/60 / 5 µm	-160 ± 30 pC/N	9.2
PZT 52/48 / 4 µm	-92 ± 5 pC/N	10.2
PZT 60/40 / 5 µm	-98 ± 4 pC/N	10.9

High $d_{33,f}$ coefficients are partially due to high (100) orientation. All 5 µm thick films had high degree of (100) orientation. Such high values for $d_{33,f}$ were reported by Chen [3] for PZT 52/48 composition. At 5 µm thickness $d_{33,f}$ around 270 pC/N was reported. However, such high $d_{33,f}$ as found in PZT 40/60 cannot be only due to high degree of (100) orientation and thus there must have been other, extrinsic contribution like activated 90° domain wall motion or 90° domain switching. The relatively low $e_{31,f}$ of PZT 40/60 film compared to the $d_{33,f}$ value suggests that the domain switching from a to c domains took place during poling. Further, it can be concluded that no 90° domain switching occurs during piezoelectric testing and thus the major extrinsic contribution

can be limited to 90° domain wall oscillations. Thus, the results suggest that in 5 µm thick films the domain walls are less pinned than in thinner films.

This results are in good agreement with the result of Xu et al. Xu et Al [17] found similar enhanced $d_{33,f}$ in thick films (above 3 µm) due to less severe non-180° domain walls pinning. The argument was based on the existence of an interface layer between PZT film and the platinum bottom electrode as mentioned earlier. In thick films the influence of this interfacial layer is weaker because the thickness ratio of the films and the interfacial layer is large and thus the domain switching is easier, if sufficient field was applied during the poling.

Similarly to the tetragonal composition the extrinsic contribution of PZT 60/40 must be enhanced if this is due to 71° or 109° domains in rhombohedral crystallographic structure. The results also suggest that the strain-related domain wall motion in rhombohedral films is enhanced already at lower poling fields than the tetragonal [235].

The $d_{33,f}$ of the PZT 52/48 film was lower in comparison to the $d_{33,f}$ of the other 5 µm films. This sample was also only 4µm thick which could be not as sufficient thickness to neglect the influence of the interfacial layer. It is quite possible that this film was not fully poled. As mentioned in previous section, the PZT 52/48 films were more difficult to pole as these films comprise the tetragonal and rhombohedral phase. To enhance the non-180° domain switching in the tetragonal phase, it is necessary to pole at temperatures higher than 130°C and at relative high fields of above 160 kV/cm. However, the 4 µm thick PZT 52/48 film suffered dielectric breakdown when poled at such conditions, possibly due to high sensitivity of rhombohedral phase to high temperature and high fields. Similar results on PZT 52/48 ceramics suggest that the rhombohedral phase is much easier to pole than the tetragonal phase [236].

The $d_{33,f}$ values of the PZT 40/60 films deposited on compressed substrates were similar to those obtained from the films deposited on non-compressed substrates. The 3.4 µm thick film of Pt/Al_2O_3 substrate exhibited $d_{33,f}$= 68 ±1 pC/N which corresponds to the $d_{33,f}$ values obtained on films with mixed orientation as this film in deed had a mixed (100) and (111) orientation.

The 2 µm thick film on Pt/Si had the $d_{33,f}$ around -75±8 pC/N and similar to (100) oriented PZT 40/60 films although it was 80% (111) oriented. The fraction of *c* domains based on the (002)/(200) ratio was very negligibly low. This result suggests that there was a high extrinsic contribution to the $d_{33,f}$, possibly due to compressive stress. The results from the ferroelectric hysteresis loop have showed indications of imprint but lower than in other PZT 40/60 films on Pt(111)/Si substrate. In this sample the Pt from the bottom electrode was constrained and not free to recrystallise which could have led to thinner interfacial layer. Some self-polarization was found; when the electric field during poling was reversed a maximum value around 50 pC/N was obtained.

On LNO/Si substrate PZT 52/48 exhibited $d_{33,f}$ around 71 pC/N in average, with maximum measured value of 92±6 pC/N. The $e_{31,f}$ was in average around 9.45 C/m² for all 2 µm thick films on LNO/Si. The maximum measured $e_{31,f}$ was 10.1 and thus the PZT 52/48 films exhibited similar values like the PZT 52/48 films deposited onto Pt/Si substrate. However, the PZT 52/48 films on LNO substrate had much lower degree of (100) orientation and thus there must be other reasons why the properties are comparable to the highly (100) oriented PZT 52/48 films on Pt(111). PZT 52/48 films on LNO/Si have shown good lattice match to the substrate and it is likely that these films have thinner interfacial layer, so that the 90° domain wall motion is not as suppressed as in PZT 52/48 films on Pt(111). The high dielectric constant and piezoelectric properties suggest that the conductivity of the LNO electrode is acceptable and the replacement of Pt by LNO would not sacrifice the film electrical properties.

3.6.6 Observation of ferroelectric domains

Some of the images were captured using the experimental set-up and the imaging contrast according to [12, 237-238]. In this contrast mode the accelerating voltage of the primary beam is so chosen that the number of electrons from the primary beam equals the sum of secondary and back scattered electron yielded from the sample. At such accelerating potential no surface charge results from the sample surface which allows a differentiation between the domains in their sense of polarization. Domains with positive polarization attract the escaping secondary electrons back to the surface and

appear dark. The domains with negative polarization to the surface repel any secondary electrons and these areas appear white. This contrast is referred to as brightness contrast. Apart of contrast imaging there is also the piezoelectric imaging where the topographic image of the sample displacement is detected.

As already mentioned in previous section, in PZT 52/48 the different microstructure was observed if the film was grown on compressive stress rather than tensile stress. The same PZT 52/48 films as introduced in sections 3.4.7 and 3.5.3 are depicted in Fig. 3.93 and 3.94.

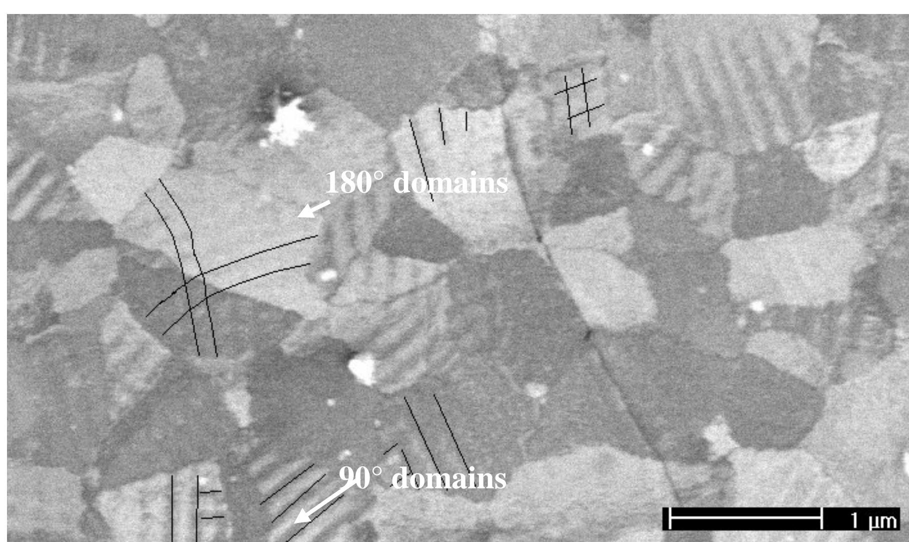

Fig. 3.93: Surface image of PZT 52/48 grown under tensile stress. Some of the different kinds of domain patterns were highlighted with black lines.

The tensile films are depicted in Fig. 3.93. The film was not poled before the examination in the SEM. Various patterns were observed like lamellar patterns within one grain or dark and bright areas within one grain. Such lamellar domains were usually observed in tetragonal PZT films and were contributed to 90° domains [239]. The lamellar width of 100 nm corresponds closely to the values reported by Zheng et al [239]. From the phase-field calculations [188] it follows that under the tensile strain the following four variants of tetragonal domain would be stable: [100], [-100], [010] and [0-10]. Thus, the lamellar domains were most likely to be 90° domains consisting of [100] and [010] domains. The other non-lamellar domains were most likely the single-

grain domains of these variants or 180° domains. Also, some grains with three-domain structure similar to those reported by [9] or by [240] were observed.

In the PZT 52/48 film grown on compressed substrate mostly areas of different contrast can be found. The lamellar patterns were rare. According to the domain pattern for PZT 52/48 film under compression calculated using the phase-field approach [9] 4 variants of the rhombohedral phase and the (001) of the tetragonal phase would be stable along with a low fraction of the orthorhombic phase. The domain pattern from Fig. 3.94 and Fig. 3.a ref [188] correlate roughly. However, the domain pattern was reported for (001) epitaxial films so that only limited correlation can be found between this work and the work of Choudhury et al [9].

Zheng et al [239] investigated the domain pattern via PFM in tetragonal PZT films and suggested that the 90° domain formation is due to tensile stress so that a lamellar pattern is formed. The 180° domains would form in a grain as a result of compressive stress around the grain. Thus, the areas of dark and bright contrast can be attributed to the 180° domains.

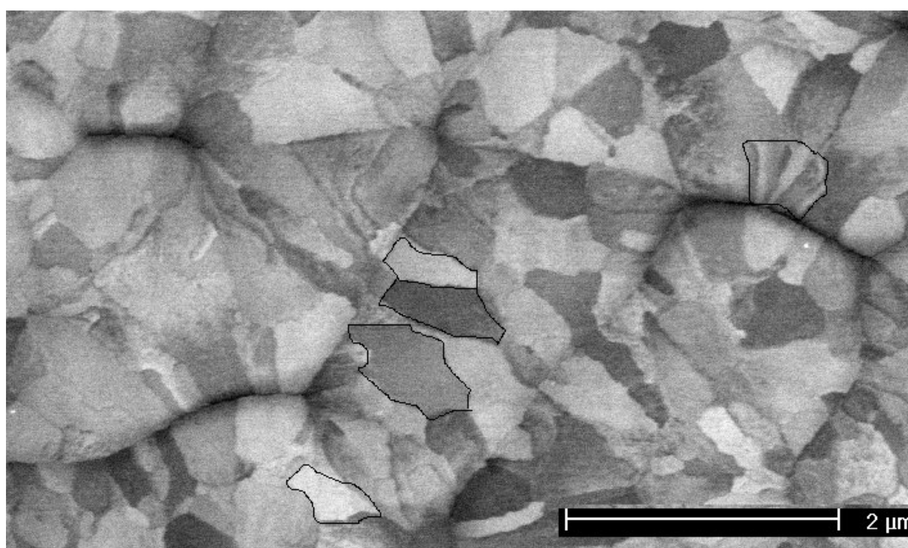

Fig. 3.94: Surface image of a PZT 52/48 film deposited onto compressed substrate. Some grain boundaries are highlighted with black lines.

All the PZT films introduced in the previous paragraph were not poled before the examination in the SEM. The following paragraph focuses on the poled PZT 40/60 film

using Corona poling method and reports the observations of domain patterns after poling.

The film in Fig. 3.95 and 3.96 is a 2 µm PZT 40/60 film deposited on 4“ wafer, with around 75% (111) orientation. The majority of the grains showed lamellar domain pattern like grain 1 in Fig. 3.95. The approximate lamellar width was around 100 nm (grain 1) but larger spacing was found in some of the grains (grain 2), Fig. 3.95. Due to the high (111) orientation of the film and the high fraction of single grains with lamellar domains the lamellar domains were contributed to the (111) domains. Stable lamellar domain patterns in (111) tetragonal PZT films with inclined domain wall boundaries along {110} plains were shown by [8]. It must be noted that the contrast was maximized in this image and in the following images. The very dark areas between the bright grains are not pores, only areas where the signal was much weaker, e.g. the grains that did not contribute to the signal.

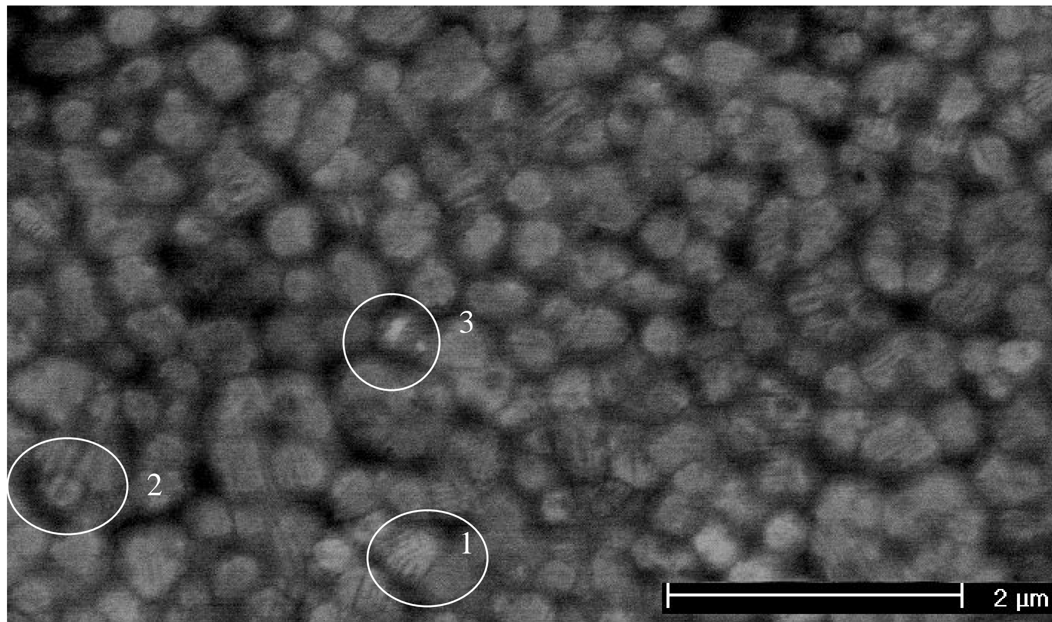

Fig. 3.95: Domain imaging in a poled PZT 40/60 films.

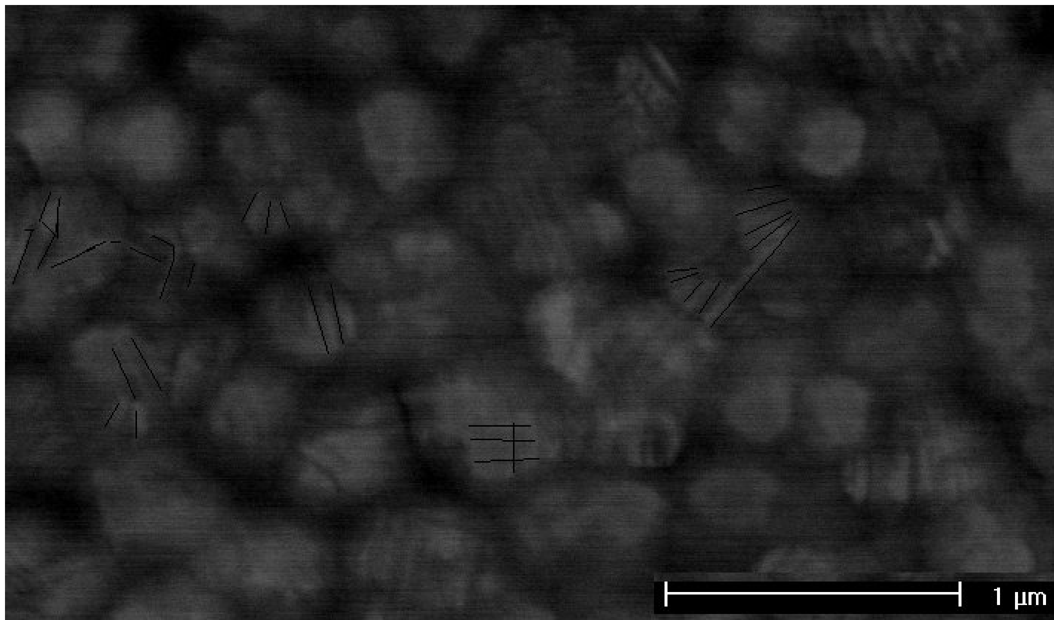

Fig. 3.96: Enlargement of the same film as in Fig. 3.95. Some of the observed domain patterns are highlighted with black lines.

Also, a small fraction of 180° was observed, Fig. 3.96 grain 3. The 180° domain had stronger bright-dark contrast. Because the highest polarization in PZT 40/60 films is along [001] and the correlating small fraction of (001) orientation in this sample to the low fraction of 180° domains this domains were most likely [001] 180° domains.

Chapter 4: General discussion

4.1 Introduction to the Chapter

This chapter discusses the relationship between the orientation and stress in PZT films and connects the not discussed aspects of orientation in Sections 3.3 and 3.4. The source of errors in the stress analysis is introduced in this chapter. The electric properties of the films are discussed in relation to film orientation and thickness.

4.2 PZT nucleation

The fabrication of the PZT films is usually carried out using two-step heating method, by which it is possible to fabricate PZT films with different orientations e.g. by variation of pyrolysis temperature [78, 135, 241]. In this work it was shown that PZT film with increased thickness cannot be processed under two-step conditions because they crack at certain thickness. The investigation of processing parameters has shown that thermal treatment at four distinct temperatures allows fabrication of crack-free PZT films. This also means that the thermal treatment temperatures cannot be changed and that different orientations of PZT films cannot be obtained by temperature variation. Another method for fabrication of PZT films with different orientations is by variation of time at certain temperatures and is referred to as annealing time variation [135]. The method of annealing time variation is usually applied in connection with rapid thermal annealing. Thus, the method of variation of annealing times was applied in this work but the PZT films were processed on the hotplates rather than in rapid thermal annealing furnace (RTA). All films experienced drying at 100°C for one minute. At other temperatures 300°C, 450°C and 550° (or 630°) the thermal treatment period was varied.

The obtained films have shown considerable differences in orientation (Section 3.3) indicating that the different orientations can be obtained by variation of thermal treatment period at the same temperatures. In the following paragraph the influence of the processing conditions on the orientation and crystal growth will be discussed. The differences between the PZT compositions will be pointed out. The effects of the

substrate, intermetallic phase formation and stress will be discussed in the following subsections.

To show the influence of the processing conditions on the orientation of PZT films with different compositions the orientation of all PZT films from the sample batches PZT 40/60-Pt(111)/Si-3µm-10, PZT 60/40-Pt(111)/Si-3µm-6, PZT 52/48-Pt(111)/Si-2µm-10 are summarized in Tab. 4.1. The data at lowest available thickness was summarized, e.g. 1 µm for PZT 40/60 and PZT 60/40 films and 2 µm for PZT 52/48 films. The film thickness of 1µm correlates to 5 coatings and film thickness of 2µm correlates to 10 coatings. The lowest thickness of the PZT films is chosen in order to show the film orientation in the film layers closest to the substrate because the data after the deposition of the first layer was not determined.

It was shown in Section 3.3 that the orientation changes with thickness. The change of orientation was stronger in thicker films than in thinner films. Although it can be assumed that there were probably some changes in orientation between the 1 µm thick films and the first coated PZT layer that nucleated directly on the Pt electrode, it can be assumed that this difference is not as significant as in much thicker films, e.g. when 1µm and 3 µm thick films are compared. Also, the results from Section 3.3 the change of orientation was mostly through faster (100) crystal growth compared to crystal growth in (111) direction. Thus, it can be assumed that the degree of (111) orientation was probably higher in the first PZT coating, next to the substrate, than in the films at thicknesses compared in Tab. 4.1.

The relative diffracted intensity of (111) lattice planes at the compared thickness (Tab. 4.1) showed that most films from the sample batch of PZT 52/48 films were preferred (111) oriented. Also, most films of the sample batch from PZT 60/40 films showed high relative diffracted intensity of (111) lattice planes. This result indicates that the nucleation in PZT 52/48 and PZT 60/40 films was highly influenced by the substrate and the lattice match between the Pt(111) and PZT (111) lattice planes. In contrast, in the sample batch of PZT 40/60 films only three films out of ten have shown high relative diffracted intensity of (111) lattice planes indicating that the nucleation in PZT 40/60 films was less influenced by the substrate and the lattice match between PZT (111) and Pt(111).

A comparison of the orientation in the PZT films processed under same processing conditions (grey shading in Tab. 4.1) showed very different orientation in PZT films of different composition. For instance, for the PZT 40/60 films, very low diffracted intensity of (111) lattice planes was detected (rows 1, 3, 8) while the PZT 52/48 films processed under the same conditions as PZT 40/60 films showed very high (111) diffracted intensity even at much high thickness than PZT 40/60 films. Furthermore, the processing conditions of the PZT 40/60 film (row 2) showed high (111) intensity in PZT 40/60 film but very low (111) intensity in PZT 52/48 film. This result indicated that the same processing conditions have different effects on the orientation of the PZT films with different compositions. Furthermore, no correlation between the orientations of PZT films with different compositions can be found using the same processing conditions. Thus, the processing conditions for each PZT composition must be investigated separately. If e.g. PZT 40/60 films with certain orientation are needed, the processing conditions must be investigated for the PZT 40/60 compositions. The processing conditions in PZT 52/48 films suitable to obtain films of e.g. (111) orientation will not have the same effect on the orientation if applied to PZT 40/60 films. Furthermore, this result indicates major differences in the nucleation mechanisms between PZT films of different compositions.

Tab. 4.1: Percentages of (111) orientation in 1µm PZT 40/60 and PZT 60/40 films and 2 µm PZT 52/48. Each value represents one sample; the films with grey shading were processed under the same conditions.

Row Nr.	Sample	PZT 40/60	sample	PZT 52/48	sample	PZT 60/40
1	film1	0	film11	97	film2	42
2	film2	89	film4	14	film3	53
3	film3	19	film6	65	film4	83
4	film4	23	film7	23	film5	40
5	film5	0	film3	25	film6	72
6	film6	88	film2	60		
7	film7	67	film5	78		
8	film8	12	film9	87		
9	film9	2	film1	77		
10	film10	37	film10	68	film1	56

The PZT 60/40 films were not mentioned in the previous paragraph due to low comparability of the PZT 60/40 films to the PZT 40/60 and PZT 52/48 films. PZT 60/40

films contain higher zirconium content. It required higher temperature and time to crystallise, therefore, for this study, only two films were processed under the same conditions (row 4 and 10) as PZT 52/48 or PZT 40/60 films. As mentioned in Section 3.3, in all 1 μm thick PZT 60/40 films, pyrochlore phase was, more or less, detected and the films had to be annealed for extra 40 minutes at 630°C to completely crystallize. Evidence for more difficult crystallization of zirconium rich PZT compositions was provided by Reaney et al [217] who found lead deficient and zirconium rich areas in the film surface which could not be crystallized. Ledermann et al [185] provided further evidence for easier crystallization of titanium rich PZT compositions and more difficult crystallization in zirconium rich PZT compositions. Ledermann et al found a gradient distribution of zirconium and titanium throughout each PZT film layer, whereby titanium concentration was higher at the bottom of the layer and the zirconium concentration was higher at the surface of the layer. Such compositional gradient reflects the fact that for Ti rich compounds, the activation energy for nucleation is smaller than for zirconium rich compounds.

The different processing conditions between PZT 60/40 films and PZT films of other compositions together with the additional annealing step in PZT 60/40 can have significant impact on the orientation. Thus, the modified processing conditions in PZT 60/40 films do not allow any assumption or correlation of the influence of the processing conditions on the orientation as there were too many variables that can affect the film orientation.

4.2.1 Nucleation of PZT 40/60

In Section 3.3 it was concluded that the variation of thermal treatment period at 450°C has significant impact on the film orientation. The PZT 40/60 films treated for longer time at 450°C, e.g. 5 minutes, showed preferred (111) orientation. In contrast, the PZT 40/60 films treated for shorter time at 450°C, e.g. 2 minutes, showed preferred (100) orientation.

This result corresponds to the work of Liu and Phule [187] on PZT 40/60. Liu and Phule fabricated sol-gel derived PZT 40/60 films using two or three step processing. Films treated under two step processed were exposed to drying temperature at 300°C

and to the crystallization temperature above 600°C. The orientation of the latter films was predominately (100). PZT 40/60 films treated under three step processing were exposed also to the thermal treatment at 300°C and the same crystallization temperature, but were additionally treated to the 400°C for 30 minutes after drying and before crystallization. Such films showed predominant (111) orientation. In the work of Liu and Phule the temperature at 400°C was attributed to the pyrolysis temperature and thus to the pyrochlore formation temperature. The difference in the pyrochlore formation temperature in this work to the work of Liu and Phule is likely to be due to different precursor solvent.

A crystallization sequence was proposed by Brooks et al. [135], which involves the formation of metastable or stable pyrochlore phase. Dependent on the oxygen partial pressure in the sol-gel film and the choice of pyrolysis temperature and duration, either a stable or a metastable pyrochlore can be formed. Longer pyrolysis duration leads to higher oxygen partial pressure (through oxidation in ambient air) and to the more stable pyrochlore structure whereas shorter pyroloysis time leads to the oxygen deficient and metastable pyrochlore. The more stable pyrochlore phase is associated to the ordered fluorite phase [70, 183, 217]. The formation of the metastable and oxygen deficient phase leads to (100) orientation and from the stable and ordered $Pb_2(Zr,Ti)_2O_7$ phase a nucleation of (111) perovskite would result [242]. The reduction in oxygen partial pressure is believed to be a transient effect which is most pronounced during the initial stages of pyrolysis at moderate temperatures. Thus, the results obtained on PZT 40/60 films in this work correlate to the idea of the effect of pyrochlore stability on the orientation.

The influence of the thermal treatment period at 300°C on the orientation of PZT 40/60 films was not noticeable although a relation between the hydrolysis ratio and the pyrolysis temperature was reported [85]. According to Schwartz et al [85] the changes in pyrolysis behaviour of the species that accompany changes in solution hydrolysis ratio may be the cause of change in film orientation. In more hydrolysed precursors the pyrolysis temperature was observed to start at lower temperatures. The lower pyrolysis temperature would allow for crystallization to proceed at lower temperatures than in precursors prepared using lower hydrolysis ratio. In respect to this work, this would mean that the longer period at the drying temperature at 300°C would shift the

pyrochlore formation temperature to lower temperatures than e.g. 450°C, along with the shift of the crystallization temperature to lower temperatures. However, all films in this work were treated at the same temperatures and thus the pyrochlore formation could only start at 450°C and not below this temperature. If there was any influence of the drying period on the pyrolysis temperature it would possibly affect the kinetics of pyrochlore formation. Possibly the pyrochlore could transform to the more stable phase in shorter time if longer drying times at 300°C were employed. However, no significant effect of the drying period on the orientation was observed in this work. In addition, the effect of the drying period on the orientation could be more pronounced if the PZT films were heated continuously from the room temperature to the crystallization temperature e.g. in the RTA furnace.

A clear relation between the annealing duration and the orientation could not be derived. It was observed that PZT 40/60 films were fully crystallized after only 2 minutes annealing. However, it would be more appropriate to consider the duration at the annealing temperature in connection with the duration at the pyrochlore formation temperature. Dependent on the duration at the pyrochlore formation temperature the stability of pyrochlore phase is altered. When the film is transferred to the next higher temperature the nuclei form and grow dependent on the stability of pyrochlore, giving rise to the energetically favourable events at the crystallization temperature. Thus, if very large number of (111) nuclei is formed before the grain growth occurs, the longer annealing time would allow the (111) grains to consume the pyrochlore matrix. If equal number of (111) and (100) nuclei was formed longer times at crystallization temperature would result in predominant (100) orientation as the lateral growth of (100) crystallites would suppressing the growth in (111) direction. Thus, there are several factors that influence the film orientation at the annealing temperature. The formation and the density of interface nuclei is the first factor. The low density of the interface nuclei will allow the formation of other nucleation mechanisms. The kinetics of the grain growth is another time-dependent factor. The third factor of the crystal growth and the orientation is the role of stress at the crystallization temperature and is proposed in this work. However, before the role of stress is discussed the formation of intermetallic phase Pt_3Pb needs to be mentioned as the Pt_3Pb phase was reported to interact strongly in the orientation formation of PZT 30/70 films [243].

4.2.1.2 The role of the intermetallic phase Pt_3Pb formation

In PZT films with PZT 30/70 composition and thus very similar to PZT 40/60 the formation of Pt_3Pb intermetallic phase was reported by Huang et al [243]. The formation of Pt_3Pb phase was associated to the improvement of the lattice match between PZT (111) and Pt(111). The low degree of (111) orientation in PZT 40/60 films suggest that this mechanism was mostly suppressed in PZT 40/60 films in this work. A more detailed analysis of the occurrence of this phase showed that the drying and pyrolysis temperature greatly affected the formation and stability of the Pt_3Pb phase. When the PZT 30/70 films were dried at 300°C and pyrolysed at 440°C the Pt_3Pb phase was stable for only 3 minutes [244]. These processing conditions are in correlation to this work. Thus, Pt_3Pb phase was less stable in the PZT 40/60. Also, the single layer thickness is different in this work to the work of Huang et al which could affect the stability of the Pt_3Pb phase.

4.2.1.3 The role of stress on the orientation

The role of stress on the orientation has been shown on the example of PZT 40/60 films. The PZT 40/60 films processed under the same processing conditions but on substrate with different stress showed also a different orientation. PZT 40/60 films deposited on tensile substrate showed high degree of (100) orientation. In contrast, PZT 40/60 films deposited on compressive substrate showed high degree of (111) orientation. There are two possibilities how stress affects the orientation of the film. The first mechanism is direct influence on the nucleation mechanism e.g. by promotion of the Pt_3Pb phase formation or increasing the pyrochlore stability. The second mechanism affects the change of orientation with thickness by stabilizing the (100) lateral growth under tensile stress and suppressing the (100) lateral growth under compressive stress. Unfortunately, the change of orientation in films grown on compressive substrate was not studied in this work. However, the degree of the (111) orientation in the films grown on compressive and tensile substrate under the same processing conditions can be considered to estimate which mechanism of the two mentioned is primary influence by the stress.

The diffracted intensities of the films processed under the same conditions but on substrates with different stress was shown in Section 3.4, Tab. 3.12 and 3.13. The PZT 40/60 film 17 exhibited 83% (111) diffraction intensity at 2 μm thickness. It is interesting to note that this was also the highest degree of (111) orientation obtained in 2 μm thick PZT 40/60 films. PZT 40/60 film 8 was processed under the same conditions but on tensile substrate and exhibited only 11% of (111) diffraction intensity at 2μm thickness. If the nucleation mechanisms were only affected by the stress and the lateral growth of (100) was not influenced by the stress state, then much lower degree of (111) orientation than found should be expected in 2 μm thick film (film 17). In contrast, it is also possible that the (111) orientation was promoted by the compressive stress in such strong manner that the lateral growth in (100) direction was only minimal as there were only few (100) oriented grains. In any case, the high degree of (111) orientation in film 17 suggests very high effect of the stress on nucleation mechanism, probably by supporting the mechanisms responsible for PZT (1111) nucleation.

The PZT 40/60 film deposited on sapphire substrate (film 15) was under compressive stress at the room temperature but at the crystallization temperature it was most likely under tensile stress. Such change of compressive stress was reported by [183] for PZT films deposited on MgO and is due to the difference of the thermal expansion between PZT film and the MgO or PZT film and Al_2O_3 substrate. Thus, a PZT film deposited on tensile substrate and Film 15 should exhibit same preferred orientation if processed under the same processing conditions, as both films were under tensile stress at the crystallization temperature. However, this was not the case. Film 15 exhibited only 54% (100) orientation and the PZT 40/60 film on tensile substrate showed 89% of (100) diffraction intensity in 3 μm thick film. Supposed the stress would mainly affect the lateral growth in (100) direction much higher (100) orientation should be obtained in Film 15, especially as the film thickness was above 3 μm. The fact that this was not the case suggests that the stress might have only secondary effect on the change of orientation with thickness.

The main difference between the film deposited on tensile substrate and Film 15 is the different state of stress in the substrate. This effect of substrate stress was already mentioned in Section 3.4.6. The change of wafer bending from compressive shape to tensile shape implies large changes in the dimensions of the substrate and directly

affects the stress in the film. From the considerations of thermal expansion coefficients in Film 15 it can be assumed that the stress change from compressive to tensile takes place above the phase transition temperature. Thus, Film 15 is under compressive stress and changes to tensile stress immediately at above the crystallization temperature.
From the observations on Film 15 and 17 it can be concluded that the stress had major effect on the nucleation mechanisms. Further, it can be said that the compressive stress supports the (111) orientation. However, it can not be concluded whether the promotion of (111) orientation is due to increased stability of pyrochlore phase due to compressive stress or possibly due to formation of the intermetallic phase Pt_3Pb.

4.2.2 Nucleation in PZT 52/48

Compared to PZT 40/60 films, the PZT 52/48 showed very different influence of the processing parameters on the orientation. The PZT 52/48 films treated for a shorter time at 450°C temperature had mainly (111) orientation and those treated for a longer period had predominant (100) orientation. Thus, the nucleation mechanism in PZT 52/48 cannot be explained only on the model of pyrochlore stability.

Investigations of the pyrolysis temperature on the orientation of PZT 52/48 films were performed by Marshall et al [215]. The pyrolysis temperature was varied between 200°C and 420°C and it was reported that the pyrolysis above 400°C supports predominately (111) orientation along with some (100) orientation. The predominant (111) orientation was explained as being due to formation of Pt_3Pb phase. However, the unit cell parameters of PZT 52/48 films are different from those of PZT 40/60 as shown in Section 3.5.1 and thus it is possible that the stability range of Pt_3Pb phase is increased in PZT 52/48 films compared to PZT 40/60.

In PZT 52/48 films no clear relation between the processing temperatures and film orientation was observed as in PZT 40/60 films. The sol stochiometry can also greatly affect the formation of pyrochlore phase [183]. According to the results from Section 3.2.6 the temperature range for PZT 52/48 for pyrochlore formation and crystallization were slightly different from in PZT 40/60. The crystallization in PZT 52/48 films occurred already at 475°C indicating faster formation of intermediate pyrochlore phase. It is likely that PZT 52/48 pyrochlore formation is mush faster than in

PZT 40/60 and that stable pyrochlore phase forms already after 2 minutes so that no major difference between pyrolysis duration for 5 minutes and 2 minutes can be observed in PZT 52/48. The high density of interface nuclei does not allow formation of other nuclei, e.g. (100), on the interface. Thus, the crystallite growth of (111) lattice plains is less suppressed through crystallite growth of (100) lattice planes and explains why PZT films at 2 micron thick show very high (111) orientation.

4.3 On the residual stress

4.3.1 Calculation assumption

In Chapter 3.4.2 it was assumed that the wafer is flat at the crystallization temperature and according to this assumption the stress was calculated. The assumption of flat wafer at the crystallization temperature is difficult to prove. The considerations of the stress in platinum and the curvature calculations show that there is a good agreement between this assumption and the experiment. The only way to prove this would be in-situ curvature measurement. Some authors reported in-situ stress measurement in PZT films, like Sengupta et al [245], Park et al [164] and Garino et al [129]. From all reported results the measurements preformed by Garino et al [129] were most comparable to this work. Garino et al showed a decrease of stress below 50 MPa towards the crystallization, if e.g. the initial stress was around 300 MPa. The results of Park et al and Sengupta et al are not comparable as these authors deposited PZT sol directly on silicon substrate without platinum electrode. Thus, a lead silicate formation was found and the films were not completely crystallized.

In this work the processing conditions were chosen in the way to minimize the occurrence of stress and thus differ from all other reported works on stress in PZT films. One indication of zero-stress after the crystallization in PZT films in this work is the stability of microstructure of PZT films after complete crystallization. In Chapter 3.3.4 it was shown that post-annealing had no effect on the PZT orientation if the film was fully crystallized before post-annealing and if the same temperature was used as the crystallization temperature. Supposed the film was not in equilibrium after crystallization the strain in the film could act as a driving force for grain growth during

the post-annealing which would be observed in different orientation after annealing. The fact that such grain growth was not observed supports the assumption of flat wafer.

This assumption is very important as it may change the magnitude of the stress results drastically. For instance, if a shrinkage of 0.1% of PZT is assumed at the crystallization temperature the calculated stress in the PZT film would be 140 MPa instead of 60 MPa that was calculated assuming the flat wafer. The strain at room temperature would then add up to 0.0016 instead of 0.0006. To limit and reduce further the uncertainty of this point, the residual stress results were compared to the micro strain determination via Williamson-Hall method. The strain results are given for both methods, Tab. 4.2. The linear regression of the Williamson Hall plot was carried out. The relatively large error in the Williamson-Hall plots is due to high degree of texture in the PZT films and low intensity of some peaks. In the 2µm thick (100) oriented PZT 52/48 films there were only 2 pairs of peaks that could be used for the analysis which is not sufficient for the linear regression. Also, the phase coexistence in PZT 52/48 films limits further the accuracy of the Williamson-Hall method and only results of the tetragonal phase were given. Except for 2 films (underlined in Tab. 4.2), the results of Williamson-Hall plot and residual strain calculation using the Townsend-Model and wafer curvature measurements show a reasonable match.

Tab. 4.2: Strain in PZT films of different composition, based on the stress results, Section 3.3.

		strain calculated using the stress model		Williamson-Hall plot	r^2, Will.-Hall plot
PZT composition	Film thickness	Pt at RT	PZT at RT	strain in PZT	
PZT 52/48 (100)	2 µm	0.0029	0.00022	not possible	
PZT 52/48 (100)	3 µm	0.0029	0.0002	<u>0.0011</u>	0.90
PZT 52/48 (111)	3 µm	0.0029	0.00066	0.001	0.7
PZT 52/48 (111)	4 µm	0.0034	0.0011	0.0012	0.6
PZT 60/40 film 1	5 µm	0.0034	0.00073	0.0005	0.8
PZT 60/40 film 2	5 µm	0.0034	0.000725	0.0005	0.9
PZT 40/60, 2”	2 µm	0.0029	0.00011	-	0.1
PZT 40/60, 4”	2 µm	0.0033	0.00012	<u>0.0011</u>	0.66
PZT 40/60 on sapphire	3.4 µm	0.0014	-0.0014	-0.0012	0.8

In the PZT 52/48 film some discrepancy between the results of the two methods can be due to the phase coexistence as no results could be given for the rhombohedral phase. Supposed compressive microstrain was found in the rhombohedral phase and high tensile strain in the tetragonal phase then the resultant macrostrain would be the sum of the strain of the individual phases. In the PZT 40/60 4” the large deviation of the results was not clear.

Thus, with both methods similar results are obtained. By refining the Williamson-Hall method, e.g. the resolution of the x-ray scan and longer scan times, a better peak-to-noise ratio could be obtained and thus more accurate peak fit results with Williamson-Hall plot would be obtained. The results from the Williamson-Hall plot or any other method could be used to limit or rule out any uncertainty from the basic assumption used in the stress calculation. Also, if any deviation from the assumption would be known, it could be easily implemented into the model.

4.3.2 Sources of error in stress calculation

The experimental error was deduced from several measurements which included the reproducibility of the measurement along the same line with and without removing the wafer between the measurements. The total experimental error was limited to 0.5 μm. The PZT deflection results were fitted using the linear regression in order to check the used coefficients. The linear regression of the deflection differed from film to film. However, the maximum deflection deviation value that was used for stress calculation was below 0.1 μm. The maximum error in terms of PZT stresses for such deflection deviation was around 0.3 %. The good reproducibility of stress was observed on two PZT 60/40 films, Fig. 4.1.

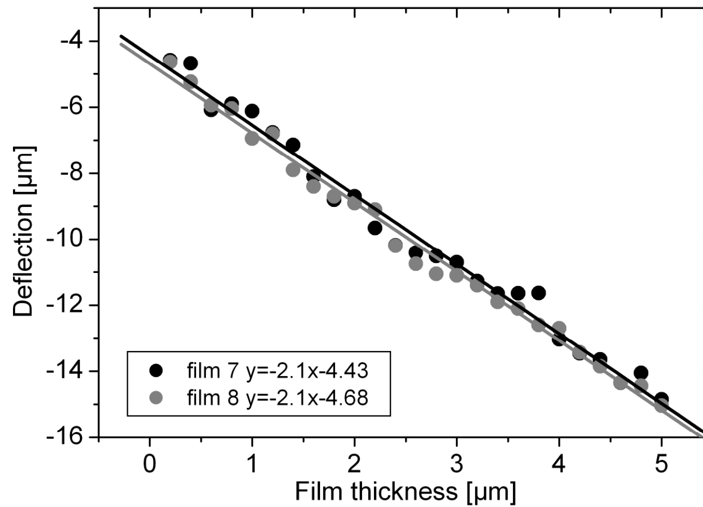

Fig. 4.1: Stress measurement and orientation reproducibility.

The two PZT 60/40 films (film 7 and 8, App. A) were deposited under similar conditions, but the difference was the drying time. Film 8 was dried for 3 minutes at 300°C and film 2 for 5 minutes. The stress difference was 1 MPa between two films and the orientation was (100) orientation for both films. The percentage of (100) orientation was 85% for the first film and 90% for the second film. This can be considered as very good reproducibility of the experimental results. In the stress calculation there are two sources of error. The first one was the assumption of the initial wafer curvature and was already discussed. The weighted average of TEC is the other one. It was also assumed that the thermal stress builds up linearly with cooling. The results of Garino et al [129] and Tuttle et al [183] suggest that the stress in PZT is not exactly linear with temperature upon cooling. Two ranges were distinguishable. The first range is below the crystallization temperature and above the transition temperature where the tensile stress is linearly increasing. In second temperature range below the transition temperature and room temperature the stress was linearly decreasing. In this work the same results were found if the stress was calculated separately for the two ranges. However, the stress difference was the same and was equal if the stress was calculated using the weighted average TECs. This was expected and thus justifies the use of the weighted average TECs. Nevertheless, some error was introduced assuming that the thermal expansion coefficient of the substrate, e.g. TEC of silicon, is linear with

temperature. To increase the accuracy of the calculation, the stress could be calculated in the whole temperature range between room temperature and 550°C using the temperature-dependent TECs and Youngs Moduli of each phase. However, such calculation requires the uses of the TECs data and the Young's Moduli of PZT 40/60 and PZT 60/40 in the temperature range; however, these data are not available. The error introduced using the linear TECs and reproducing the figures from the literature to determine the TEC is estimated to be below 15%.

4.3.3 Stress results correlation to the results determined using the Stoney Equation

The residual stress calculated using the Townsend model correlates to the results obtained using the simpler Stoney Equation [246]. The origin of the Townsend model and Stoney Equation is the same, but the Stoney Eq. is a further approximation for thin films deposited on thick substrates. The stress can be calculated after Stoney Eq. [160] as

$$\sigma = \frac{1}{6}\left(\frac{1}{R_{post}} - \frac{1}{R_{pre}}\right)\frac{Y}{(1-\upsilon)}\frac{t_s^2}{t_f} \qquad (4.1)$$

where R_{post} and R_{pre} are the radii of curvature before and after PZT deposition, E/(1-v) is the biaxial Young's Modulus of the substrate, t_s the thickness of the substrate and t_f is the film thickness. The use of the complex Townsend Model instead of the simpler Stoney Equation may not be justified at first, as many approximations must be made with the Townsend model and the residual stress results of both methods correlate. However, the Stoney Equation in connection with ex-situ curvature measurement cannot give any insight into the origin of stress. With Stoney Eq. it cannot be concluded if the residual stress is the product of thermal mismatch between the layers or due to intrinsic stress in PZT. Using the Townsend Model a more detailed stress analysis was possible and it was shown that the TEC and Youngs Modulus difference between PZT and the substrate have major contribution to the stress in PZT. Also, the contribution of the substrate was characterized. Furthermore, the stress analysis carried out with the

Townsend Model enables the estimation of stress without experimental data collection, supposed the TEC and Young's Modulus of the substrate is known. Also, the optimization of residual stress for e.g. MEMS design would be possible using the results obtained from the stress analysis. However, the requirement of the Townsend Model for all material parameters to be known for the calculation is a major disadvantage. For instance, the experimental stress data was collected for PZT 52/48 on LNO/Si substrate but due to the lack of the TEC and Young's Modulus of LNO in the literature the stress analysis could not be carried out.

4.3.4 Residual stress in PZT films

The residual stress determined in this work correlates roughly to the residual stress in sol-gel films reported in the literature. Most authors reported the PZT stress at certain thickness. Such measurement with increasing thickness was only reported by [201] but on ZrO_2/Si substrate. However, no stress measurement in PZT films with different orientation was reported in the literature. Also no stress measurement was reported in PZT films with pure rhombohedral compositions. The available residual stress measurement data found in the literature is summarized in Tab. 4.3. It can be seen that the residual stress results in PZT 52/48 films on Pt/Si in this work are in good agreement with the results reported by [11, 117, 134]. The difference in residual stress with PZT composition is in agreement with the work of [200] where higher stress was found in PZT 52/48 than in PZT 40/60. The effect of stress during PZT processing on the orientation of PZT films was already discussed.

One other effect of the stress on the PZT structure is the domain orientation at the transition temperature as reported by Tuttle et al [11, 123, 122]. In tensile PZT 40/60 films with high degree of (100) orientation the maximum *c* domain fraction was around 30% showing equal fractions of a_1, a_2 and c domains. Thus, the total fraction of *a*-domains was larger as a result of tensile stress at the transition temperature.

The PZT 40/60 film on sapphire substrate showed 55% of *c* domains relative to *a* domains, and the PZT 40/60 film deposited on sapphire substrate without platinum electrode exhibited 46% of *c*-domains. This difference can only be due to compressive stress at the transition temperature.

Tab. 4.3: Summary of sol-gel related residual stress reported in literature.

PZT composition	**PZT film thickness**	**Stress [MPa]**	**Substrate**	**stress determination method**	**Author**
53/47	not reported	100	Pt/Si	wafer curvature	[11]
	not reported	-470	MgO	wafer curvature	
53/47	0.172 µm	200		raman spectroscopy	[247]
	0.172 µm	133		XRD	
52/48	1.7 µm	250	Pt/Si	XRD	[199]
	1.1 to 1.8 µm	135 to 197 MPa	Pt/Si	wafer curvature	[134]
52/48	0.22 µm to 0.8 µm	113 to 165	$Ta/Pt/SiO_2$ /Si	wafer curvature	[248]
53/47	0.4 µm	200	Pt/Si	in situ curvature	[129]
40/60	1.2 µm	160		XRD	[200]
52/48	1.2 µm	350			
53/47		120 to 140		wafer curvature	[164]
50/50	0.220 µm	113		wafer curvature	[117]
54/46	0.4 µm	200-250	$Pt/Ti/SiO_2$ /Si	wafer curvature	[249]

The equilibrium domain formation due to stress that accumulates between the crystallization and the transition temperature dictates the ratio of (001) to (100) orientations. Furthermore the ratio of (100) to (001) oriented crystallites will influence further shrinkage or expansion of the PZT films between the transition temperature and the room temperature and thus affects the total residual stress. In PZT 40/60 films from the sample batch PZT 40/60-Pt(111)/Si-3µm-10 all films showed similar ratio of (001) to (100) orientation and thus the c/a-ratio was in the same range for all films. Also, the thermal expansion coefficient of such PZT 40/60 films was equal to the average TEC for randomly oriented PZT and thus no anisotropy of the thermal expansion was noticed. However, the films showed very low residual stress.

The films PZT 40/60 films deposited under compressive stress at the room temperature showed higher fraction of (001) to (100) and also some difference in the c/a-ratio. The variation of the lattice parameters is dependent upon the residual stress in the PZT film which goes back to the ratio of (001) and (100) orientation and the anisotropic thermal expansion coefficients. This was shown on the dependence of the

c/a-ratio on the degree of (100) orientation in PZT 40/60 films. Thus, the stress at the transition temperature will affect the residual stress significantly.

The effect of the anisotropic thermal expansion was first noticed in PZT 52/48 films on the large residual stress variation of PZT 52/48 films with different orientation. In PZT 52/48 films the stress at the transition temperature dictates the phase and domain orientation formation. According to the phase field calculation [188] first the tetragonal split occurs and afterwards the rhombohedral phase was formed. Thus, PZT 52/48 has more variables to react to stress than PZT 40/60. This explains why in PZT 52/48 films grown on tensile substrate much higher fraction of (001) domains to (100) domains can be found than in PZT 40/60. Thus, the ratio of the (001) to (100) orientation alters the total in-plane thermal expansion coefficient. The rhombohedral phase in this PZT composition has probably not as high anisotropy of the thermal expansion as tetragonal PZT. A smaller variation of the thermal expansion and thus the lattice parameter can be expected for rhombohedral phase which was observed in Chapter 3.5.1. The sequence of the phase formation in PZT 52/48 during cooling explains why the relation between the rhombohedral phase and the tetragonal c/a-ratio was found. It can be assumed that the phase formation in PZT 52/48 is quite complex. The phase field calculations suggest that the phase formation does not occur at one discreet temperature but moreover in the whole temperature range above the room temperature. Thus, even slight strain variation in PZT films can result in different phase content at a given orientation. It is also imaginable that the ratio of the tetragonal phase in the (100) oriented PZT 52/48 film can alter the stress in the film and dictate the rhombohedral phase formation. However, this goes beyond the scope of this work.

4.3.5 Residual stress and fracture

In the thick films processed in this work no major stress increase with thickness was observed. The stress increase in the films is in the range of 1 to 2 MPa. Other authors have reported major stress increase with layer deposition. The results show either reduction of the stress with increasing thickness [250] or major stress increase with film thickness increase [201]. The experimental results in this work have shown that after the

deposition of the first PZT layer the stress does not change significantly with further PZT deposition. This is in agreement with the observation that the films do not crack after e.g. 25 layers were deposited. The bending strength of PZT ceramics was determined to be around 90 MPa [127]. Taking into account that the bending strength is probably higher in PZT films than [249] in ceramics, due to substrate clamping, the residual stresses in the PZT films are probably just below the maximum bending strength. Thus, a high incremental stress in PZT films would approximate or exceed the bending strength after only couple of layer deposition and the films would crack. The fact that cracking was not observed after the deposition of 25 layers supports the results that the incremental stress was only minimal.

4.4. Piezoelectric response of PZT films

The investigation of piezoelectric and dielectric properties has shown that the piezoelectric and dielectric properties were both PZT composition and orientation dependent. Some dependence of the electric properties on the thickness was found.

The highest piezoelectric response was found in PZT 52/48 film at comparable thickness of 2-3 µm to other PZT compositions. This was expected from the observation on PZT ceramics and films and was reported by several authors [185, 231, 233].

Highest $d_{33,f}$ and $e_{31,f}$ were determined for (100) orientation, both in PZT 40/60 films and PZT 52/48 films (sample batches PZT 52/48-Pt(111)/Si-2µm-10 and PZT 40/60-Pt(111)/Si-3µm-10). According to the maximum polarization in tetragonal films along the direction <001> the highest polarization would be expected for films with high fraction of c-domains. As the (100) oriented PZT films comprise always a mixture of (100) and (001) domains it is reasonable to assume higher piezoelectric response in (100) oriented films than e.g. in predominately (111) oriented PZT films. Also, during poling some switching can occur and increase the fraction of c-domains.

The piezoelectric response of 3 µm thick rhombohedral films from the batch PZT 60/40-Pt(111)/Si-3µm-6 could not be correlated to the film orientation as all PZT 60/40 films had mixed orientation. However, the piezoelectric response of the PZT 60/40 film deposited on Pt(200) substrate was higher than on Pt(111) due to high (100) intensity. In the rhombohedral PZT films the highest piezoelectric response can be

expected along the pseudocubic (100) direction according to the results reported in Ref. [19-20].

The piezoelectric coefficient of two other PZT compositions PZT 40/60 and PZT 52/48 deposited on Pt(200) substrate was comparable to the (100) oriented PZT 52/48 films and PZT 40/60 respectively. The PZT 40/60 film exhibited slightly lower $d_{33,f}$ values on Pt(200) than on Pt(111). However, the PZT 40/60 film was also only 2 µm thick whereas the PZT 40/60 films on Pt(111) were 3 µm thick. In PZT 40/60 films the clamping to the substrate has shown most pronounced effect compared to PZT 52/48 and PZT 60/40 films. The in-plane tensile stress stabilizes a-domains at room temperature and the 90° domain switching was enabled only if the poling temperature was noticeably increased. The increase of poling temperature leads to the lower thermal strain in the film and thus the switching of 90° domains was easier. The effect of stress on the piezoelectric response was evident in the sample PZT 40/60- Pt(111)/Si/Pt/2" - 2 µm film 17. This PZT 40/60 film 17 although only 2 µm thick and predominantly (111) oriented exhibited $d_{33,f}$= -75 pC/N which is comparable to (100) oriented 3 µm PZT 40/60 films on tensile substrate.

As mentioned earlier, the effect of substrate clamping in PZT 40/60 films was most pronounced in PZT 40/60 films due to lower degree of switchable domains. In 5 µm PZT 40/60 film the highest piezoelectric response was found. This can be attributed to the lower substrate clamping of PZT 40/60 films with thickness around 5 µm.

The effect of substrate clamping on the piezoelectric response was also observed in PZT 60/40 films. A $d_{33,f}$ around 98 pC/N was measured for 5 µm PZT 60/40 films. The high piezoelectric response was partly due to the high degree of (100) orientation but most likely due to the weaker substrate clamping in thicker films. A comparable 5 µm thick PZT 52/48 film was not obtained in this work. The highest thickness of PZT 52/48 films was 4 µm and thus only limited comparison was possible. Also, some difficulties were observed during poling of PZT 52/48 films.

The piezoelectric response was dependent on the existence of an interfacial layer between the PZT film and the electrode. This interfacial layer is probably only a couple of unit cells thick and thus it is difficult to observe it. However, Grossmann et al [227-228] established a model of such interfacial layer and explained its effect on the domain

pinning and depolarization. According to Grossmann et al the thickness of such interfacial layer is dependent on the composition.

The existence of the interfacial layer was correlated to the films in this work. In PZT 40/60 films the largest dependence of the piezoelectric properties was observed and was attributed to the substrate clamping. Also, the PZT 40/60 films were mostly (100) oriented regardless the orientation of the bottom electrode and the lattice match of PZT(111) and Pt(111). Usually, PZT does not nucleate directly on Pt and thus there must be a matching layer between PZT and platinum to improve the adhesion. This layer needs to be not more than a couple of atomic layers thick. The orientation and crystal growth in PZT 60/40 and PZT 52/48 were different to PZT 40/60 and showed a higher degree of (111) orientation on Pt(111) and higher (100) orientation if Pt(200) substrate was employed. According to the better match of PZT 52/48 and PZT 60/40 orientation to the orientation of Pt it can be assumed that the interfacial layer in PZT 60/40 and PZT 52/48 is thinner than in PZT 40/60 films.

Another indication of the influence of the interfacial layer in PZT films was observed in the shift of the hysteresis loop. All PZT films showed a hysteresis shift towards positive electric field at increased temperature. The shift was most pronounced in PZT 40/60 films. According to Grossman the interfacial layer thickness can increase at higher temperature. The highest shift in PZT 40/60 films is another indication of the thicker interfacial layer in PZT 40/60 films. This result is well in agreement with the proposed influence of the interfacial layer on the piezoelectric response in PZT 40/60 films.

The $e_{31,f}$ coefficient was also found to be higher in PZT films with higher (100) orientation. However, in 5 µm thick PZT 40/60 and PZT 60/40 a lower increase of $e_{31,f}$ coefficient was found relative to the $d_{33,f}$. This is probably due to the effect of in-plane tensile stress as the $e_{31,f}$ is more sensitive to stress [251]. Comparable $e_{31,f}$ values to this work were reported by [185]. The $e_{31,f}$ in this work exhibited higher values than the $e_{31,f}$ reported by [223, 231, 252].

The PZT 52/48 films deposited on LNO have shown good piezoelectric and dielectric properties comparable to films deposited on Pt(111) substrates, although these films had lower degree of (100) orientation. Due to good lattice match between PZT and LNO it is also expected that the interfacial layer in PZT films deposited on LNO is

lower and thus higher extrinsic contribution of PZT 52/48 can be assumed. Enhancement of piezoelectric response could be expected in such films if the degree of (100) orientation was increased.

Chapter 5: Conclusions and further work

5.1 Conclusions

5.1.1 Thick film processing

The processing parameters, the orientation, residual stress and the electric properties of the sol-gel PZT films of three different compositions were studied. The PZT compositions were the tetragonal PZT 40/60, the rhombohedral PZT 60/40 and a composition at the morphotropic phase boundary PZT 52/48.

The stress development during sol-gel film processing was studied. It was found that the key processing parameter to obtain crack-free thick films was the choice of an appropriate thermal profile. Thus a four-step process was established. Using such thermal profile films with total thickness up to 5 μm were fabricated. All PZT films were treated at the same temperatures. The variation of the duration at the processing temperatures enabled fabrication of films with different crystallographic orientation.

The stress-related processes were systematically studied in PZT films with different compositions and in films of the same composition but produced with sol of different concentration. It was found that there were some minor differences between the PZT compositions, for example, pyrochlore phase starts forming at lower temperature in PZT 60/40 films than in PZT 40/60 films. Processing of films with thickness increased single layers using 1M sol has shown that in such films the most critical processing step is the drying of the films.

The PZT stress development was studied on different types of substrate and it was found that the type of substrates influenced the initial temperatures of pyrochlore formation and PZT crystallization. Also, the stress in the substrate showed large contribution to the total stress. A stress-related recrystallization of platinum was found. The kinetics of the recrystallization was strongly dependent on the thickness of the titanium adhesion layer.

The thickness of a single crack-free was increased up to 500 nm. However, such films were difficult to crystallize and some residual pyrochlore was detected. Thus, the

most film characterization was conducted on films with 200 nm single layer thickness. Maximum total thickness of such PZT films was 5 µm. All such PZT films were dense and crack-free. It must be noted that 5 µm was not the critical thickness of the films and probably much thicker films can be obtained if more layers were coated.

5.1.2 Control of crystallographic orientation

The orientation of all three PZT compositions was intensively studied on Pt(111)/Si substrates. The nucleation and the influence of the processing parameters on the orientation in each composition were discussed. It was concluded that PZT 40/60 films nucleate and grow preferably in (100) orientation as the thermal processing parameters were not favourable to form the intermetallic phase Pt_3Pb which would support the (111) nucleation. Also, the role of pyrochlore formation and stability played an important role in the orientation selection. It was concluded that longer time at the pyrolysis temperature resulted in much more ordered pyrochlore and thus in (111) orientation. Zr- rich PZT films tended to form pyrochlore easily, which was responsible for higher fraction of (111) orientation in the PZT 52/48 and PZT 60/40 films.

Change of orientation with thickness was observed in all films. In all PZT compositions, the decrease of (111) texture and the increase of (100) orientation in thicker films were observed, and in PZT 60/40 films crystallite growth in (211) or (110) direction was observed beside the (100) crystal growth. All 5 µm thick films were strongly (100) textured. The increase of (100) orientation was attributed to the faster crystallite growth of PZT in (100) direction than e.g. in (111) direction and thus faster lateral growth in (100) direction.

5.1.3 Residual stress

The stress development in the PZT films was explained. The substrate type and dimensions have a large influence on the stress in the film and depending on the stress in the substrate the films with completely different orientations could be obtained. In PZT 40/60 films deposited in compressive substrate showed predominant (111)

orientation whereas PZT 40/60 films deposited on tensile substrate and processed under the same conditions showed predominant (100) orientation.

It was shown that the residual stress is mainly due to thermal mismatch of PZT, after crystallization, to the substrate layers. The accumulated stress at the transition temperature dictates the formation of equilibrium domain orientation according to Tuttle et al. This was confirmed in this work. Furthermore, the domain orientation and the anisotropy of the thermal expansion coefficients of PZT had significant effect on the residual stress. The in-plane expansion of *a* oriented domains upon cooling compensated for the contraction of *c* domains and thus very low residual stress can be found, depending on the ratio of *c* to *a* domains. In PZT 40/60 films the same fraction of c, a_1 and a_2 domains was observed so that the overall TEC was coincidence with the average TEC. The highest effect on the anisotropic thermal expansion was found in PZT 52/48 films. In these films the phase formation and tetragonal splitting occur below the transition temperature showing higher flexibility to react to stress, e.g. by formation of various ratio of *c* to *a* domains or different ratio of tetragonal to rhombohedral phase. Thus, higher fraction of *c*-domains can be obtained.

The tetragonal split was studied on the c/a-ratio in PZT 40/60 and PZT 52/48. It was shown that the c/a-ratio depends on the fraction of (100) oriented domains in PZT 40/60 films. In PZT 52/48 films the c/a-ratio dependence on stress was more complex than in PZT 40/60 films. A relation between the c/a-ratio of the tetragonal phase and the content of (100) oriented rhombohedral phase was found. The lattice parameters of the rhombohedral phase were also dependent on the content of (100) oriented rhombohedral phase in PZT 52/48 films.

Between the three PZT compositions the highest stress was found in (111) oriented PZT 52/48 films followed by PZT 60/40 films. Very low stress was found in (100) oriented PZT 52/48 films and the lowest stress was found in PZT 60/40 films.

The effect of the substrate stress on phase formation was shown in PZT 52/48. On tensile substrates rhombohedral and tetragonal phase coexisted while on compressive substrates only rhombohedral and probably completely distorted *a* domain oriented tetragonal phase were found. The results were in agreement with the phase-field calculations.

5.1.4 Piezoelectric properties

The piezoelectric properties were measured for all films and were analyzed in films with different composition, orientation and thickness. The highest piezoelectric coefficients in 3 μm thick films or below 3μm were found for (100) orientation in all compositions. The highest piezoelectric coefficients $d_{33,f}$ and $e_{31,f}$ were found in PZT 52/48 film composition.

In the films with thicker single layers the magnitude of piezoelectric coefficient was in the same range as in the films with thinner single layers.

The observation of thickness dependent electrical properties leads to the assumption of the existence of an interfacial layer in all films. The thickness of this layer was different in different PZT compositions and its thickness can vary depending on the lattice match between the film and the substrate.

Five micron thick PZT 40/60 and PZT 60/40 films were fabricated. The piezoelectric response in 5 micron thick films was enhanced exhibiting $d_{33,f}$ = 160 pC/N in the PZT 40/60 film and $d_{33,f}$ = 98 pC/N in PZT 60/40 films. The enhanced piezoelectric response was attributed to the weaker substrate clamping in thick films.

5.2 Further work

The future work should address following points:

- further film thickness increase and investigation of piezoelectric properties
- measurement of the piezoelectric coefficient $d_{31,f}$ and coupling coefficient $k_{31,f}$
- lattice parameter investigation
- stress modelling in MEMS devices design and fabrication
- domain switching during poling

5.2.1 Further film thickness increase

The desirable single layer thickness for MEMS applications would be ideally around 1 μm per layer. Thus, more work is required to investigate the possibilities to fabricate

such thick films. Also, more work is needed on films with 500 nm thick single layer, e.g. orientation and characterization of properties. A deposition of 5 µm thick films with only 10 layers e.g. would be desirable. Study of the piezoelectric properties of such films is of great importance. Two factors regarding, and possibly limiting, the thick sol-gel film fabrication are the adhesion of the bottom electrode to the substrate and the heating rate during sol-gel processing needs to be varied to find the best drying profile. It is also not excluded that at some point the sol precursor needs modification.

5.2.2 Measurement of the piezoelectric coefficient $d_{31,f}$ and the coupling coefficient $k_{31,f}$

Within this project cantilever devices were produced for determination of $d_{31,f}$ coefficient and $k_{31,f}$ coefficient. Unfortunately, the Polytech™ vibrometer for cantilever device testing was not accessible for large period of time and the cantilevers could not be tested. Thus, this part of the project was not mentioned within this thesis as no measurement results were obtained. This is one of the primary objectives of further work on PZT film for MEMS devices.

The device design for determination of piezoelectric coefficients is depicted in Fig. 5.1. The cantilever beam length was varying between 400 and 1000 µm and between 500 and 2500 µm with the width fixed at 300 and 500 µm respectively. From each four inch wafer processing a maximum of 2 equal sets of 44 cantilever beams with different size were obtained. The cantilever beams were fabricated using surface and bulk micromachining. In the ready available cantilever beams 2 µm thick PZT 40/60 was employed.

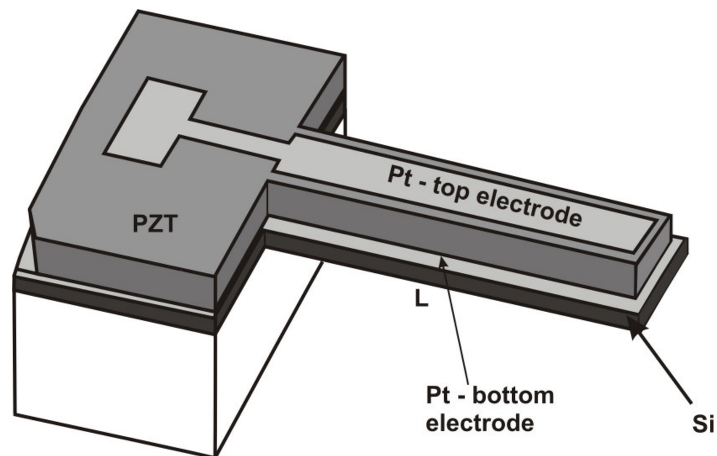

Fig. 5.1: Design of piezoelectric unimorph microactuator.

5.2.3 Improvement of Piezoelectric properties

The highest piezoelectric response was found in 5 micron thick films due to weaker influence of the substrate clamping in such thick films. The investigated compositions were PZT 40/60 and PZT 60/40. It can be assumed that in PZT 52/48 even higher piezoelectric response would occur. Also, due to faster growth of (100) oriented crystallites higher (100) orientation was obtained in 5 µm thicker films. It is worth investigating how the piezoelectric response could be maximized, if. e.g. higher (100) orientation as the intrinsic response should be maximized or if other, extrinsic effects have higher influence on the piezoelectric response.

Also, the piezoelectric response was slightly higher in films grown on compressive substrate compared to films grown on tensile substrates but with same orientation. It would be interesting to see how the compressive stress affect the piezoelectric response in thick films.

5.2.4 Stress Modelling

Modelling the residual stress within this work has pointed out the major influences in films processing on residual stresses and stress development in PZT. The existing model could be extended to include the orientation dependent stress and calculate the stress at

any temperature in the film-substrate structure. With the results from films on different substrates a model could be established which could be used for stress analysis in MEMS structures.

5.2.5 Lattice parameters

The lattice parameter analysis in PZT 52/48 films has shown some promising results regarding the relationship of thermal strain and orientation and phase content. A more detailed analysis of these films with e.g. higher resolution in XRD measurements and stress analysis could be performed to correlate residual stress to lattice parameter in more accurate way.

5.2.6 Domain switching in films during poling

To further study the extrinsic contribution and switching behaviour in PZT films the ratio of (002)/(200) domains changes during poling. The switching can be studied by means of XRD if sample with sufficient dimensions is prepared. The sufficient sample for XRD would be at least 7x7mm. Such sample size cannot be poled using contact poling. Corona poling would be ideal for such sample size. However, the films are sensitive to Corona poling and tend to cracking. Thus, the poling conditions must be adapted and optimized for Corona poling first. Some work on Corona poling has been done by [215] and thus some directions for best poling were established. These poling conditions investigated by [215] could be used and modified, if necessary. The $d_{33,f}$ measurement could serve as the monitoring of the degree of poling in the films.

References:

[1] S. Trolier-Mckinstry, P. Muralt: Thin film piezoelectrics for MEMS, *J. Electroceram. 12 (2004), p.7*

[2] R. W. Whatmore, Q. Zhang, Z. Huang, R. A. Dorey: Ferroelectric thin and thick films for microsystems, *Materials Science in Semiconductor Processing 5 (2003), p.65*

[3] H. D. Chen, K.R. Udayakumar, Ch. J. Gaskey, L.E. Cross: Fabrication and electrical properties of lead zirconate titanate thick films, *J. of Am. Ceram. Soc. 79 [8] (1996), p. 2189*

[4] B. Jaffe, W.R. Cook Jr. and H. Jaffe, Piezoelectric Ceramics. *Academic Press, Inc., 1971*

[5] P. Curie, J. Curie: Development by pressure of polar electricity in hemihedral crystals with inclined faces, *Bull. Soc. Min. de France 3 (1880), p.90*

[6] M.E. Lines and A.M. Glass: Principles and applications of ferroreletrics and related materials, Edited by: W. Marshall and D.H. Wilkinson, *The international Series of Monographs on Physics, Clarendon Press, Oxford, 1979*

[7] W. Kleber: »Einführung in die Kristallographie«, *Verlag Technik GmbH, 17. Auflage, Berlin, 1990*

[8] A. E. Romanov, M. J. Lefevre, J. S. Speck, W. Pompe, S. K. Streiffer, C. M. Foster: Domain pattern formation in epitaxial rhombohedral ferroelectric films. II. Interfacial defects and energetics, *J. of Appl. Phys. 83 [5], (1998), p.2754*

[9] A. L. Roytburd, S. P. Alpay, L. A. Bendersky, V. Nagarajan, R. Ramesh: Three-domain architecture of stress-free epitaxial ferroelectric films, *J. Appl. Phys. 89 [1] (2001), p.553*

[10] C. E. Zybill: The mechanism of polarisation inscription into ferroelectric (111) PZT and 100 SBT films, *Materials Science and Engineering C 18 (2001), p.191*

[11] B.A. Tuttle, J.A. Voigt, T.J. Garino, D.C. Goodnow, R.W. Schwartz, D.L.Lampa, T.J. Headley, M. O. Eatough: Chemically prepared pb(zr,ti)o, thin films: the effects of orientation and stress, *Proceedings of the Eighth IEEE International Symosium on Applications of Ferroelectrics, New York, 30 August–2 September (1992), p.344*

[12] S.K. Streiffer, C.B. Parker, A.E. Romanov, M.J. Lefevre, L. Zhao, J.S. Speck, W. Pompe, C.M. Foster, G.R. Bai: Domain patterns in epitaxial rhombohedral ferroelectric films. I. Geometry and experiments, *J. Appl. Phys 83 [5] (1998), p.2742*

[13] Y. L. Li, S. Choudhury, Z. K. Liu, L. Q. Chen: Effect of external mechanical constraints on the phase diagram of epitaxial $PbZr_{1-x}Ti_xO_3$ thin films - thermodynamic calculations and phase-field simulations, *J. Appl. Phys. 83 [8] (2003), p.1608*

[14] J.F.Nye: Physical properties of crystals, *Oxford Press 1985*

[15] R N Torah, S P Beeby and N M White Experimental investigation into the effect of substrate clamping on the piezoelectric behaviour of thick-film PZT elements, *J. Phys. D: Appl. Phys. 37 (2004), p.1074*

[16] S. Li, W. Cao, and L.E. Cross, “The extrinsic nature of nonlinear behavior observed in lead zirconate titanate ferroelectric ceramic,” *J. Appl. Phys. 69 [10] (1991), p.7219*

[17] F. Xu, S. Trolier-McKinstry, W. Ren, B. Xu, Z.-L. Xie, K. J. Hemker: Domain wall motion and its contribution to the dielectric and piezoelectric properties of lead zirconate titanate films, *J. Appl. Phys. 89 Nr. 2 [15] (2001), p.1336*

[18] F. Xu, PhD Thesis: Longitudinal piezoelectric characterization and domain wall contributions in lead zirconate titanate thin films, *(1999), Pennstate University*

[19] X.H. Du, U, Belegundu, K. Uchino: Crystal orientation dependence of piezoelectric properties in lead zirconate titanate: Theoretical expectations for thin films, *Jpn. J. Appl. Phys. 36 (1997), p.5580*

[20] D. V. Taylor, D. Damjanovic: Piezoelectric properties of rhombohedral Pb(Zr, Ti)O_3 thin films with (100), (111), and ‘‘random’’ crystallographic orientation, *Appl. Phys. Lett. 76 [12] (2000), p.1615*

[21] A. J. Moulson, J. M. Herbert: Electroceramics – Materials-Properties-Applications, *Chapman & Hall, London, 1990*

[22] D.R. Uhlmann, J.T. Dawley, W.H. Poisl, B.J.J.Zelinski, G. Teowee: Ferroelectric Films, *J. Sol-Gel Sci. Technol. 19 [1-3] (2000), p.53-64*

[23] J. Baborowski: Microfabrication of piezoelectric MEMS, *J. Electroceram. 12 (2004), p.33*

[24] M. Lukacs, M. Sayer, S. Foster: Single element high frequency (<50 MHz) PZT sol gel composite ultrasound transducers, *IEEE Transactions on Ultrasonics, Ferroelectrics, and Frequency Control 47 [1] (2000), p.148*

[25] H. Yu and E.S. Kim: Noninvasive acoustic-wave microfluid driver, *Proceedings of IEEE International Micro Electro Mechanical Systems Conference, (2002), p.126*

[26] J. M. Zara, S. M. Bobbio, S. Goodwin-Johansson, S. W. Smith: Intracardiac ultrasound scanner using a micromachine (MEMS) actuator, *IEEE Transactions on Ultrasonics, Ferroelectrics, and Frequency Control 47 [4] (2000), p.984*

[27] H. G. Yu, L. Zoub, K. Deng, R. Wolf, S. Tadigadapa, S. Trolier-McKinstry: Lead zirconate titanate MEMS accelerometer using interdigitated electrodes, *Sensors and Actuators A 107 (2003), p.26–35*

[28] F.F.C.Duval, R.A.Dorey, R.W.Right, Z.Huang, R.W. Whatmore: Fabrication and modelling of high-frequency PZT composite thick film membrane resonators, *IEEE Transactions on Ultrasonics, Ferroelectrics and Frequency control 51 [10] (2004), p.1255*

[29] T. Morita, M. Kurosawa, T. Higuchi: An ultrasound micromotor using a bending cylindrical transducer based on PZT thin film, *Sensors and Actuators A50 (1995), p.75*

[30] G.De Cicco, B. Morten, M. Prudenziati: A new ultrasonic composite transducer implemented with thick film technology, *IEEE Transactions on Ultrasonics, Ferroelectrics and Frequency control 44 [5] (1997), p.992*

[31] F. Akasheh, T. Myers, J. D. Fraser, S. Bose, A. Bandyopadhyay: Development of piezoelectric micromachined ultrasonic transducers, *Sensors and Actuators A 111 (2004), p.275*

[32] P. Muralt, J. Baborowski: Micromachined ultrasonic transducers and acoustic sensors based on piezoelectric thin films, *J. Electroceram. 12 (2004), p.101*

[33] P. Muralt, N. Ledermann, J. Baborowski, A. Barzegar, S. Gentil, B. Belgacem, S. Petitgrand, A. Bosseboeuf, N. Setter: Piezoelectric micromachined ultrasonic transducers based on PZT thin films, *IEEE Transactions on Ultrasonics, Ferroelectrics, and Frequency Control 52 [12] (2005), p.2276*

[34] J. Baborowski, N. Ledermann, P. Muralt: Piezoelectric micromachined transducers (pMUTs) based on PZT thin films, *IEEE on Ultrasonics Symposium (2002), p.1051*

[35] J. Baborowski, N. Ledermann, Paul Muralt, D. Schmitt: Simulation and characterization of piezoelectric micromachined ultrasonic transducers (PMUT's) based on PZT/SOI membranes, *Integrated Ferroelectrics, 54 (2003), p.557*

[36] K. Dogheche, B. Cavallier, P. Delobelle, L. Hirsinger, E. Cattan, D. Rémiens, M. Marzencki, B. Charlot, S. Basrour, S. Ballandras: A bi-stable micro-machined piezoelectric transducer for mechanical to electrical energy transformation, *Integrated Ferroelectrics 80 (2006), p.305*

[37] H. Mohamed, D. Polla, E. Ebbini, S. Zurn: Micromachined piezoelectic ultrasonic imaging transducer, *44th IEEE Midwest Symposium on Circuits and Systems Dayton, OH 14-17 (2001) 2, p.726*

[38] S. Shin, J.-K. Paik, N.-E. Lee, H.-D. Park, J.-S. Park, J. Lee: Gas sensors based on piezoelectric micro-diaphragm transducer, *Integrated Ferroelectrics, 69 (2005), p.333*

[39] Y. Yang, T.-L. Ren, Y.-P. Zhu, X.-M. Wu, N.-X. Zhang, L.-T. Liu: PMUTs for handwriting recognition, *Integrated Ferroelectrics 69 (2005), p.341*

[40] L.-P. Wang, K. Deng, L. Zou, R. Wolf, R. J. Davis, S. Trolier-McKinstry: Microelectromechanical systems (MEMS) accelerometers using lead zirconate titanate thick films, *IEEE Electron Device Letters 23 [4] (2002), p.182*

[41] L.-P. Wang, R. A. Wolf, Y. Wang, K.K. Deng, L. Zou, R. J. Davis, Susan Trolier-McKinstry: Design, fabrication, and measurement of high-sensitivity piezoelectric microelectromechanical systems accelerometers, *J. Microelectromechanical Sys. 12 [4] (2003), p.433*

[42] W.-M. Lin, A. Schroth, S. Matsumoto, L. Chengkuo, R. Maeda: Two-dimensional microscanner actuated by PZT thin film, *Proceedings of the*

SPIE - The International Society for Optical Engineering, 3892 (1999), p.133

[43] L. Zhang, W.-M. Lin, R.Maeda: Microscanner actuated by double PZT thin film, *Proceedings of the SPIE - The International Society for Optical Engineering 4408 (2001), p.528*

[44] D.L. Polla, L.F. Francis: Ferroelectric thin films in micro-electromechanical systems applications, *MRS Bulletin 21 [81] (1996), p.59*

[45] C. Lee, T. Itoh, G. Sasaki, T. Suga: Sol-gel derived PZT force sensor for scanning force microscopy, *Mater. Chem. Phys. 44 (1996), p.25*

[46] T. Kanda, T. Morita, M. Kurosawa, T. Higuchia: Rod-shaped vibro touch sensor using pzt thin film, *Proceedings MEMS 98. IEEE. Eleventh Annual International Workshop on Micro Electro Mechanical Systems. An Investigation of Micro Structures, Sensors, Actuators, Machines and Systems (Cat. No.98CH36176), (1998), p.378*

[47] J.-T. Huang, S.-C. Cheng: Study of injection molding pressure sensor with low cost and small probe, *Sensors and Actuators A 101 (2002), p.269*

[48] J.H. Park, T.Y. Kwon, D.S. Yoon, H. Kim, T.S. Kim: Fabrication of microcantilever sensors actuated by piezoelectroc $Pb(Zr_{0.52}Ti_{0.48})O_3$ thick films and determination of their electromechanical characteristics, *Adv. Funct. Mater. 15 (2005), p.2021*

[49] V. Ferrari, D.Marioli, A. Taroni: Thick-film resonant piezo-layers asnew gravimetric sensors, *Meas. Sci. Technol. 8 (1997), p.42*

[50] R.G. Polcawich, M. Scanlon, J. Pulskamp, J. Clarkson, J. Conrad, D. Washington, R. Piekarz, S. Trolier-Mckinstry, M. Dubey: Design and fabrication of a lead zirconate titanate (PZT) thin film acoustic sensor, *Integrated Ferroelectrics 54 (2003), p.595*

[51] Y. Tomikawa, T. Ogasawara, T. Takano: Ultrasonic motors: construction, characteristics, applications, *Ferroelectrics 91 (1989), p.163*

[52] A. M. Flynn: Piezoelectric Micromotors for Microrobots, *IEEE J. Microelectromechanical Sys. 1 (1992), p.1*

[53] M. A. Dubois, P. Muralt, PZT thin film actuated elastic fin micromotor, *IEEE Trans. Ultrasonics. Ferroelec. Control 45 [5] (1998), p.1169*

[54] G.A.Racine, P.Muralt, M.A.Dubois: Flexural-standing-wave elastic force motor using ZnO and PZT thin film on micromachined silicon membranes for wristwatch applications, *Smart Mater. Struct. 7 (1998), p.404*

[55] T. Morita, M. K. Kurosawa, T. Higuchi: A cylindrical shaped micro ultrasonic motor utilizing PZT thin film (1.4 mm in diameter and 5.0 mm long stator transducer), *Sensors and Actuators 83 (2000), p.225*

[56] S. Roundy, P. K. Wright: A piezoelectric vibration based generator for wireless electronics, *Smart Mater. Struct. 13 (2004), p.1131*

[57] Y.B. Jeon, R. Sood, J.-H. Jeong, S.-G. Kim: MEMS power generator with transverse mode thin film PZT, *Sensors and Actuators A 122 (2005), p.16*

[58] F. Lu, H.P. Lee, S.P. Lim: Modeling and analysis of micro piezoelectric power generators for micro-electromechanical-systems applications, *Smart Mater. Struct. 13 (2004), p.57*

[59] S.R. Platt, S. Farritor, H. Haider: On low-frequency electric power generation with PZT ceramics, *IEEE/ASME Transactions on Mechatronics 10 [2] (2005), p.240*

[60] S. Zurn, M. Hsieh, G. Smith, D. Markus, M. Zang, G. Hughes, Y. Nam, M. Arik, D. Polla: Fabrication and structural characterization of a resonant frequency PZT microcantilever, *Smart Mater. Struct. 10 (2001), p.252*

[61] T. Yan, B.E. Jones, R.T. Rakowski, M.J. Tudor, S.P. Beeby, N.M.White: Design and fabrication of thick-film PZT-metallic triple beam resonators, *Sensors and Actuators A 115 (2004), p.401*

[62] J. G. Smits, K. Fujimoto, V. F Kleptsyn: Microelectromechanical flexure PZT actuated optical scanner: static and resonance behavior, *J. Micromech. Microeng. 15 (2005), p.1285*

[63] C. Zinck, D. Pinceau, E. Defaÿ, E. Delevoye, D. Barbier: Development and characterization of membranes actuated by a PZT thin film for MEMS applications, *Sensors and Actuators A 115 (2004), p. 483*

[64] N.R. Harris, M. Hill, R. Torah, R. Townsend, S. Beeby, N.M. White, J. Ding: A multilayer thick-film PZT actuator for MEMs applications, *Sensors and Actuators A 132 (2006), p.311*

[65] A. Schroth, C. Lee, S. Matsumoto, R. Maeda: Application of sol–gel deposited thin PZT film for actuation of 1D and 2D scanners, *Sensors and Actuators 73 (1999), p.144*

[66] F. Filhol, E. Defay, C. Divoux, C. Zinck, M.-T. Delaye: Resonant micro-mirror excited by a thin-film piezoelectric actuator for fast optical beam scanning, *Sensors and Actuators A 123–124 (2005), p.483*

[67] J.J. Bernstein, J. Bottari, K. Houston, G. Kirkos, R. Miller, B. Xu, Y. Ye, E.L. Cross: Advanced MEMS ferroelectric ultrasound 2-dimensional arrays, *Proceedings of IEEE Ultrasoncis Symposium (1999), p.17*

[68] J.J. Bemstein, J. Bottari, K. Houston, G. Kirkos, R. Miller, B. Xu, Y . Ye, L.E. Cross: In-plane polarization for high sensitivity ferroelectric MEMS ultrasound transducers, *Procedeeings of Ultrasonic Symposium (2001) 37*

[69] R.W. Schwartz: Chemical solution deposition of perovskite thin films, *Chem. Mater. 9 (1997), p.2325*

[70] M.S. Bhuiyan, M. Paranthaman, K. Salama: Solution-derived textured oxide thin films - a review, *Supercond. Sci. Technol. 19 (2006), p.R1*

[71] J. Fukushima, J. Kodaira and T. Matsushita: Preparation of ferroelectric PZT films by thermal decomposition of organometallic compounds, *J. Mat. Sci. 19 (1984), p.595*

[72] K.D. Budd, S.K. Dey and D.A. Payne, Sol-gel processing of $PbTi0_3$-$PbZr0_3$ and PLZT thin films, *Brit. Ceram. Soc. Proc. 36 (1985), p.107*

[73] S.K. Dey, K.D. Budd and D.A. Payne: Thin film ferroelectrics of PZT by sol-gel processing, *IEEE Trans. UFFC 35(1) (1988), p.80*

[74] C.K. Barlingay, S.K. Dey: Observation of sol-gel solid phase epitaxial growth of ferroelectric Pb(Nb,Zr,Ti)O_3 thin films on sapphire, *Appl. Phys. Lett. 61 (1992), p.1278*

[75] G.H. Haertling: PLZT thin films prepared from acetate precursors, *Ferroelectrics 116 (1991), p.51*

[76] Q. Zhang, Z. Huang, M.E. Vickers and R.W. Whatmore, *Integrated Ferroelectrics, 23 (1999), p.215*

[77] Q. Zhang, Z. Huang, R.W. Whatmore: Studies of lead zirconate titanate sol ageing part I: Factors affecting particle growth, *J. Sol-Gel Sci. Technol. 23 (2002), p.135*

[78] S.-Y. Chen, I.W. Chen: Texture development, microstructure evolution, and crystallization of chemically derived PZT thin films, *J. Am. Ceram. Soc. 81 [1] (1998), p. 97*

[79] N. Y. Turova, M. I. Yanovskaya: Metal alkoxides – precursors for ferroelectric materials, *Ferroelectric thin films: Synthesis and basic properties, Edited by C.P. Araujo, J.F. Scott, G.W. Taylor, Gordon and Breach Publishers, UK, 1996*

[80] R.A. Assink, R.W. Schwartz: $_1$H and $_{13}$C NMR investigations of Pb(Zr,Ti)O_3 thin film precursor solutions, *Chem. Mater. 5 (1993), p.511*

[81] T. J. Boyle, D. Dimos, R. W. Schwartz, T. M. Alan, M. B. Sinclair and C. D. Buchheit, D. Buchheit: Aging characteristics of a hybrid sol-gel Pb(Zr,Ti)O_3 precursor solution, *J. Mater. Res. 12 (1997), p.1022*

[82] R. W. Schwartz, T. J. Boyle, S. J. Lockwood, M. B. Sinclair, D. Dimos, C.D. Buchheit: Sol-gel processing of PZT thin films: A review of the state-of the art and process optimization strategies, *Integrated Ferroelectrics 7 (1995), p.259*

[83] C. D. E. Lakeman, Z. Xu, and D. A. Payne: On the evolution of structure and composition in sol–gel-derived lead–zirconate–titanate thin-layers, *J. Mater. Res. 10 (1995), p. 2042*

[84] A. P. Wilkinson, J. S. Speck, A. K. Cheetham, S. Natarajan, J. M. Thomas: In situ X-ray diffraction study of crystallization kinetics in $PbZr_{l-x}Ti_x0_3$ (PZT, x = 0.0, 0.55, 1.0), *Chem. Mater. 6 (1994), p. 750*

[85] R.W. Schwartz, J.A. Voigt, B.A. Tuttle, D.A. Payne, T.L. Reichert, R.S. DaSalla: Comments on the effect of solution precursor characteristics and thermal processing conditions on the crystallization behaviour of sol-gel derived lead zirconate titanate films, *J. Mater. Res. Vol. 12, No 2 (1997), p.444*

[86] D.P. Birnie III, M. Manley: Combined flow and evaporation of fluid on a spinning disk, *Phys. Fluids 9 (1997), p.870*

[87] D.P. Birnie III: Combined flow and evaporation during spin coating of complex solutions, *J. of Non-Cryst. Sol. 218 (1997), p.174*

[88] D. Meyerhofer: Characteristics of resist films produced by spinning, *J. Appl. Phys. 49 (1978), p.3993*

[89] D.P. Birnie III, R.N. Vogt, M.N. Orr, J.R. Schifko: Coating uniformity and device applicability of spin coated sol-gel PZT films, *Microelectronic Engineering 29 (1995), p.189*

[90] M. Sayer, G. Yi, M. Spidlar: Comparative sol gel processing of PZT thin films, *Integrated Ferroelectrics, v7, n1-4 pt2, (1995), p.247*

[91] H. Kozuka, S. Takenaka: Single-step of gel-derived lead zirconate titanate films: Critical thickness and gel film to ceramic film conversion, *J. Am. Ceram. Soc. 85 [11] (2002), p.2696*

[92] Y.L.Tu, S.J. Milne: Processing and characterization of Pb(Zr,Ti)O3 films, up to 10 µm thick, produced from a diol sol-gel route, *J. Mater. Res. 11 [10] (1996), p.2556*

[93] R.A. Dorey, R.W. Whatmore: Electrical properties of high density PZT and PMN-PT/PZT thick films produced using ComFi technology, *J. Eur. Ceram. Soc. 24 (2004), p.1091*

[94] J. Cheng, Z. Meng: Thickness-dependent microstructures and electrical properties of PZT films derived from sol-gel process, *Thin Solid Films 385 (2001), p.5*

[95] J. Cheng, W. Zhu, N. Li, L.E. Cross: Dielectric properties of (100) textured thick $Pb(Zr_xTi_{1-x})O_3$ films with different Zr/Ti atom ratios, *J. Appl. Phys., 91 [9] (2002), p.5997*

[96] S.H. Hu, X.J. Meng, G.S. Wang, J.L. Sun, D.X. Li: Preparation and characterisation of multi-coating PZT thick films by sol-gel process, *J. Cryst. Growth 264 (2004), p.307*

[97] G. Yi, Z. Wu, M. Sayer: Preparation of $Pb(Ti,Zr)O_3$ thin films by sol gel processing: electrical, optical, and electro-optic properties, *J. Appl. Phys. 64 (5) (1988), p.2717*

[98] X, Pu, W. Luo, A.Ding, H. Tian, P. iu: Preparation of PZT thick films by one-step firing sol-gel process, *Mat Res Bull. 36 (2001), p.1471*

[99] H. Kozuka, S. Takenaka: Single-step of gel-derived lead zirconate titanate films: Critical thickness and gel film to ceramic film conversion, *J. Am. Ceram. Soc., 85 [11] (2002), p.2696*

[100] K. Maki, N. Soyama, S. Mori, K. Ogi: Evaluation of CSD-PZT thick films with different density, ISAF 2000, *Proceedings of the 12th IEEE International Symposium on Applications of Ferroelectrics (2000), p.957*

[101] S. Takenaka, H. Kozuka: Sol-gel preparation of single layer, 0.75 µm thick lead zirconate films from lead nitrate-titanium and zirconium alkoxide solutions containing polyvinypyrrolidone, *Appl. Phys. Lett. 79 [21] (2001), p.3485*

[102] Y.T. Tu, S.J. Milne: A study of the effects of process variables on the properties pf PZT films produced by a single-layer sol-gel technique, *J. Mater. Sci. 30 (1995), p.2507*

[103] A.L. Kholkin, V.K. Yarmarkin, A. Wu, M. Avdeev, P.M. Vilarinho, J. L. Baptista: PZT-based piezoelectric composites via a modified sol-gel route, *J. Eur. Ceram. Soc. 21 (2001), p.1535*

[104] Y. Ohya, S. Itoda, T. Ban, Y. Takashi: Lead zirconate thick films fabricated from sols with and without its powder, *Jpn. J. Appl. Phys. 41 (2002), p.270*

[105] T. Tsurumi, S. Ozawa, S.Wada: Preparation of PZT thick films by an interfacial polymerization method, *J. Sol-Gel Sci. Technol. 26 (2003), p.1037*

[106] R.A. Dorey, S.B. Stringfellow, R.W. Whatmore: Effect of sintering aid and repeated sol infiltrations on the dielectric and piezoelectric properties of a PZT composite thick film, *J. Eur. Ceram. Society 22 (2002), p.2921*

[107] M. Yamane: Preparation of thick PZT ceramic film by an interfacial polymerization, *J. Sol-Gel Sci. Technol. 13 (1998), p.821*

[108] R. Seveno, P. Limousin, D. Averty, J.-L. Charier, R. Le Bihan, H.W. Gundel: Preparation of multi-coating PZT thick films by sol-gel method onto stainless steel substrates, *J. Eur. Ceram. Soc. 20 (2000), p.2025*

[109] T. Kobayashi, J. Tsaur, M. Ichiki, R. Maeda: Fabrication and performance of a flat piezoelectric cantilever obtained using a sol–gel derived PZT thick film deposited on a SOI wafer, *Smart Mater. Struct. 15 (2006), p.S137*

[110] M. D. Losego, S. Trolier-McKinstry: Mist deposition of micron-thick lead zirconate titanate films, *Mat. Res. Soc. Symp. Proc. 784 (2004), p.553*

[111] J. Lu, J. Chu, W. Huang, Z. Ping: Microstructure and electrical properties of Pb(Zr,Ti)O3 thick films prepared by electrostatic spray deposition, *Sensors and Actuators A 108 (2003), p.2-6*

[112] J. Van Tassel, C. A. Randall: Electrophoretic deposition and sintering of thin/thick PZT films, *J. Eur. Ceram. Soc. 19 (1999), p.955*

[113] S. Marson, R.A. Dorey, Q. Zhang, R.W. Whatmore, A. Hardy, J. Mullens: Direct patterning of photosensitive chenical solution deposition PZT layers, *J. Eur. Ceram. Soc. 24 (2004), p.1925*

[114] S. Marson, R.A. Dorey, Q. Zhang, R.W. Whatmore: Thick PZT micro-features obtained by direct patterning of photosensitive precursor solution, *Integrated Ferroelectrics 54, (2003), p.585*

[115] N. Futai, K. Matsumoto, I. Shimoyama: Fabrication of high-aspect-ratio PZT thick film structure using sol-gel technique and Su-8 Photoresist, *Proceedings of IEEE international conference on micro electro mechanical systems 15, Las Vegas NV , ETATS-UNIS (2002), p.168*

[116] G. Yi, M. Sayer: Sol-Gel Processing of Thick PZT Films, *Proceedings of the Eighth IEEE International Symposium on Applications of Ferroelectrics (Greenville, SC, 1992). Edited by M. Liu, A. Safari, A. Kingon, and G. Haerting. Institute of Electrical and Electronic Engineers, Piscataway, NJ, (1992), p.289*

[117] G.A.C.M. Spierings, G.J.M. Dormans, W.G. J. Moors, M.J.E. Ulenaers, P.K. Larsen: Stress in Pt/Pb(Zr,Ti)O_3/Pt capacitors for integrated ferroelectric devices, *J. Appl. Phys. 78 (1995), p.1926*

[118] R.J. Ong, D.A. Payne: Densification and stress development for the chemical-solution deposition of PZT thin layers on silicon, *Proceedings of the 2000 12th IEEE International Symposium on Applications of Ferroelectrics (IEEE Cat. No.00CH37076), vol. 1 (2001), pt. 1, p.397*

[119] C. D. E. Lakeman, J. A. Ruffner, T. J. Boyle: Stress measurements and processing optimization for solution derived $SrBi_2Ta_2O_9$ thin films, *J. Sol-Gel Sci. Technol. 16 (1999), p.83*

[120] L. Lian, N.R. Sottos : Stress effects in sol-gel derived ferroelectric thin films, *J. Appl. Phys. 95 [2] (2004), p.629*

[121] A.G. Evans, J.W. Hutchinson: The thermomechnacal integrity of thin films and multilayers, *Acta Metall Mater 43 (1995), p.2507*

[122] S.Y. Kweon, S.H. Yi, S.K. Choi: Intrinsic stress dependence of *c*-axis orientation ratio in $PbTiO_3$ thin films deposited by reactive sputtering, *J. Vac. Sci. Technol. A 15 (1997), p.57*

[123] G. L. Brennecka, W. Huebner, B.A. Tuttle, P.G. Clem: Use of stress to produce highly oriented tetragonal lead zirconate titanate (PZT 40/60) films and resulting electrical properties, *J. Am. Ceram. Soc. 87 [8] (2004), p.1459*

[124] H.X. Qin, J.S. Zhu, Z.Q. Jin, Y. Wang: PZT thin films with preferred-orientation induced by external stress, *Thin Solid Films 379 (2000), p.72*

[125] J. M. Calderon-Moreno, M. Popa: Stress dependence of reversible and irreversible domain switching in PZT during cyclic loading, *Mater. Sci. Eng. A336 (2002), p.124*

[126] T. Fett, D. Munz, G. Thun: Dielectric parameters of a soft PZT under mechanical loading, *J. Mater. Sci. Lett. 21 (2002), p.849*

[127] T.Fett, D. Munz, G.Thun: Bending strength of a PZT ceramic under electric field, *J. Eur. Ceram. Soc. 23 (2003), p.195*

[128] A. F. Devonshire, Theory of barium titanate - part I and II, *Philos. Mag. 40 (1949), p.1040*

[129] T.J. Garino, H.M. Harrington: Residual stress in PZT thin films and its effect on ferroelectric properties, *Mater. Res. Soc. Symp. Proc. 243 (1992), p.341*

[130] S.B. Desu: Stress induced modifications in ferroelectric films, *Phys. Stat. Sol. (a), 141 (1994), p.119*

[131] T. Kumazawa, Y. Kumagai, H. Miura, M. Kitano: Effect of external stress on polarization in ferroelectric thin films, *Appl. Phys. Lett. 72 (1998), p.608*

[132] J.F. Shepard Jr., S.Trolier-McKinstry, M.A. Hendrickson, R. Zeto: Properties of PZT thin films as a function of in-plane biaxial stress, ISAF 1996 - *Proceedings of the Tenth IEEE International Symposium on Applications of Ferroelectrics, New Jersey, (1996), p.161*

[133] K. Franke, H. Huelz, M. Weihnacht: Stress-induced depolarization in PZT thin films, measured by means of electric force microscopy, *Surf. Sci. 416 (1998), p.59*

[134] L. Zhang, J. Tsaur, R. Maeda: Residual stress study of SiO2/Pt/Pb(Zr,Ti)O3/Pt multiplayer structure for micro electro mechanical system applications, *Jpn. J. Appl. Phys. 42 (2003), p.1386*

[135] K. G. Brooks, I. M. Reaney, R. Klissurska, Y. Huang, L. Bursill, N. Setter: Orientation of rapid thermally annealed lead zirconate titanate thin films on (111) pt substrate, *J. Mater. Res. 9 [10] (1994), p.2540*

[136] K. Wetzig, C. M. Scheider. Metal based thin films for electronics, *Whiley-VCH GmbH & Co. KGaA, Weinheim, (2003) Chapter 3, p.123*

[137] Edited by K. Seshan. Handbook of Thin Film Deposition Processes and Technologies, *Second Edition. Noyes Publications / William Andrew Publishing, Norwich, USA (200) p.319*

[138] J.A. Thornton: Influence of apparatus geometry and deposition conditions on the structure and topography of thick sputtered coatings, *J. Vac. Sci. Tech. 11[4] (1974), p. 633*

[139] D.M. Mattox. Handbook of Physical Vapour Deposition (PVD) Processing, *William Andrew Publishing/Noyes, New Jersey (1998), p.510*

[140] G.-M. Chow, L. K. Kurihara. Nanostructured materials, processing, properties and potential applications, *William Andrew Publishing, Norwich, (2002)*

[141] Q. Zhang, S. Corkovic, C. P. Shaw, Z. Huang, R. W. Whatmore: Ferroelectric $Pb(Zr_{0.3}Ti_{0.7})O_3$ thin films and the effects of nanoporosity, *Thin Solid Films 488 (2005), p.258*

[142] D. Kojima, K. Makihara, J. Shi, M. Hashimoto: Structure and electrical property of platinum film biased DC-sputter-deposited on silicon, *Appl. Surf. Sci. 169-170 (2001), p.320*

[143] E. Conforto and P. E. Schmid Pt-Si reaction through interfacial native silicon oxide layers, *Philosophical Magazine A 81 [1] (2001), p.61*

[144] R.C. Jaeger: Introduction to Microelectronic Fabrication, *Second Edition, Prentice Hall, New Jersey (2002), p.52*

[145] P.E.J. Flewitt, R.K. Wild. Physical Methods for Materials Characterisation, *Institute of Physics Publishing, London (1994), p.245*

[146] J.C. Russ: Fundamentals of Energy Dispersive X-Ray Analysis, *Butterworths Monographs in Materials, London (1984), p.17*

[147] G. Binnig, C.F. Quate, Ch. Gerber: Atomic force microscope. *Phys. Rev. Lett. 56(9) (1986), p. 930*

[148] Edited by A.T. Hubbard: *Handbook of Surface Imaging and Visualization, CRC Press, Florida (1994), p.23*

[149] T.R. Albrecht, P. Grütter, D. Horne, D.Rugar: Frequency modulation detection using high-Q cantilevers for enhanced force microscope sensitivity. *J. Appl. Phys. 69(2) (1991), p.668*

[150] M.J. Buerger: X-Ray Crystallography, *Wiley New York (1942), p.43*

[151] M.M. Woolfson: X-Ray Crystallography, *Paperback Edition, Cambridge University Press, Cambridge (1978), p.167*

[152] H.P. Klug, L.E. Alexander: X-Ray Diffraction Procedures, *2nd Edition,Wiley and Sons, New York (1974)*

[153] R. Glocker: Materialprüfung mit Röntgenstrahlen. Unter besonderer Berücksichtigung der Röntgenmetallkunde, *Gebundene Ausgabe, Springer Berlin, (1991)*

[154] Edited by E. Lifshin: X-Ray Characterization of Materials, *Wiley-VCH, Weinheim (1999), p.37*

[155] G.K. Williamson, W.H. Hall: The Diffraction Pattern of Cold Worked Metals: The Changes in Integrated Intensity, *Acta Metall. 1 (1953), p.22*

[156] J.E.A. Southin, S.A. Wilson, D. Schmitt, R.W. Whatmore: $e_{31,f}$ determination for PZT films using a conventional 'd_{33}' meter, *J. Phys. D: Appl. Phys. 34 (2001), p.1456*

[157] L.B. Valdes: Resistivity measurements on germanium for transistors, *Proceedings of the I R E 42 February (1954), p.420*

[158] S. Timoschenko: Analysis of bi-metal thermostats, *Journal of Optical Soc. Am. Rev. Sci. Inst. 11 [3] (1925), p.233*

[159] P.H. Townsend, D.M. Barnett, T.A. Brunner: Elastic relationship in layered composite media with approximation for case of thin films on a thick substrate, *J. Appl. Phys, 62 [11] (1987), p.4438*

[160] G.G. Stoney: The tension of metallic strips deposited by electrolysis, *Proc. R. Soc. London, Series A, Vol. 82, (1909), p.172*

[161] D. Bornside, C. Macosko, L. Scriven: Spin coating of a pmma/chlorobenzene solution, *J. Electrochem. Soc. 138 [1] (1991), p.317*

[162] M.–H. Zhao, R. Fu, D. Lu, T. –Y. Zhang: Critical thickness for cracking of $Pb(Zr_{0.53}Ti_{0.47})O_3$ thin films deposited on Pt/Ti/Si(100) sustrate, *Act. Mater. 50 (2002), p.4241*

[163] R. W. Schwartz, R. A. Assink, and T. J. Headley: Solution chemistry effects in PZT thin film processing: Spectroscopic and microstructural characterization, ferroelectric thin films II, *Mat. Res. Soc. Symp. Proc. (1997), p.243*

[164] S.M. Park: Densification and evolution of stress development in solution derived $PbZr_{0.53}Ti_{0.47}O_3$ thin layers, *Mat. Res. Soc. Symp. Proc. Vol. 596 (2000), p.381*

[165] C. K. Kwok, S. B. Desu, D.P. Vijay: Modified sol-gel process for preparation of lead zirconate titanate thin films, *Ferroelectric Lett. 16 (1993), p.143*

[166] Y.Z. Chen, J. Ma, J.X. Zhang: Thermal analysis of the seeded lead zirconate titanate sol-gel system, *Mater. Lett. 57 (2003), p.3392*

[167] C.D.E Lakeman, J.-F. Campion, D.A Suchicital, 1990, *IEEE 7th Int. Symp. on Appl. of Ferroelectrics (Cat. No. 90CH2800-1) (1991), p.681*

[168] J. Perez, P.M. Vilarinho, A.L. Kholkin: High-quality $PbZr_{0.52}Ti_{0.48}O_3$ films prepared by modified sol-gel route at low temperature, *Thin Solid Films 449 (2004), p.20*

[169] E. M. Grisworld, L. Weaver, M. Sayer, F. Czerwinski, J. Szpunari: Crystallization kinetics in ferroelectric thin films: Viability of Atomic Force Microscopy, *Micron 26 [6] (1995), p.559*

[170] E. Defay, C. Malhaire, C. Dubois, D. Barbier: Stress and stress relaxation study of sputtered PZT thin films for microsystems applications, *Mat. Res. Soc. Symp. Proc. 594 (2000), p.237*

[171] L. Zhang, M. Ichiki, R. Maeda: Residual stresses in Pt bottom electrodes for sol-gel derived lead zirconate titanate films, *J. Eur. Ceram. Soc. 24 (2004), p.1673*

[172] Hornbogen: Werkstoffe, *Springer Berlin, 5 Auflage (1991)*

[173] C.-L. Dai, F.-Y. Xiao, C.-Y. Lee, Y.-C. Cheng, P.-Z. Chang, S.-H. Chang: Thermal effects in PZT: Diffusion of titanium and recrystallization of platinum, *Mater. Sci. Eng. A 384 (2004), p.57*

[174] G.A.C. M. Spierings, J.B.A. Van Zon, P.K. Larsen: Influence of platinum-based electrodes on the microstructure of sol-gel and MOD prepared lead zirconate titanate films, *Integrated Ferroelectrics Vol.3 (1993), p.283*

[175] K. Screenivas, I. Reaney, T. Maeder, N. Setter, C. Jagadish, R. G. Elliman: Investigation of Pt/Ti bilayer metallization on silicon for ferroelectric thin film integration, *J. Appl. Phys. 75 [1], (1994), p.232*

[176] S.Y. Kweon, S.K. Choi, S.J. Yeom, J.S. Roh: Platinum hillocks in Pt/Ti film stacks deposited on thermally oxidized Si substrate, *Jpn. J. Appl. Phys. 40 (2001), p.5850*

[177] H.J. Nam, H. H. Kim, W.-J. Lee: The effect of the preparation conditions and heat-treatment conditions of Pt/Ti/SiO_2/Si substrates on the nucleation and growth of Pb(Zr,Ti)O3 films, *Jpn. J. Appl. Phys. Vol. 37 (1998), p. 3462*

[178] I. Chung, I.K.Yoo, W. Lee, C.W. Chung, J.K. Lee: Electrode stress effects on electrical properties of PZT thin film capacitors, *Integrated Ferroelectrics*, *v 10, n 1-4 pt 1, (1995), p.99*

[179] Dax, Grundelfinger, Häffner, Itschner, Kotsch, Staniczek: *Tabellenbuch für Metalltechnik, Handwerk und Technik, Hamburg 1991*

[180] T.C. Tisone, J. Drobek: Diffusion in thin film Ti–Au, Ti–Pd, and Ti–Pt couples, *J. Vac. Sci. Tech. 9 (1971) 271*

[181] S.Q. Wang, J.W. Mayer: Oxygen sinks in reactions of thin bilayer refractory metal films with SiO_2 substrates, *Thin Solid Films 202 (1991), p.105*

[182] K. Aoki, Y. Fukuda, K. Numata, A. Nishimura: Effects of titanium buffer layer on the lead-zirconate-titanate crystallization process in sol-gel deposition technique, *Jpn. J. Appl. Vol. 34 (1995), p.192*

[183] B. A. Tuttle, R. W. Schwartz: Solution deposition of ferroelectric thin films, *Mater. Res. Bull. 21 [6] (1996), p.49*

[184] T. Tani. Z. Xu. D.A. Payne: Preferred orientations for sol-gel derived PLZT thin layers, *Mater. Res. Soc. Symp. Proc. 310 (1993), p.296*

[185] N. Ledermann, P. Muralt, J. Baborowski, S. Gentil, K. Mukati, M. Cantoni, A. Seifert, N. Setter: {100}-Textured, piezoelectric $Pb(Zr_x, Ti_{1-x})O_3$ thin films for MEMS: integration, deposition and properties, *Sensors and Actuators A 105 (2003), p.162*

[186] Z. J. Wang. R. Maeda. K. Kikuchi: Development of phases and texture in sol-gel derived lead zirconate titanate thin films prepared by three-step heat treatment process, *J. Mater. Sci. 35 (2000), p.5915*

[187] Y. Liu, P.P. Phule: Sequence of phase formation in chemically dervied ferroelectric lead zirconate titanate $Pb(Zr_{0.40}Ti_{0.6}0)O_3$ thin films, *J. Am. Ceram. Soc. 80 [9] (1997),p.2410*

[188] S. Choudhury, Z. Li, L.-Q. Chen: A phase diagram for epitaxial PbZr1-xTixO3 thin films at the bulk morphotropic boundary condition, *J. Am. Ceram. Soc. 88 [6] (2005), p.1669*

[189] Q. Zhang, S. Corkovic, J. M. Marshall, R.W. Whatmore: Stress-induced phase formation of PZT 52/48 thin films, accepted in *Intergrated Ferroelectrics within the Proceedings of the Symposiums of Intergrated Ferroelectrics (2006)*

[190] W. Gong, J.-F. Li, X. Chu, Z. Gui, L. Li: Combined effect of preferential orientation and Zr/Ti atomic ratio on electrical properties of $Pb(Zr_xTi_{1-x})O_3$ thin films, *J. Appl. Phys. v 96 [1] (2004), p.590*

[191] B.A. Tuttle, T.J. Headley, B.C. Bunker, R.W. Schwartz, T.J. Zender, C.L. Hernandez, D.C. Goodnow, R.J. Tissot, J. Michael, A.H. Carim: Microstructural evolution of $Pb(Zr,Ti)O_3$ thin films prepared by hybrid metallo-organic decomposition, *J. Mater. Res. v 7, n 7, (1992), p.1876*

[192] T. Biggs, S.S. Taylor, E. v.d. Lingen: The Hardening of Platinum Alloys for Potential Jewellery Application, *Platinum Metals Rev. 49, [1] (2005), p.2*

[193] B. Noheda, J.A. Gonzalo, J. De Frutos, A. Gonzalez, C. Moure: Thermal expansion anomalies at the antiferroelectric-ferroelectric (F_{RL}), ferroelectric (F_{RL})-ferroelectric (F_{RH}) and ferroelectric (F_{RH})-paraelectric transitions in $PbZr_{1-x}Ti_xO_3$ (0) - x - 0.35, *J. Mater. Sci. Lett. 16 (1997), p.101*

[194] J. Kim, D.-I. Cho, and R. S. Muller, “Why is (111) silicon a better mechanical material for MEMS?,” in *Transducers’01 Eurosensors XV, 11th Int. Conf. Solid-State Sens. Actuators Jun. 10–14 (2001), p.662*

[195] M. Bengisu: Engineering Ceramics, *Springer Verlag, Berlin (2001), p.465*

[196] Y. C. Zhou, Z. Y. Yang, X. J. Zheng: Residual stress in PZT thin films prepared by pulsed laser deposition, *Surf. Coat. Technol. 162 (2003), p.202*

[197] D.R. Biswas, S. Chandratreya, J.A. Pask: Thermal expansion, elasticity, and internal friction of polycristalline PZt ceramivs, *Ceram. Bull. (1979), p.792*

[198] Q.M. Zhang, J. Zhao: Electromechanical properties of lead zirconate titanate piezoceramics under the influence of mechanical stresses, IEEE Transactions of Ultrasonics, *Ferroelectrics and Frequency control, Vol 46 [6] (1999), p.1518*

[199] K. Yao, S. Yu, F. Eng-Hock Tay: Residual stress analysis in ferroelectric $Pb(Zr_{0.52}Ti_{0.48})O_3$ thin films fabricated by a sol-gel process, *Appl. Phys. Lett. V. 82 [25] (2003), p.4540*

[200] M.S. Kennedy, D.F. Bahr, C.D. Richards, R.F. Richards: Residual stress control to optimize PZT MEMS performance, *Mat. Res. Soc. Symp. Proc. 741 (2003), p.163*

[201] E. Hong, R. Smith, S.V. Krishnaswamy, C.B. Freidhoff, S. Trolier-McKinstry: Residual stress development in Pb(Zr,Ti)O3/ZrO2/SiO2 stacks for piezoelectric microactuators, *Thin Solid Films 510 (2006), p.213*

[202] I. Demir, A.L. Olson, J.L. Skinner, C.D. Richards, R.F. Richards, D.F. Bahr: High strain behaviour of composite thin film piezoelectric membranes, *Microelectronic Eng. 75 (2004), p.12*

[203] W. R. Cook, Jr, D. A. Berlincourt, F.J. Scholz: Thermal expansion pyroelectricity in lead zirconate and barium titanate, *J. Appl. Phys. 34 [5] (162), p.1392*

[204] A. Kholkin, A.K. Taganatsev, E.L. Colla, D.V. Tyalor, N. Setter: Piezoelectric and dielectric aging in $Pb(Zr,Ti)O_3$ thin films and bulk ceramics, *Integrated Ferroelectrics 15 (1997), p.317*

[205] K. Fujito, N. Wakiya, K. Shinozaki, N. Mizutani: Change of residual stresses and electrical properties of Pb(Zr,Ti)O3 thin films upon introducing various bottom electrodes, *J. Ceram. Soc. Jpn. 110 [5] (2002), p.421*

[206] B. A. Tuttle, J.A. Voigt, D. C. Goodnow, D. L. Lamppa, T. J . Headley, M.0. Eatough, G. Zender, R. D. Nasby, and S. M. Rodgers: Highly oriented, chemically prepared Pb(Zr,Ti)O_3 thin films, *J. Am. Ceram. Soc. 76 [6] (1993), p.1537*

[207] Q. Zhang, Z. Huang, M. E. Vickers, R. W. Whatmore: Effect of the particle size in PZT precursor sols on the orientation of the thin films, *J. Eur. Ceram. Soc. 19 (1999), p.1417*

[208] Z. Huang. Q. Zhang. R. W. Whatmore: Low temperature crystallization of lead zirconate titanate thin films by a sol-gel method. *J. Appl. Phys. 85 [10] (1999), p.7355*

[209] S. Hiboux. P. Muralt: Mixed titania-lead oxide seed layers for PZT growth on Pt(111): A study of nucleation. texture and properties, *J. Eur. Ceram. Soc. 24 (2004), p.1593*

[210] R. Klissurska. Th. Maeder. K. G. Brooks. N. Setter: Microstructure of PZT sol-gel films on Pt substrate with different adhesion layers. *Microelectronic Eng. 29 (1995), p.297*

[211] G.J. Willems, D.J. Wouters, H.E. Maes, R. Nouwen: Nucleation and orienatation of sol-gel PZT films on Pt electrodes, *Integrated Ferroelectrics, Vol. 15 (1997), p.19*

[212] R. Takayama, Y. Tomita: Preparation of epitaxial $Pb(Zr_xTi_{1-x})O_3$ thin films and their crystallographic, pyroelectric and ferroelectric properties, *J. Appl. Phys. 65 [4] (1989), p.1666*

[213] G. Shirane, Hoshino, K. Suzuki: X-ray study of the phase transition in lead titanate, *Phys. Rev. 80 (1950), p.1105*

[214] J. Hector, N. Floquet, J.C. Niepce, P. Gaucher, J.P. Ganne: Texture, structure and domain microstructure of ferroelectric PZT thin films, *Microelectronic Engineering 29 (1995), p.285*

[215] J.M. Marshall PhD Thesis: Ferroelectric lead zirconate titanate (Pb(Zrx,Ti1-x)O3) thin films: Deposition, control and characterization, *(2006), Cranfield University*

[216] Cohen R. E., Heifets E., and Fu H., First-principles computation of elasticity of Pb(Zr,Ti)O3: The importance of elasticity in piezoelectrics, *Fundamental Physics of Ferroelectrics, AIP Conference Proceedings (NY) 582 (2001), p.11*

[217] I. M. Reaney, D. V. Taylor, K. G. Brooks: Ferroelectric PZT thin films by sol-gel deposition, *J. Sol-Gel Sci. Technol. 13 (1998), p.813*

[218] M. Es-Souni, A. Piorra: On the crystallization kinetics of solution deposited PZT thin films, *Mater. Res. Bull. 36 (2001), p.2563*

[219] S. Trolier-McKinstry, J. F. Shepard, Jr., T. Su, G. Zavala, J. Fendler, *Ferroelectrics 206 (1997), p.381*

[220] S. Kalpat, K. Uchino: Highly oriented lead zirconium titanate thin films: Growth, control of texture, and its effect on dielectric properties, *J. Appl. Phys. 90 Nr.6 [15] (2001), p.2703*

[221] T. Fett, D. Munz: Deformation of PZT under tension, compression, bending, and torsion loading, *Adv. Eng. Mater. 5, Nr. 10 (2003), p. 718*

[222] R. Fu, T.-Y. Zhang: Influences of temperature and electric field on the bending strength of lead zirconate titanate ceramics, *Act. Mater. 48 (2000), p.1729*

[223] R. A. Wolf, S. Trolier-McKinstry: Temperature dependence of the piezoelectric response in lead zirconate titanate films, *J. Appl. Phys. 95 [3] (2004), p.1397*

[224] S. Zhang, X. Dong, S. Kojima: Temperature dependence of the dielectric, elastic and piezoelectric properties of $Pb(Zr_xTi_{1-x})O_3$ ceramics near the morphotropic phase boundary, *Jpn. J. Appl. Phys. 36 (1997), p.2994*

[225] Z. Q. Zhuang, M. J. Haun, S.-J. Jang, L. E. Cross: Composition and temperature dependence of the dielectric, piezoelectric and elastic properties of pure PZT ceramics, *IEEE transactions on ultrasonics, ferroelectrics, and frequency control, 36 [4] (1989), p.413*

[226] R. Bruchhaus, B.-K. Moon, A. Hilliger, N. Nagel, Y. Yamada, H. Itokawa, I. Kunishima, G. Beitel: Comparison of materials for the ferroelectric thin film to be integrated into high density FeRAMs, *Integrated Ferroelectrics 64 (2004), p.115*

[227] M. Grossmann, O. Lohse, D. Bolten, U. Boettger, T. Schneller, R. Waser: The interface screening model as origin of imprint in $PbZr_xTi_{1-x}O_3$ thin films. I. Dopant, illumination, and bias dependence, *J. Appl. Phys. 92 [5] (2002), p.2680*

[228] M. Grossmann, O. Lohse, D. Bolten, U. Boettger, R. Waser: The interface screening model as origin of imprint in $PbZr_xTi_{1-x}O_3$ thin films. II. Numerical simulation and verification, *J. Appl. Phys. 92 [5] (2002), p. 2688*

[229] A. Schönecker, H.-J. Gesemann, S. Merklein, W. Grond, K. Franke, M. Weihnacht: PZT-film compositional development and physical properties, *IEEE International Symposium on Applications of Ferroelectrics*, *(1994), p 412-415*

[230] J. H. Jang, K.H. Yoon: Electric fatigue properties of sol-gel-derived $Pb(Zr,Ti)O_3/PbZrO_3$ multilayered thin films, *Appl. Phys. Lett. 75 [1] (1999), p.130*

[231] D. Remiens, E. Cattan, C. Soyer, T. Haccart: Piezoelectric properties of sputtered PZT films: influence of structure, micro structure, film thickness (Zr,Ti) ratio and Nb substitution, *Mater. Sci. Semicon. Proc. 5 (2003), p.123*

[232] W. C. Goh, K. Yao, C.K. Ong: Pseudo-epitaxial lead zirconate thin film on silicon substrate with enhanced ferroelectric polarization, *Appl. Phys. Lett. 87, 072906 (2005)*

[233] J. Ouyang, R. Ramesh, A.L. Roytburd: Theoretical predictions for the intrinsic converse longitudinal piezoelectric constant of lead zirconate titanate epitaxial films, *Communications of Advanced Engineering Materials 7 [4] (2005), p.229*

[234] D. Damjanovic, D.V. Taylor, N. Setter: Crystal structure and texture effects on piezoelectric and dielectric properties of PZT thin films, *Ferroelectric Thin Films VIII. Symposium - Materials Research Society Symposium Proceedings Vol. 596*, (*2000), p.529*

[235] A. Kholkin: Non-linear piezoelectric response in lead zirconate-titanate (PZT) films, *Ferroelectrics Vol. 238 (2000), p.235*

[236] R. C. Rogan, E. Üstündag, Bjørn Clausen, M. R. Daymond: Texture and strain analysis of the ferroelastic behaviour of $Pb(Zr,Ti)O_3$ by in situ neutron diffraction, *J. Appl. Phys. Vol 93 [7] (2003), pp.4104*

[237] S. Zhu, W. Cao: Imaging of 180° ferroelectric domains in $LiTaO_3$ by means of scanning electron microscopy, *Phys. Stat. Sol. (a) 173, 495 (1999), p.495*

[238] R. LeBihan: Study of ferroelectric and ferroelastic domain structures by scanning electron microscopy, *Ferroelectrics, 97 (1989), p.19*

[239] H.R. Zenga, H.F. Yu, X.G. Tang, R.Q. Chua, G.R. Li, Q.R. Yin: Piezoresponse force microscopy studies of nanoscale domain structures in ferroelectric thin film, *Mater. Sci. Eng. B 120 (2005), p.104*

[240] Y. L. Li, S. Y. Hu, L. Q. Chen: Ferroelectric domain morphologies of (001) $PbZr_{1-x}Ti_xO_3$ epitaxial thin films, *J. Appl. Phys. 97, 034112 (2005), p.97*

[241] J. M. Marshall, Q. Zhang and R. W. Whatmore: Orientation control of low temperature deposited sol-gel PZT52/48 films, *Ferroelectrics, 318 (2005), p.41*

[242] G.J. Norga: L. Fe, F. Vasiliu, J. Fompeyrine, J.-P. Locquet, O. Van der Biest: Orientation selection in functional oxide thin films, *J. Eur. Ceram. Soc. 24 (2004), p.969*

[243] Z. Huang, Q. Zhang, R. W. Whatmore: The role of an intermetallic phase on the crystallization of lead zirconate titanate in sol-gel process, *J. Mater. Sci. Lett. 17 (1998), p.1157*

[244] Z. Huang, Q. Zhang, R. W. Whatmore: Structural development in the early stages of annealing of sol–gel prepared lead zirconate titanate thin films, *J. App. Phys. Vol. 86, [3] (1999), p.1662*

[245] S.S. Sengupta, S.M. Park, D.A. Payne: Integrated electroceramics: Densification and stress development in sol-gel derived thin layers, *Integrated Ferroelectrics, Vol. 14, (1997), p.193*

[246] P. Gkotsis, internal presentation

[247] W.-H. Xu, D. Lu, T.Y. Zhang: Determination of residual stresses in $Pb(Zr_{0.53}Ti_{0.47})O_3$ thin films with Raman spectroscopy, *Appl. Phys. Lett. Vol. 79, [25], (2001), p.4112*

[248] E. Zakar, R. Palcawich, M. Dubey, J. Pulskamp, B. Piekarski, J. Conrad, R. Piekarz: Stress Analysis of SiO_2/Ta/Pt/PZT/Pt Stack for MEMS Application, *ISAF 2000. Proceedings of the 2000 12th IEEE International Symposium on Applications of Ferroelectrics, (2000), p.757*

[249] M.Zhang, D.L. Polla, S.M. Zurn, T. Cui: Stress and deformation of PZT thin film on silicon wafer due to thermal expansion, *Mat. Res. Soc. Symp. Proc. Vol. 574 (1999), p.107*

[250] R.J. Onga, T.A. Berfield, N.R. Sottos, D.A. Payne: Sol–gel derived $Pb(Zr,Ti)O_3$ thin films: Residual stress and electrical properties, *J. Eur. Ceram. Soc. (2005) in press*

[251] S. Seifert, D. Sporn, T. Hauke, G. Müller, H. Beige: Dielectric and electromechnical properties of sol-gel prepared PZT thin films on metallic substrates, *J. Eur. Cer. Soc. 24 (2004), p.2553*

[252] W. Gong, J.-F. Li, X. Chu, Z. Gui, L. Li: Preparation of (100)- and (111)-textured $Pb(Zr,Ti)O_3$ piezoelectric films and direct measurement of their piezoelectric constants, *Jpn. J. Appl. Phys. Vol. 42 (2003), p. L1459*

Appendix A: Sample lists

PZT 40/60

Sample batch PZT 40/60-Pt(111)/Si-3µm-10 comprised 10 samples deposited on Pt(111)/Si. Indivudual samples are film 1 to film 10. Single layer thickness is 200 nm. All films were 3 µm thick.

Tab. A1: Individual PZT 40/60 samples:

	full sample name	substrate	single layer thickness	total thickness
film 11	PZT 40/60 -Pt(111)/Si/2" - 2 µm film 11	Pt(111)/Si 2inch wafer	200 nm	2 µm
film 12	PZT 40/60 -Pt(111)/Si/2" - 2 µm film 12	Pt(111)/Si 2inch wafer	300 nm	2 µm
film 13	PZT 40/60 -Pt(111)/Si/2" - 5 µm film 13	Pt(111)/Si 2inch wafer	200 nm	5 µm
film 14	PZT 40/60 Pt(200)/Si/3" - 2 µm film 14	Pt(200)/Si 3inch wafer	200 nm	2 µm
film 15	PZT 40/60 Pt(111)/Al_2O_3/3" - 3.4 µm film 15	Pt(111)/Al_2O_3 3inch wafer	200 nm	3.4 µm
film 16	PZT 40/60 -Al_2O_3 - 1.2 µm film 16	Al_2O_3	200 nm	1.2 µm
film 17	PZT 40/60 Pt(111)/Si/Pt/2" - 2 µm film 17	Pt(111)/Si/Pt 2inch wafer	200 nm	2 µm
film 18	PZT 40/60 Pt(111)/Si/Pt/4" - 2 µm film 18	Pt(111)/Si/Pt 4inch wafer	200 nm	2 µm
film 19	PZT 40/60 Pt(111)/SOI/4" - 2 µm film 19	Pt(111)/SOI 4inch wafer	200 nm	2 µm

PZT 52/48

Sample batch PZT 52/48-Pt(111)/Si-2µm-10 comprised 10 samples deposited on Pt(111)/Si. Indivudual samples are film 1 to film 10. Single layer thickness is 200 nm. All films were 2 µm thick.

Tab. A2: Individual PZT 52/48 samples

	full sample name	substrate	single layer thickness	total thickness
film 11	PZT 52/48-Pt(111)/Si - 3 µm -film 11	Pt(111)/Si	160 nm	2.2 µm
film 12	PZT 52/48-Pt(111)/Si - 3 µm -film 12	Pt(111)/Si	200 nm	3 µm
film 13	PZT 52/48-Pt(111)/Si - 3 µm -film 13	Pt(111)/Si	130 µm	1.7 µm
film 14	PZT 52/48-PbO/Pt(111)/Si/3”- 3 µm-film 14	PbO/Pt(111)/Si 2inch wafer	200 nm	2 µm
film 15	PZT 52/48-LNO/Si/2”- 2.4 µm-film 15	LNO/Si 2inch wafer	200 nm	2 µm
film 16	PZT 52/48-LNO/Si/2”- 2 µm-film 16	LNO/Si 2inch wafer	200 nm	2 µm
film 17	PZT 52/48-LNO/Si/2”- 2 µm-film 17	LNO/Si 2inch wafer	200 nm	2 µm
film 18	PZT 52/48-LNO/Si/2”- 2 µm-film 18	LNO/Si 2inch wafer	200 nm	2 µm
film 19	PZT 52/48-Pt(200)/Si/3”- 2 µm-film 19	Pt(200)/Si 3inch wafer	200 nm	2 µm
film 20	PZT 52/48-Pt(111)/Al_2O_3/3” - 1.2 µm-film 20	Pt(111)/Al_2O_3	200 nm	1.2 µm
film 21	PZT 52/48-Pt(111)/Si/2”- 2 µm - film 21	Pt(111)/Si 2inch wafer	200 nm	4 µm
film 22	PZT 52/48-Pt(111)/Si/4”DS- 2 µm - film 22-side A	Pt(111)/Si 4inch wafer, double side polished	70 nm	1.1 µm
film 23	PZT 52/48-Pt(111)/Si/4”DS- 2 µm - film 23-Side B	Pt(111)/Si 4inch wafer, double side polished	70 nm	0.9 µm
film 24	PZT 52/48-Pt(111)/Si/2”- 3 µm-film 24	Pt(111)/Si 2inch wafer	200 nm	3.4 µm

PZT 60/40

Sample batch PZT 60/40-Pt(111)/Si-3µm-6 comprised 6 samples deposited on Pt(111)/Si. Indivudual samples are film 1 to film 6. Single layer thickness is 200 nm. All films were 3 µm thick.

Tab. A3: Individual PZT 60/40 films:

	full sample name	substrate	single layer thickness	total thickness
film 7	PZT 60/40-Pt(111)/Si/2” - 5 µm -film 7	Pt(111)/Si 2inch wafer	200 nm	5 µm
film8	PZT 60/40-Pt(111)/Si/2” - 5 µm -film 8	Pt(111)/Si 2inch wafer	200 nm	5 µm
film 9	PZT 60/40-Pt(200)/Si/3” - 2 µm -film 9	Pt(200)/Si 3inch wafer	200 nm	2 µm

Appendix B: Phase identification in sol-gel PZT films with different Zr/Ti ratio

From the X-ray diffraction patterns, the peak position and splitting of (111) and (002)/(200) peaks were used for evidence of the rhombohedral and the tetragonal phases, respectively. An example of detected peak positions for (111) peaks of the rhombohedral, the tetragonal and MPB PZT phases are depicted in Fig. B1. The tetragonal phase, PZT 40/60, has one (111) peak at 2θ= 38.251° due to tetragonal crystal symmetry. The $d_{(111),t}$=2.351 Å. The rhombohedral phase, PZT 60/40, shows two peaks (111) and (-111) at 2θ =37.97° and 2θ =38.45°, respectively, due to its rhombohedral crystal symmetry. The lattice spacing is $d_{(111),r}$=2.368 Å and $d_{(-111),r}$= 2.339 Å. These two peaks are usually overlapping and could be revealed only if both peaks were present and their intensity was sufficient for a peak deconvolution. The rhombohedral peaks can shift their positions towards lower 2θ−angles in comparison to the tetragonal phase. The peak shift is due to the larger unit cell parameters given above.

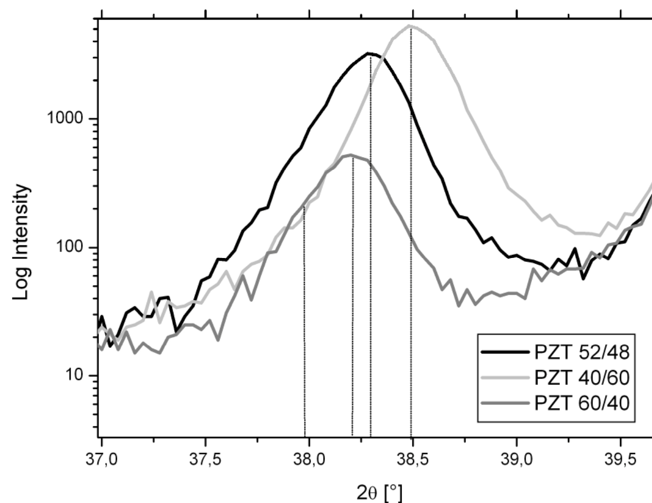

Fig. B1: Positions of (111) peak of all three PZT compositions.

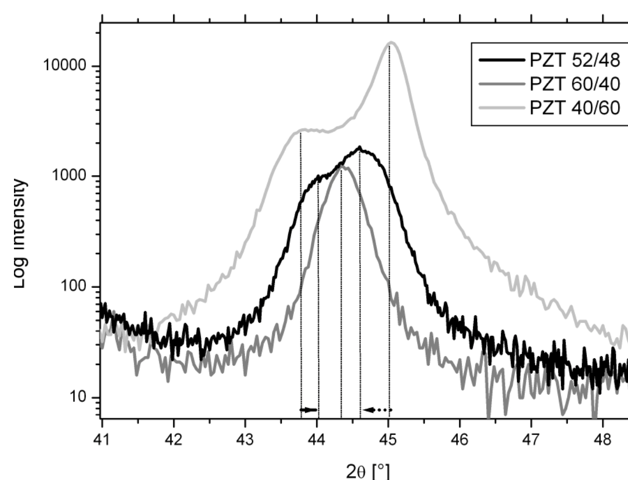

Fig. B2: Positions of (200)/(002) peaks in all three PZT compositions.

The peak positions of single phase PZT were usually found at the peak positions as depicted in Fig. B1. The (111) peak of PZT 52/48 was usually slightly shifted towards lower 2θ−angles when compared to the corresponding peak positions of single phases PZT 40/60 and PZT 60/40. Depending on the phase content and the texture of the phases a maximum of three peaks can be present in the film. In the diffractorgram this would appear as one large peak with one or two broadening towards either the tetragonal or rhombohedral phase. When both phases were present and if both phases showed a sufficient peak intensity in the XRD data, the (111) peak of PZT 52/48 could be deconvolved into 3 peaks. A peak split of the PZT 52/48 (111) peak into at least two peaks was evident for the existence of the rhombohedral phase.

Fig. B2 gives the peak positions of the (200) lattice plane of three compositions. The tetragonal peak split of PZT 40/60 was well pronounced, the peak positions were 2θ=43.626° and 2θ =44.879° according to the PCPDF file. This equals the lattice parameters d_{002}=2.073Å and d_{200}=2.018Å. The rhombohedral (200) peak was positioned between the two tetragonal peaks with the 2θ=44.56° and a=4.064 Å.

The (200) peak of the PZT 52/48 showed some splitting which was evidence for the tetragonal phase existence. The peak positions were closer to each other in the MPB PZT than in the tetragonal phase, indicating different unit cell parameters. Supposed the rhombohedral phase had a strong (200) preferred orientation it would be possible that the rhobomhedral peak overlapped and covered the tetragonal peaks and as a result only

one broad peak would have been detected. Such peaks could have been easily misinterpreted.

The determination of peak positions and number through deconvolution method and the comparison with the single phase PZT enabled the structural identification of MPB PZT. PZT 52/48, as a composition at the morphotropic phase boundary, can exist as a mixture of both phases and only a careful analysis of both peaks, (111) and (200) gave full indication of the film phase content. The peak positions of the rhombohedral phase of PZT 60/40 and of the tetragonal phase are given in Tab. B1 and B2 respectively, and those of the tetragonal phase PZT 40/60 in Tab. 2. The peak positions calculated by Marshall [215] is included for comparison.

Tab. B1: Peak positions [in degrees] of PZT 60/40films.

	peak position [°]			
	1µm	**2µm**	**3µm**	**Marshall [215]**
(100)	21.73	21.77	21.79	21.85
std. dev.	0.034008	0.006557	0.015341	
2*(200)	44.36	44.37	44.39	44.56
std. dev.	0.052824	0.01536	0.0129	
(111)		38.076	38.130	37.97
std. dev.		0.030806	0.111225	
(-111)	38.324	38.170	38.212	38.45
std. dev.	0.612104	0.084642	0.011234	

Tab. B2: Peak positions [in degrees] of PZT 40/60.

	(001)	**(100)**	**(002)**	**(200)**	**(111)**
1 µm	21.542	22.067	44.015	45.104	38.507
deviation	0.161	0.018	0.298	0.018	0.014
2 µm	21.504	22.006	43.840	45.103	38.4907
deviation	0.128	0.216	0.057	0.026	0.030434
3 µm	21.479	22.045	43.809	45.073	38.46878
deviation	0.147	0.058	0.056	0.057	0.050633

Phase identification in PZT 52/48

An optimum resolution of peaks (111) and (200) in PZT 52/48 is shown in Fig. B3. In both peaks there was some evidence of both phases and thus the measured peaks were each deconvolved into 3 peaks. These are also shown in Figure B4. The peak fit r^2 was better than 0.999. However, in some films the peaks were overlapping and the deconcolution was difficult due to the higher texture of one phase over the other phase.

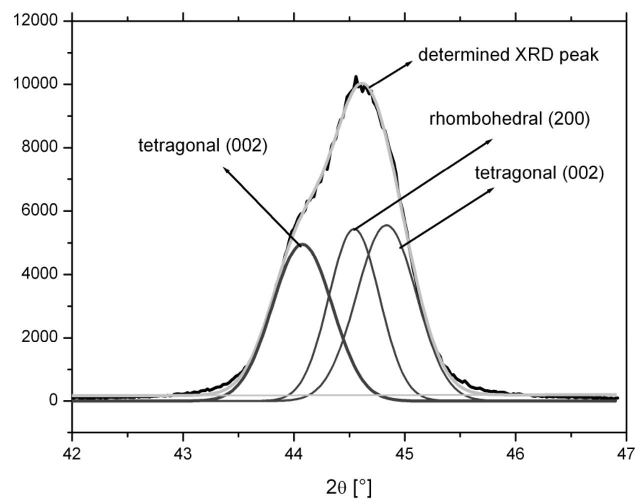

Figure B3: Deconvolved (200) peaks PZT 52/48.

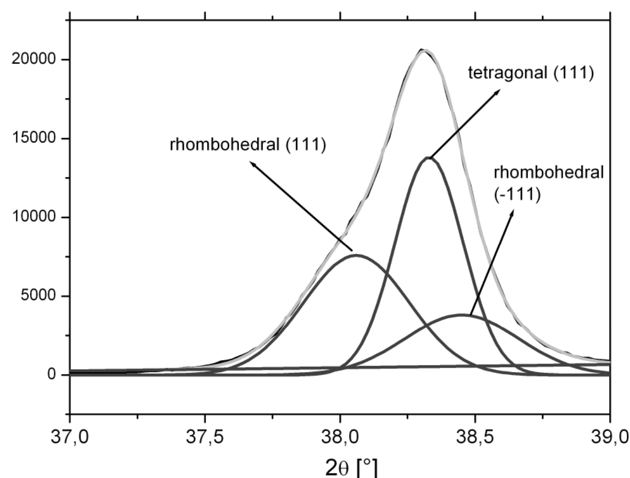

Figure B4: Deconvolved (111) peaks in in PZT 52/48

Appendix C: Anisotropic wafer bending

Some initial deformation was found in all new siliocn wafers, introduced through the manufacturing processes, such as polishing or cleaning procedures. The initial curvature and the wafer shape differed from wafer to wafer and the deflection was mostly in the range between -10 and 10 µm for a 2″ wafer. To characterize the wafer bending platinum was sputter coated followed by PZT deposition. PZT film was 2 µm thick. Several parallel and equidistant scans were taken across the wafer, all having the starting point along the same line as indicated by the square and the arrows in Fig. C1. Then the wafer was turned for 90° and the scans were repeated in the same way. The results are depicted in Fig. C2. During the measurement it was noticed that the deflection towards the edges of the wafer was highere. Such deflection is obtained if the total length of the wafer is different from scan to scan although the scan length was same in all cases. In Figure B2a it is shown how larger deflection of longer total length can be obtained although the curvature is the same for both lengths. The scan length was always the same but the total length of the wafer was different from scan to scan, dependent on the position on the wafer. In longer pieces of the wafer lower deflection can be found although the wafer curvature was the same as in the shorter piece. This influence of the wafer length on the deflection can be misleading and was mathematically corrected for all results.

Both diagrams in Fig. C2b and C2c are pointing into the same direction. In both diagrams stronger deflection was found towards the flats of the wafer, indicated by the red circles. In the centre of the wafer lower deflection was found and in the Fig. C2b some positive deflection in the centre was found even if the total deflection was negative. The total deflection in the Fig. C2b is much lower than in Fig. C2c. Thus, the wafer shows saddle shape due to the silicon wafer anisotropy [C1]. The other possible shape due to anisotropy can be a cup shape but has not been found in any substrate. The anisotropic wafer bending shows another limitation and possible error source for the stress measurement. To minimize the error the measurement must always be taken along the same line and in the same direction of the wafer. Only values obtained along the same line are comparable. Also, wafers with the same shape and orientation should be used. The length of a scan should be always the same. Considering all points the

accuracy of the measurement was determined experimentally by repeating the scans for 5 times along the same line and also by removing and replacing the wafer onto the jig. The measurement error was determined to be below 5%. For the stress calculation the measured data need to be fitted and the curvature had to be calculated. The best curvature results were obtained for the fit of a polynomial function of the 8th order when the 5% of the edges was not considered in the fit.

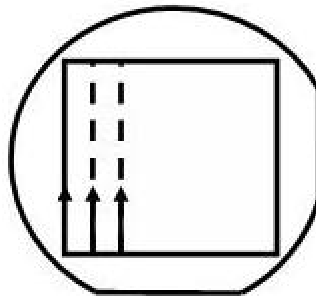

Fig. C1: Scan measurement direction in respect to the wafer orientation.

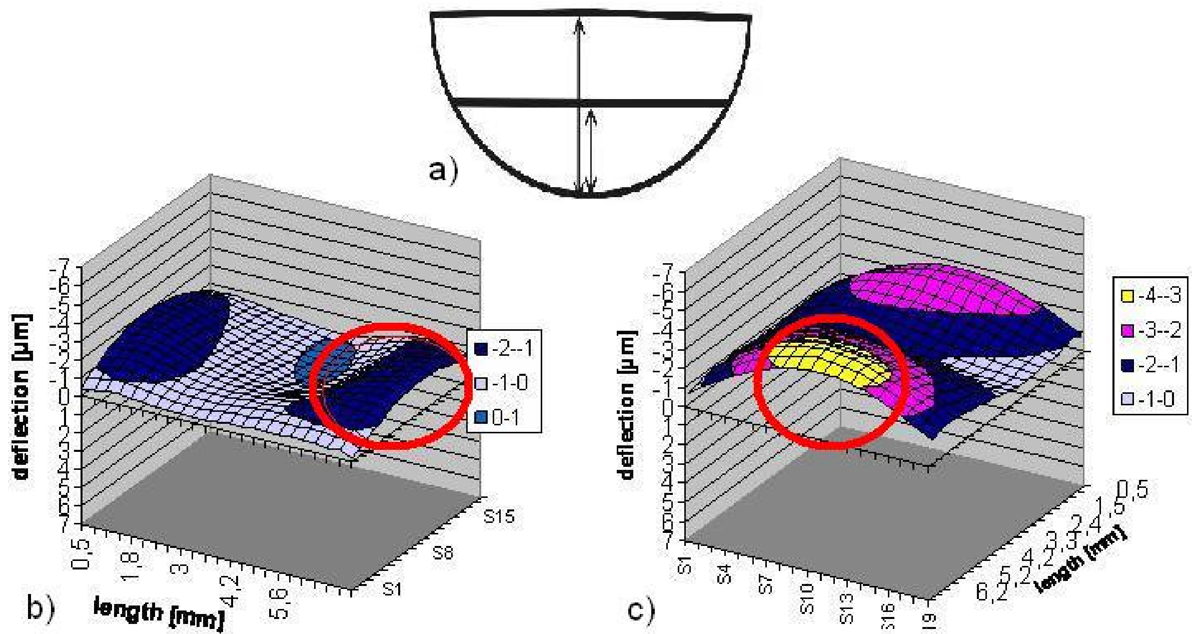

Fig. C2. a) Wafer size influence on the measurement, having the same curvature but different length which may result in different measured deflection values. b) Wafer bending after PZT deposition and c) A scan performed perpendicular to the scan in Fig.

b). Both diagrams were orientated facing into same direction. The wafer size was considered and the curvature was recalculated according to the figure in a).

[C1] Y. Li, A. Khounsary, M. Gosz: Effect of anisotropy on mirror substrate design, Advances in Mirror Technology for X-Ray, EUV Lithography, Laser and other Applications II, *Proceedings of SPIE Vol. 5533 (2004)*